Modelling water isotopes in polar ice sheets

Nicolas Lhomme

DEPARTMENT OF EARTH
AND OCEAN SCIENCES
The University of British Columbia
6339 Stores Road
Vancouver, BC V6T 1Z4
Canada

LABORATOIRE DE GLACIOLOGIE
ET GEOPHYSIQUE DE L'ENVIRONNEMENT
UMR5183
Centre National de la Recherche Scientifique
Université Joseph Fourier
54, rue Molière – Domaine Universitaire
BP 96 – 38402 – Saint Martin d'Hères Cedex France

MODELLING WATER ISOTOPES IN POLAR ICE SHEETS

NICOLAS LHOMME

Doctor of Philosophy in the Faculty of Graduate Studies (UBC)
Earth and Ocean Sciences

Thèse de doctorat de l'Université Joseph Fourier (Grenoble 1)
(Arrêtés ministériels du 5 juillet 1984 et 30 mars 1992)
Sciences de la Terre et de l'Univers

Defense/Soutenance : 30 November 2004

Jury :

Prof. David McClung	*President*
Prof. Kurt Cuffey	*Reporter*
Prof. Daniel Moore	*Reporter*
Prof. Dominique Weis	*Reporter*
Ass. Prof. Susan Allen	*Examiner*
Prof. Garry Clarke	***Thesis director***
Dr. Catherine Ritz	***Thesis co-director***

The University of British Columbia

CNRS CENTRE NATIONAL DE LA RECHERCHE SCIENTIFIQUE
Observatoire OSUG des Sciences de l'Univers de Grenoble
UNIVERSITE JOSEPH FOURIER SCIENCES.TECHNOLOGIE.SANTÉ

Abstract

Concentrations of water isotopes in marine sediments and ice cores are a key indicator for estimating global and regional fluctuations of past temperatures. Interpreting these concentrations requires an understanding of the storage capacity and exchanges among the ocean, atmosphere and cryosphere as well as an understanding of the dynamical behaviour of these reservoirs. The contribution of the latter remains poorly established because of the paucity of deep ice cores in Greenland and Antarctica and the difficulty of interpreting these cores.

To obtain the water isotope composition of polar ice sheets and gain an understanding of their stratigraphy, I develop a tracer transport method first proposed by Clarke and Marshall (2002) and significantly improve it by introducing an interpolation technique that accounts for the particular age–depth relationship of ice sheets. I combine the tracers with numerical models of ice dynamics to predict the fine layering of polar ice masses such that it is locally validated at ice core sites, hence setting a new method to constrain reconstructions of ice sheets' climatic and dynamic histories.

This framework is first applied and tested with the UBC Ice Sheet Model of Marshall and Clarke (1997). I predict the three-dimensional time-evolving stratigraphy of the Greenland Ice Sheet and use the ice core records predicted at GRIP, Dye 3 and Camp Century to better determine the minimal ice extent during the Eemian, 127 kyr ago, when the Earth's climate was somewhat similar to the present. I suggest that 3.5–4.5 m of sea level rise could be attributed to melting in Greenland. Tracers are also applied to Antarctica with the LGGE Ice Sheet Model of Ritz et al. (2001). The three-dimensional model is compared to simple flow models at the deep ice core sites of Dome C, Vostok and Dome Fuji to test the hypotheses on depositional and dynamical conditions used for interpreting ice cores. These studies lead to a well-constrained stratigraphic reconstruction of the Greenland and Antarctic Ice Sheets and allow me to produce the first-ever self-consistent prediction of their bulk isotopic composition, hence closing the global water isotope budget of the Earth.

Résumé

La concentration en isotopes de l'eau dans les glaces polaires et les sédiments marins est un précieux indicateur des températures passées. L'interprétation de ces concentrations nécessite de bien comprendre les échanges isotopiques entre l'océan, l'atmosphère et la cryosphère. La capacité de stockage et la dynamique de cette dernière restent très mal connues à cause de la rareté des échantillons de glace prélevés en Antarctique et au Groenland. Cette thèse met au point une méthode de traçage particulièrement adaptée à la glace polaire et combine des modèles 3D de dynamique de la glace pour prédire la fine stratigraphie des calottes du Groenland et de l'Antarctique. Cette méthode est validée en comparant la prédiction du modèle avec la stratigraphie aux sites de forage polaire profonds, ce qui permet de retrouver les conditions climatiques et dynamiques de formation des calottes de glace. En utilisant le modèle d'évolution du Groenland de l'UBC développé par Marshall at Clarke (1997) et les traceurs pour les sites de GRIP, Dye 3 et Camp Century, je parviens à déterminer plus précisément l'extension minimale de la calotte groenlandaise lors de la précédente période inter-glaciaire. Mes analyses suggèrent une montée de 3.5 à 4.5 m du niveau des mers il y a 127000 ans due à de la fonte au Groenland. Les conditions de formation des carottes de glace profonde prélevées en Antarctique à Vostok, Dome Fuji et Dome C sont aussi examinées en combinant les traceurs au modèle 3D du LGGE de Ritz et al. (2001). On peut ainsi tester les hypothèses utilisées pour interpréter ces enregistrements climatiques et révèler les changements d'altitude et de morphologie de la surface des calottes. En prédisant ainsi la fine stratigraphie des calottes groenlandaise et antarctique, mon étude fournit la première estimation glaciologique de la composition isotopique moyenne de la glace pour le présent et le passé et permet de boucler le budget en isotope de l'eau de notre planète.

Table of contents

List of Tables

List of Figures

List of symbols

A	Accumulation rate	m yr^{-1}
$\mathcal{A}$	Surface area	m^2
$\dot{b}$	Surface mass balance	m yr^{-1}
B	Bebrock elevation above modern sea level	m
B_0	Glen flow law constant	Pa^{-3} yr^{-1}
BP	Before Present, Present defined as year 1950	
c	Specific heat capacity of ice	J kg^{-1} $^\circ$C^{-1}
D_{acc}	Precipitation sensitivity	$^\circ$C^{-1}
E	Enhancement factor in the ice flow law	
E_{G}	Enhancement factor for ice deposited during a glacial period	
E_{I}	Enhancement factor for ice deposited during an interglacial period	
$\dot{f}$	Basal melt rate	m yr^{-1}
H	Ice thickness	m
K	Thermal conductivity of ice	W m^{-1} K^{-1}
k_{sl}	Sliding parameter (Weertman-type law)	m yr^{-1} Pa^{-2}
L	Time integral of annual layers	m
n_ψ	Quantity of species ψ (e.g., number of moles)	
P	Precipitation rate	m yr^{-1}
q_{geo}	Geothermal heat flux	mW m^{-2}
Q	Creep activation energy	J mol^{-1}
R	Ideal gas constant	J mol^{-1} K^{-1}
S	Surface elevation above modern sea level	m

t	Time	yr
T	Temperature	K
t_{init}	Initial time for a simulation	kyr BP
T_{s}	Surface temperature	°C
t_{d}	Depositional age	kyr BP
X	Direction parallel to longitude 90°E for Antarctica	km
x_{d}	Depositional coordinate along X	km
Y	Direction parallel to longitude 0°E for Antarctica	km
y_{d}	Depositional coordinate along Y	km
z	Elevation above modern sea level	m
α	Fractionation coefficient	
α_{c}	Climate isotopic sensitivity	$‰\,°\mathrm{C}^{-1}$
α_{cE}	Isotopic sensitivity during the Eemian	$‰\,°\mathrm{C}^{-1}$
α_{cG}	Isotopic sensitivity during glacial periods	$‰\,°\mathrm{C}^{-1}$
α_{cH}	Isotopic sensitivity during the Holocene	$‰\,°\mathrm{C}^{-1}$
β_δ	Isotopic lapse rate (for $\delta^{18}\mathrm{O}$)	$‰\,\mathrm{m}^{-1}$
β_{T}	Temperature lapse rate	$°\mathrm{C}\,\mathrm{m}^{-1}$
γ	Topographic effect on precipitation	
δ	Isotopic ratio	‰
δ_0	Initial isotopic ratio during fractionation	‰
$\delta\mathrm{D}$	Deuterium ratio	‰
$\delta\mathrm{D}_{\mathrm{sw}}$	Deuterium ratio of sea water	‰
$\delta^{18}\mathrm{O}$	Oxygen isotopic ratio	‰
$\delta^{18}\mathrm{O}_{\mathrm{atm}}$	Oxygen isotopic ratio in atmospheric O_2	‰
$\delta^{18}\mathrm{O}_{\mathrm{c}}$	Oxygen isotopic ratio of calcite	‰
$\delta^{18}\mathrm{O}_{\mathrm{sw}}$	Oxygen isotopic ratio of sea water	‰
ΔT	Change of temperature	°C
ΔT_{c}	Change of temperature in the climate over an ice sheet	°C
ΔT_{s}	Change of surface temperature	°C
τ	thinning	
$\dot{\epsilon}_{jk}$	strain rate tensor	yr^{-1}
θ_{d}	Depositional latitude (for Greenland)	°N
κ	Coefficient of proportionality	
λ_{d}	Depositional longitude (for Greenland)	°E
ξ	Reduced vertical coordinate	
Ξ	Strain heating due to ice deformation	$\mathrm{J}\,\mathrm{m}^{-3}\,\mathrm{yr}^{-1}$
ρ	Density	$\mathrm{kg}\,\mathrm{m}^{-1}$
σ'_{ik}	Deviatoric stress tensor	Pa
ϕ	Compressive thinning in reduced coordinate	
Φ	Integral of thinning within a given layer	m
ψ	Compressive thinning of an annual layer	
Ψ	Property to be tracked	
ω	Thickness of an annual layer of ice	m
ω_0	Initial thickness of an annual layer of ice	m
Ω	Cumulative mass balance function	m

Preface

This manuscript was submitted to obtain both the degree of Doctor of Philosophy from the University of British Columbia and the title of Docteur ès Sciences from Université Joseph Fourier, as part of a co-directed study with Garry Clarke at UBC and Catherine Ritz at Laboratoire de Glaciologie et Géophysique de l'Environnement.

Because parts of Chapters 3, 4, 5, and of Appendices B and C contain material from the papers by Clarke et al. (in press) and Lhomme et al. (in press) that have recently been accepted for publication in Quaternary Science Reviews, I would like to clarify what corresponds to my personal contribution here. In Chapter 3, Sections 3.2.2 and 3.2.3 rephrase and add scientific arguments to the discussion written by Clarke (Section 2, Clarke et al., in press) to justify the principles of tracer transport that he first introduced in Clarke and Marshall (2002). Appendix B describes his manner of implementing tracers on a geographically-oriented grid. The rest of Clarke et al. (in press) appears in Chapter 4 and represents my own research and ideas: the modifications to the ice dynamics model and to the climate forcing and the resulting stratigraphic sections. Chapter 5 and most of Appendix C correspond to Lhomme et al. (in press). Marshall is associated with both papers as the designer of the original ice sheet model that was applied for studying Greenland.

Acknowledgements

First of all, I would like to thank Garry Clarke at UBC for offering me his trust, his advice, the freedom to find my own path and organize my time between Vancouver and Grenoble, and for letting me borrow his ingenious tracer scheme upon which my research project was founded. I would also like to thank Catherine Ritz at UJF/LGGE for initiating me to the field of glaciology even though she knew from the start that I wanted to go abroad for my PhD, for helping me organize a co-directed thesis that greatly benefited me and for providing counsel even during the toughest times. Shawn Marshall at U. of Calgary has been very generous by giving me his world of an ice sheet model and the essential keys for understanding the complexity of this monster. Susan Allen at UBC helped with pertinent suggestions for my manuscript.

It has been a pleasure interacting both scientifically and socially with the glaciology and paleoclimatology community. The glaciology group at UBC is a friendly and stimulating bunch. Special thanks to Tim Creyts, Gwenn Flowers, Dave Hildes and Fern Webb. In Grenoble, I especially thank Frédéric Parrenin for engaging discussions and precious reviews, Christian Vincent for loading me like a mule as often as I wanted to during the field season, and Dominique Raynaud for his inspiring energy. Thanks to Jean Jouzel, Valérie Masson and Georg Hoffmann for interesting discussions on isotopes and good advice, Kurt Cuffey and Richard Alley for sharp and challenging reviews, Peter Clark for inviting me to the EPILOG meeting, where my project stemmed. I thank for their funding the UBC Graduate Fellowships (UGF), the Lorntzen & MacKay Fund, the Natural Sciences and Engineering Research Council of Canada (NSERC), the Region Rhone-Alpes' program for co-directed theses (EURODOC) and the Conseil General du Haut-Rhin. Most of the computation was performed on the MIRAGE platform at UJF.

Living and studying both in Vancouver and in Grenoble has exposed me to wonderful persons that contributed in one way or another to my inspiration, enlightenment and/or entertainment. Thanks to all the fellow graduate students and scientists from UBC and LGGE, your welcome and kindness made this thesis an almost painless experience. More specifically, in Vancouver, my friends Len, Nigel, Steve and Phil have been the funniest bunch in the coffee room, and also the companions and instigators of many parties, trips and adventures. They greatly helped making Vancouver a second home for me. Terry, Laurent, Candice, Meg&Mike, Mandy, Dave W., Chris&Tamsin, Kim&Colin, Mélanie and Katrin all contributed in their manner to my scientific achievements or to my entertainment. Thanks to Tony and Margret for hosting me and revealing me where to satisfy my delicate taste buds. Cumulating many visits, I spent about one year over the past five in France, which helped me continue to preserve and grow my essential scientific and friendship connections. Roy, Olivier, Raphaël, Patrick, Sébastien, David, Olivier (aka Mortel), Vincent, Ulrika, Fredrik and Jérémie fuelled me up with their good humour and the many fun trips we took in the Alps.

Finally, I would like to thank my family. My parents, for their constant inspiration and support. My brother Stanislas, for hosting me and feeding me every time I arrived in Grenoble like a ski-bum, and also for cheering me up during this long stretch of a thesis. Kristina, thank you for accompanying me here with your love, your patience and support.

à ma famille,

CHAPTER 1

Introduction

1.1 Context and objectives

Climate has changed; it still does. A vast majority of those involved in the scientific study of the Earth, Ocean and Atmosphere are convinced that our planet is experiencing "Global Warming" that is clearly linked to the greenhouse-gas emissions associated with the use or abuse of natural resources. The recent but long-term impact of humankind on the global environment and on the climate is such that the beginning of a human-dominated geological era coined the "Anthropocene" has been suggested (Crutzen, 2002). Indeed, according to the last report of the *Intergovernmental Panel on Climate Change* (IPCC, 2001), the global average surface temperature on Earth has risen by $\sim$0.6°C over the past century, the largest change over the past 1000 years, with a clear acceleration over the past two decades. The IPCC Summary for Policymakers also shows soaring temperatures in the lower 8 km of the atmosphere, a decrease in snow cover and ice extent, an increase in sea level and in ocean temperature and many other climatic changes that seem to especially affect regions of high latitudes like the Canadian Arctic. Predictions with scientifically reliable models suggest that temperature is going to continue to climb over the 21$^{\text{st}}$ century by 1.4 to 5.8°C, along with changes in climate patterns and extreme events for which our societies appear ill-prepared. The tone may sound apocalyptic and has attracted the public attention, but uncertainties in those predictions have also instigated doubt, if not suspicion. Research to improve comprehension of the climate-system operation is therefore essential to persuade both the public and the decision makers.

Climate mechanisms and sensitivity to change have been particularly well revealed by the study of past climatic events, from which we have learned, for example, that dramatic shifts can happen in less than a few decades (e.g., Severinghaus and Brook, 1999). Paleoclimate research involves two distinct processes: the collection and analysis of data (e.g., meteorologic stations, cores in marine and lacustrine sediments and in glacier ice, but also tree rings, pollens, dates of grape harvests) and the imagination and modelling of the natural phenomena that are responsible for the changes measured in the records. The most used, if not the best, indicators of past temperature are the stable oxygen isotope ratio $^{18}\text{O}/^{16}\text{O}$ and the deuterium/hydrogen ratio (D/H) of water, because temperature exerts a strong control on the evaporation and precipitation rate of water with different isotopic composition (Dansgaard, 1964), as illustrated in Fig. 1.1. This fractionation is the base for interpreting ice-core and marine-sediment-core records that sample up to hundreds of thousand years of climatic history. The final composition of water also depends on the original availability of the different isotopic species; thus, we must know the past and present volume and isotopic composition of the main water reservoirs (atmosphere, hydrosphere, cryosphere). The volume of the cryosphere significantly varied over the past 2 Myr as the Earth's climate was marching through a succession of periods like the present called interglacials, and 80-kyr-long glacial periods during which extensive ice sheets grew and covered up to half of North America (Laurentide Ice Sheet) and most of Northern Europe (Fennoscandian Ice Sheet). These variations strongly disrupted the entire water cycle and drew down sea level by as much as 135 m (e.g., Yokoyama et al., 2000; Clark and

Mix, 2002). The composition of the cryosphere and hydrosphere varied accordingly because of the changes in temperature and the storage of large quantities of ^{18}O-depleted water on the continents (Fig. 1.1). History clearly demonstrates that continental ice is an important component of the climate system: an actor, a reservoir and, as we shall see, a precious archive. However, as I clearly became aware during the excellent EPILOG meeting at Mt. Hood in September 2000 (Clark and Mix, 2002)), the volume and isotopic composition of past ice sheets is poorly known (Duplessy et al., 2002). This uncertainty maintains a long-standing debate about past temperature conditions and sea levels at critical stages of Earth's past climatic history (Emiliani, 1955; Dansgaard and Taubert, 1969; Waelbroeck et al., 2002).

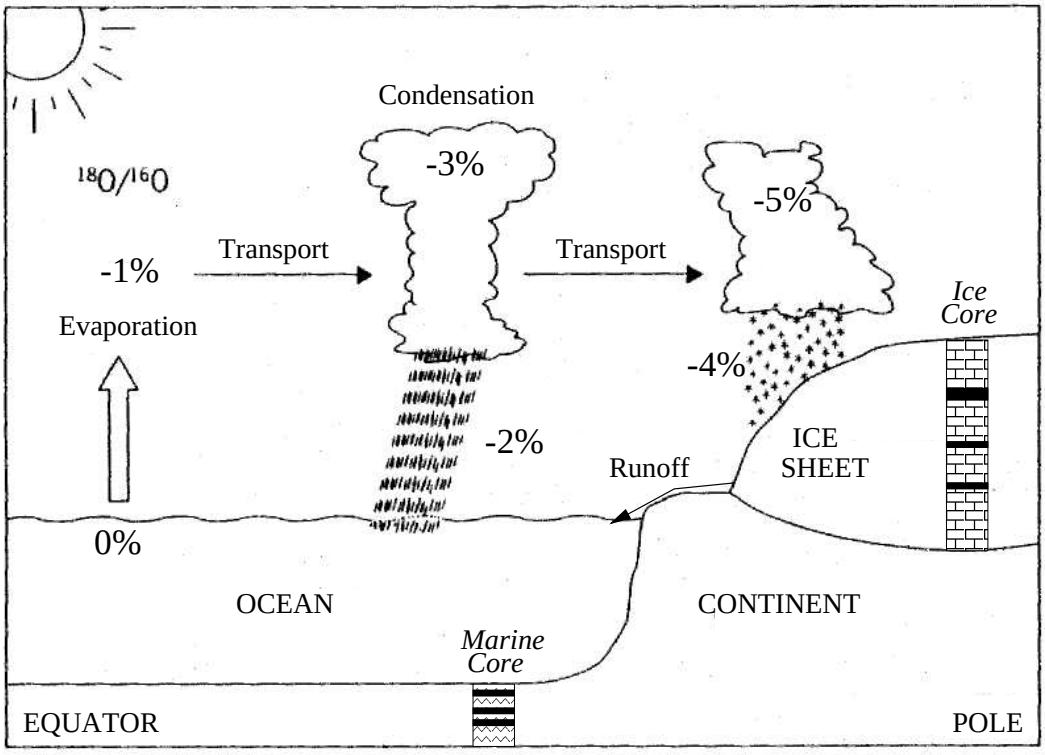

Figure 1.1: The global water isotope fractionation cycle and exchanges between the main reservoirs. Separation between light ^{16}O and heavy ^{18}O occurs during evaporation and condensation; the degree of separation between oxygen isotopes relative to ocean water composition is indicated as %. Adapted from Joussaume (1999).

Modern ice sheets and glaciers, the only remnants of the vast disappeared ice masses, also remain to be fully understood. For a paleoclimatologist, they consitute both an invaluable archive of the chemical makeup of the atmosphere with their ice core records, and a poorly known reservoir of water isotopes. For a climatologist, they represent a large and potentially unstable threat to modern sea level. For a glaciologist, they are a living example of the disappeared Laurentide and Fennoscandian giants; thus, they are a natural laboratory with particular geometric and flow features that can be used as indicators or constraints to understand internal ice dynamics and assess the sensitivity to and the role of ice sheets in past climatic events. Their ice core records have generated much attention because they can contribute to the interests of all these communities. Ideally, they can provide a detailed history and a continuous sampling of the depositional conditions above Greenland and

Antarctica. Their vertical stratigraphy carries a signature of the ice flow, which can be an obstacle to interpretation of the age–depth relation, but is also a precious indication of flow regime and ice rheologic properties for glaciologists and ice sheet modellers. An integrative approach to the study of ice sheets and ice cores has yet to be achieved.

Relying on numerical models of ice dynamics (Marshall and Clarke, 1997; Ritz et al., 2001), my thesis attempts to reduce some of the aforementioned uncertainties and devise an integrative approach by developing a method to follow water isotopes and other properties in ice. In this manner, we can better account for the ice-core information and estimate the bulk isotopic composition of the Greenland and Antarctic Ice Sheets. Devising this tracing approach has sprouted many possible applications that here serve as intermediate but nonetheless informative steps of my research. Tracers are used to simulate the global stratigraphy of an ice sheet, giving a result that depends on the history of climate and ice dynamics that was assumed. The accuracy of the prediction can be locally checked at ice core sites, a criterion which, combined with other requirements, can validate the assumed history and help better constrain our reconstruction of crucial periods of the past. Of special interest are the Last Glacial Maximum (LGM) about 20 kyr ago, when climate reached its coldest stage and ice sheets their maximum extent, and past interglacial periods, when climatic conditions where somewhat analogous to the present. Accurate matching of ice core records also exposes the complex interplay of climate and ice flow that produced these invaluable records and thus promotes understanding of their climatic signature by removing the effect of changes in surface topography and ice origin. This capability could additionally be used to facilitate recovery of the chronology and exact timing of past climate events.

My research was mostly conducted at UBC within the glaciology group, but my progress and awareness have greatly benefited from several stays at the Laboratoire de Glaciologie et Géophysique de l'Environnement (LGGE, UJF–CNRS) in Grenoble, where I spent a total of one year and was exposed to the many questions surrounding Antarctic climate records, and a couple of visits to the Laboratoire des Sciences du Climat et de l'Environnement (LSCE, CEA–CNRS) in Saclay, where the secrets of isotopes were opened to me. I close this introductory chapter by summarizing the outline and content of the main chapters to help the reader navigate through this manuscript.

1.2 Thesis outline

The first chapter introduces the general phenomena and questions that are necessary to understand and pursue this research. I start by reviewing the role of ice sheets in the climate and the concept of astronomic influence on glacial–interglacial cycles. I acquaint the reader with the Antarctic and Greenlandic ice core records and the wealth of information about the Earth's past atmosphere encrypted in polar ice. Then I explain how stable water isotopic concentrations retain a signature of past temperature, how that signature is preserved in ice and how ice flow models can be employed to assess the evolution of ice sheets or reveal the chronology of past events.

The next chapter introduces the principles and methods I used and developed to model tracers in ice sheets, starting from Garry Clarke's intuition that transport of depositional age and origin can yield more information and accuracy on ice stratigraphy than direct modelling of water-isotope concentration in ice (Clarke and Marshall, 2002). The method is perfected and applied to the Greenland Ice Sheet and subsequently extended to the Antarctic Ice Sheet.

The following chapters present a series of applications and validation tests that culminate in chapter 8 with the prediction of the past and present bulk isotopic composition of the Greenland

and Antarctic Ice Sheets, and their contribution to sea level and seawater isotopic composition at critical periods of the past. Chapter 4 and 5 focus on the Greenland Ice Sheet. The stratigraphy and glacial history is predicted with the UBC ice sheet model designed by S. J. Marshall in chapter 4. Ice core records are accurately matched, demonstrating that a large scale ice dynamics model with coarse resolution and simple parameterization of the climate can predict the fine layering of deep ice core records and represent most of the variability found in these records. Chapter 5 builds on these premises to explore a range of climatic and dynamic parameters to estimate the uncertainty on ice sheet reconstructions and estimate the minimum volume of the ice sheet during the last interglacial period.

Chapters 6 and 7 apply the combined ice sheet–tracer approach to examine the stratigraphy of the Antarctic Ice Sheet and the ice flow regime at ice core sites. There I use the ice sheet model designed by C. Ritz at LGGE. Chapter 6 focuses on the origin and age layering of the ice sheet, while chapter 7 uses the three-dimensional thermomechanical ice sheet model to test the assumptions on past origin, elevation, velocity profile and thinning rate used by simple flow models to date ice core records harvested in central East Antarctica. These results lead naturally to chapter 8 and to a summary and conclusion with chapter 9, while technical details are consigned to the appendices.

Before allowing the reader to proceed with this document, I shall clarify the strict limits of my study. The leading objective is to develop and apply tracer deposition and transport methods to answer a number of scientific questions by means of two state-of-the-art ice sheet models from UBC and LGGE. I concentrate on the new benefits of tracers rather than on the development of particular features and parameterizations for the ice sheet models. Therefore, I use the standard configuration of these models as defined by recent studies by Marshall and Cuffey (2000), Clarke and Marshall (2002) and Ritz et al. (2001) in order to directly compare my results to these studies and similar ones (Huybrechts, 2002; Tarasov and Peltier, 2003) and highlight the progress accomplished by including tracer methods. My study suggests that many improvements to ice dynamics models should be performed, for instance, by treating the particular flow regime at domes or the spatial variability of the bedrock properties (geothermal heat flux, sediments, lake). Simulations should ideally be coupled with an atmospheric general circulation model that includes isotopic processes, but the reality of computational time presently impeaches that option. Instead, sensitivity tests on climatic and dynamic parameters are performed to account for missing processes. Minor functionalities are, however, added to the reference models to address special concerns, but I consider that major changes in the models are beyond the scope of my thesis and leave them aside for further studies. This approach alone yields significant new results regarding the climatic and dynamic history of Greenland and Antarctica and their influence in the global hydrological cycle, results that model improvements would certainly refine but probably not refute.

CHAPTER 2

Polar ice sheets: actors in the climate system, archives of the past

Polar ice sheets are an invaluable archive of the past climate if one understands the physical and chemical processes that lead to the deposition, burial, conservation and transport of chemical species, air bubbles and dust in the ice matrix. In this chapter, I describe these processes in order to design an optimum method to track water isotopes in ice. I first explain the role and influence of ice sheets in the climate system, then introduce the ice core records from Greenland and Antarctica used in this study, review the assumptions used for dating the records and summarize the climatic insight they provided. Then I justify the use of water stable isotopes as a thermometer and consider the diffusive properties of firn and ice and their ability to preserve the water isotope record, which motivates our choice of a non-diffusive tracer transport scheme. Finally, I restate the physical laws that rule deformation and storage at depth of annual ice layers, present the principles of ice sheet modelling and close with a discussion of the climate parameterization used for this study.

2.1 Ice sheets and climate

2.1.1 Polar ice sheets: big, white and cold

A glimpse through the window of a plane during a transatlantic flight shows vast and intriguing, almost mystical, white fields beyond the reach but not the imagination of the common mortal. Vast, they are indeed. The Greenland Ice Sheet is over 2500 km long from South to North and close to 1000 km at its widest, for a total volume of 2.9×10^6 km^3 (Letreguilly et al., 1991). The volume of the Antarctic Ice Sheet is almost ten times as large and the ice-covered region measures over $4000\,\mathrm{km}$ across. The gigantic glaciers of Antarctica and Greenland are called “ice sheets” because, with an ice thickness of 2.5–3.5 km and a spread of several thousands of km, their aspect ratio makes them comparable to the sheets of paper used to print this manuscript. Together, the Greenland and Antarctic ice sheets constitute by far the largest present freshwater reservoir and contain enough water to raise global sea level by $\sim$70 m if they were to melt, 61 m coming from the Antarctic Ice Sheet (Huybrechts, 2002) and 7 m from the Greenland Ice Sheet (Letreguilly et al., 1991). The large polar ice masses do not merely store water, they play an active role in the climate system.

2.1.2 Actors in the climate system

Ice looks white. A simple fact, but with crucial implications for the radiative budget of our planet, as most of the external energy brought to the Earth comes from the visible radiation of the Sun. Snow and ice have an albedo of 0.6–1, which indicates that they reflect most of the incoming solar radiation; thus, polar regions tend to cool the planet. The phenomenon is amplified in the winter time when large areas are covered in seasonal snow, leading to a positive feedback. The polar energy

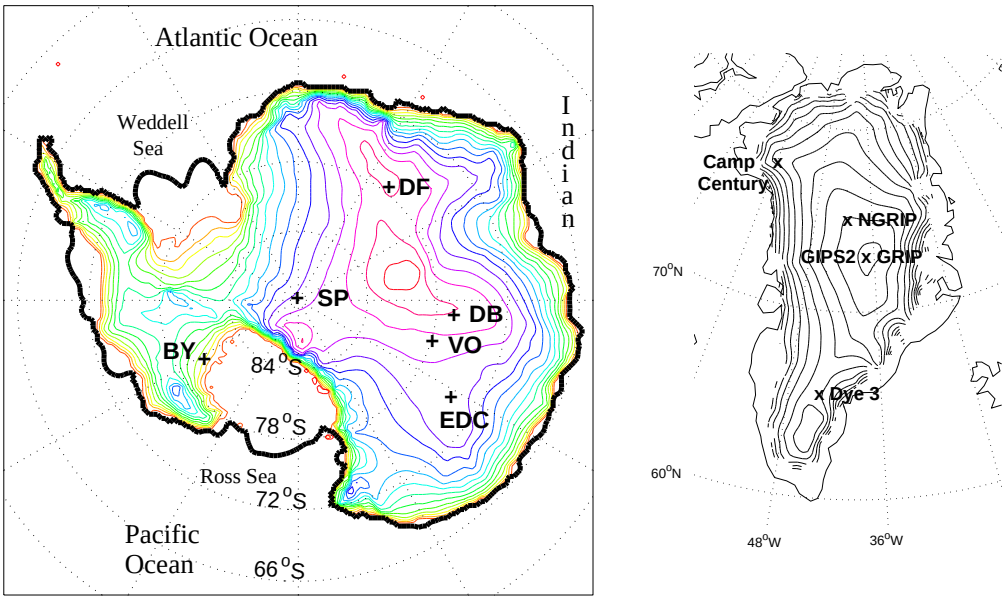

Figure 2.1: Left: Present elevation of the Antarctic Ice Sheet simulated with the LGGE ice sheet model and location of drilling sites: DC=Dome C, VO=Vostok, DF=Dome Fuji, BY=Byrd.
Right: Present elevation of the Greenland Ice Sheet simulated with the UBC ice sheet model and ice core sites.

sink also drives the general circulation of the ocean and atmosphere because of the large contrast in temperature between the poles and the tropics, which receive most of the solar energy because of the relative tilt of the Sun's ray with the normal to the Earth's surface: energy absorbed in the tropics is exported to higher latitudes through atmospheric and oceanic flow. The positive feedback on the radiative budget is also excited during glacial periods, when large ice sheets were stimulated to grow and cover extensive areas by a decrease in incoming solar radiations above the Arctic Circle, as explained by the Milankovitch theory.

2.1.3 Astronomic theory of climate change

The relative position and orientation of the Earth during its yearly elliptical journey around the Sun determines how much solar radiation is received at different latitudes during a year. The received radiation is controlled by three orbital parameters described in Fig. 2.3: the obliquity or tilt of the Earth polar axis relative to the elliptic plane, the precession of equinox that corresponds to the season when the Earth is closest to the Sun on the ellipse (perihelion), and the eccentricity that describes the degree of elongation of the ellipse. Tilt causes seasons because the hemisphere pointing toward the Sun receives more radiation. Change in tilt between 22° and 25° occurs with a 41 kyr (thousand years) periodicity and controls the intensity of seasonality: the larger the tilt, the larger the insolation contrast between the two hemispheres. Today the Earth reaches the perihelion in January, causing slightly milder winters in the Northern Hemisphere, as opposed to 11 kyr ago when perihelion was approached in July (19 kyr and 23 kyr periodicity). Eccentricity varies in 100 kyr and 400 kyr cycles and controls how the timing of perihelion combines with seasonality (tilt); thus, the relative severity of summer and winter time in each Hemisphere.

Milankovitch (1930) calculated the past position and inclination of the Earth and associated the changes in seasonality with the glacial–interglacial cycles that have characterized the Earth's climate for the past 2 Myr. Ice ages, cold temperatures and large ice volume, correlate well with the 65°N summer insolation (Emiliani, 1955; Berger, 1978), as shown on the Vostok record Fig. 2.2; thus, small changes in insolation get amplified by feedbacks in the climate system that lead to a global cooling of ∼5°C and the inception and growth of large ice sheets that drew down sea level by 120–135 m (e.g., Yokoyama et al., 2000). If insolation is indeed the "pacemaker of ice ages" (Hays et al., 1976), future glaciations can be predicted and the next one should not happen before at least 50 kyr (Berger and Loutre, 2002). However, the astronomical theory of climate does not tell how warm the climate is going to be nor how high sea level will rise over the next decades and centuries; thus, I will especially focus on the climate and behaviour of ice sheets during former periods that most resembled modern conditions and try to improve the understanding of glacial archives by predicting the conditions under which they were generated and preserved.

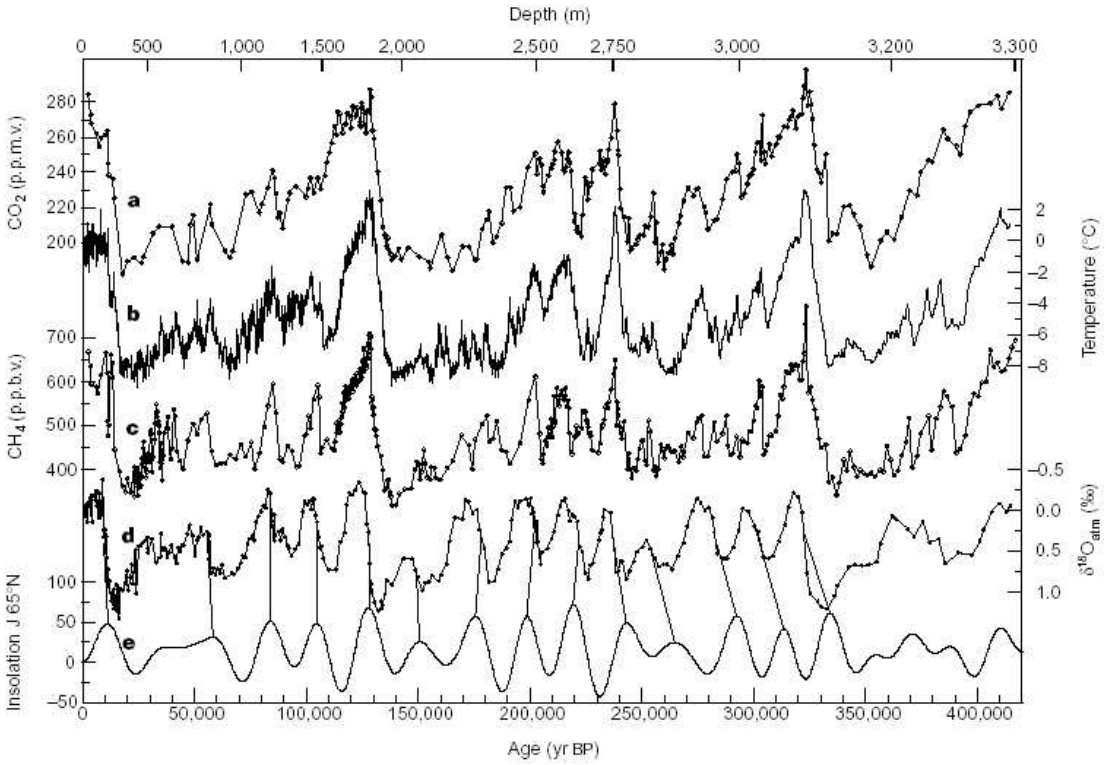

Figure 2.2: Vostok time series and insolation. Series with respect to time (GT4 timescale for ice on the lower axis, with indication of corresponding depths on the top axis) of: a, CO_2; b, isotopic temperature of the atmosphere; c, CH_4; d, $\delta^{18}O_{atm}$; and e, mid-June insolation at 65°N (in W m^{-2}). From Petit et al. (1999).

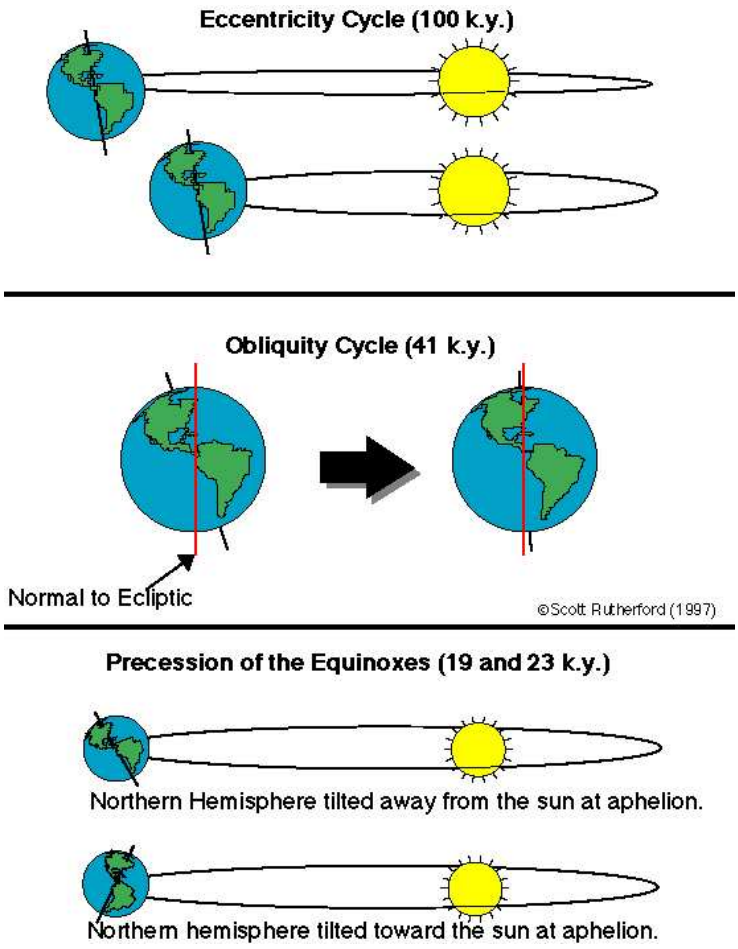

Figure 2.3: Orbital parameters: eccentricity, obliquity and precession.
From http://deschutes.gso.uri.edu/∼rutherfo/milankovitch.html.

2.1.4 Ice sheets and fast climate change

Though the Milankovitch theory may well explain the inception and expansion of large ice sheets, isotopic and geomorphologic records display a high frequency variability during glacial periods that is not present in the insolation signal. For instance, deep-sea sediment records in the North Atlantic (Fig. 2.4) contain a series of layers that are rich in sediments also found in eastern Canada and poor in foraminifera, thus reflecting cold sea-surface temperature. These records suggest that intense and short-lived release of large armadas of icebergs released from the Laurentide Ice Sheet exported enough freshwater to shut down the thermohaline circulation of the ocean, effectively cooling down the climate in the North Atlantic region by $\sim 5^{\circ}$C. These Heinrich Events (Heinrich, 1988; Bond et al., 1992) are believed to result from surges or oscillations in the ice stream regime of the Laurentide Ice Sheet and have motivated the development of the UBC Ice Sheet Model used for my studies of Greenland (Marshall, 1996). These events reflect the dynamic role of internal ice dynamics on the global climate and stimulate further research to better understand the flow of ice sheets.

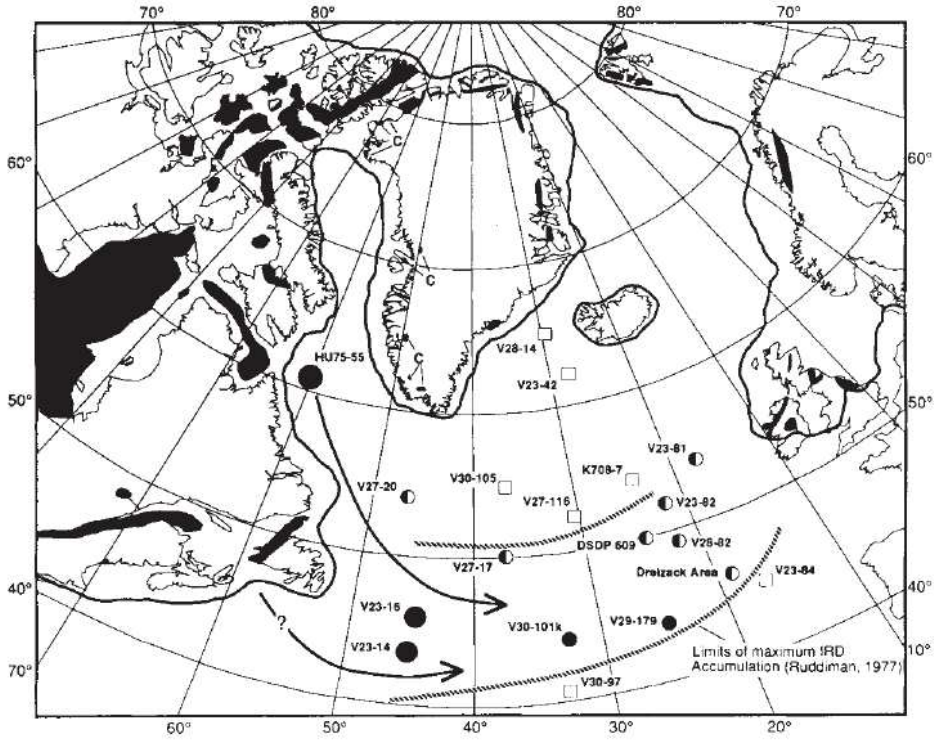

Figure 2.4: Ice sheet extent during glacial periods and location of sea-sediment cores containing ice rafted debris (IRD) carried by icebergs released from the Laurentide Ice Sheet. The thick solid line near coast lines maps the maximum limit of ice sheets during the last glaciation. Black patterns map the origin of IRDs. From Bond et al. (1992)

2.2 Ice core records

Accumulation of snow on glaciers and ice sheets builds a record of the atmospheric composition by locking water, air and particles in the ice matrix. In central regions of Antarctica and Greenland or in high mountain glaciers, cold summer temperatures limit any melting; thus, yearly snow and ice layers can be preserved, yielding a continuous record of past atmospheric conditions. Therefore modern ice sheets and glaciers constitute a wealthy and abundant archive for glaciologists interested in Earth's climate history. The following review is inspired from Parrenin (2002).

2.2.1 A brief history of ice core drilling

The potential of the glaciological archive was understood about 60 years ago, but the remoteness and harsh climatic conditions of polar ice sheets and the resulting technical and financial burden have so far limited the use of the "glaciological mine" (Reeh et al., 1987) to a dozen ice cores. Scientific expeditions aimed at understanding the climate in Antarctica started in 1957–1958 during the International Geophysical Year, followed the next year by a 1400-km traverse organized by the Americans and a decade later by deep drilling operations.

The first deep ice core campaign was inaugurated in Northwest Greenland at Camp Century. Bedrock was reached in 1966, with a 1390-m deep core that spans $\sim$100 kyr of climatic history

(Dansgaard et al., 1969). In Antarctica, 2000 m of ice containing $\sim$75 kyr of history were extracted at Byrd near the Ross and Amundsen Sea in 1968 (Epstein et al., 1970). In the early 1970's, the Russians installed a station at Vostok in central east Antarctica, one of the coldest places on our planet with an average temperature of $-55°$C and extreme temperature of $-89°$C. Several ice cores were drilled and successively reached 500 m in 1970, 950 m in 1974 (Barkov and Gordienko, 1976) and much deeper more recently. Also in East Antarctica, the French extracted a 900-m core at Dome Concordia in 1978 (Lorius et al., 1979). Drilling returned to Greenland and in 1981, the Danes, Swiss and Americans pulled a 2000-m ice core at Dye 3 in the southern part of the ice sheet. The record contains over 100 kyr of climatic history (Dansgaard et al., 1982), but the lower part of the record is difficult to interpret because it is strongly affected by ice flow, an inescapable problem for flank flow sites, an issue I will try to address with three-dimensional modelling of ice flow.

Drilling resumed at Vostok in 1982 with a Russian–French association that benefited from American logistic support. High expectations were put on this operation because the low surface accumulation rate, only 2 cm per yr, raising the possibility that the age of the ice might greatly exceed that for the previously drilled sites. Efforts were soon rewarded with a 2000-m ice core spanning 150 kyr of climate history (Lorius et al., 1985), providing the first detailed record reaching beyond the last glacial cycle and into the next one, embracing an interglacial period somewhat similar to modern conditions about 125 kyr ago, an epoch called Eemian or Marine Isotope Stage 5 (MIS 5) in reference to the chronology of marine isotopic records (Martinson et al., 1987). Drilling reached a final depth of 3623 m in 1998, just 80 m above the large subglacial Lake Vostok, with 3310 m of ice spanning 420 kyr of climatic history (Petit et al., 1999, and Fig.2.2), the bottom 300 m originating from basal freeze-on of water from Lake Vostok. The record thus contains four glacial–interglacial cycles and reaches MIS 11 (395–420 kyr BP), a long interglacial period of special interest because its astronomical parameters resemble modern conditions (Drowler et al., 2002).

In the early 1990's, Europeans and Americans drilled two deep ice cores 28 km away from each other near the 3300-m-high Summit of the Greenland Ice Sheet. The European GRIP project reached the 3029-m-deep bedrock in July 1992 (GRIP Members, 1993), the American GISP2 project 3087 m the following summer (Grootes et al., 1993). Their deep ice from the last interglacial period led to much speculation about rapid climate variability. However, comparison of greenhouse gases with the Vostok record clearly proved the Greenland cores had been corrupted by strong flow disturbances that had mixed ice deposited during the Eemian (Chappellaz et al., 1997). A new drilling program aiming at better sampling Eemian ice in Greenland was started in 1996 at NorthGRIP, 300 km North of the Summit sites. Bedrock was finally reached in 2003 and appears to contain ice up to 123 kyr BP, that is ice reaching into a stable part of the Eemian (NGRIP Members, 2004).

Besides the Vostok program, other deep ice cores have recently been drilled in Antarctica. The Japanese went to Dome Fuji, 1500 km away from Vostok and closer to the Atlantic Ocean, and extracted 2503 m of ice before the drill got trapped into the ice. The ice core record showed three glacial cycles strikingly similar to Vostok, providing evidence of an homogeneous climate over most of Antarctica (Watanabe et al., 2003). Europeans started a new deep drilling project (EPICA) at the French–Italian base of Dome C (DC) in 1998. In 2003, they recovered 3190 m of ice spanning the longest-to-date ice-core record with up to eight glacial cycles of climatic history (EPICA community members, 2004).

2.2.2 Methods for dating ice

Although annual ice layers can preserve their original chemical content, the climatic history can be obscured by the thinning and deformation processes resulting from ice flow; thus, determining the age of ice can be a real challenge. Annual layers tend to merge at greater depth, especially in Antarctica where initial layers are already thin because of low surface accumulation. As previously seen, flow disturbances have also particularly affected sites like GRIP and GISP2. Each ice core record has its own flow and accumulation rate characteristics, therefore many strategies have been applied to recover the essential chronology of events.

I distinguish three main classes of methods for extracting the age of ice along a core: (1) Counting of annual layers, which is accurate (Alley et al., 1997) if layers are thick enough. It has been applied for dating the youngest 37.8 kyr of the GISP2 record (Meese et al., 1997) and from 8.2 to 11.5 kyr BP for GRIP (Johnsen et al., 1997). Accumulation rate is too low in central Antarctica for this method. (2) Use some level of comparison to a chronology or to dated events, either by referring to time markers (e.g., ^{10}Be peak, ^{14}C, or U-Th Genty et al., 2003) and other dated time series, or by applying an orbital tuning by linking the measured changes in the core to the well known insolation signal (Berger, 1978). Time markers are useful but limited to 10's kyr. Orbital tuning assumes a linear response of the climate system to change in insolation, introducing a 6 kyr uncertainty on age (Parrenin, 2002). The method has been widely used both on ice and marine core records (e.g., Meese et al., 1997; Martinson et al., 1987; Bassinot et al., 1994). Chronologies can also be synchronized by correlating the isotopes of atmospheric oxygen, a method also compatible with marine records because the composition of the ocean and the atmosphere change simultaneously (Bender et al., 1994), or by methane concentration to compare Antarctic and Greenland records (e.g., Blunier and Brook, 2001), because methane is well mixed in the atmosphere. (3) Ice flow modelling, which requires assumptions concerning the simplicity of ice flow, on past surface elevation and origin of ice, and an accumulation model. This method is satisfying because it includes the physics of ice, but is highly dependent on the accumulation scenario, which is generally tied to the isotopic variations in the record. Such relations have been shown to fail at particular periods (Cuffey and Clow, 1997), explaining for instance the continuing debate on the chronology of Summit ice cores (Grootes et al., 1993; Meese et al., 1997; Johnsen et al., 1995, 2001; Shackleton et al., 2004). Vostok experiences all the difficulties of the modelling approach because of a distant origin of deep ice (Ritz, 1992), rough underlying topography (Siegert and Kwok, 2000) and possible hiatus in surface accumulation (Parrenin et al., 2001). The methods can be combined (e.g., GRIP-SS09 chronology, Johnsen et al., 2001) and Parrenin (2002) has recently developed a highly promising "federative approach" that picks up the best features of all these dating techniques to obtain the age–depth relationship of the Vostok, DC and Dome Fuji records.

2.2.3 What do we learn from ice cores?

Polar archives contain a rich and diverse record of atmospheric history. Water stable isotopic ratios in the ice reflect the temperature where the snow formed and second order information on the temperature of the oceanic site where the water first evaporated. Gas bubbles sample the composition of the atmosphere, for instance carbon dioxide (CO_2), methane (CH_4) and nitrous oxide (N_2O), so that past greenhouse gases concentrations can be compared to temperature. The isotopic composition of gases also relates to past sea levels and biologic productivity through their ^{18}O signature, to sources and sinks of methane through ^{13}C and to the rhythm of climate change, especially through argon and

nitrogen isotopes (^{40}Ar,^{38}Ar, ^{36}Ar, ^{15}N, ^{14}N). Aerosols in snow and ice (Na^+, Na^{2+}, Cl^-, SO_4^{2-}, NO_3^{2-}, ^{10}Be, dust) reflect the chemistry of the atmosphere, mark volcanic eruptions and measure cosmogenic production of radioactive isotopes.

Ice records have played a key role in understanding global climate change. In the early 1980's, Vostok helped validate the orbital theory of climate that had already been observed in marine sediments. Measurement of CO_2 and CH_4 in bubbles provided compelling evidence of the link between greenhouse gases and climate change (e.g., Barnola et al., 1987) and proved that greenhouse-gas levels in the atmosphere over the past hundreds of kyr had never been as high as those of the industrial era, raising awareness of the impact of humankind on the climate. Ice cores from GRIP and GISP2 attested of the extreme sensitivity of the climate system, showing that rapid warmings of $\sim$10°C can occur in less than a human lifetime (Dansgaard et al., 1993; Severinghaus and Brook, 1999).

2.2.4 Past and future climate

Ice core records have opened a window on our past that helps scientists realize the fragility of the equilibrium between the different actors in the climate system. Though mankind is a recent player, looking at past periods can help scientists distinguish the natural variability of climate from changes induced by human activity. Interglacial periods with climate similar to modern conditions are particularly interesting. Given the difficulty of obtaining useful information on the distant past, great effort and hopes have been placed in the most recent interglacial. This was the motivation for drilling in Greenland, where the high snow accumulation rate offers high resolution data. A variety of records for that period indicate that the climate was warmer than modern conditions, sea level was $\sim$5 m higher and greenhouse-gas concentration was close to the pre-industrial period, $\sim$30% less than today. Therefore the current increase in temperature and greenhouse-gas emissions raises concern about the possible disintegration of the Greenland Ice Sheet or the West Antarctic Ice Sheet in the near future (Oppenheimer, 1998). I will assess the contribution of the Greenland Ice Sheet to past sea level rise by using an array of deep Greenland ice cores to constrain predictions of the past extent of the ice sheet. Because the current 10-kyr-long warm period, the Holocene, has already lasted nearly as long as the Eemian, the possibility of an imminent glaciation has been suggested, but the astronomical theory predicts that the Holocene could last for another 50 kyr (Berger and Loutre, 2002) if human intervention is taken out of the equation. Orbital calculations also indicate that the best analogue to the modern state is MIS 11, $\sim$400 kyr ago, an exceptional 30-kyr-long interglacial period when sea level was probably 13 to 20 m above current levels. Many questions arise from that discovery: was climate warmer than today? Why and how did sea level rise? Why did it last so long? These questions are very important, especially for those living in coastal regions. The recently drilled EPICA-Dome C record with its 800 kyr of history might help answer some of these questions. I believe that my method can also provide useful insight by combining ice core records to constrain the reconstruction of polar ice sheets during interglacial periods, test the sensitivity of ice sheets to climate warming and estimate the resulting effect of their full or partial desintegration on sea level and ocean composition.

2.3 Inferring past temperature from water isotopes

Stable isotopes of oxygen and hydrogen in water are widely used to reconstruct past temperature from ice and marine sediments because origin effects and temperature-dependent processes influence the final composition of water isotopes found in polar ice, sea water, atmospheric vapour and meteoric water. This section explains the different processes and outlines the principles of the isotopic paleo-thermometer.

2.3.1 Stable water isotopes

Oxygen has three stable isotopes, ^{16}O (99.76% of all O), ^{17}O (0.04%) and ^{18}O (0.20%); hydrogen has two stable isotopes, ^{1}H (H hereafter, 99.985% of all hydrogen) and ^{2}H (or D, deuterium, 0.015% of all H), and one radioactive isotope, ^{3}H (tritium). Together, oxygen and hydrogen form water, but they are also found in many other combinations in the Earth's hydrosphere, biosphere, and geosphere. For instance, hydrogen constitues 75% of normal matter in the universe by mass whereas oxygen is the most abundant element in the Earth's crust. Among the nine possible configurations of water, the most common are $H_2^{16}O$, $HD^{16}O$ and $H_2^{18}O$. The proprieties of these types of water are presented in Table 2.1.

For practical use, the ratio of one isotope relative to the other ($R_{\rm O}$=$^{18}{\rm O}/^{16}{\rm O}$ or $R_{\rm H}$=H/D) in a given compound is measured against a reference ratio $R_{\rm SMOW}$ taken from the global ocean and called the *Vienna Standard Mean Ocean Water* (V-SMOW) and expressed as

$$\delta = (\frac{R_{\rm sample}}{R_{\rm SMOW}} - 1) \times 1000. \tag{2.1}$$

I adopt the following isotopic ratios for the SMOW: $R_{\rm O.SMOW}$=2005.20$\times 10^{-6}$ (Baertschi, 1976) and $R_{\rm H.SMOW}$=155.95$\times 10^{-6}$ (Dewit et al., 1980).

Property	$H_2^{16}O$	$HD^{16}O$	$H_2^{18}O$
Density (at 20°C, kg m^{-3})	997	1105	1111
T of max density (at 760 torr, °C)	3.98	11.24	4.30
Melting point (at 760 torr, °C)	0.00	3.81	0.28
Boiling point (at 760 torr, °C)	100.00	101.42	110.14
Vapour pressure (at 100°C, torr)	760.0	721.6	.
Viscosity (at 20°C, centipoise)	1.002	1.247	1.065

Table 2.1: Properties of $H_2^{16}O$, $HD^{16}O$ and $H_2^{18}O$.

2.3.2 Isotopic fractionation

In general, the isotopic ratio of a given compound (i.e. molecule containing different isotopes of the same element) in a given phase can vary because of an isotope exchange reaction, an unidirectional reaction or a physical process such as evaporation, condensation or melting. The differences in physical and chemical properties of isotopic compounds and the resulting partitioning are caused by mass differences of the atomic nuclei. These differences have two implications. First the heavier

isotopes have a lower mobility. Indeed, the kinetic energy of a molecule is determined by temperature: $kT = 1/2mv^2$ (k = Boltzmann constant, T = absolute temperature, m = molecular mass, v = average molecular velocity); thus, molecules with higher m have lower v at a given temperature. Therefore heavier molecules have lower diffusion velocity and lower chemical reactivity (lower collision frequency). Secondly, the heavier molecules generally have higher binding energies; thus, light elements are more sensitive to isotopic fractionation than heavy isotopes because they require less energy supply to break that bond. Temperature influences this fractionation process because it takes more vibrational energy to break the stronger bond of a heavy isotope with its carrying molecule. At high temperature the differences between binding energies of isotopic molecules becomes smaller, resulting in a disappearing isotopic effect (Mook and de Vries, 2001).

For water and the range of temperature in the climate system, most of the fractionation occurs during physical processes. As seen in Table 2.1, the difference in mass between the isotopic forms of water implies that the various configurations have different saturation vapour pressure and molecular diffusivities (in air); thus, fractionation processes separate these configurations during evaporation and precipitation events.

2.3.3 Fractionation during precipitation

Equilibrium between the vapour and liquid phase of a given type of water of isotopic composition $^{a}\mathrm{HH}^{b}\mathrm{O}$ can be expressed as:

$$^{a}\mathrm{HH}^{b}\mathrm{O}_{(\mathrm{l})} \quad \underset{k2}{\overset{k1}{\Leftrightarrow}} \quad ^{a}\mathrm{HH}^{b}\mathrm{O}_{(\mathrm{v})} \tag{2.2}$$

where (v) is the water vapour phase, (l) is the liquid phase, and the rate of exchange $k1(^{a}\mathrm{HH}^{b}\mathrm{O})$ and $k2(^{a}\mathrm{HH}^{b}\mathrm{O})$. Although the rate $k1$=$k2$=k for a given type of water, the rate varies between the different types of water that co-exist in each of the liquid and vapour phases. "Regular" water $\mathrm{H_2O}$ has the highest rate (e.g., $k(^{16}\mathrm{O})$>$k(^{18}\mathrm{O})$); thus $\mathrm{H_2O}$ preferentially enters the vapour phase. The reasoning is similar with vapour pressure because, for water, the higher the mass number, the lower the equilibrium vapour pressure. Therefore, at equilibrium, $H_2^{18}\mathrm{O}/H_2^{16}\mathrm{O}_{(\mathrm{l})} < H_2^{18}\mathrm{O}/H_2^{16}\mathrm{O}_{(\mathrm{v})}$ and $^{18}\mathrm{O}$ becomes enriched in the condensated water and $^{16}\mathrm{O}$ in water vapour.

This physical process, called equilibrium fractionation, controls most of the fractionation that separates the different types of water. Its effect can be quantified by a fractionation factor defined as the ratio α between the rate of exchange of the heaviest and lightest isotope-bearing molecules (equal to the ratio between the saturation vapour pressures) that mostly depends on temperature (Fig. 2.5), but also on the phase change.

Comparing the occurence of $\mathrm{H_2O}$, $\mathrm{HD}^{16}\mathrm{O}$ and $\mathrm{H_2^{18}O}$ in nature, their respective molecular mass imply more fractionation of water for the hydrogen isotope (18 and 19 g mol^{-1}) than for the oxygen isotope (18 and 20 g mol^{-1}). Craig (1961) found that the corresponding $\delta\mathrm{D}$ and $\delta^{18}\mathrm{O}$ in precipitation are predictible and fall along the so-called global meteoric water line (GMWL):

$$\delta\mathrm{D} = 8\delta^{18}\mathrm{O} + 10‰. \tag{2.3}$$

This relationship is explained by the relative difference of their equilibrium fractionation factors (ratio of α-1), which ranges from 7 to 10. More recent compilation of world-wide measurements (Rozanski et al., 1993), shown in Fig. 2.6, give slightly different coefficients.

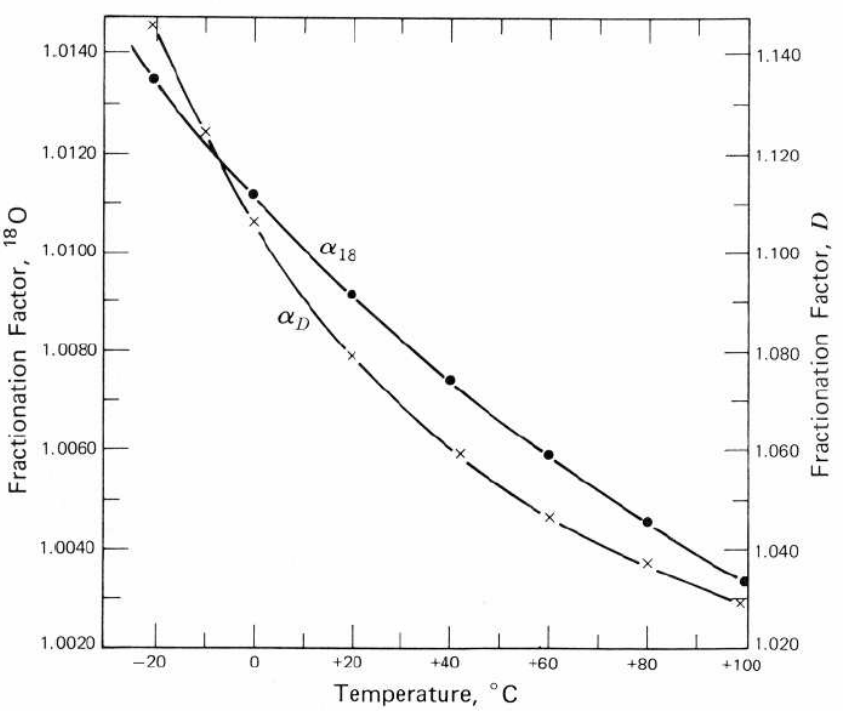

Figure 2.5: Equilibrium fractionation factor of ^{18}O (α^{18}) and D (α^{D}) between the vapour and liquid water phases as a function of temperature. Attention, different vertical scales apply for ^{18}O (left side) and D (right side). From Faure (1986).

2.3.4 Fractionation during evaporation

Kinetic fractionation is similarly related to mass differences and is associated with incomplete and unidirectional processes such as evaporation and diffusion. In evaporation, water vapour is enriched in ^{16}O and H, whereas the remaining liquid water is enriched in ^{18}O and D. Lighter H_2O molecules diffuse faster in air. Therefore they cause an additional off-equilibrium effect during otherwise-equilibrium reactions by favouring the vapour phase. Consequently, in evaporation, $H_2^{18}O$ is enriched in liquid water by 1% relative to its concentration in water vapour at the same temperature. Factors such as humidity, salinity and temperature affect kinetic fractionation of water during evaporation. For instance, the lower the humidity, the faster the evaporation rate and the greater the kinetic fractionation; the effect is more pronounced for oxygen than for hydrogen, which means that the rate of change of the water meteoric line is diminished to 4–5 below 75% humidity (Clark and Fritz, 1997). Because deuterium is the least affected by kinetic processes and therefore carries a temperature signature that is easier to interpret, preference has been given to δD for the study of the Vostok and DC ice core records. The deuterium excess defined as $d = \delta\mathrm{D} - 8\delta^{18}\mathrm{O}$ and used as an index for non-equilibrium conditions (Dansgaard, 1964) has provided precious additional information about the evaporation site (Vimeux et al., 2001).

An additional fractionation process takes place in the biosphere and is named the "Dole effect" (Dole, 1935). The modern $^{18}\mathrm{O}/^{16}\mathrm{O}$ ratio of atmospheric O_2 is higher than that of average seawater by 23.5‰ (Kroopnick and Craig, 1972) because of discrimination against ^{18}O during respiration and photosynthesis in plants, leading to an evaporative enrichment of ^{18}O in leaf water. Respiration

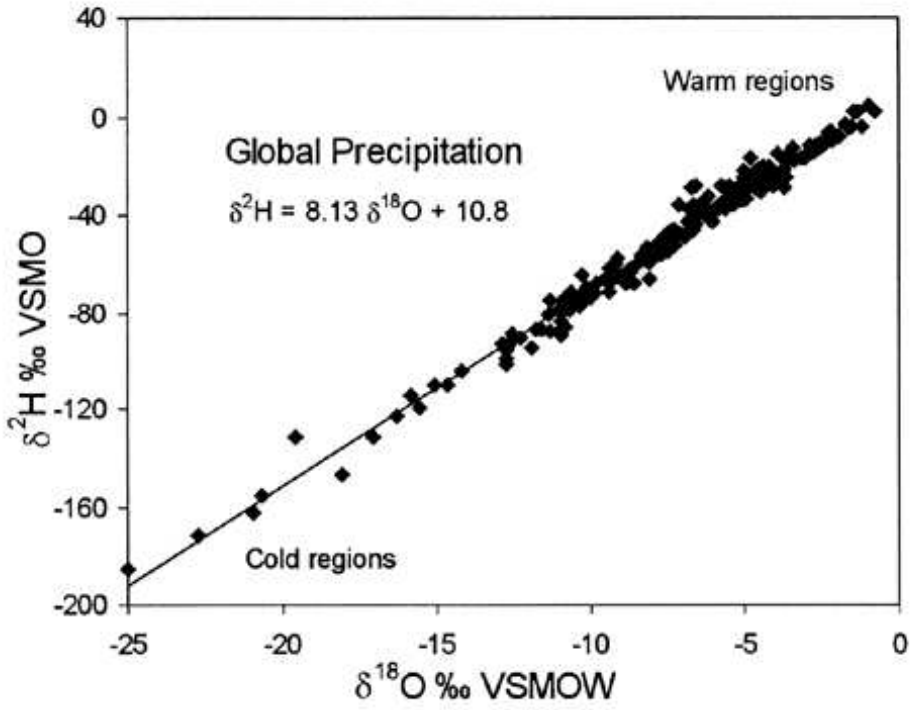

Figure 2.6: Water meteoric line from the Global Network for Isotopes in Precipitation (GNIP). Compiled by Rozanski et al. (1993), adapted from Clark and Fritz (1997). VSMOW or VSMO is Vienna SMOW.

in the deep ocean plays an important role because changes in seawater composition ($\delta^{18}O_{sw}$) are transmitted to O_2 in air through photosynthesis. Because of the long turnover time of atmospheric O_2 ($\sim$1.2 kyr) relative to the mixing time of the atmosphere ($\sim$1 yr), the $\delta^{18}O$ of O_2 ($\delta^{18}O_{atm}$) is the same throughout the atmosphere, thus the same above oceans and ice sheets. Therefore simultaneous changes of $\delta^{18}O_{atm}$ and $\delta^{18}O_{sw}$ are incorporated in the gas bubbles that are trapped in ice and in the foraminifera that form marine sediments. This can be used to correlate the age of marine sediment records with that of air bubbles trapped in ice core records (Bender et al., 1994, and Fig. 2.2, d).

2.3.5 Rayleigh distillation

Precipitation events impoverish clouds in ^{18}O and D because the heavy isotopes preferentially migrate to the condensated phase. Therefore, clouds become more depleted after every rain, this is called the "rainout effect". This effect is particularly strong above continents because clouds cannot reload from evaporation. The combination of rainout and equilibrium fractionation is often described in terms of Rayleigh distillation, which has largely been used to model the partitioning of isotopes in the water reservoir (the cloud) and understand precipitation above ice sheets (e.g., Dansgaard, 1964):

$$\delta = \delta_o f^{(\alpha-1)} \tag{2.4}$$

where δ_o is the initial isotopic ratio, δ the ratio in the cloud after the rain, α the fractionation factor and f the residual vapour fraction. The model, illustrated in Fig. 2.7, adequately represents gen-

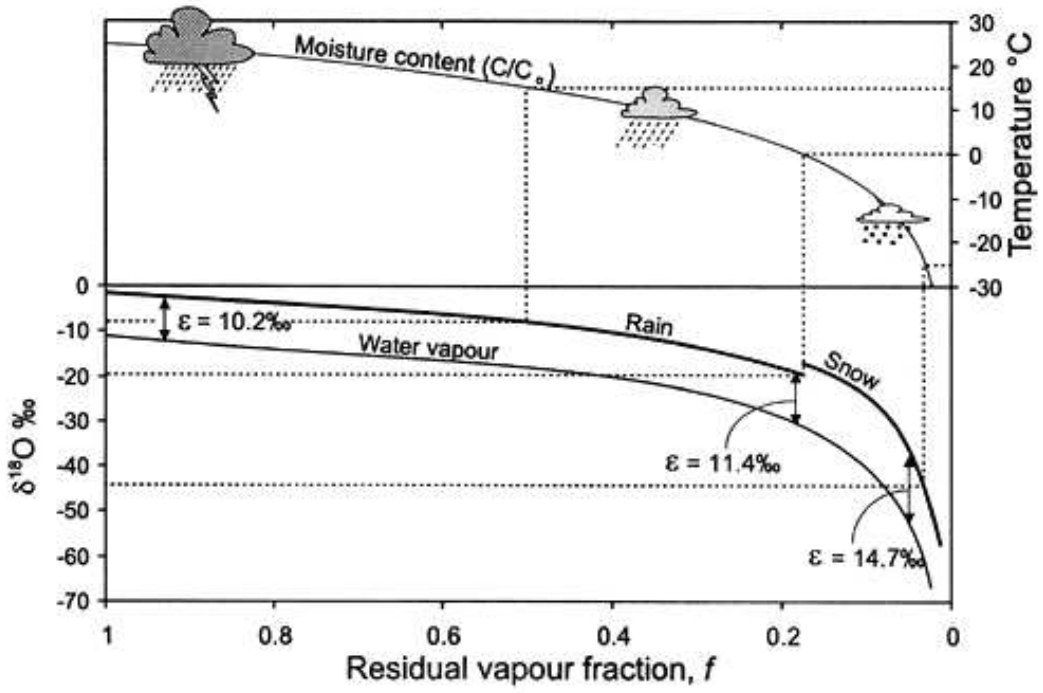

Figure 2.7: Change in the ^{18}O content of rainfall according to a Rayleigh distillation, starting with $\delta^{18}\mathrm{O}_{\mathrm{vapour}} = -11‰$ and temperature = 25°C, and a final temperature of −30°C. At 0°C, fractionation between snow and water vapour replaces rain-vapour fractionation. Remaining fraction is calculated from the decresase in moisture carrying capacity of air at lower temperatures, starting at 25°C. Dashed lines link δ^{18}O of precipitation with temperature of condensation. (From Clark and Fritz, 1997).

eral aspects of isotopic deposition and is useful for estimating the dominant effects. However, its simplicity has shortcomings. For instance, it neglects evaporative recharge (over water and land) and transport effects, only droplets in equilibrium with water vapour are considered (no kinetic processes) and exceptional events cannot be accounted for. Therefore, isotopic fractionation processes have more recently been included in Atmospheric General Circulation Models (AGCM) to resolve the complexity of the full hydrological cycle (Jouzel et al., 1991; Hoffmann et al., 2000).

2.3.6 Principle of isotopic thermometry

Figs. 1.1 and 2.7 summarize the fractionation processes that affect water from evaporation on the ocean to deposition on polar ice sheets after a series of rainout events. Because the remaining water vapour is transported poleward by the general atmospheric circulation and temperature is correlated with latitude and longitude, ice sheets receive highly impoverished isotopic water, even more so at sites far from the coast. Not surprisingly, δ^{18}O and δD measured in their snow show a strong correlation with temperature (average annual surface temperature T_{s})

$$\Delta\delta = \kappa \Delta T_{\mathrm{s}}, \tag{2.5}$$

with $\kappa = 6.04‰\,\mathrm{K}^{-1}$ for δD in Terre Adélie, Antarctica (Lorius and Merlivat, 1977) and $\kappa = 0.67‰\,\mathrm{K}^{-1}$ for δ^{18}O in Greenland (Johnsen et al., 1989). These observations provided the first basis for estimating past temperature directly from the isotopic ratio measured in ice core records.

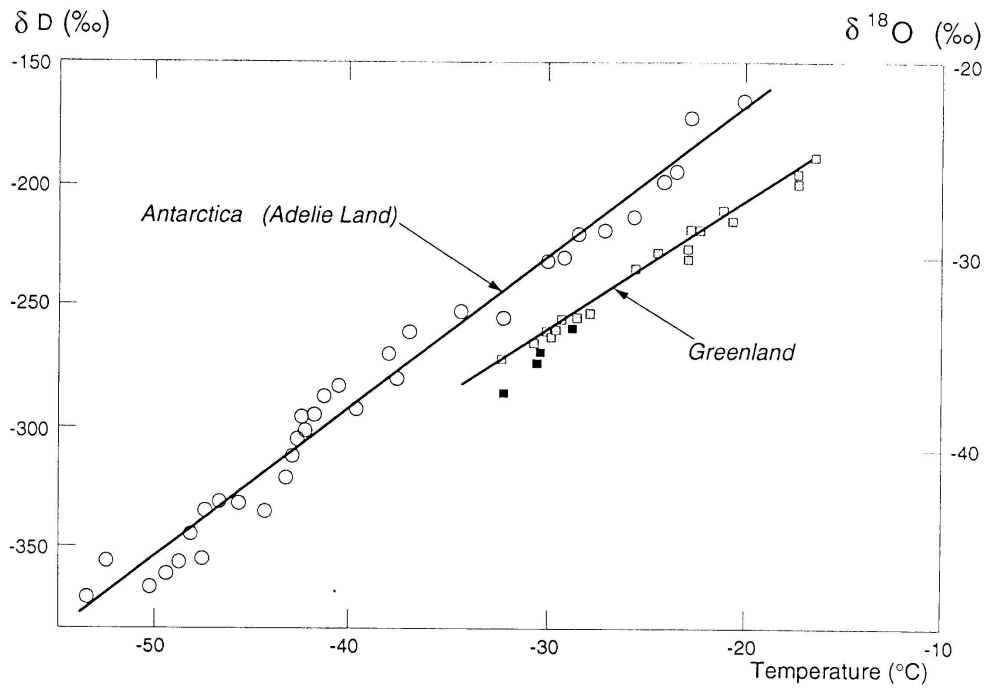

Figure 2.8: Observed relationship between temperature and δ^{18}O in Greenland and Antarctica. Compilation of Lorius and Merlivat (1977) and Johnsen et al. (1989) from Jouzel et al. (1997).

The "spatial slope" method assumes that modern spatial variations from temperature and isotope remain valid at a given local site to predict the past variations in surface temperature and isotopic deposition in a colder climate ("temporal slope"). Borehole temperature measurements at GRIP (Johnsen et al., 1995; Dahl-Jensen et al., 1998) and GISP2 (Cuffey et al., 1995) and analysis of nitrogen and argon isotopes (Severinghaus and Brook, 1999) have independently proven that the spatial slope underestimates glacial–interglacial variation by 100% in central Greenland. Such results are more difficult to obtain in central Antarctica because of the lower accumulation rate, smaller glacial–interglacial temperature amplitude than in Greenland and presence of several glacial cycles in the ice column. For instance, an earlier study at Vostok (Ritz, 1989) can be interpreted as a $\pm$20% uncertainty on the isotope–temperature relationship from borehole-temperature constraints. Conditions around isotopic fractionation and deposition could differ for several reasons.

Values suggested hereabove apply to surface temperature, whereas temperatures involved in fractionation processes are those of evaporation and precipitation events. The atmosphere above cold polar regions generally presents an inversion layer in which temperature increases with elevation, e.g., from -55°C to -39°C at 500 m above the surface at Vostok. This is the case for most of Antarctica; in Greenland where temperature is on average $\sim$20°C warmer, there is an inversion in modern winter conditions and probably for a longer season during glacial periods. Given that precipitation forms in the warmest tropospheric layer, isotopes in precipitation reflect temperature at the inversion level rather than at the surface; thus, δ^{18}O and δD can vary because of a relative change between inversion and surface temperature. Atmospheric models are best equipped to estimate these changes and find a small effect, though their results may be tainted by uncertainty on past sea surface temperatures and their resolution and assumptions on past and present topography

(Krinner and Genthon, 1997).

A more likely cause is change in seasonality. In Greenland, under modern conditions, precipitation is well distributed during the year; thus, depositional isotopes evenly sample summer and winter temperatures and the concentration of isotopes in modern annual layers of snow adequately averages mean annual temperatures. Experiments with AGCMs suggest that most of annual precipitation fell in the summer time during glacial periods, reflecting only isotopic values from summer conditions and causing a bias (Krinner and Genthon, 1997; Jouzel et al., 2000; Werner et al., 2000). Similar experiments on Antarctica tend to suggest a weak opposite effect (Krinner and Genthon, 1997; Delaygue et al., 2000).

Another possibility is the effect of exceptional events, e.g. when warm air brings large precipitation during glacial periods which are typically low in surface accumulation. AGCMs are not yet capable of predicting such events. Changes in moisture origin or sea ice extent because of glacial modification of sea surface temperature and changes in atmospheric circulation patterns can also affect the isotopic content of precipitation. Nevertheless, atmospheric and borehole studies agree that water isotopic content is a valid surrogate for past temperature, provided that a calibrated time-and-space dependent use of the temperature–isotope relationship is made (Cuffey et al., 1995; Jouzel et al., 1997, 2003). Therefore, we will apply such calibrated thermometers to estimate past isotopic depositional rate in Greenland and Antarctica.

2.4 Conservation of the water-isotope signal in snow and ice

Estimates of past temperatures from ice cores heavily rely on the δ^{18}O and δD records. Before we proceed to design a model of water-isotope transport in an ice sheet, understanding how these quantities are preserved in snow and ice is essential. One particular concern for paleoclimate scientists wishing to infer a reliable temperature history is whether the seasonal signal is conserved. As noted in Cuffey and Steig (1998), such information could be used to infer changes in mean summer and winter temperature, changes in annual temperature variability, spatial pattern of climate change, reconstruction of sea-ice extent (from source effect), and of course to better calibrate the problematic isotope–temperature relationship presented in the previous section and assess the seasonality of precipitation.

2.4.1 Diffusion in the firn

Before transforming into ice, deposited snow is buried and compacted by the wind and the weight of overlying layers. That snow layer called "firn", with density from 0.4 (deposition) to 0.83 (close off of the air space), roughly covers the uppermost 50 m in Greenland and 120 m in central Antarctica. Firn is a porous medium; therefore, it is subject to air convection (in the upper part) and diffusion. The possibility of air flow is a critical issue when estimating the composition of the atmosphere (O_2, N_2, CO_2, CH_4...) at a given time because young air gets trapped within older deposited snow when the air space closes off; thus, gas in air bubbles is always younger than the surrounding ice in any ice core record. Firn densification models (e.g., Goujon et al., 2003), not presented here, try to predict that age difference, which is crucial for examining the leads and lags of temperature and greenhouse gases and tie records from Greenland and Antarctica (Bender et al., 1994; Steig et al., 1998; Petit et al., 1999; Blunier and Brook, 2001).

For our special purpose, we are interested in preservation of the annual isotopic signal in the

firn to assess our potential error when ignoring the firn in our ice sheet models and using a simple annually updated isotopic depositional model. Of concern is the susceptibility of ice-core isotopic records to diffusion, a process that tends to homogenize and smooth the variations in depositional δ^{18}O and δD. Many studies show these records are indeed continuously modified by diffusion (e.g., Whillans and Grootes, 1985; Cuffey and Steig, 1998; Jean-Baptiste et al., 1998; Johnsen et al., 2000), but fortunately for us, these studies find that diffusion acts on a length scale that is generally small compared to the recorded individual climatic events, 4–6 cm or 1–3 yr for conditions typical of Antarctica, 8–10 cm or 0.5–1 yr for Greenland (Cuffey and Steig, 1998). Theory and experiments show that the firn smoothing rate is highly dependent on the wavelength of the isotopic signal, which is a function of the temperature and surface accumulation rate (Jean-Baptiste et al., 1998; Johnsen et al., 2000). Though most of the sub-annual signal is permanently lost by diffusion, seasonal amplitude can be reasonably reconstructed in central Greenland (Cuffey and Steig, 1998). Because of its higher concentration in vapour, ^{18}O diffuses faster so stronger smoothing can be expected for δ^{18}O than for δD, potentially introducing an artificial seasonality to the deuterium excess, an indicator of the temperature at the evaporative site, but raising also the possibility of using the different diffusion lengths as a paleoclimate indicator, if temperature is cold enough (Johnsen et al., 2000).

Waddington et al. (2002) ask a different question that should precede this discussion: "can stable isotopes be reversibly deposited in polar snow?". Snow is exposed to the water vapour from the atmosphere before getting buried in the firn. During that period near the surface, temperature and wind bring moisture and heat to the snow pack, potentially stimulating sublimation process and thus fractionation of δ^{18}O and δD, altering their original signature. The study finds that snow in central Greenland is certainly unaffected because the high accumulation rate ensures rapid burial. In contrast, Antarctica is much dryer and near surface snow may be affected in the windy slopes of the ice sheet. Ice core records in central regions, e.g., Dome C, are likely preserved thanks to moderate wind and the stabilizing effect of cold temperature. Therefore, we can conclude from these analyses that absence of firn in the ice sheet model is non-prejudicial to our study.

We note that firn processes affecting other chemical species have played an important role in ice core studies. Fractionation in firn of argon and nitrogen during fast climate warming events (Dansgaard-Oeschger events, Younger Dryas) provides a means for estimating the amplitude of these temperature variations and confirm a $\sim$20°C change since the glacial period (e.g., Severinghaus and Brook, 1999).

2.4.2 Diffusion in ice

Below firn, pore space is closed: self-diffusion in ice crystals is expected to govern any additional smoothing. Self-diffusion of hydrogen and oxygen in ice is weak: $\sim 6\times10^{-9}$ m^2 yr^{-1} at –30°C (Jean-Baptiste et al., 1998), $\sim 5\times10^{-8}$ m^2 yr^{-1} at –20°C (Whillans and Grootes, 1985). Johnsen et al. (2000) find that the 1 yr frequency is detectible in all of GRIP Holocene ice but that damping is larger than predicted by the self-diffusion theory, suggesting a 1×10^{-7} m^2 yr^{-1} excess diffusivity that possibly originates in exchanges in the interstitial water in veins along grain boundaries, as earlier suggested by Nye (1998), though their explanation remains incomplete. In any case, all studies to date agree that diffusion of the climatic (pluri-annual) δ^{18}O and δD signals is negligible in ice; thus, we can consider water isotopes as passive tracers in ice sheets.

2.5 Modelling ice-sheet evolution

Ice core records dated by glaciological methods usually assume simple ice flow at the site and a predefined history of past surface elevation. At a dome, the flow is taken as uni-dimensional, as done for instance at GRIP, Dome C and Dome Fuji. A 2.5-dimensional model has been applied for Vostok to account for the flow originating from the 300-km-upstream Ridge B and for divergence along the flow line (Ritz, 1992; Petit et al., 1999; Parrenin et al., 2001). One of the objectives of this thesis is to predict the fine stratigraphy of ice core records using a three-dimensional ice sheet model, a method that could be regarded as the ultimate dating model because it would include most of the thermodynamics of ice flow and be free from any assumption about past variations in dome position, ice origin and surface elevation. Before developing a tracer transport model, I quickly review the basis of ice sheet modelling and some of the assumptions we shall make to predict the past evolution of the Greenland and Antarctic ice sheets.

2.5.1 Dynamics of ice flow

For the following presentation of the three-dimensional flow of ice I adopt the summation convention and use the letter j for two-dimensional (i.e., horizontal) fields or operations, k for three-dimensional, (i, k) for a 3×3 tensor and the conventional x, y and z for specific directions. I take t to denote time, $\mathrm{d}/\mathrm{d}t$ the material derivative, x_k the three-dimensional spatial coordinates, ∂_k=$\partial/\partial x_k$ the derivation operator, v_k the velocity, ρ the ice density, σ_{ik} the stress tensor, $\dot{\epsilon}_{ik}$ the strain tensor, f_k a specific body force, u the specific internal energy, a a specific energy supply, q_k the conduction flux. Ice is a viscous material that obeys the standard balance equations:

$$\text{local mass balance:} \qquad \frac{\partial \rho}{\partial t} + \partial_k(\rho v_k) = 0 \tag{2.6}$$

$$\text{linear momentum balance:} \qquad \rho \frac{\mathrm{d}v_k}{\mathrm{d}t} = \rho f_k + \partial_i \sigma_{ik} \tag{2.7}$$

$$\text{angular momentum balance:} \qquad \sigma_{ik} = \sigma_{ki} \tag{2.8}$$

$$\text{local energy balance:} \qquad \rho \frac{\mathrm{d}u}{\mathrm{d}t} = \dot{\epsilon}_{ik}\sigma'_{ki} + \rho a - \partial_k q_k \tag{2.9}$$

with Ξ=$\dot{\epsilon}_{ik}\sigma'_{ki}$ the strain heating and σ'_{ik} the stress deviator tensor defined as the stress tensor minus the hydrostatic component: σ'_{ik}=$\sigma_{ik} - \frac{1}{3}\delta_{ik}\sigma_{kk}$ with δ_{ik} the Kronecker delta. Remembering that the strain tensor is defined as

$$\dot{\epsilon}_{ik} = \frac{1}{2}\Big(\partial_i v_k + \partial_k v_i\Big), \tag{2.10}$$

ice sheet models use as the constitutive law of continental ice the flow law derived from Glen (1955):

$$\dot{\epsilon}_{ik} = B_0 \exp\Big(-\frac{Q}{RT}\Big)(\Sigma'_2)^{(n-1)/2}\,\sigma'_{ik}, \tag{2.11}$$

with B_0 a flow law constant, Q the creep activation energy, T the temperature, R the ideal gas constant, n an integer generally equal to 3 in ice sheet studies and Σ'_2=$\sigma'_{ik}\sigma'_{ki}$ the second invariant of the deviator stress tensor. These equations are generally integrated by assuming that ice is incompressible: $\mathrm{d}\rho/\mathrm{d}t$=0.

2.5.2 Principles of ice sheet modelling

Most numerical models of ice dynamics are based on earlier work from Mahaffy (1976), Jenssen (1977), Huybrechts (1990) and use the "shallow ice" approximation, which assumes that ice flow is governed by vertical shear deformation under gravitationally-induced stresses so that longitudinal stresses can be neglected. The UBC (Marshall, 1996; Clarke and Marshall, 2002) and LGGE (Ritz et al., 1997, 2001) ice sheet models employed in my study are in that class of models. The geometrical evolution of an ice sheet is obtained by vertically integrating the mass balance equation (Mahaffy, 1976):

$$\frac{\partial H}{\partial t} = -\partial_j(v_j H) + \dot{b} \tag{2.12}$$

where H is the ice thickness and $\dot{b} = \dot{b}(x, y, t)$ is the mass balance function (accumulation, ablation, basal melting and basal freeze-on). Denoting S the surface elevation and B the bedrock elevation, S=H+B and the flow-driving components of surface slope are $\partial_x S$ and $\partial_y S$. Thus, the flow law gives (j=x,y):

$$\dot{\epsilon}_{jz} = \frac{1}{2}\frac{\partial v_j}{\partial z} = B_0 \exp(-Q/RT)\Big(\rho g(S-z)\frac{\partial S}{\partial x_j}\Big)^n \tag{2.13}$$

which can be vertically integrated once to obtain horizontal velocity, noting that T=$T(x, y, z)$ for polythermal ice. Vertical velocity can be calculated from Eq. 2.6. Surface and ice thickness evolution is found by vertically integrating Eq. 2.13 a second time to obtain horizontal ice fluxes, which can be injected back into Eq. 2.12. The ice temperature field is found by solving Eq. 2.9, which is equivalent to the advection-diffusion equation:

$$\frac{\partial T}{\partial t} = -v_k \partial_k T + \frac{1}{\rho c}\partial_k(K\partial_k T) + \frac{1}{\rho c}\Xi \tag{2.14}$$

with K the thermal conductivity of ice and c its specific capacity, so that the temperature-dependent flow law coefficient ($B_0 \exp(-Q/RT)$) can be calculated. Note that the term a disappears because energy supply is assumed to vanish in ice sheets. Hence the ice sheet model can predict the surface elevation and velocity fields at any given time, provided that it is fed with a surface mass balance forcing and thermal boundary conditions above (surface temperature) and underneath (geothermal heat flux) the ice.

2.5.3 Parameterization of the climate over ice sheets

Surface temperature (T_s) and sea level history are the most important forcings applied to ice sheets. Sea level, which controls the fate of the West Antarctic Ice Sheet, is discussed in a later chapter. I discuss temperature here because assumptions concerning that forcing will determine the choice of a tracer method. As shown hereafter, surface temperature exerts a strong influence on surface mass-balance through its effect on precipitation and ablation rate; thus, T_s fuels ice flow. As a surface boundary condition, T_s also affects the thermodynamical evolution of ice, thus the propensity of ice to deform.

Given our interest in the glacial–interglacial evolution of ice sheets, an Atmospheric General Circulation Model (AGCM) (Jouzel et al., 1991; Krinner and Genthon, 1998; Hoffmann et al., 2000) would ideally complement our ice dynamics models by prescribing the changing conditions at the surface of the ice sheet. AGCMs, which use the most comprehensive and physically based representation of mass and energy transfers, could potentially provide prediction of past changes

in climate patterns. However, the computational requirements of such models currently forbid us to use them for long-term simulations. We can at best use instantaneous snap-shots of past periods to provide an indication of the climate at that time, though such predictions would be highly dependent on assumptions regarding sea surface temperatures and ice sheet topography (Hoffmann, *pers. comm.*). Therefore, our approach to simulate past climate, like most previous studies to date, is to use present-day observations of temperature and precipitation and apply perturbations inferred from proxy data, usually ice core records (Huybrechts, 1990; Ritz et al., 1997; Marshall and Clarke, 1999; Payne et al., 2000; Cuffey and Marshall, 2000; Clarke and Marshall, 2002; Huybrechts, 2002; Tarasov and Peltier, 2003).

Past temperatures are taken to be a linear combination of the present distribution of surface temperature $T(x, y, 0)$, a spatially uniform climate forcing ΔT_{c} (inferred from an ice core $\delta^{18}\mathrm{O}$ record) and the elevation change ΔS:

$$T(x, y, t) = T(x, y, 0) + \Delta T_{\mathrm{c}} + \beta_{\mathrm{T}} \Delta S \tag{2.15}$$

with β_{T} the temperature lapse rate that we assume constant and spatially uniform. Details concerning how to infer ΔT_{c} from ice cores and values for β_{T} are given in later chapters, when we apply the ice sheet models to the study of Greenland and Antarctica.

Surface mass balance is the net result of accumulation and ablation. Like temperature, past surface mass balance is derived from its modern distribution. Precipitation rate in Greenland and Antarctica relate exponentially to temperature (Robin, 1977), a result of the strong dependence of precipitation on the water vapour contained in the atmosphere. Therefore I define past precipitation rates P according to the thermodynamically driven equation

$$P(x, y, t) = P(x, y, 0)\ \exp\Big(D_{\mathrm{acc}}[T(x, y, t) - T(x, y, 0)]\Big) \tag{2.16}$$

with D_{acc} a precipitation sensitivity (tested for values in the range 0.07–0.90 K^{-1}). Ablation is computed from annual and summer temperatures according to the standard positive-degree day method of Reeh (1991). Present temperature and precipitation maps for Greenland and Antarctica are presented in Appendix A.

CHAPTER 3

Three-dimensional tracer modelling

3.1 Motivation

As mentioned in the introductory chapter, modern ice sheets contain a great wealth of information on the past climate of the Earth and also constitute a large scale laboratory to understand the past and future behaviour of ice sheets and their influence on the climate. Tracer transport modelling can simultaneously address many of these questions by predicting the fine three-dimensional time-evolving structure of ice sheets, so that modelled details at any given depth can provide information both on chemical and ice flow properties. Achieving these objectives has been a leading unsolved problem of ice sheet modelling. Previous studies have shown some success by restricting their model to limited spatial and temporal coverage, two-dimensionality or steady-state assumptions (e.g., Waddington and Clarke, 1988; Weertman, 1993; Abe-Ouchi et al., 1994). Difficulties have been encountered for more ambitious studies (Greve, 1997) because of the instability of Eulerian computational schemes for this purpose. The first success with a three-dimensional model running over a full glacial–interglacial cycle was reported by Clarke and Marshall (2002) with a semi-Lagrangian method that forms the basis of the present study. The principles and difficulties of the model are described in the following sections. Other methods have recently been explored, using either semi-Lagrangian tracers with an impractical level of spatial resolution to directly predict $\delta^{18}\mathrm{O}$ at Summit in Greenland (Tarasov and Peltier, 2003), or with Lagrangian tracers in steady-state mode (Rybak and Huybrechts, 2004). These methods are further discussed next.

3.2 Transport of provenance variables

3.2.1 Technical context

Our method is built on the premise that an ice sheet model can describe the temporal evolution of surface elevation and ice flow when forced by a climatic history. The tracer model comprises two components: a tracking module that follows ice particles and a depositional module to specify the spatial and temporal properties of deposited ice at the surface. The practical implementation of the method is later performed using the UBC Ice Sheet Model (Marshall, 1996) for Greenland and using the LGGE Ice Sheet Model (Ritz et al., 2001) for Antarctica, models whose operating principles were described in chapter 2; presentation of their practical details is kept until their application. Given that the two models use different coordinate systems, the former geographically oriented, the latter cartesian, we proceed with the following presentation using a cartesian (x, y, z) coordinate system and leave transformations to the Appendices. To circumvent the complication of a vertical grid that varies because of changes in ice thickness H and surface elavation S, Marshall (1996) and Ritz et al. (2001) have separately introduced their own reduced vertical coordinate that we shall call ξ: $\xi = \exp[A(S - z)/H]$ with A a scaling factor usually equal to 0.97 for the UBC model, and $\xi = (S - z)/H$ for the LGGE model. The variable ξ has 21-evenly spaced levels on

the ice dynamics grid. In this manner, we obtain a fixed computational grid (x, y, ξ) with regular spacing ($\Delta x, \Delta y, \Delta\xi$=1/20) in all three directions. The following presentation uses alternatively the natural and intuitive (x, y, z) system to explain the general concepts and (x, y, ξ) for practical implementation. I will often refer to the GRIP record and the Greenland Ice Sheet because these were used to develop, test and validate the method. Nevertheless, the principles equally apply to the Antarctic Ice Sheet.

3.2.2 Tracer principles

Consider a particle P of ice travelling through an ice sheet. The particle moves as the ice body flows and deforms; thus, the velocities v_p of the ensemble of individual particules P in the ice mass define a velocity field $v_p = (v_x, v_y, v_z)$, with components $v_x(x, y, z, t)$, $v_y(x, y, z, t)$ and $v_z(x, y, z, t)$ expressed in our coordinate system (x, y, z). The rate of change of position for a material particle at position (X, Y, Z) is given by the equations

$$\frac{\mathrm{d}X}{\mathrm{d}t} = v_x(X, Y, Z, t) \tag{3.1}$$

$$\frac{\mathrm{d}Y}{\mathrm{d}t} = v_y(X, Y, Z, t) \tag{3.2}$$

$$\frac{\mathrm{d}Z}{\mathrm{d}t} = v_z(X, Y, Z, t). \tag{3.3}$$

This set of equations can be used to track the flow of any ice particle during its journey through an ice sheet. Assume initial position $X(t_0)$=X_0, $Y(t_0)$=Y_0 and $Z(t_0)$=Z_0, the particle can be uniquely identified by its present position (X, Y, Z) or by the position it started from (X_0, Y_0, Z_0) (e.g., Malvern, 1969, pp. 138–143). If the material particle P carries along some time-invariant scalar property Ψ, then Ψ will remain unchanged as it is transported with the flow and satisfy the equation

$$\frac{\mathrm{d}\Psi}{\mathrm{d}t} = 0. \tag{3.4}$$

The derivative operator is called the material derivative and corresponds to a Lagrangian description of the properties entrained with the flow. In the Eulerian point of view, it can equivalently be expressed as a simple advection equation relative to a spatially-fixed coordinate system

$$\frac{\partial\Psi}{\partial t} + v \cdot \nabla\Psi = 0. \tag{3.5}$$

Given their low diffusivity in ice (section 2.4.2), we can assume that δ^{18}O and δD are time-invariant properties and apply either method to model the stratigraphy of ice sheets. The isotopic layering of an ice sheet is a highly spatially variable property with climatically-informative jumps and spikes occurring within a few meters, especially at greater depth where annual layers thin (e.g., the isotopic record of Vostok in Fig. 2.2). Therefore, direct modelling of δ^{18}O and δD would require an unpractically large number of particles to resolve the many significant individual climatic events recorded at depth. Similar considerations apply to the GRIP record (GRIP Members, 1993) and motivated the choice of Tarasov and Peltier (2003) to resort to over one thousand vertical grid points and increased horizontal resolution to resolve the 3000 m thick stratigraphy. The computational demands of their method limits their prediction to the Summit area and makes it unsuitable for our larger purpose. High vertical resolution was required because the authors were trying to directly

match every $\delta^{18}\mathrm{O}$ oscillation. Flux form methods (Rasch and Lawrence, 1998) can offer a better alternative for those interested in the $\delta^{18}\mathrm{O}$ stratigraphy only. The method consists in modelling the integral of the property Ψ from an outside boundary to a given layer or interface and calculating the flux of Ψ through that interface. That technique avoids many difficulties thanks to the inherent monotonicity of the integral approach. I tested the method and recognized that it is highly efficient and intrinsically conservative even at moderate resolution as opposed to the potential problems of dissipation or over-shooting that Eulerian and semi-Lagrangian schemes encounter when modelling $\delta^{18}\mathrm{O}$. However, there are other reasons for not directly modelling $\delta^{18}\mathrm{O}$ and $\delta\mathrm{D}$ that will soon be apparent.

Clarke and Marshall (2002) earlier acknowledged and circumvented those difficulties with an indirect method that consists in tracking the provenance labels or "birth certificate" of particles relative to their deposition at the surface of the ice sheet. These labels are the depositional position $(x_\mathrm{d}, y_\mathrm{d})$ and depositional date (t_d) of a particle, which also are time-invariant properties. In this manner, marked particles are tracked during their journey through the ice sheet and can be used to predict the three-dimensional-time-evolving structure of provenance labels. In parallel to simulating ice flow and tracer transport, an archive storing depositional conditions such as $\delta^{18}\mathrm{O}$ and surface elevation S is built, like a "birth registry", detailed in a later section. The isotopic signature of any ice particle can then be recovered by cross-referencing its "birth certificate" and "birth registry". The method offers a much wider range of application than direct modelling of $\delta^{18}\mathrm{O}$ because we can additionally access the deposition origin, age and elevation of any particle, which can assist the interpretation of ice core records. Calibration of the isotopic depositional rate and pattern can also be performed independently of the ice dynamics and tracer calculations, as we shall see later, because ice flow is insensitive to the $\delta^{18}\mathrm{O}$ composition of ice.

3.2.3 Eulerian, Lagrangian, or semi-Lagrangian scheme?

The foregoing transposition of the problem assures easier implementation on the coarse grid of an ice sheet model and should yield greater accuracy because provenance labels are a smooth field in most of the ice sheet thanks to the continuity of ice flow, though potential problems can arise depending on the choice of a Lagrangian (Eq. 3.4) or an Eulerian (Eq. 3.5) description. Traditionally, Eulerian schemes have been preferred because ice sheet models are expressed in that manner. Numerical problems associated with non-physical oscillations and artificial diffusion of tracers are known to plague resolution of advection-diffusion-type equations in an Eulerian framework (e.g., Vreugdenhil, 1993). Therefore, previous attempts using such methods have failed. Indeed, Eq. 3.5 requires that the modelled property Ψ be field-like with spatial gradients defined everywhere, except maybe at a reasonable number of traceable interfaces. Though ice flow is by nature continuous, ice masses can merge and bring together ice with different origins, resulting in a jump, possibly in all three provenance variables. This can also happen if occasional surface melting removes ice layers in the accumulation zone, hence breaking the annual continuity and propagating the discontinuity through the ice sheet once positive mass balance is re-established and ice is advected within the flow. Such circumstances are fatal for standard Eulerian methods and would necessitate a very high order numerical scheme to resolve such shock-wave-type features, especially in a three-dimensional context, a cost that current ice sheet models cannot support. Another unacceptable remedy would be to introduce high levels of artificial tracer diffusion to smooth any discontinuity, but this would be absurd since our primary goal is to model non-diffusive tracers.

Lagrangian methods using Eq. 3.4 can avoid that precipice and have therefore been widely used

in tracer modelling studies and recently for predicting the age distribution in the Antarctic Ice Sheet (Rybak and Huybrechts, 2004). In this formulation, particles are followed along their trajectory and keep their properties; thus, no gradient is calculated and there is great robustness to discontinuous interfaces between particles of different age or origin (e.g., the two-dimensional study of Waddington and Clarke, 1988). Only the position needs to be updated according to Eqs. 3.1–3.3; in the case of an ice sheet model with a spatially-fixed grid, this requires three-dimensional interpolation of the velocity field because particles are generally not located at grid points. Rybak and Huybrechts (2004) settle for piece-wise linear interpolation, though less accurate than cubic spline, because the computer requirements of high order schemes are presently not manageable. Though elegant, the formulation faces additional shortcomings inherent to the divergence of ice flow: ice particles are irregularly dispersed in the ice sheet. This can leave shaded areas that deposited particles never reach; thus, iterations need to be performed to predict beforehand where a high density of particles should be deposited to fill those void cavities. Interpolation of ice sheet stratigraphy needs to be performed with a highly irregular distribution of ice particles, which is unpractical for common plotting routines and can also lead to severe information loss where particles are scarce. The most tedious aspect of the method is the substantial book-keeping involved, with the constant need to introduce new particles at the surface and to remove old non-informative particles concentrated near the base of the ice sheet.

Clarke and Marshall (2002) opted for the semi-Lagrangian scheme, a method that combines the best features of the Eulerian and Lagrangian frameworks. Though little-used in glaciological studies, semi-Lagrangian tracers are a standard approach in atmospheric studies (e.g., Staniforth and Côté, 1991). The aim is to provide the solution on a regular computational grid, in our case the ice dynamics grid, by identifying the set of particles that exactly reaches the grid at the end of a time step. As opposed to the Lagrangian scheme, a different set of particles is used at each time step, hence the name of the method. Consider a material point P at time t with coordinates $(X(t), Y(t), Z(t))$. According to Eqs. 3.1–3.3, its previous location at time $t - \Delta t$ can be roughly described by

$$X(t - \Delta t) = X(t) - v_x(X, Y, Z, t)\,\Delta t \tag{3.6}$$

$$Y(t - \Delta t) = Y(t) - v_y(X, Y, Z, t)\,\Delta t \tag{3.7}$$

$$Z(t - \Delta t) = Z(t) - v_z(X, Y, Z, t)\,\Delta t. \tag{3.8}$$

Time-invariance of an attached property Ψ implies that

$$\Psi[X(t), Y(t), Z(t), t] = \Psi[X(t - \Delta t), Y(t - \Delta t), Z(t - \Delta t), t - \Delta t]. \tag{3.9}$$

Thus, the value of Ψ at grid-point $P(t) = [X(t), Y(t), Z(t), t]$ is determined by its value at an upstream point $P(t-\Delta t)$ at an earlier time $t-\Delta t$. That departure point $P(t-\Delta t)$ is not necessarily located at a grid node. Therefore $\Psi[X(t-\Delta t), Y(t-\Delta t), Z(t-\Delta t), t-\Delta t]$ has to be interpolated from gridded values of Ψ at the previous time $t - \Delta t$. Meteorologists specially favour this method because it offers great stability relative to the Eulerian scheme: large time steps can be achieved because the process is free from temporal and spatial derivatives, thus exempt from the Courant-Friedrichs-Levy (CFL) restrictions. Potential sources of error are identification of the departure point and interpolation of Ψ at time $t - \Delta t$ (e.g., Riishϕjgaard et al., 1998). Clarke and Marshall (2002) opted for trilinear interpolation and a small time step corresponding to the ice dynamics in their simulations of the Greenland Ice Sheet. Difficulties and remedies are discussed in the following.

3.3 Specificity of the age–depth relationship

Recall that Clarke and Marshall (2002) and I chose to model the three-dimensional time-evolving structure of provenance tags of an ice sheet, namely $x_{\rm d}$, $y_{\rm d}$ and $t_{\rm d}$. That approach has similarities to the problem of dating ice cores because most of the difficulties lie in the age–depth relation of the specific ice sheet. Let us consider the one-dimensional case of the vertical motion of a particle P which arrives at a grid point z_j at time t and departed from a point $z^{\rm D}$ at time t–dt. The invariance condition implies that $\Psi(z^{\rm D}, t - {\rm d}t)$=$\Psi(z_j, t)$. The crux of the semi-Lagrangian method is to first determine the coordinates of the departure point and then to accurately estimate the property Ψ at that point.

3.3.1 Sources of error

Clarke and Marshall (2002) used linear interpolation to estimate depositional time $t_{\rm d}(z^{\rm D}, t - {\rm d}t)$ at the departure point $z^{\rm D}$. Further studying the age–depth accuracy of this interpolation, I found that the deglacial transition was displaced by $450\,{\rm m}$ for the GRIP ice core. The cause of this misfit was not immediately obvious. Possible causes included underestimation of the surface accumulation rate, or incorrect calculation of the vertical component of ice flow. Extensive testing eliminated these possibilities and indicated that the source of misfit was simplistic numerical analysis. As I shall show, the problem is related to the underlying physics and not to the order or resolution of the scheme.

The age–depth profile of an ice sheet is an expression of the stacking and thinning of annual layers of ice. Over the length of an ice core, the thickness of annual layers varies because of variations in the surface accumulation rate and because layer compression increases with depth. Fig. 3.1a shows the mass balance history inferred for GRIP from 50 kyr BP (Before Present, taken as year 1950) to 2 kyr BP. The most conspicuous feature of this record is the 3–4-fold increase in surface accumulation rate that accompanied the transition from glacial to interglacial climate, 11 kyr ago (e.g., Alley et al., 1993). In Fig. 3.1b, the solid line indicates the depth–age relationship $z(t_{\rm d})$ obtained by integrating this balance record to obtain the cumulative mass balance. The deglacial transition appears as a change in the slope of this curve.

Let us now shift the focus to the challenge of accurately modelling the age–depth relationship using a semi-Lagrangian scheme. Consider a regularly sampled vertical grid z_k (Fig. 3.1b, ordinate, k=1 at the base) with associated ages $(t_{\rm d})_k$ for the GRIP age–depth relationship. The modelling objective is to accurately interpolate the depositional time variable $t_{\rm d}$=$t_{\rm acc}$ at the departure point $z^{\rm D}$. Linear and cubic interpolation perform adequately when the balance rate is constant, but not for realistic cases (e.g., Fig. 3.1a). If the characteristics of the data are ignored and standard linear interpolation (dashed line) or cubic spline (dot-dash line) are employed, depositional time is poorly estimated (Fig. 3.1b, inset). A second source of error is the flow-related variation in layer thickness with depth. Linear and cubic interpolation schemes misrepresent this process in different ways. Linear schemes assume constant layer thickness within a grid cell, whereas cubic schemes distort the layer thickness variation in a systematic but uncontrolled manner. Interpolation accuracy can be improved by increasing the vertical resolution of the computational grid as earlier mentioned for Tarasov and Peltier (2003) but this is an impractical remedy to model the stratigraphy of the entire ice sheet — a leading objective of my study.

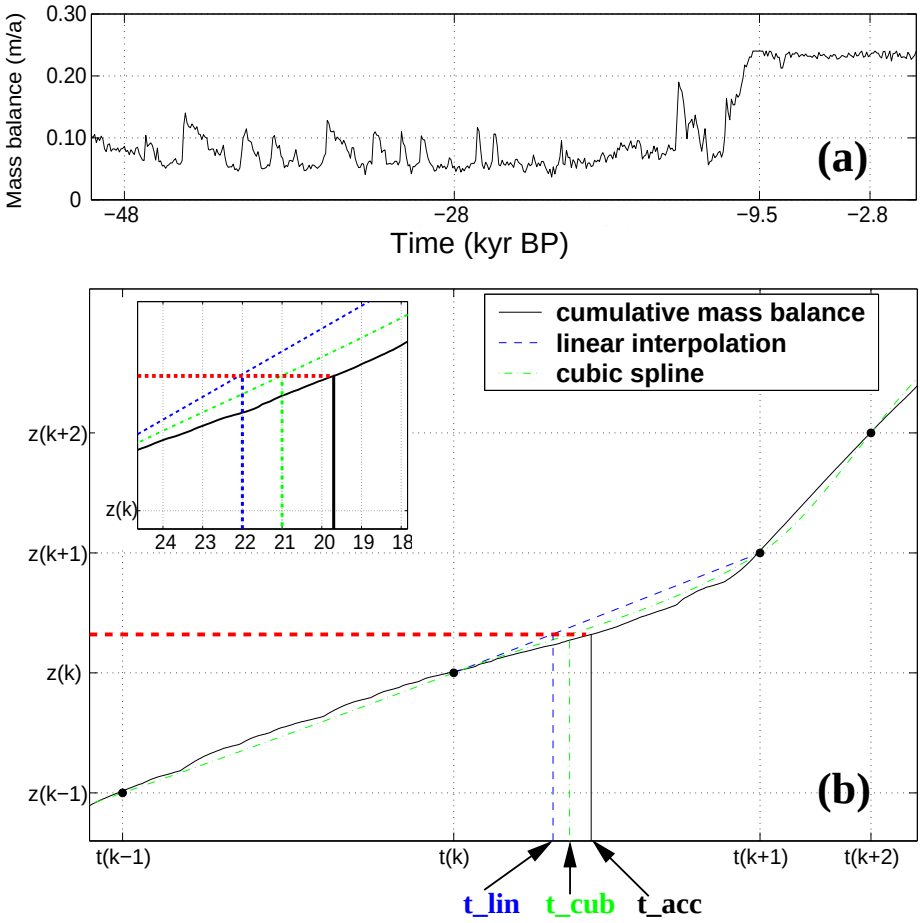

Figure 3.1: (a) GRIP mass balance history between 50 kyr BP and present. (b) Age–depth profile of the GRIP record for a depth range corresponding to that period, and a computational grid $z(k)$. In the semi-Lagrangian framework, a particle reaching $z(k)$ originates at altitude z^{D}. Because accumulation rate varies between times $t(k)$ and $t(k+1)$, age at z^{D} is overestimated with linear interpolation (t_{lin}) and with cubic spline with the four closest neighbours (t_{cub}). Cumulative balance (solid line), which accounts for changes in accumulation rates yields better estimates of the age of a particle.

3.3.2 A balance-based interpolation method

The interpolation method that I have developed is indirectly inspired by flux methods (Rasch and Lawrence, 1998). Of the two processes that complicate age–depth interpolation, I assign primary importance to mass balance changes and secondary importance to thinning processes.

The difference in age of ice at the surface h_s and at depth h_s–z is the sum of the inverse annual layer thicknesses $\omega(z)$ (e.g., Parrenin, 2002)

$$t_{\mathrm{d}}(h_s) - t_{\mathrm{d}}(z) = \int_z^{h_s} \frac{\mathrm{d}z'}{\omega(z')}. \tag{3.10}$$

The thickness of a layer is the ratio of the initial thickness $\omega_0(z)$ and the compressive thinning $\psi(z)$

of that layer

$$\psi(z) = \frac{\omega_0(z)}{\omega(z)}. \tag{3.11}$$

The initial thickness $\omega_0(z)$ of ice at z deposited at time t_d is equal to the annual surface mass balance $\dot{b}(t_\mathrm{d})$ at that time; thus, Eq. 3.10 implies for a layer of thickness dz spanning $\mathrm{d}t_\mathrm{d}$ years that

$$\mathrm{d}t_\mathrm{d} = \frac{\psi(z)}{\omega_0(z)}\mathrm{d}z, \tag{3.12}$$

equivalent to

$$\dot{b}(t_\mathrm{d})\,\mathrm{d}t_\mathrm{d} = \psi(z)\mathrm{d}z. \tag{3.13}$$

To illustrate the implications for a semi-Lagrangian scheme, consider a particle that arrives at grid point z_k at time t from a higher elevation z^D, lying between z_k and z_{k+1} and closer to z_k. The crucial step consists in finding t_d=$t_\mathrm{d}(z^\mathrm{D}, t-\mathrm{d}t)$ given $(t_\mathrm{d})_k$=$t_\mathrm{d}(z_k, t-\mathrm{d}t)$ for all k. Because surface mass balance is a function of time, I take Eq. 3.13 and integrate $\dot{b}(t)$ from $(t_\mathrm{d})_k$ to t_d, and $\psi(z)$ from z_k to z^D to obtain

$$\int_{(t_\mathrm{d})_k}^{t_\mathrm{d}} b(t)\mathrm{d}t = \int_{z_k}^{z} \psi(z')\mathrm{d}z'. \tag{3.14}$$

The above equation is the fundamental equation that defines t_d.

To find t_d, I must first determine $\psi(z)$ between z_k and z^D. The thinning ψ is a regular continuous function of depth. Defining ψ_k as an average thinning of layer $[z_k; z_{k+1}]$

$$\psi_k = \frac{1}{z_{k+1}-z_k}\int_{z_k}^{z_{k+1}} \psi(z)\mathrm{d}z \tag{3.15}$$

and then invoking Eq. 3.14 leads to

$$\psi_k = \frac{1}{z_{k+1}-z_k}\int_{(t_\mathrm{d})_k}^{(t_\mathrm{d})_{k+1}} b(t)\mathrm{d}t. \tag{3.16}$$

For practical implementation and higher accuracy (see Appendix C), I use the ξ coordinates instead of z, with z_k and z^D corresponding to ξ_k and ξ^D, respectively. Defining f_ξ=$(\xi^\mathrm{D}$–$\xi_k)/\Delta\xi$, I interpolate ψ at mid-trajectory between ξ_k and ξ^D according to

$$\frac{1}{\widetilde{\psi}} = \frac{1}{2}\left[(1-f_\xi)\frac{1}{\psi_{k-1}} + (1+f_\xi)\frac{1}{\psi_k}\right]. \tag{3.17}$$

Lastly, I define a cumulative-balance function

$$\Omega(t_\mathrm{d}) = \int_{t_\mathrm{ref}}^{t_\mathrm{d}} \dot{b}(t)\mathrm{d}t \tag{3.18}$$

constructed from the local surface mass balance integrated from a time t_ref, much older than t_init. In Appendix C, I show that practical construction of Ω based on modelled surface mass balance at the GRIP site for Greenland, the Dome C site for Antarctica, can be applied to interpolate age for the entire ice sheet and yield satisfactory accuracy. Eq. 3.18 then becomes

$$\Omega(t_\mathrm{d}) \approx \Omega((t_\mathrm{d})_k) + \widetilde{\psi}(z^\mathrm{D} - z_k) \tag{3.19}$$

from which t_d can be extracted. Note that the above presentation gets easily transposed for a particle moving upward or if the departure point is located closer to but below z_{k+1}.

3.3.3 Age boundary conditions

Boundary conditions require a special treatment. At the surface, when surface mass balance is positive, the depositional age is the current time. When it is negative, I assume that $\widetilde{\psi} = \psi_k$ if the departure point z^{D} is closer to the surface than to the first level below or use Eq. 3.17 otherwise. Age at the base can be more problematic and will depend whether previous age was older than t_{ref}, which can happen for 600 kyr simulations of Antarctica. When that is the case, for basal ice and even higher up in the ice column, I directly interpolate t_{d} by applying a cubic spline using the former age at the arrival point and the two levels immediately above. Otherwise, the balance method can be applied. If ice originates from above, the distance between the departure and the arrival point is generally small relative to the separation between two grid points; thus, the average thinning of the grid layer misrepresents thinning along the trajectory. Therefore I introduce a fictitious additional layer below the base layer with a doubled rate of thinning, which is equivalent to having an additional grid point with an age difference twice as large. The case of bottom freeze-on, upward velocity at the basal grid point, is more of a philosophical question. Assigning the new basal ice a contemporaneous age would be erroneous, both computationally, because that would introduce an age inversion, and chemically, because the frozen water comes from the basal hydrological system that samples ice of many different ages and composition. Therefore, that new basal age is given as

$$t_{\mathrm{d}}(B,t) = t_{\mathrm{d}}(B,t-dt) + 2\frac{-\dot{f}}{dz}(t_{\mathrm{d}}(B,t-dt) - t_{\mathrm{d}}(B+dz,t-dt)) \tag{3.20}$$

with $\dot{f}$ the basal melt rate, here negative from freeze-on, and dz the vertical grid spacing. Again, this boundary condition operates as if there were a fictitious grid point below the ice base with an age difference twice as large, hence the factor 2. Alternative boundary conditions were tested without a noticeable effect either on basal age or above. Because of the mostly downward nature of ice flow and the interpolation chosen above, any occasional error in basal age is unlikely to contaminate upper layers.

3.3.4 Three-dimensional implementation

Continuity and smoothness of the flow of an ice sheet model imply that ice layers are locally parallel and generally follow iso-ξ coordinate contours. The balance-based interpolation is extended to three dimensions by first bilinearly interpolating over (x, y) planes (Appendix B) and then applying the balance-based vertical interpolation for ξ. The cumulative-balance function for Greenland is built as the simulation proceeds with the simulated mass balance at GRIP with a time step of 100 yr, matching the temporal resolution of the δ^{18}O timeseries used for the climate forcing. Similar implementation is applied to Antarctica, taking mass balance at EPICA–Dome C, where the climate forcing used originates. Longer time steps for the tracer transport are achieved by temporally integrating the velocity field provided by the ice dynamics model. Higher accuracy in determining the departure point of a particle might be achieved by an iterative process (e.g., ECMWF model, Riddaway, 2001) but I have found this complication to be unwarranted. I effectively limit the length of the time steps to 20–50 yr to limit errors at the margins, though I find that longer time steps of 100–200 yr work well for central regions when using three iterations like the ECMWF model. In terms of computational requirements for the tracer model, the variables needed to proceed from one time step to the next are the ice surface elevation, bed elevation, integrated velocity field and tracer provenance fields. Activating the tracing capability increases memory use by 20% and computation time by 5%.

3.4 Depositional model

3.4.1 An archive like a "birth registry"

As presented above, the three-dimensional time-evolving ice sheet stratigraphy is predicted in terms of provenance labels, not chemical concentrations of any sort. With this method, the place and time of arrival of any particle at the surface of the ice sheet can be recovered. Deposited particles are generally snow/ice; the isotopic composition of which is interesting for paleoclimate studies. A particle can also carry ash from a distant volcanic eruption, or dust resulting from intense weathering and advected by the strong winds that are typical of glacial periods (Taylor et al., 1993). Any of these non-diffusive properties contribute to the particular chemical, tephraic and dielectric structure of the ice sheet and constitutes a host of information we may wish to include. Thus, an archive is built like a "birth registry" of delivered particles to store the time-evolving spatial distribution of depositional conditions at the surface of the ice sheet as a simulation of Greenland or Antarctica proceeds.

Several steps are taken for designing an efficient archive. First, I follow the lead of Clarke and Marshall (2002) to store "construction variables" instead of accounting for the many possible chemical species deposited at any given time. These variables are the paleoelevation $S(x, y, t)$, paleotemperature $T_{\mathrm{s}}(x, y, t)$ and paleomass balance $\dot{b}(x, y, t)$ at the surface of the ice sheet and can be used in conjunction with the provenance labels to recover the stratigraphy of a given property. For instance, tephra layers are associated with particular events having short duration; thus, their stratigraphic structure simply follows isochrones. $\delta^{18}\mathrm{O}$ is space and temperature-dependent; its special treatment is presented in the next section. The great advantage of such a formulation is that relationships between properties of interest and the provenance and construction variables can be calibrated at will after an ice sheet simulation is completed because these properties have no influence on ice flow, at least in many cases. Dust and impurities deposited during glacial periods are known to have a pronounced influence on ice deformation (Thorsteinsson et al., 1999). This effect can be included in the ice flow law by modifying the effective ice viscosity according to its age, softer for glacial ice. This possibility of an age-dependent ice rheology illustrates another significant possibility opened by this tracer transport method and which was used at the earliest stage of this research to diagnose the age–depth discrepancy in Clarke and Marshall (2002).

As a second practical step, we adopt the same horizontal grid as the tracer and ice dynamics grids; thus, we expect the depositional properties to have a smooth spatial variability. Third, the storage time step is adapted to the relevant characteristic time scale of the ice sheet: I take 100 yr because that corresponds to the resolution of the temperature forcing timeseries. Shorter time steps have been tested and found to be redundant. Because the oldest ice gets concentrated at greater depth and the archive grows considerably for simulations of 3 to 6 glacial–interglacial cycles, I increase the time step to 500 yr before 250 kyr ago, 200 yr before 100 kyr ago and keep 100 yr for the most recent 100 kyr.

3.4.2 Present isotopic distribution

As discussed in the previous chapter, water isotope concentrations found in precipitation vary according to the temperature at the place and time. To predict the isotopic stratigraphy, one needs to know the present surface distribution of isotopes and to model its past evolution during colder periods. The following presentation focuses on depositional $\delta^{18}\mathrm{O}$ and I assume that $\delta\mathrm{D}$ can be directly

inferred from $\delta^{18}\mathrm{O}$ by the water meteoric line $\delta\mathrm{D} = 8\delta^{18}\mathrm{O} + 10$, a simple and mostly reasonable choice given their observed and modelled general behaviour, but a relationship that fails to capture spatial and temporal variations in deuterium excess due to changes at evaporative sites.

Present distribution is inferred from measurements at the surface of Greenland and Antarctica. Given the size and the harsh climate of the ice sheets, sampling has been limited to particular locations around drilling sites, traverses and coastal stations. Thus I will make use of some sort of interpolation to model the present distribution. Various relationships involving our construction variables have been suggested. The simplest just involves surface temperature:

$$\Delta\delta\mathrm{D} = \alpha_1 \Delta T_\mathrm{s} \tag{3.21}$$

in Antarctica (Lorius and Merlivat, 1977) and

$$\delta^{18}\mathrm{O} = \alpha_2 T_\mathrm{s} - \delta_2 \tag{3.22}$$

in central Greenland (Johnsen et al., 1989), with α_1=6.04‰ $^\circ\mathrm{C}^{-1}$, α_2=0.67‰ $^\circ\mathrm{C}^{-1}$, δ_2=13.7‰ and T_s in °C.

Using an updated and larger compilation of observations, Zwally and Giovinetto (1997) and Giovinetto and Zwally (1997) performed regression analyses to test possible refinements to include the influence of latitude (θ), elevation (S) and distance to open water (d_sea). These variables have a second order effect on surface $\delta^{18}\mathrm{O}$ because they already make a large contribution to surface temperature, as shown in Appendix A. Their analysis shows that

$$\delta^{18}\mathrm{O} = 0.691 T_\mathrm{s} - 13.4‰ \tag{3.23}$$

defines a robust bivariate model (R=0.986, root mean square rms=0.55) for present precipitation in Greenland, and that for a significantly larger dataset including ice shelves

$$\delta^{18}\mathrm{O} = 0.852 T_\mathrm{s} - 6.78‰ \tag{3.24}$$

provides an acceptable model (R=0.959, rms=3.04) for precipitation over the entire Antarctic Ice Sheet. I adopt these parameterizations to model present surface distribution of $\delta^{18}\mathrm{O}$ at the surface of the ice sheets. Although the parameterization is somewhat less acurate for Antarctica, the reward for including θ, S and d_sea is negligible (R=0.976, rms=2.33) relative to the difficulty of tracking the present and past sea ice extent, which is not predicted by our models of ice sheet evolution. An alternative approach would be to use the $\delta^{18}\mathrm{O}$ fields given by an AGCM with isotopic processes, for instance with the ECHAM model (Werner et al., 2000) or the GISS model (Jouzel et al., 1991), though complicated interpolation would also be required because of the coarse spatial resolution (2.5–10°) of their grid and the inherent misrepresentation of surface topography.

3.4.3 Past isotopic distribution

Past $\delta^{18}\mathrm{O}$ depositional rate is a more delicate issue as sampling of old ice only comes from scarce ice core records. Experiments with AGCMs are limited by uncertainties on surface topography (ice sheet elevation and extent) and sea surface (temperature at evaporative source, sea ice extent). Qualitatively, these models provide a useful explanation for differences between surface slope and temporal slopes (section 2.3.6), but the predicted isotopic deposition rates cannot be directly applied without spatial interpolation and substantial correction of surface elevation (based on now-outdated

ice–4G ice-sheet reconstruction„ Peltier, 1995), which may influence the processes. Therefore I prefer a parametric approach of a temperature–isotope relationship and will carry out sensitivity tests on its calibration, taking advantage of the flexibility of the archive.

I assume that past $\delta^{18}\mathrm{O}(x, y, t)$ at position (x, y) and time t is related to its present value $\delta^{18}\mathrm{O}(x, y, 0)$, to local change in surface elevation ΔS and to temperature change over the ice sheet $\Delta T_\mathrm{c}(t)$ according to (Cuffey, 2000)

$$\delta^{18}\mathrm{O}(x, y, t) = \delta^{18}\mathrm{O}(x, y) + \alpha_\mathrm{c}\Delta T_\mathrm{c}(t) + \beta_\delta \Delta S(x, y, t) \tag{3.25}$$

where α_c is the isotopic sensitivity and β_δ the isotopic lapse rate, as described in chapter 2. For Greenland, based on borehole-temperature analysis at GRIP and GISP2 (Cuffey and Clow, 1997; Dahl-Jensen et al., 1998), I use different values of α_c for ice deposited during the Holocene (0.34–0.40$^\circ/_{\circ\circ}\,\mathrm{K}^{-1}$), the glacial era (0.32–0.34$^\circ/_{\circ\circ}\,\mathrm{K}^{-1}$) and the last interglacial (0.25–0.50$^\circ/_{\circ\circ}\,\mathrm{K}^{-1}$); the exact value chosen within the range depends on the climate forcing used. The temperature lapse rate is –7.5K km^{-1}, the isotopic lapse rate is –6.2$^\circ/_{\circ\circ}\,\mathrm{km}^{-1}$ based on present day observations (Johnsen et al., 1989). Both lapse rates are assumed to remain constant in time. I also test an alternative calibration by taking the spatial distribution of the temporal slopes predicted with the GISS model over Greenland (Jouzel et al., 2000).

For Antarctica, I take α_c=0.6–0.8$^\circ/_{\circ\circ}\delta^{18}\mathrm{O}\,^\circ\mathrm{C}^{-1}$. Large values are in agreement with observations across most of Antarctica and especially in the central part, where most of the ice is stored ($\mathrm{d}\delta\mathrm{D}/\mathrm{d}T$=6.0–6.5$^\circ/_{\circ\circ}\delta\mathrm{D}\,^\circ\mathrm{C}^{-1}$ Petit et al., 1999; Masson et al., 2000) while lower values may better reflect Western Antarctica (e.g., Steig et al., 1998). The isotopic lapse rate is derived from 11 ice cores and set to β_δ=–11.2$^\circ/_{\circ\circ}\,\mathrm{km}^{-1}$ (Masson et al., 2000) for a temperature lapse rate of –9.1$^\circ\mathrm{C}\,\mathrm{km}^{-1}$ (Huybrechts, 2002).

3.5 Practical application

3.5.1 Tracer transport flow chart

Fig. 3.2 outlines the basic steps of the tracer tracking method for both Greenland and Antactica: a climate forcing (here derived from an ice core record) prescribes the time-evolving temperature (T_s) and mass balance (b_s) at the surface of the ice sheet as a simulation proceeds. This feeds the ice sheet model which in return calculates the three-dimensional velocity field in the ice (v_I) and surface elevation (h_s) that gets used by the tracer model to transport provenance labels in the ice sheet. Hence the provenance stratigraphy of the ice sheet is computed and can be stored at chosen periods in a "provenance archive". In parallel, the depositional archive is built to store the changing surface conditions on the ice sheet (T_s, b_s, h_s). The chemical composition of ice is obtained at a later "post-processing" stage.

3.5.2 Construction of tracer stratigraphy

The fine stratigraphy of the ice sheet can be predicted for any given time t_strat of interest stored in the provenance archive. The archives contain for that time t_strat the distribution of provenance labels $(x_\mathrm{d}, y_\mathrm{d}, t_\mathrm{d})$ on the ice dynamics grid $(x_\mathrm{G}, y_\mathrm{G}, z_\mathrm{G})$=$(i, j, k)$. The stratigraphy is obtained as follows. The ice sheet is assumed to be constituted of an ensemble of juxtaposed vertical ice columns. For a position i, j at the surface of the ice sheet at time t_strat, we consider the ice column of

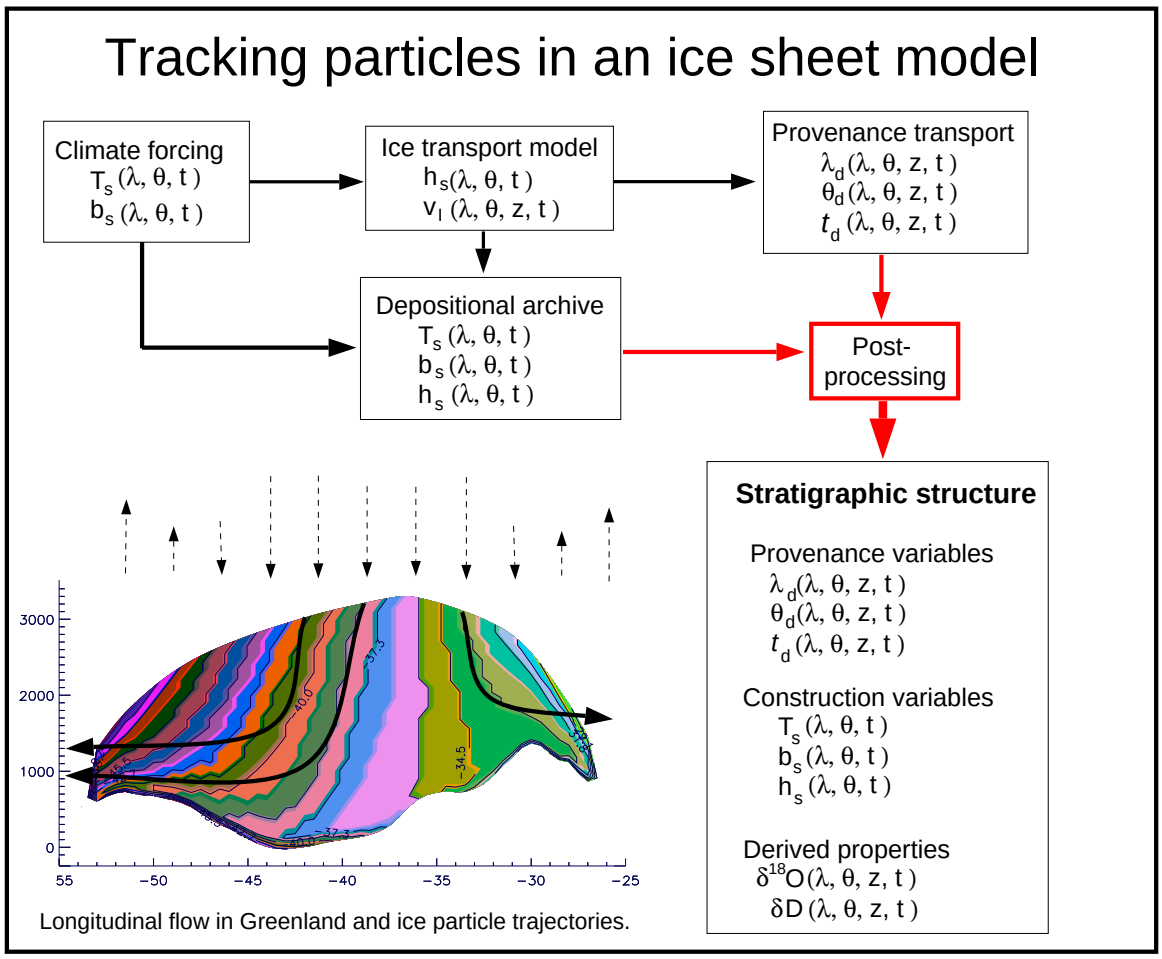

Figure 3.2: Flow chart for tracer modelling. $[\lambda, \theta]$ defi ne position for Greenland. For Antarctica a similar chart applies by replacing $[\lambda, \theta]$ with $[x, y]$. Arrows over the ice sheet represent the sign of surface mass balance.

provenance variables $(x_\mathrm{d}, y_\mathrm{d}, t_\mathrm{d})$, which we interpolate from their grid values to obtain a continuous stratigraphy $\{(x_\mathrm{d}(i,j,t_\mathrm{strat},z), y_\mathrm{d}(\ldots), t_\mathrm{d}(\ldots))\}_z$, using a piecewise linear interpolation for x_d, y_d and the cumulative balance function for t_d. Then, reading the depositional archive from its oldest time toward time t_strat, increasing dates t_arch are compared to interpolated provenance ages in the ice column until they match.

Each match at a time t_arch=t_n in the depositional archive defines a level z_n in the ice column such that t_n=$t_\mathrm{d}(i,j,t_\mathrm{strat},z_n)$ for an ice particle at position (i,j,z_n) and origin $[x_n$=$x_\mathrm{d}(i,j,t_\mathrm{strat},z_n)$, y_n=$y_\mathrm{d}(i,j,t_\mathrm{strat},z_n)$, $t_n]$. Chances are that the spatial origin (x_n, y_n) of the ice particle at the surface of the ice sheet does not coincide with a gridded point. Therefore we perform a bilinear interpolation between the four surrounding grid nodes to derive its depositional properties (T_s, b_s, h_s) from the depositional archive. The process is repeated to scan the entire depositional archive until the time t_strat so that we can span the whole ice column; this procedure is repeated for every glaciated point (i,j) of the ice sheet to obtain its global content.

3.5.3 Global properties

The above process allows one to recover the construction variables associated to the deposition of any ice particle. Calculation of the bulk ice sheet properties such as $\delta^{18}\mathrm{O}$ is performed in two steps: use a relationship to obtain the concentration of a given property from the construction variables, e.g., get $\delta^{18}\mathrm{O}$ from T_s, ΔS and ΔT_c and transform it into the [^{18}O] concentration, then integrate over the entire ice sheet, that is over the vertical column of every glaciated cell. Integration is started from the oldest time in the depositional archive. The volume of the ice sheet at time t is simply

$$V_\mathrm{I}(t) = \int_\mathcal{A} H_{ice} d\mathcal{A} \tag{3.26}$$

with $\mathcal{A}$ the surface area.

Other properties are less straightforward because surface melting ($\dot{b}(z)$ or $\dot{b}(t_\mathrm{d}) < 0$) may have removed some ice layers from the stratigraphy. Although the top boundary condition of the tracer model should expose older ice after melting, a chronological hiatus remains possible if at a given location a melting event is followed by years of positive surface mass balance while mass balance remains positive at GRIP or Dome C, the forcing site where the cumulative-balance function Ω was defined. Let us consider the integration of a property Ψ (e.g., age, isotopic concentration) between computational levels z_k and z_{k+1} (z_k<z_{k+1}), which correspond to the depositional times t_k and t_{k+1}. I assume that surface melting conditions result in removal of the immediately underlying ice layers, assuming that thinning as not yet taken place because melting occurs soon after deposition of upper layers, and that removal cannot affect layers below z_k. I construct a test on cumulated annual layers that uses a function

$$L(t_p, t_q) = \int_{t_p}^{t_q} \dot{b}(t) dt \tag{3.27}$$

that depends on the local cumulative surface mass balance, and an iterative process starting at [t_p=t_k; t_q=t_k+dt], with dt the time step of the depositional archive. At each iteration I test the sign of $L(t_p, t_q)$ to check whether melting has exceeded accumulation between times t_p and t_q and forbid melting beyond time t_k (level z_k). Then t_q is increased by dt until $t_q = t_{k+1}$. The process can be described as follows:

$$\begin{aligned} \text{if } L(t_p, t_q) \geq 0 \ : \ \text{then } \ t_q &= t_q + dt \\ \text{else set: } \ L(t_p, t_q) &= 0 \ \text{ and } t_p = t_q + dt \end{aligned}$$

so that L remains positive. Layer k contributes to the ice column only if the final value of $L(t_p, t_{k+1})$ is strictly positive. In most cases, $t_p = t_k$ because melting events are scarce in the accumulation zone. Otherwise, the year t_k and subsequent years have melted away, so that the oldest annual layer is t_p. Therefore I reset t_k to t_p and denote

$$dz_{ijk}(t) = L(t_k, t_{k+1}) = \int_{t_k}^{t_{k+1}} \dot{b}(x_n, y_n, t_n, z) dt. \tag{3.28}$$

Then the quantity n_Ψ of Ψ (e.g., number of moles) in level k in the ice column is

$$n_\Psi(i, j, k, t) = \frac{z_k - z_{k+1}}{dz_{ijk}(t)} \int_{t_k}^{t_{k+1}} \Psi(x_n, y_n, t_n, z) \dot{b}(x_n, y_n, t_n, z) dt \times d\mathcal{A}_{ij} \tag{3.29}$$

if $dz_{ijk}(t) > 0$ or $n_\Psi(i,j,k,t) = 0$ otherwise. The pre-multiplied scaling term accounts for the thinning of ice layers subsequent to deposition. The post-multiplied term is the surface area of the computational cell centered at grid point (i,j). Finally, the bulk concentration of property ψ for the entire ice sheet is

$$[\Psi]_\mathrm{I}(t) = \frac{1}{V_\mathrm{I}(t)} \int_\mathcal{A} \Big\{ \sum_{k=1}^{n_z-1} n_\Psi(i,j,k,t) \Big\} \, d\mathcal{A}_{ij} \tag{3.30}$$

with n_z=21 the number of vertical levels. Occurrence of melted layers within the provenance stratigraphy is so exceptional that negligible differences were found between this method and alternative schemes, e.g., scaling lost layers over an entire ice column or counting only the years of positive mass balance (without any removal), as done in Clarke and Marshall (2002).

3.5.4 Average isotopic concentration

Construction variables provide the depositional $\delta^{18}\mathrm{O}$ of ice particle. Because by definition $\delta^{18}\mathrm{O}$ is not a concentration, the procedure described hereabove cannot be directly applied to estimate the bulk composition of the ice sheet. For this study we assume that ice density is constant ρ_I=910 kg m^{-3} so the ice mass is m_I=$\rho_\mathrm{I} V_\mathrm{I}$, that the ice sheet is made of common water with molar mass M_0=$18.01528\,\mathrm{g}$ so the molar concentration of water is c_0=$\rho_\mathrm{I}/M_0\,\mathrm{mol}$ and the ice sheet of volume V_I contains n_0=$c_0 V_\mathrm{I}\,\mathrm{moles}$ of water. We have seen previously that the predominant forms of water are, in order of abundance, $\mathrm{HH}^{16}\mathrm{O}$, $\mathrm{HH}^{18}\mathrm{O}$ and $\mathrm{HD}^{16}\mathrm{O}$. Their concentrations are denoted c_1, c_2 and c_3, respectively, keeping these indexes in the following to define their number of moles n_1, n_2 and n_3. Because the six other forms of water represent less than 0.05% of all available water, the concentrations sum to

$$c_1 + c_2 + c_3 = c_0 \tag{3.31}$$

in any given volume of water. In terms of individual isotopes, we note that $[\mathrm{H}]$=$2c_1 + 2c_2 + c_3$, $[^{16}\mathrm{O}]$=$c_1 + c_3$, $[^{18}\mathrm{O}]$=c_2, $[\mathrm{D}]$=c_3. Recalling the definition of $\delta^{18}\mathrm{O}$ and $\delta\mathrm{D}$ in Eq. 2.1, we obtain the relationships:

$$\frac{\delta^{18}\mathrm{O} R_{\mathrm{O-SMOW}}}{1000} + 1 = \frac{n_2}{n_1 + n_3} = \frac{c_2}{c_1 + c_3} \tag{3.32}$$

$$\frac{\delta^{18}\mathrm{O} R_{\mathrm{H-SMOW}}}{1000} + 1 = \frac{n_3}{2n_1 + 2n_2 + n_3} = \frac{c_3}{2c_1 + 2c_2 + c_3} \tag{3.33}$$

that can be combined with Eq. 3.31 to determine the concentrations c_1, c_2 and c_3 in a deposited ice particle. Eqs. 3.29–3.30 can then be applied to determine the bulk composition of an ice sheet at any given time.

The influence of variations of ice volume on the average composition of the ocean is similarly calculated with Eqs. 3.31–3.33 by assuming that the present ocean mass is 1.37×10^{21} kg and that ocean area remained constant at 3.61×10^{8} km^2.

3.5.5 Application of tracer modelling

Developing the tracer transport method, I found that its applications exceeded the scope of its original goal of predicting the bulk isotopic composition of the ice sheets. Interactively tracking the age of ice allows the inclusion of age–dependent rheologic properties for the ice. The deepest and oldest predicted ice at ice core sites can also help put constraints on past ice sheet extent during

large ice-sheet retreat, for instance in Greenland during the Eemian (chapter 5). Tracking origin and recovering depositional elevation, we can cross check the common assumptions used for dating ice core records and infer past temperatures in Greenland and Antarctica. Simple flow models usually assume local origin at domes and imposed or fixed elevation history. The problem is especially complex for the Vostok ice core, where distant ice origin is convolved with a higher upstream location and global changes in ice sheet thickness. Profiles of thinning rates and surface accumulation rates can also be compared. More figuratively, the age of calving icebergs can be predicted, as I was asked by the writer/illustrator of a children's book.

CHAPTER 4

Global stratigraphy of the Greenland Ice Sheet

4.1 Introduction

The tracer tracking method presented in the previous chapter was first developed and tested on the Greenland Ice Sheet (Clarke and Marshall, 2002), which has often been used as a training ground for innovations in ice sheet modelling because of its relatively small size and the wealth of data. The capability and promises of the coupled ice sheet–tracer model to predict the fine three-dimensional and time-evolving ice layering of the Greenland Ice Sheet are now put to a real large scale test. In this chapter, I first introduce and describe the ice sheet model used for all my studies of Greenland (this chapter and the following ones) and then proceed to illustrate the provenance stratigraphy of the Greenland Ice Sheet by a series of relevant longitudinal and latitudinal cross sections located in Fig. 4.1. The actual validation of the fine ice sheet layering is achieved by predicting the isotopic stratigraphy of the ice core records recovered at Camp Century (Dansgaard and Johnsen, 1969), Dye 3 (Dansgaard et al., 1982), near the Summit at GRIP (GRIP Members, 1993) and GISP2 (Grootes et al., 1993) and most recently at NorthGRIP (Johnsen et al., 2001).

4.2 Model and experiment

4.2.1 Ice dynamics

I use the University of British Columbia three-dimensional thermomechanical continental ice dynamics model that was developed by Marshall and Clarke (1997) to predict the evolution of the Laurentide Ice Sheet and understand the role and behaviour of ice streams. The model has since also been used to study the Greenland Ice Sheet, especially the migration of the main ice divide during the last glacial cycle and the possible effect on Summit ice cores (Marshall and Cuffey, 2000), and the maximum contribution of the ice sheet to sea level rise during the Eemian (Cuffey and Marshall, 2000). In the current configuration, the ice sheet model uses a geographically-oriented computational grid with 0.5° longitudinal and 0.25° latitudinal resolution and 21 vertical grid points. Therefore the tracer transport scheme has to be adapted according to the transformations described in Appendix B. The core features of the model (heat transfer, isostatic adjustment) and the assumed deglaciated bed topography follow the standards adopted by the EISMINT intercomparison project (Payne et al., 2000) and remain mostly unchanged from previous studies. Deviations are highlighted hereafter.

I modify the standard ice flow law

$$\dot{\epsilon}_{xz} = EB_0 \exp(-Q/RT)\sigma_{xz}^n \tag{4.1}$$

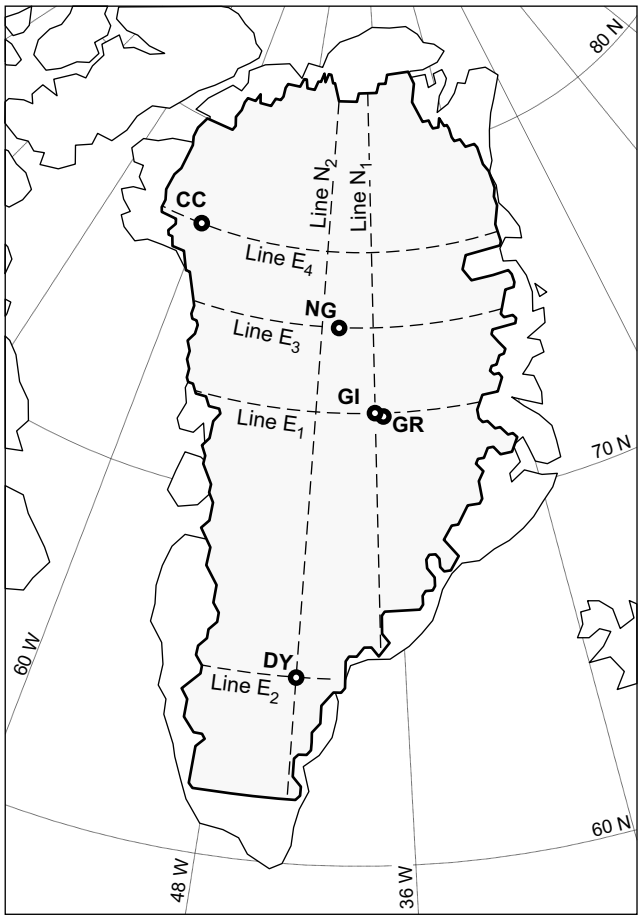

Figure 4.1: Map indicating the location of simulated stratigraphic cross sections and sites of Greenland deep ice cores. The ice core sites are Camp Century (CC), NorthGRIP (NG), GRIP (GR), GISP2 (GI) and Dye 3 (DY).

(Glen, 1955, and Eq. 2.11), which relates the shear strain rate $\dot{\epsilon}_{xz}$ to the shear stress σ^n_{xz}, by allowing age-dependence in the flow enhancement factor E to account for the softening of the effective viscosity of glacial ice. This parameterization was stimulated by the observation from Thorsteinsson et al. (1999) on borehole tilt measurements that the impurity content in ice correlate well with enhanced ice deformation at Dye 3. The larger amount of impurities in glacial ice than in modern ice is attributed to intense erosion, increased exposure of continental shelves and strengthened aeolian transport during glacial periods (Taylor et al., 1993). That refinement was initially implemented at the beginning of my research to understand the mismatch in the age–depth relationship in the pioneering study of Clarke and Marshall (2002) by differentiating the viscosity of glacial and interglacial ice, expecting that faster flow for glacial ice could help recent Holocene ice penetrate deeper into the ice sheet. Though such differentiation proved to have little effect at dome sites like GRIP because of its low stress regime, the parameter E showed a significant impact on the dynamics of the Greenland Ice Sheet, an influence that I study in greater detail in the next chapter. Variation of the enhancement factor E with depth in an ice sheet are justified by the evolution of the ice fabric (normal grain growth) as a result of the cumulative stress since ice deposition. The presence of impurities in ice tends to limit grain size and favours high local strain, as observed in

the EPICA-Dome C ice core (Durand, 2004); thus, larger enhancement can be applied to glacial ice, especially at greater depth. For simplicity, I assume in the following that ice sheets are made of two ice types: glacial (E=E_{G}) and interglacial (E=E_{I}). I assess model sensitivity to the assignment of E_{G} and E_{I} in the ranges $3 \leq E_{\mathrm{G}} \leq 7$ and $1 \leq E_{\mathrm{I}} \leq 7$, consistent with values inferred from Dye 3 borehole tilt measurements (Thorsteinsson et al., 1999). Within the ice sheet, depositional age t_{d} has a time-evolving three-dimensional structure; thus, ice rheology itself is time-evolving (Abe-Ouchi et al., 1994) and three-dimensional.

4.2.2 Climate forcing

The present distribution of surface temperature $T(x, y, 0)$ is taken from Ohmura (1987) and Huybrechts (2002) and shown in appendix A. To obtain a long-term climatic history, I take the same approach as Marshall and Cuffey (2000) and extend the GRIP $\delta^{18}\mathrm{O}$ ice core with a Vostok-derived record (Petit et al., 1999) for ages older than 97.8 kyr BP. The focus of my study is on the ice sheet layering, the variations in elevation and origin and the configuration of Greenland Ice sheet during the Eemian. Therefore I choose to adopt the GRIP-SS09 chronology (Johnsen et al., 1997) to ease the comparson with previous studies (Cuffey and Marshall, 2000; Marshall and Cuffey, 2000; Tarasov and Peltier, 2003). Different or updated chronologies for GISP2 (Meese et al., 1997) and

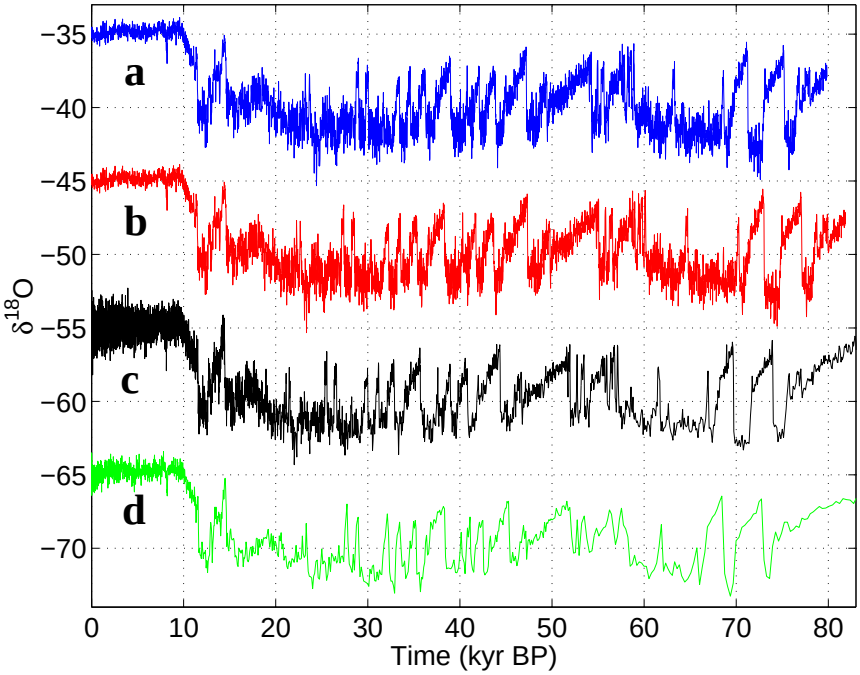

Figure 4.2: Chronologies for the Summit ice cores for the past 80 kyr. a. SFCP2004 by Shackleton et al. (2004), b. GRIP-SS09sea by Johnsen et al. (2001), c. GRIP-SS09 by Johnsen et al. (1995), d. GIPS2 by Meese et al. (1997).

GRIP (Johnsen et al., 2001; Shackleton et al., 2004), shown on Fig. 4.2, can certainly provide better age constraints for parts of the past glacial cycle, but solving any discrepancies in the GRIP and GISP2 chronologies is beyond the ambition of the present work. Additional sensitivity studies, not

presented here, also show that differences of 2–3 kyr in the glacial chronology have minor effects on the predicted elevation and ice provenance of any site.

Temperatures $T_{\rm obs}(t)$ at the surface of the ice sheet are inferred from $\delta^{18}{\rm O}$ following Cuffey (2000)

$$\Delta T_{\rm c}(t) = \frac{1}{\alpha_{\rm c}}[\Delta\delta^{18}{\rm O}(t) - \beta_\delta \Delta S_{\rm G}(t)] \tag{4.2}$$

$$\Delta T_{\rm obs}(x,y,t) = \Delta T_{\rm c}(t) + \beta_{\rm T}\Delta S(x,y,t) \tag{4.3}$$

as in Eq. 2.15, where $\Delta S_{\rm G}(t)$ is the surface elevation change between the deposition site and present GRIP site and $\Delta S(x,y,t)$ is the surface elevation change at the time and location where the climate forcing is applied. Depositional elevation of ice from the GRIP core is not known during a simulation and is an output of the tracer model; I therefore assume that $\Delta S_{\rm G}$ is equal to the difference between the instantaneous maximum modelled surface elevation and present elevation at Summit; I check this assumption upon completion of the run. The assumed uniform temperature lapse rate $\beta_{\rm T}$=$-7.5\,{\rm K\,km^{-1}}$ and annual temperature amplitudes follow a standard parameterization (Ritz et al., 1997; Huybrechts, 2002). The $\delta^{18}{\rm O}$ lapse rate β_δ=$-6.2\,{}^\circ\!/_{\circ\circ}\,{\rm km^{-1}}$ is derived from observations in Central Greenland (Johnsen et al., 1989). Interpretation of borehole thermometry at the GRIP and GISP2 sites indicates that at the Last Glacial Maximum, the temperature at Summit was about $23\,^\circ$C colder than present (Cuffey et al., 1995; Dahl-Jensen et al., 1998). Thus one can define a climatic isotope sensitivity parameter or "temporal slope" (Jouzel et al., 1997) $\alpha_{\rm c}$=$\mathrm{d}(\delta^{18}{\rm O})/\mathrm{d}T$ with a value for glacial periods of $\sim$0.33$^\circ\!/_{\circ\circ}\,{\rm K^{-1}}$ — less than the present observed "surface slope" of $0.67\,{}^\circ\!/_{\circ\circ}\,{\rm K^{-1}}$ (Johnsen et al., 1989). The parameter $\alpha_{\rm c}$ varies between glacial and interglacial periods (Cuffey and Clow, 1997) and is critical for estimating the contribution of Greenland to sea level rise during the Eemian when using such climate forcing (Cuffey and Marshall, 2000). Similarly to Tarasov and Peltier (2003), I use different values of $\alpha_{\rm c}$ ($0.25 \leq \alpha_{\rm c} \leq 0.6\,{}^\circ\!/_{\circ\circ}\,{\rm K^{-1}}$) for each of three distinct stages of past climate history: $\alpha_{\rm cE}$ for the Eemian, $\alpha_{\rm cG}$ for all glacial periods and $\alpha_{\rm cH}$ for most of the Holocene. To better account for variations in the upper part of the GRIP borehole, I impose for the past 2 kyr (Late Holocene) a linear cooling trend that reaches $\Delta T_{\rm c}$=-0.5°C 900 years ago, followed by a linear warming towards present. Past surface snow accumulation is derived by perturbing the present distribution of precipitation (Ohmura and Reeh, 1991), shown in appendix A, according to Eq. 2.16 and by accounting only for the fraction of precipitation that falls as snow (Marshall and Clarke, 1999).

4.2.3 Practical details

The ice dynamics and tracer models use the same geographically-oriented grid with $138 \times 106 \times 21$ computational points. The stretching parameter A for the reduced vertical coordinate is equal to 0.97, thus an almost linear vertical sampling. Bilinear interpolation was applied to adapt the 40-km bedrock topography of the ice sheet (Letreguilly et al., 1991) to our coordinate system. Additionally, the initial bedrock elevation at ice core sites is adjusted so that simulated present bed elevation matches that at ice core sites; this facilitates direct comparison of the predicted ice core stratigraphy and borehole temperature profiles for these sites. A variable time step of 1–4 yr is used for integration of the ice dynamics equations and 20 yr for thermodynamics and isostatic adjustment. Simulations proceed from $t_{\rm init}$=$320\,{\rm kyr\,BP}$ and run until the present time. The exact value of key climate and ice dynamics parametrs correspond exactly to those of model C4 presented in the following chapter (Table 5.1).

The initial state of the ice sheet at $t_{\rm init}$ is taken to coincide with the $0\,{\rm BP}$ final state of a previous model run. Thus the initial ice surface and bed topography closely approximate those for present-day Greenland. Experiments, not presented here, confirm that the effect of initial conditions is erased after two $\sim 100\,{\rm kyr}$ glacial cycles. To initialize the tracer provenance labels, the depositional ages computed from the previous run were adjusted by subtracting $320\,{\rm kyr}$. It follows that the modelled Greenland ice sheet contains ice older than $320\,{\rm kyr\,BP}$ and as old as $640\,{\rm kyr\,BP}$. The model is initialized using present bed and surface topography as initial conditions and launched at $t_{\rm init}$=$320\,{\rm kyr\,BP}$ to run until the present time.

4.3 Depositional provenance stratigraphy

The traced properties are the ice provenance labels: depositional longitude $\lambda_{\rm d}$, depositional latitude $\theta_{\rm d}$ and depositional time $t_{\rm d}$. Following the procedure described in Clarke and Marshall (2002), we use these provenance labels, in conjunction with a depositional archive containing information that yields the time-varying surface distribution of mass balance $b(\lambda,\theta,t)$ and isotopic content of the precipitation $\delta^{18}{\rm O}$, to generate the time-evolving stratigraphic structure of the ice sheet. The simulated stratigraphy of the tracer provenance labels $(\lambda_{\rm d},\theta_{\rm d},t_{\rm d})$ for a longitudinal cross section ${\rm E}_1$ that follows latitude $72.625\,{\rm N}$ and passes near the GRIP ice core site (triangle annotations on frame boundaries) is presented in Fig. 4.3. The depositional longitude (Fig. 4.3a) shows a fairly regular structure with evidence of a persistent flow divide near the present elevation maximum. Not surprisingly, the surface values of depositional longitude coincide with the actual geographical longitude. At depth the contours of equal depositional longitude splay away from the flow divide, indicating that the deep ice originates from an upstream depositional site. Near the bed, several of these contours show a discontinuous change in curvature, indicating that the deepest ice has not travelled far from its initial position. The contour plot of depositional latitude (Fig. 4.3b) isolates the effects of N–S ice flow. Although the pattern is rich, the actual magnitude of this flow is small. The largest latitudinal ice displacement is less than 0.5°. Isochronal surfaces are contoured in Fig. 4.3c. For this cross section, the upper half of the ice sheet consists of Holocene ice and thus would be isotopically heavy relative to the lower half.

Similar information for the latitudinal cross section ${\rm N}_1$ is given in Fig. 4.4. This profile follows longitude $37.75\,{\rm W}$ and also passes near the GRIP ice core site (triangle annotations on frame boundaries). The plot of depositional longitude (Fig. 4.4a) indicates that in the latitude band 67–$76\,{\rm N}$ there is very little E–W displacement of the depositional provenance. At the northern and southern ends of the ${\rm N}_1$ profile there is an eastward component the flow that leads to a displacement between the actual longitude and the depositional longitude of as much as 5° near $79\,{\rm N}$. For this profile the plot of depositional latitude (Fig. 4.4b) shows little N–S flow in the southern part of this profile (66–$73\,{\rm N}$). Above latitude $73\,{\rm N}$ there is a pronounced northward component of ice flow and a displacement of as much as 3° between the actual latitude and depositional latitude of deep ice. The contoured isochronal surface for cross section ${\rm N}_1$ (Fig. 4.4c) shows that the southernmost part of the Greenland Ice Sheet contains no old ice, a consequence of partial deglaciation of Greenland during the Eemian. In contrast, the northern Greenland Ice Sheet is underlain by old ice and was continuously ice-covered during the Eemian. Taken together, Figs. 4.3 and 4.4 indicate that, based on the modelling, Summit Greenland is an especially favourable location for ice core drilling because the flow history has remained uncomplicated throughout the last glacial cycle and the ice depositional source was never far from the present location of GRIP.

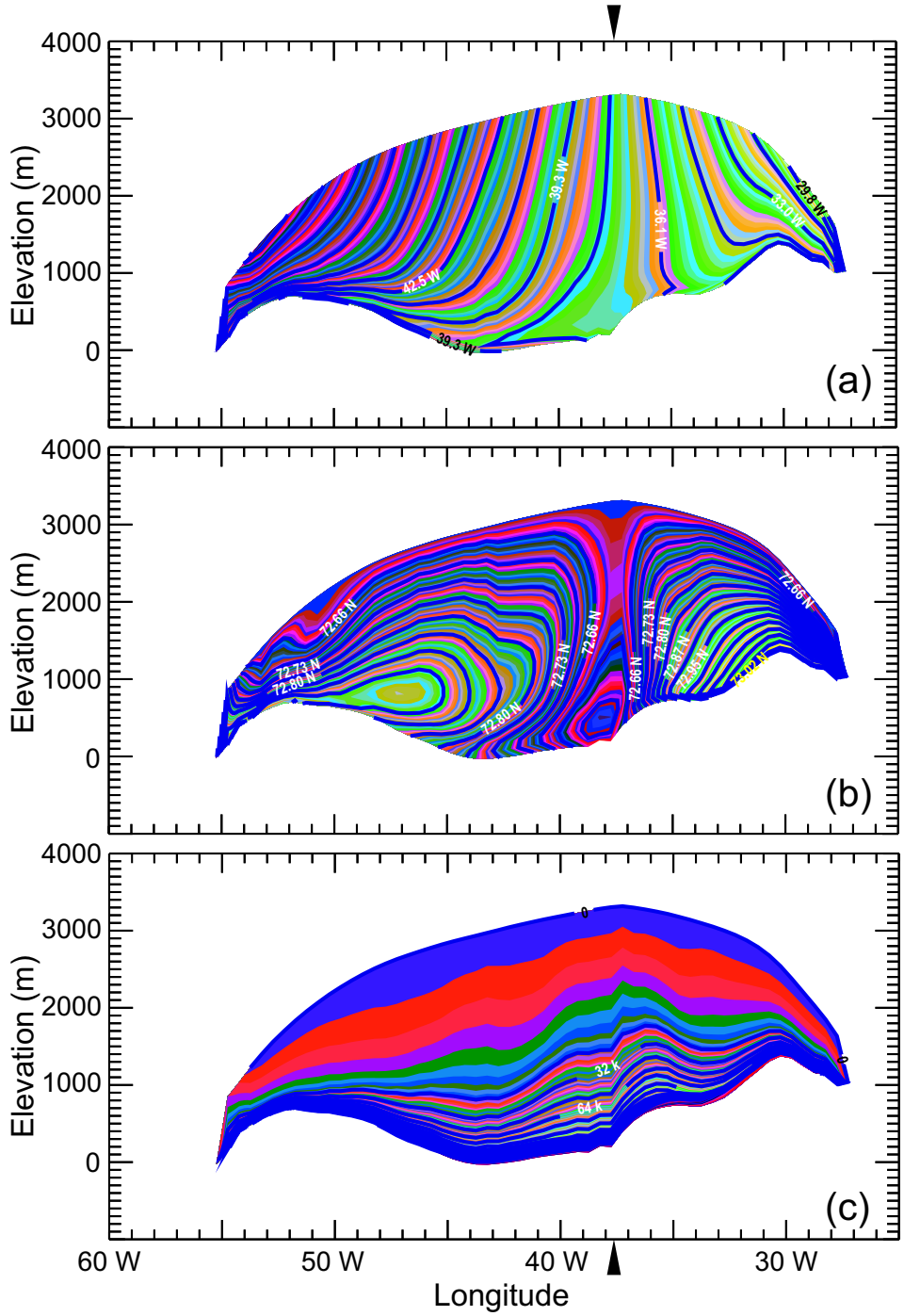

Figure 4.3: Simulated cross section E_1 of tracer provenance variables for a longitudinal cross section passing through 72.625 N near the GRIP site. The longitude corresponding to the GRIP site is indicated by arrow annotations on the frame boundary. (a) Depositional longitude. (b) Depositional latitude. (c) Depositional date. Colour version of this graph and the following ones can be found in Clarke et al. (in press).

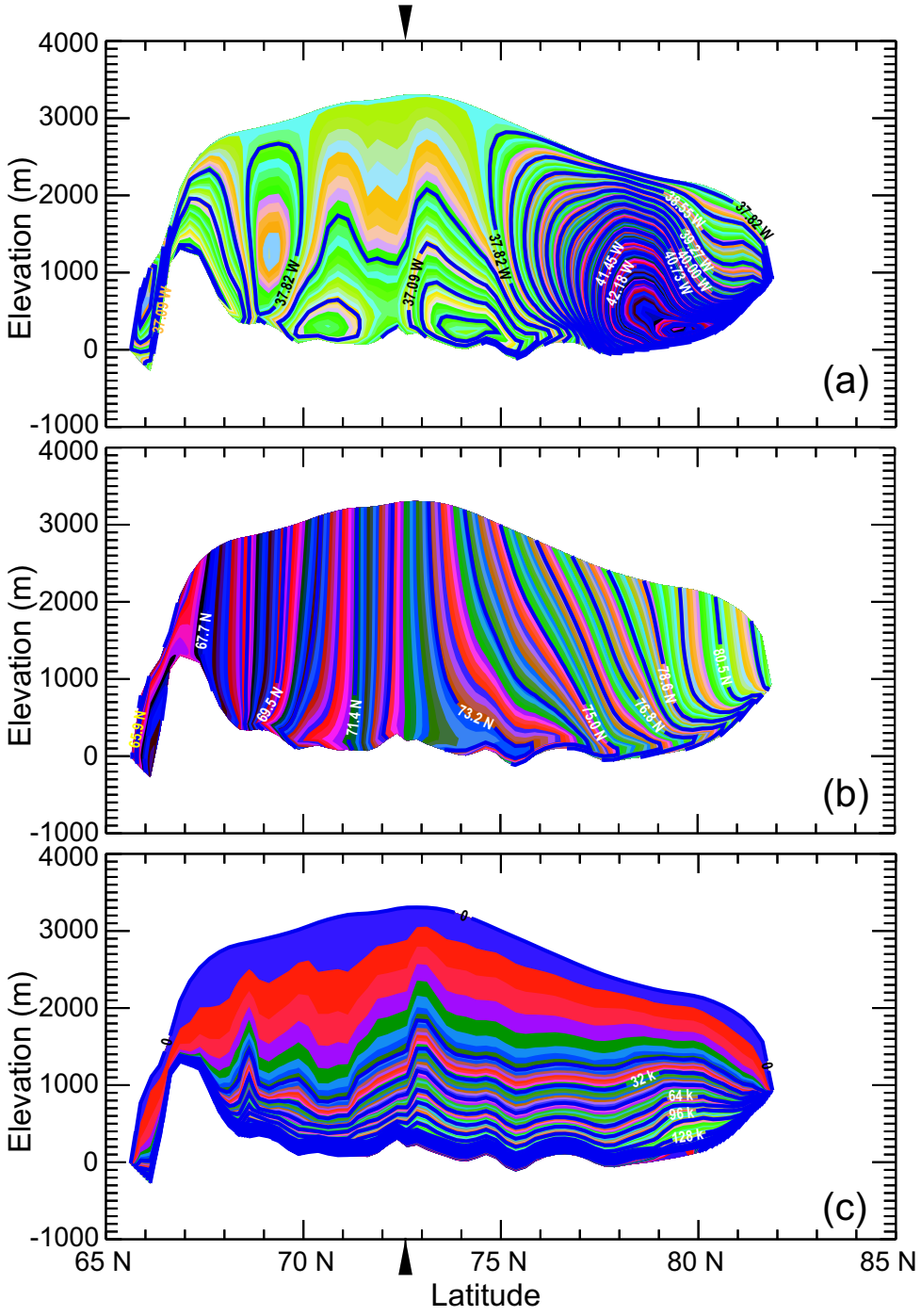

Figure 4.4: Simulated cross section N_1 of tracer provenance variables for a latitudinal cross section following $37.75\,\mathrm{W}$ passing near the GRIP site. The latitude corresponding to the GRIP site is indicated by arrow annotations on the frame boundary. (a) Depositional longitude. (b) Depositional latitude. (c) Depositional date.

Simulation results for a second latitudinal cross section N_2, which follows longitude $43.75\,\mathrm{W}$ and passes near the Dye 3 ice core site (triangular annotations on frame boundaries), are given in

Fig. 4.5. This line lies to the west of Summit and the plot of depositional longitude (Fig. 4.5a) reflects a general westward ice flow with the maximum rate of flow occurring in the latitude band 69–75 N. The plot of depositional latitude (Fig. 4.5b) shows the effects of a N–S flow divergence in the vicinity of the elevation maximum (72–82 N) and also of N–S divergence in the vicinity of the southern elevation maximum (63–67 N). Near 69 N there is a collision between deep ice of northern and southern provenance. As in Fig. 4.4c, the isochronal cross section (Fig. 4.5c) shows that basal ice in the southern part of the Greenland Ice Sheet is young relative to that in the northern part.

Next we present longitudinal profiles of depositional time for profiles E_1, E_2, E_3 and E_4 which pass near the GRIP, Dye 3, NorthGRIP and Camp Century ice core sites, respectively (triangular annotations on frame boundaries of Fig. 4.6). The horizontal and vertical scales differ for each of the plots as does the colour coding for the shaded isochronal contours. Our objective is to highlight the qualitative structural aspects rather than the quantitative ones. In terms of complexity, the isochronal surfaces for E_1, E_2 and E_3 appear comparatively simple in the vicinity of the associated deep drilling sites. In contrast Camp Century (along E_4) is near the ice margin where the flow is complex and the layer thickness for old ice is highly compressed relative to that of interior ice.

Figs. 4.3–4.6 present depositional provenance information that is relevant to both existing and potential ice core sites. By shifting attention from cross sectional slices to the geographical coordinates of existing sites such as GRIP (Fig. 4.7a–c), Dye 3 (Fig. 4.7d–f) and Camp Century (Fig. 4.7g–i), we can discuss the model predictions of the provenance structure with specific reference to each core. Note that the vertical and horizontal scales for these plots vary from core to core. The simulation results predict that the GRIP core does not contain ice from distant depositional sources. The depositional longitude (Fig. 4.7a) of deep ice is displaced from that of surface ice by no more than 0.6°, with deep ice being deposited somewhat to the east of the drill site and suggesting that the ice divide has migrated slightly west since the deep ice was deposited. The depositional latitude for GRIP ice (Fig. 4.7b) varies with depth but the deep ice was deposited no more than 0.06° from the depositional latitude of surface ice. The simulated age–depth curve for GRIP (Fig. 4.7c) predicts that the basal ice dates to around $380\,\mathrm{kyr\,BP}$. Because the ice flow model contains no physics that would allow tectonic disturbance of the deep ice, predicted basal ages should be viewed with a degree of scepticism.

The predicted depositional provenance labels for Dye 3 and Camp Century present an interesting contrast to those for GRIP. The depositional longitude for Dye 3 (Fig. 4.7d) is displaced as much as 1° from the actual site longitude and the latitudinal displacement (Fig. 4.7e) is as much as 0.7°; thus the depositional catchment zone for the Dye 3 core is substantially larger than that for GRIP. According to the simulation model, the worst characteristic of the Dye 3 core is that it contains no ice deposited before $200\,\mathrm{kyr\,BP}$ and that the record for 50–190 $\mathrm{kyr\,BP}$ is compressed into the bottom $100\,\mathrm{m}$ of the core (Fig. 4.7f). For Camp Century, the longitudinal displacement (Fig. 4.7g) is as large as 2°, latitudinal displacement (Fig. 4.7h) is as much as 0.45° and the depositional time for the basal ice is $240\,\mathrm{kyr\,BP}$.

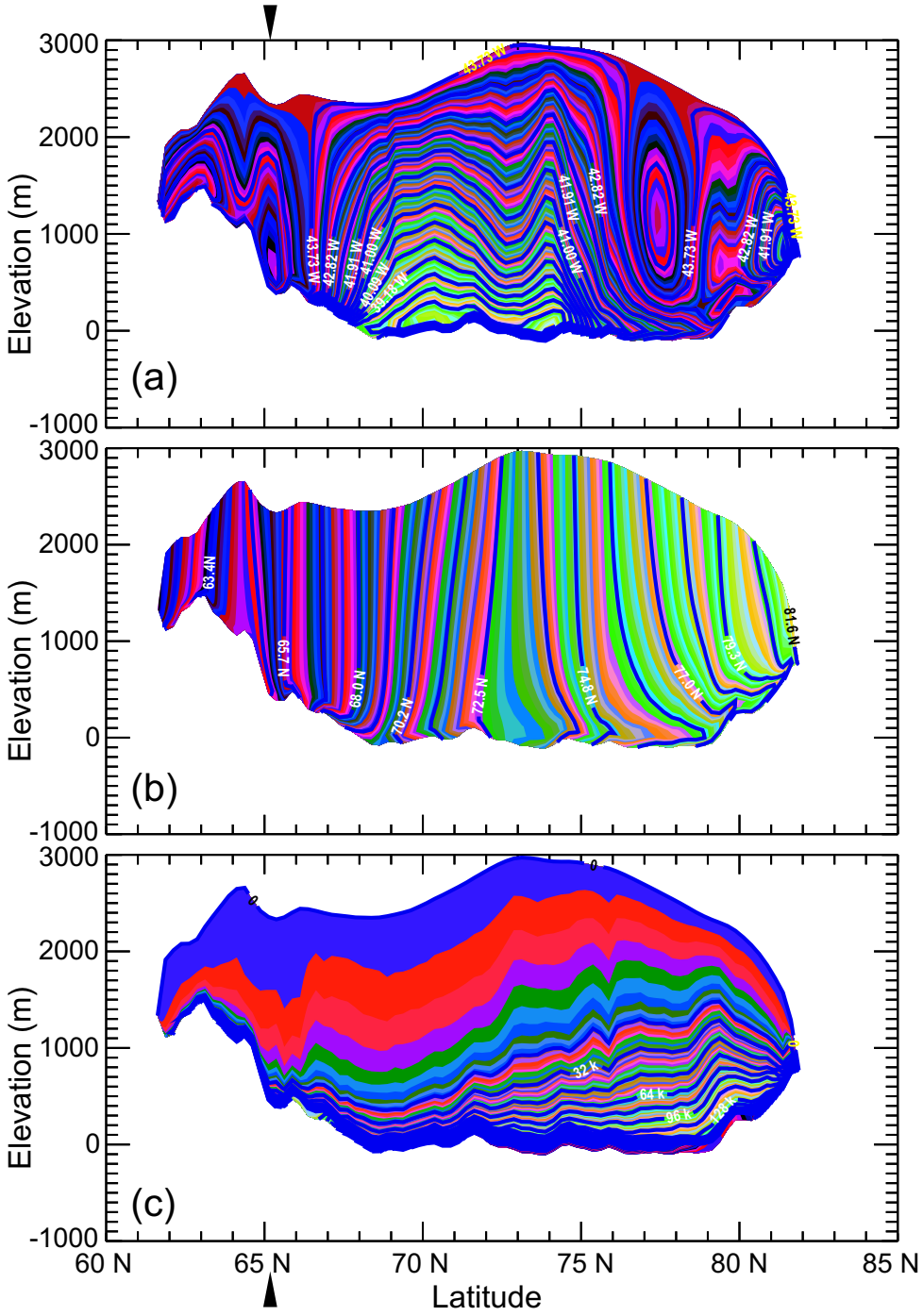

Figure 4.5: Simulated cross section N_2 of tracer provenance variables for a latitudinal cross section following $43.75\,\mathrm{W}$ passing near the Dye 3 site. The latitude corresponding to the Dye 3 site is indicated by arrow annotations on the frame boundary. (a) Depositional longitude. (b) Depositional latitude. (c) Depositional date.

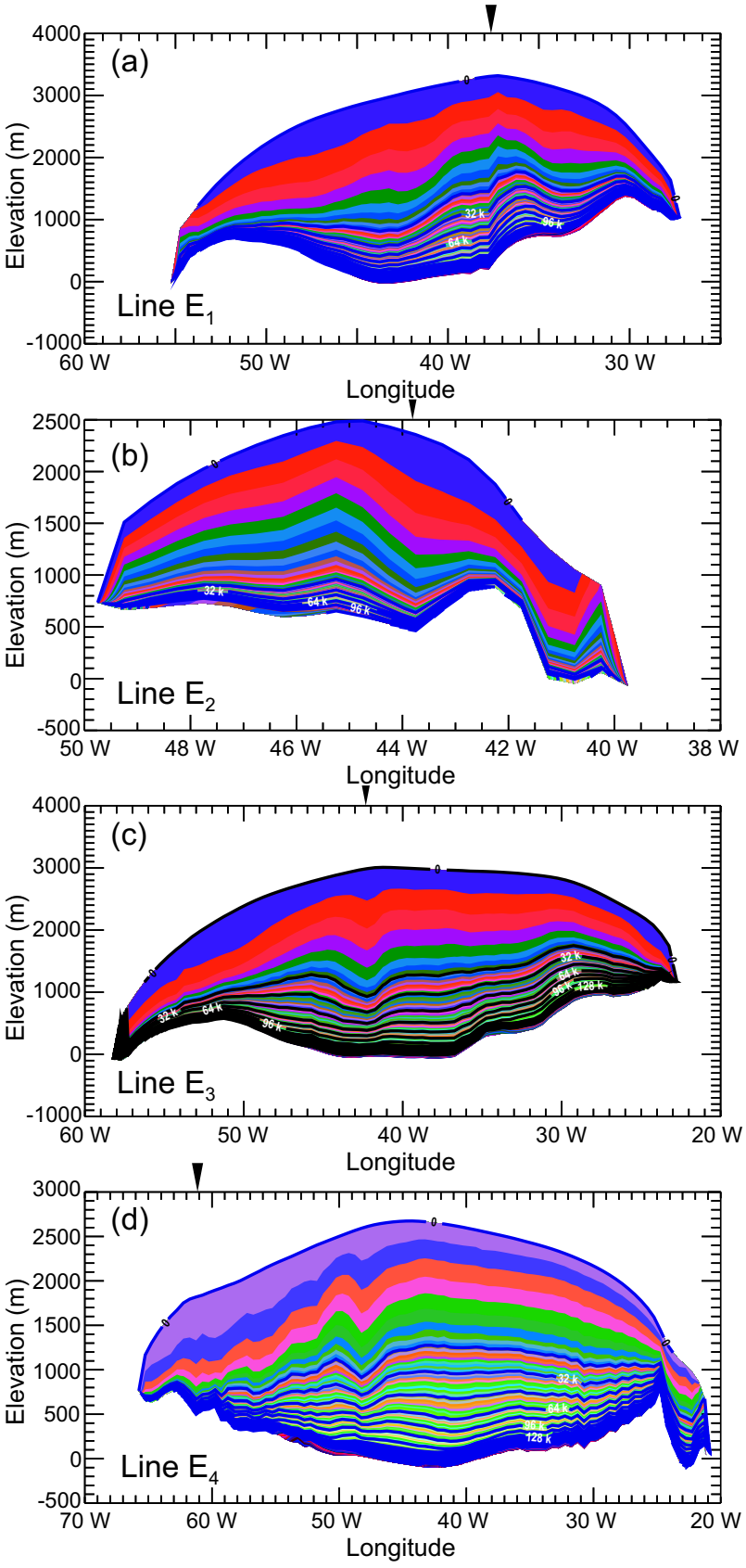
(a)
Line E1
Elevation (m)
Longitude
60 W
50 W
40 W
30 W
(b)
Line E2
50 W
48 W
46 W
44 W
42 W
40 W
38 W
(c)
Line E3
60 W
50 W
40 W
30 W
20 W
(d)
Line E4
70 W
60 W
50 W
40 W
30 W
20 W
32 k
64 k
96 k
128 k

Figure 4.6: Longitudinal cross sections of simulated depositional age stratigraphy. The longitudes corresponding to the respective drill sites are indicated by arrow annotations on the frame boundaries. (a) Cross section E_1 following latitude $72.625\,\mathrm{N}$ passing near the GRIP site. (b) Cross section E_2 following latitude $65.125\,\mathrm{N}$ passing near the Dye 3 site. (c) Cross section E_3 following latitude $75.125\,\mathrm{N}$ passing near the NorthGRIP site. (d) Cross section E_4 following latitude $77.125\,\mathrm{N}$ passing near the Camp Century site.

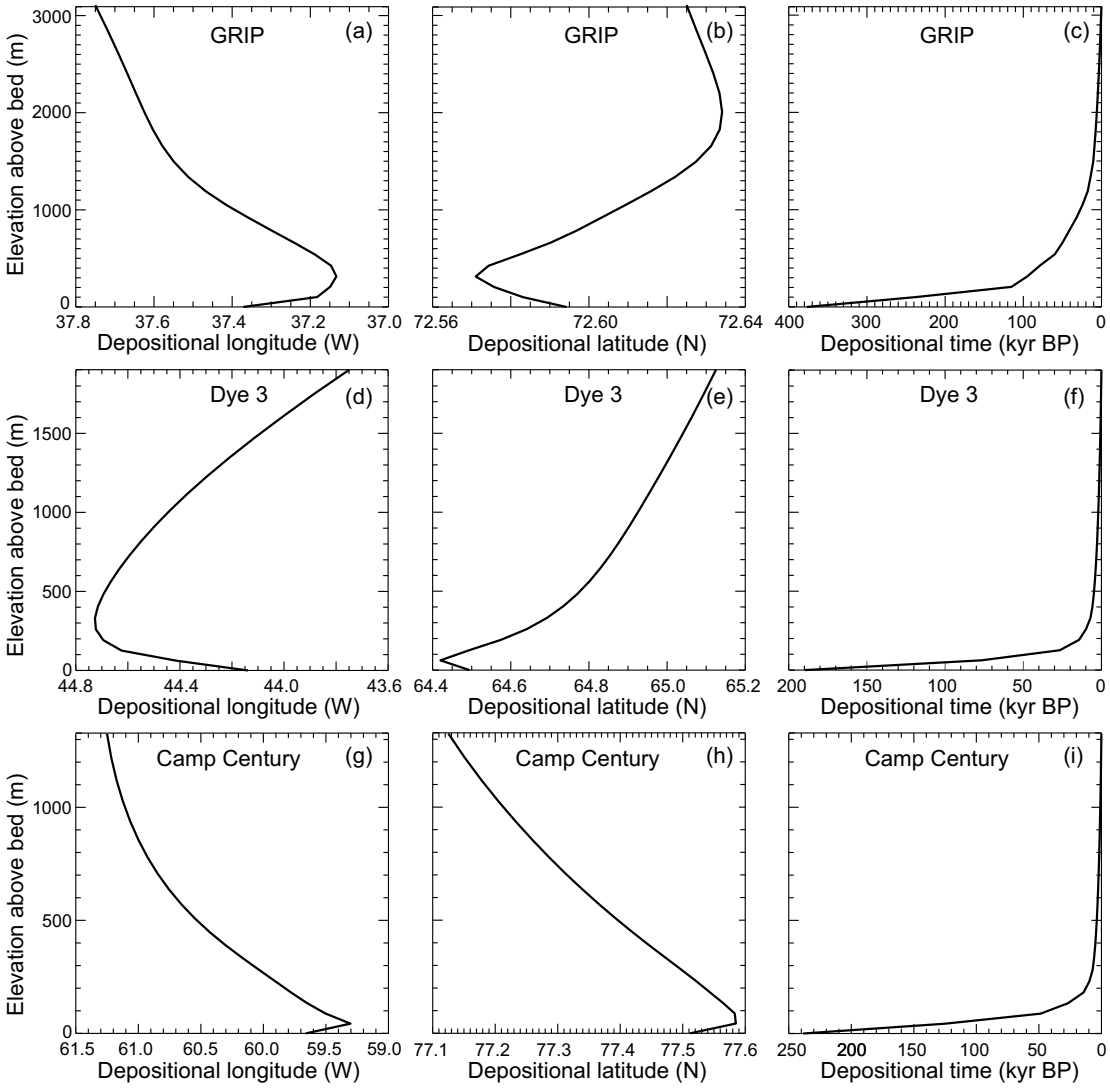

Figure 4.7: Simulated depth variation of tracer provenance variables for GRIP, Dye 3 and Camp Century sites. (a) Depositional longitude vs. elevation above bed for GRIP. (b) Depositional latitude vs. elevation above bed for GRIP. (c) Depositional time vs. elevation above bed for GRIP. (d) Depositional longitude vs. elevation above bed for Dye 3. (e) Depositional latitude vs. elevation above bed for Dye 3. (f) Depositional time vs. elevation above bed for Dye 3. (g) Depositional longitude vs. elevation above bed for Camp Century. (h) Depositional latitude vs. elevation above bed for Camp Century. (i) Depositional time vs. elevation above bed for Camp Century.

4.4 Stratigraphy at ice core sites

4.4.1 Isotopic stratigraphy

As a stringent test of the assumed climate forcing and the physical models for ice and tracer dynamics, we compare the observed and simulated isotopic stratigraphy of the principal Greenland ice cores. Fig. 4.8 presents measured (thick lines) and modelled (thin lines) variations of $\delta^{18}\mathrm{O}$ for the GRIP, GISP2, Dye 3 and Camp Century cores. At the time of writing, measured values for NorthGRIP were not openly available so we have only presented simulation results for this site. Good agreement with the NorthGRIP record is not expected because of the large discrepancy between the spatially constant value of geothermal flux assumed in the modelling and the much higher value that seems to apply at this site (e.g., Fahnestock et al., 2001, and next chapter). To facilitate comparison of measured and modelled results, we have right-shifted the simulation results by a constant offset. In comparing measured and modelled curves, we emphasize the following criteria: (i) agreement between measured and modelled ice column height at the drill sites (in every case very good); (ii) agreement from the core-bottom to core-top on the absolute value of $\delta^{18}\mathrm{O}$ (in our judgement good); (iii) agreement on the depth at which climate excursions are expressed in the ice cores (GRIP excellent and Dye 3 and CC quite good).

Observed and simulated $\delta^{18}\mathrm{O}$ records for the GRIP ice core (GRIP Members, 1993; Johnsen et al., 1997) are plotted in Fig. 4.8a. The simulated record (thin line) has been right-shifted by $6‰$ to facilitate comparison. Note the excellent agreement in terms of the magnitude of the isotopic fluctuations and the baselines for the two curves as well their close agreement on the depth of the deglacial transition (around $1400\,\mathrm{m}$) and other climate events down to an elevation of around $300\,\mathrm{m}$. As discussed in the following chapter, reaching such a fit is not a trivial task or a circular argument because the final stratigraphy depends on several climatic and dynamic parameters. Below that depth, which corresponds to an age of $\sim$98 $\mathrm{kyr\,BP}$, the quality of the match decreases, in part because of well known problems with the Eemian section of the GRIP record (Alley et al., 1995; Chappellaz et al., 1997).

Observed and simulated records for the GISP2 core (Grootes and Stuiver, 1997) are presented in Fig. 4.8b; as for GRIP the plotted simulations results (thin line) have been right-shifted by $6‰$. Again there is excellent correspondence between the fluctuation magnitudes and base line levels for the two curves. Depth matching for climate events is good to a depth of roughly $750\,\mathrm{m}$, at which point there is a progressively increasing offset as the bed is approached. The simulated GRIP and GISP2 cores bear a close resemblance to each other but the agreement between data and predictions for GISP2 is less satisfactory at depth. We have also presented simulation results for NorthGRIP (Fig. 4.8c) but no actual data because these, as yet, are not freely available.

Data and simulation results for the Dye 3 ice core are presented in Fig. 4.8d with the modelled curve (thin line) right shifted by $10‰$. The correspondence of the baselines and fluctuation magnitudes is very good as is depth agreement for the deglacial transition at around $300\,\mathrm{m}$. The simulations resolve the glacial climate (bottom $200\,\mathrm{m}$) more finely than does the ice core record. For the Camp Century ice core (Fig. 4.8e) the simulation results are right-shifted by $10‰$ relative to the ice core data. The baselines and fluctuation magnitudes match well and the depth agreement for the deglacial transition (near $250\,\mathrm{m}$) is reasonably good. Again the simulation results for the bottom $200\,\mathrm{m}$ of the core contain more fine structure than the actual ice core data.

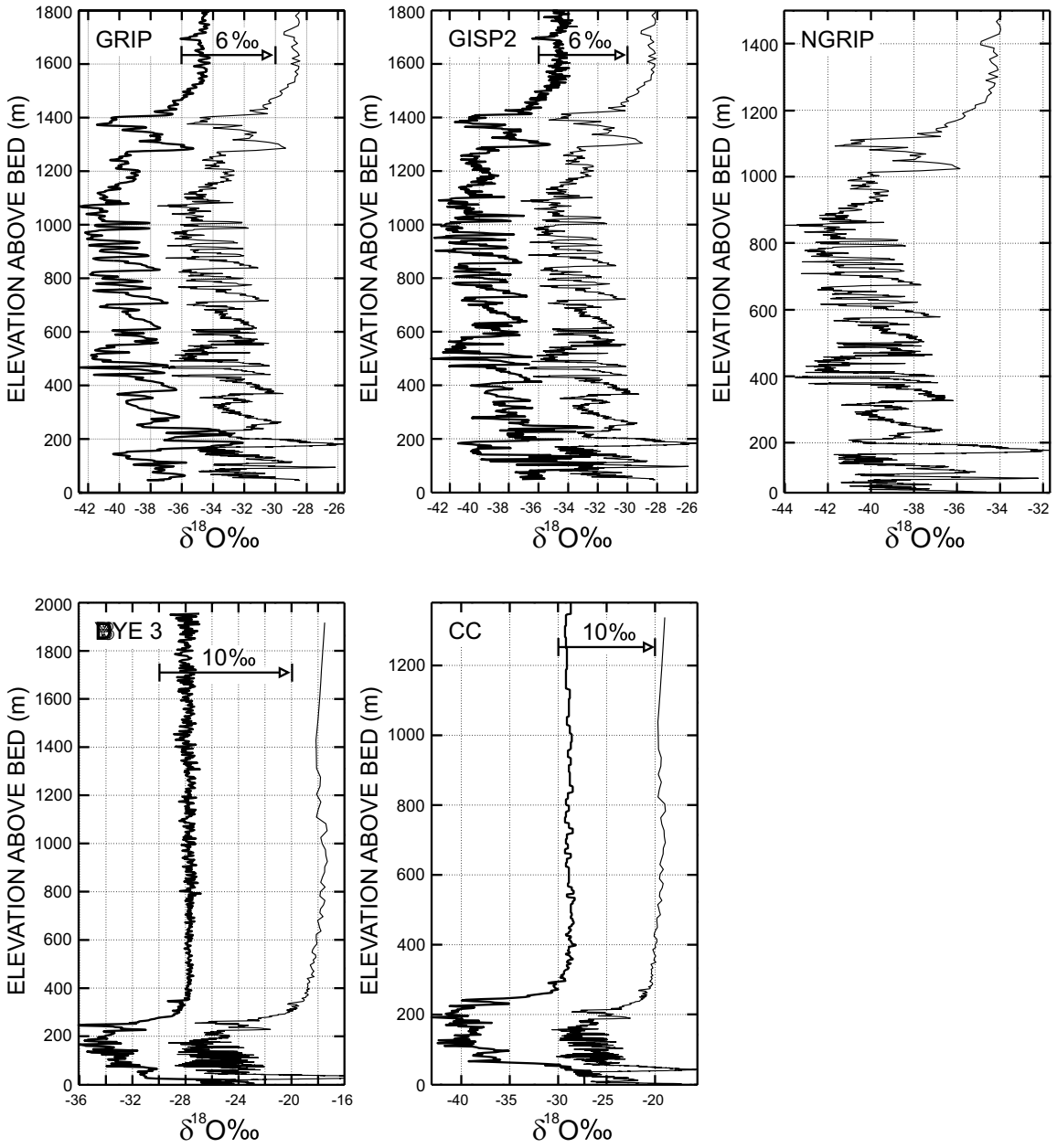

Figure 4.8: Comparison of modelled and observed oxygen isotope ratios in Greenland ice cores. Data are plotted with a thick line, modelled variations are plotted with a thin line and right-shifted to facilitate comparison. (a) GRIP. Modelled curve is right-shifted by $\delta^{18}\mathrm{O} = 6^{\circ}/_{\circ\circ}$. The measured ice thickness at this site is $3293\,\mathrm{m}$ and the modelled thickness is $3304\,\mathrm{m}$. (b) GISP2. Modelled curve is right-shifted by $\delta^{18}\mathrm{O} = 6^{\circ}/_{\circ\circ}$. The measured ice thickness at this site is $3251\,\mathrm{m}$ and the modelled thickness is $3269\,\mathrm{m}$. (c) NorthGRIP. Simulation model results are presented but ice core data are not yet available. (d) Dye 3. The modelled curve is right-shifted by $\delta^{18}\mathrm{O} = 10^{\circ}/_{\circ\circ}$. The measured ice thickness at this site is $2490\,\mathrm{m}$ and the modelled thickness is $2361\,\mathrm{m}$. (e) Camp Century. The modelled curve is right-shifted by $\delta^{18}\mathrm{O} = 10^{\circ}/_{\circ\circ}$. The measured ice thickness at this site is $1886\,\mathrm{m}$ and the modelled thickness is $1849\,\mathrm{m}$.

4.4.2 Borehole catchment

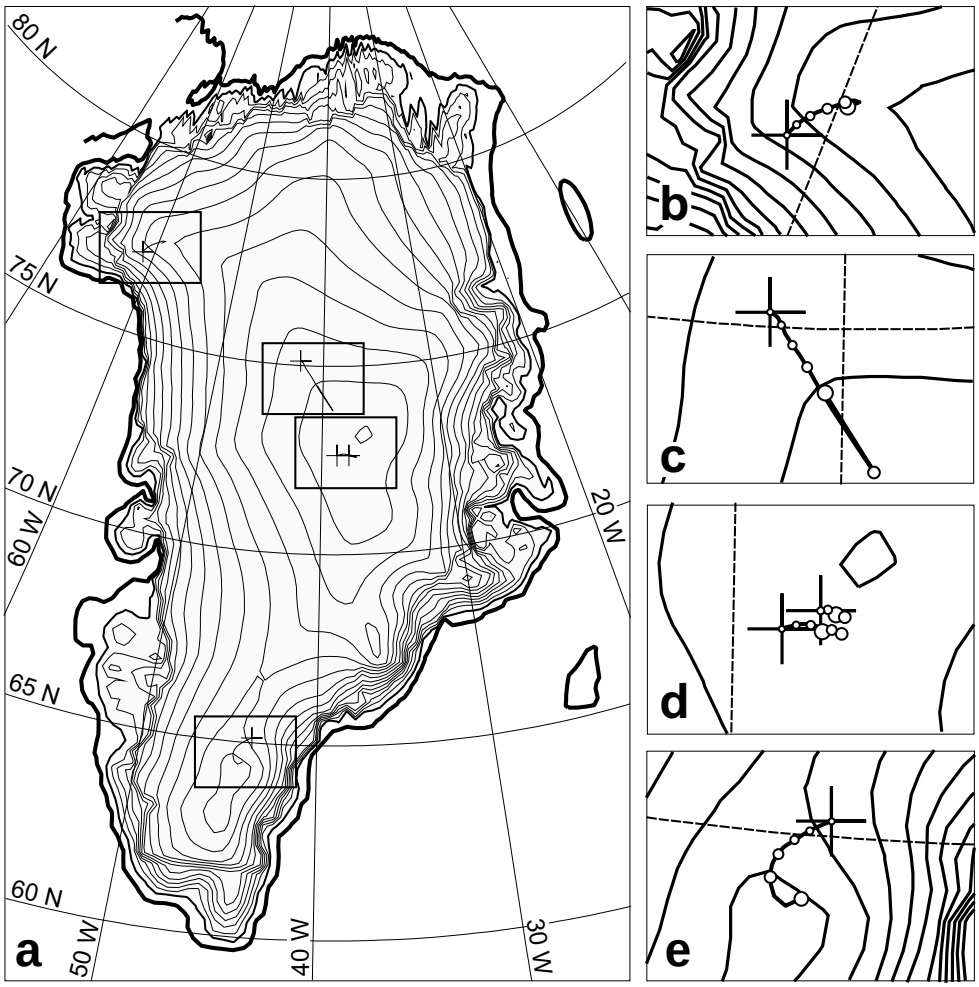

Figure 4.9: Simulated trajectory of depositional source for Greenland ice cores (drill sites are marked by plus signs). The maps illustrate that different levels of the cores were deposited at different geographical positions. These trajectories are plotted as curves upon which circles of varying radius have been superimposed. The radii of these circles increase systematically with increasing ice depth. (a) Location map showing simululated elevation contours for the present and identifying the boundaries of the detailed site maps. (b) Detailed map in vicinity of Camp Century. (c) Detailed map in vicinity of NorthGRIP. (d) Detailed map in vicinity of GRIP and GISP2 sites. The geographical positions of the sites have been displaced slightly (GRIP to the south and GISP2 to the north) so that the individual trajectories can be distinguished. (e) Detailed map in vicinity of Dye 3.

The variation of depositional latitude and longitude with depth provides an indication of the size of the catchment region for a given borehole. Fig. 4.7 indicates that the ice catchment area for the GRIP core is geographically localized whereas that for Camp Century ranges over several degrees of longitude. The age span associated with individual plots varies from hole to hole, ranging from the age of the surface ice (zero in the accumulation zone) to the age of the basal ice. A map perspective of the simulated ice catchments for the Greenland deep ice core sites is presented in Fig. 4.9. Clearly

the simulation indicates that the ice catchment areas for GRIP and GISP2 sites near Summit (Fig. 4.9d) are small, whereas that for NorthGRIP (Fig. 4.9c) is not.

4.5 Age of Greenland ice

4.5.1 Age of deep ice

Fig. 4.10 shows the areal distribution of the age of near-bottom ice, taken 50 m above the bedrock. According to the simulation results the GRIP, GISP2 and NorthGRIP sites are underlain by old ice, whereas the deep ice at Camp Century and Dye 3 is considerably younger. One aim of ice core drilling is to extract the longest possible climate record so from this perspective the three sites in

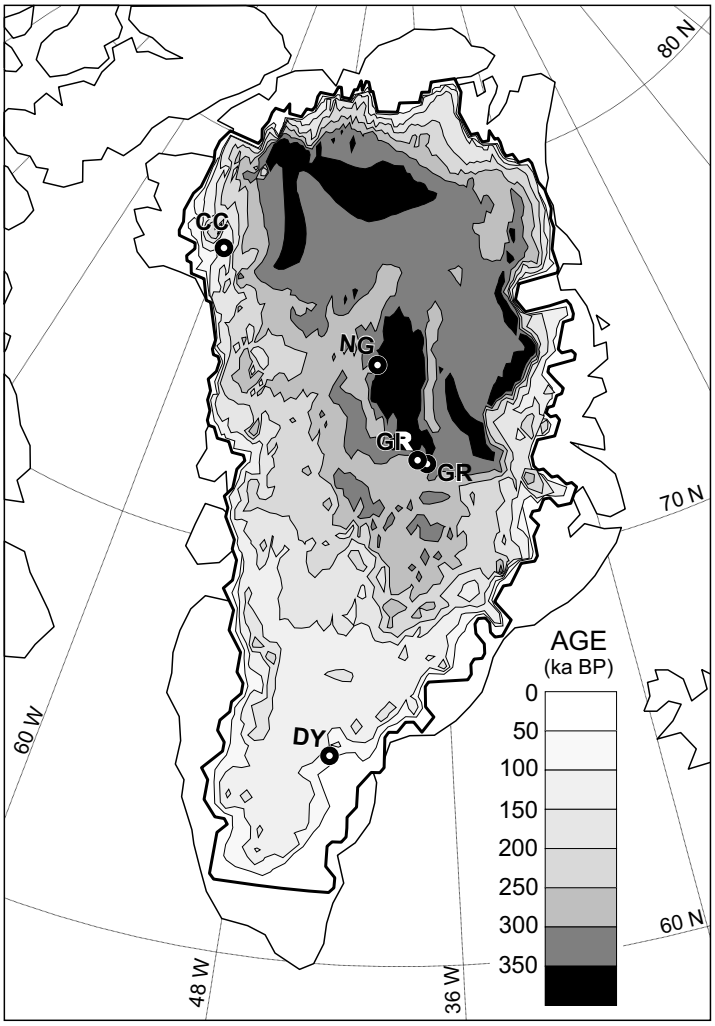

Figure 4.10: Map of simulated depositional age of ice at an elevation of $50\,\mathrm{m}$ above bed. Deep ice core drilling sites are labelled.

central Greenland were well judged. The model suggests that other regions warranting consideration can be found in north and east Greenland, although ice cores in these regions would be subject to

greater disturbance by ice flow. Deconvolving flow effects should become less of a problem when the skill of tracer models improves.

Caution must be exercised when interpreting Fig. 4.10 because we suspect that the model overestimates the age of deep ice. The age of bottom ice is highly dependent on the history of basal melting which, in turn, depends on the areal distribution of geothermal flux as well as the glacial history. For the present study we have followed the EISMINT conventions and assumed a spatially constant geothermal flux for the entire Greenland Ice Sheet. In regions where the geothermal flux is higher than our assumed value, bottom melting could have removed much of the oldest ice. Simplified model physics and our assumed ice rheology could also lead to overestimation of the age of deep ice. The flow law that we employ is the standard n=3 Glen law and the ice dynamics model assumes the usual shallow ice approximation (Hutter, 1983). Thus at low stresses, which prevail near flow divides, ice stiffness is likely to be overestimated and the deep ice will be immobilized. In the absence of bottom melting, the modelled age of the bottom ice for central regions of the Greenland Ice Sheet would coincide with the t_{d} assumed in the initialization, a model input rather than a model result. Thus the map in Fig. 4.10 presents the age of ice $50\,\mathrm{m}$ above the bed rather than at the bed itself and we regard this as a general indicator of old vs. young ice rather than a precise prediction of the model. The model-predicted ages take no account of the stratigraphic disturbance by ice flow that would be expected in real ice cores; thus the age of the oldest undisturbed ice could be substantially less than the estimated $50\,\mathrm{m}$ age.

4.5.2 Average age of the ice sheet

Finally, volume integration of the depositional age stratigraphy of the Greenland Ice Sheet predicts that the average age of the ice sheet is $\sim 43 \pm 2$ kyr at present and was $\sim 56 \pm 3$ kyr at LGM, 20 kyr ago. The modern ice sheet is relatively younger (30%) because the 3–4-fold increase in accumulation rate since the last glacial period imply that Holocene annual layers are much thicker, effectively occupying a larger volume for a younger bulk age, thus refreshing Greenland ice. The point is illustrated in the cross sectional age profiles and at ice core drilling sites, where the upper half of the ice sheet appears constituted of ice from the last 12 kyr.

4.6 Conclusion

This study proves that tracer transport modelling using a semi-Lagrangian method is highly effective to simulate the stratigraphy of an ice sheet. By combining a climate-forced thermomechanical ice dynamics model with models of tracer deposition and transport, it is possible to simulate the time-evolving isotopic stratigraphy of the Greenland Ice Sheet. Sampling model-predicted stratigraphy at the existing deep ice core sites and present time can yield reasonably accurate predictions of the observed isotopic profiles at these sites, a remarkable success because it indicates that, when compensated for the effects of ice flow and elevation, all the deep cores relate a coherent glacial history over the past 120,000 years. This conclusion, first noted by Johnsen et al. (2001), is highly reassuring because it implies that paleoclimatic studies and cryospheric modelling efforts are on convergent paths where each community can contribute to an enriched understanding of both the climate history and glacial history of Greenland. Sites such as Dye 3 and Camp Century, which constitute less-than-ideal archives of the environmental record, can provide far tighter constraints on the glacial history than interior sites such as GRIP, GISP2 and NorthGRIP. Limiting ice coring

studies to domes and ice divides, while a good place to start, is not necessarily the best place to finish. Simulation results suggest that the catchment area for GRIP and GISP2 is much smaller than that for NorthGRIP, Camp Century and Dye 3. Even at domes and ice divides the flow history, though possibly simple, may nevertheless complicate the interpretation of ice core records. Successful validation of the model at existing ice core sites, while not definitive, inspires confidence in the model's ability to predict characteristics of prospective drill sites. The model suggests that the central Greenland sites (GRIP, GISP2 and NorthGRIP) are situated over a region where the deep ice is oldest but that old ice may also be found in north and east Greenland. Further applications of tracer transport modelling in Greenland are explored in the following chapter.

CHAPTER 5

Constraints on Greenland ice cores and glacial history

5.1 Introduction

The depth variation of water-isotope concentrations in Greenland deep ice core records expresses the interplay of regional surface climate and ice flow dynamics. Similarities among these ice cores suggest that large-scale climatic changes affected the entire ice sheet; explanation and comparison to large events having affected the climate system, can be performed provided that an accurate chronology valid for all these cores is achieved. Counting of annual ice layers is an accurate method for dating the upper part of ice core records (Alley et al., 1997): the most recent $37.9\,\mathrm{kyr}$ for GISP2 (Meese et al., 1997), to the $8.2\,\mathrm{kyr}$ cold event for Dye 3 (Hammer et al., 1986), from 8.2 to $11.5\,\mathrm{kyr}$ for GRIP, using correlation with Dye 3 for the earlier part (Johnsen et al., 1997). Thinning at depth limits the method so chronologies are extended by matching well dated events recognizable in the ice-core isotopes and using simple models to interpolate between these events. In this manner, GISP2 is orbitally tuned to the SPECMAP chronology (Martinson et al., 1987) until $100\,\mathrm{kyr}$ ago whereas GRIP age is derived from dated tie points and one-dimensional models of ice flow and surface accumulation (SS09, Johnsen et al., 1997; SS09sea, Johnsen et al., 2001). Although these methods have provided the most essential information on past climatic changes, their chronologies differ even for the adjacent GRIP and GISP2 sites (Grootes et al., 1993) because their method assumes a certain degree of simplicity in the climate system or in the ice flow. Thus, chronologies are frequently revisited (e.g., Shackleton et al., 2004, and Fig. 4.2) to improve age constraints on particular events.

Three-dimensional thermomechanical ice sheet models (ISMs) can help to test and validate some of the assumptions used for dating and relating the ice core records by simulating a global history of ice sheet evolution (e.g., Huybrechts, 2002; Ritz et al., 1997; Payne, 1999). The method can be validated by matching areal extent, surface and bedrock topography and was used, for instance, to assess the stability of ice divides and track the variations in surface elevation (Marshall and Cuffey, 2000). Recently, methods for estimating the age–depth profile in ice sheets have been explored (e.g., Greve, 1997; Rybak and Huybrechts, 2004), but the full power of an integrated approach has not been exploited. Clarke and Marshall (2002) were the first to successfully couple an ISM with a tracer transport model. If sufficiently accurate, an ISM with tracers has the potential to complement and even replace ice core dating models, helping to put all ice cores on a single time scale and facilitating interpretation of isotopic records by separating the effects of temperature, origin and elevation. However, a Monte Carlo search for optimal dynamical and climatic parameters is not yet feasible because of the computational demands from an ISM. Calculations for a single glacial cycle already impose a heavy computational burden that forces the use of coarse spatial resolution and parameterized climate forcing. These considerations must be kept in mind in the use of an ISM to

interpret ice core records.

In this chapter, I apply the coupled ice sheet and tracer model introduced in the previous chapter with three scientific aims: (1) to explore climatic and dynamic parameters and seek models of Greenland climatic and dynamic history that match ice sheet geometric features and ice core constraints at GRIP, GISP2, DYE3 and Camp Century, and using these selected models, (2) to reconstruct the depositional elevation history of ice cores and assess the stability of the Summit dome and (3) to examine the configuration of the Greenland Ice Sheet during the last interglacial period and its contribution to sea level at that time.

5.2 Validation process and effect of model parameters

As demonstrated in the previous chapter, it is possible to model the isotopic stratigraphy of the Greenland Ice Sheet with sufficient accuracy that the stratigraphic structure of deep ice cores is reasonably well matched. I use this result to constrain the model and test the sensitivity of this agreement to plausible variations in environmental conditions and model parameters. In this manner, I can arrive at good (though not optimal) parameter selections and apply these to later examine the state of the Greenland Ice Sheet during the Eemian.

5.2.1 Methodology and validation process

Aside from limitations due to model resolution, the leading sources of uncertainty that can be controlled in the Greenland simulations are the climatic parameters α_{cE}, α_{cG} and α_{cH} (isotopic sensitivity, section 4.2.2), D_{acc} and F_{acc} (precipitation sensitivity, Eq. 2.16) and the ice dynamic parameters E_{I} and E_{G} (flow enhancement, section 4.2.1). The situation is more complex in nature. For instance, the hypothesis of uniform climate forcing fails to capture regional patterns that certainly affect most marginal areas. In this sensitivity study, I subject the results to two rounds of critical scrutiny: agreement with contemporary ice geometry and with the GRIP datasets; consistency with the isotopic stratigraphy of the remaining deep ice cores. For the first round, numerical tests are accepted when they meet the following conditions: (1) Present ice sheet volume and areal extent are matched within 5%. This requirement is easily achieved because the topography and coastline largely control the geometry of the ice sheet. (2) The modelled present surface elevation at the GRIP site matches the present elevation within $15\,\mathrm{m}$. Initial bedrock elevation (at t_{init}) is iteratively adjusted so that the present bedrock elevation resulting from the isostatic response to changes in ice thickness is matched within $5\,\mathrm{m}$. Thus vertical profiles can be directly compared. (3) The depth of climatic events in the predicted GRIP ice core matches the record within 10 m for the upper $2000\,\mathrm{m}$ and within $40\,\mathrm{m}$ for the next $800\,\mathrm{m}$. (4) The amplitude of the isotopic fluctuations in the synthetic GRIP core matches that of the GRIP record within $0.1{}^{\circ}\!/_{\circ\circ}$. (5) The simulated borehole temperature profile for GRIP matches the observed temperature (Dahl-Jensen et al., 1998) to within $0.25^{\circ}\mathrm{C}$ at any depth and the amplitude of the temperature change (ΔT_{bor}) measured in the borehole between depths of 600 m and 1500 m within $0.10^{\circ}\mathrm{C}$. Matching ΔT_{bor} assures that the model captures the amplitude of the climatic shift during the last glacial–deglacial transition and compensates the offset caused by potential errors in the present surface temperature.

The above selection process isolates a suite of models that are highly correlated with the GRIP records. As I shall show, satisfactory models can be obtained for a wide range of input parameters so that many combinations of climate and ice dynamics parameters yield similar predictions for GRIP.

However, only a small subset of the satisfactory models gives good agreement with the ice cores from GISP2, Dye 3 and Camp Century. In my second round of scrutiny, I seek the most plausible parameter combinations. With these, I tackle the problem of Greenland during the Eemian.

5.2.2 Best parameters

Model	α_{cE} $‰\,\mathrm{K}^{-1}$	α_{cG} $‰\,\mathrm{K}^{-1}$	α_{cH} $‰\,\mathrm{K}^{-1}$	E_{G}	E_{I}	D_{acc} K^{-1}	F_{acc}
A1	0.25	0.34	0.35	5.5	2.0	0.068	0.92
A2	0.25	0.32	0.32	6.0	2.0	0.067	0.95
A3	0.25	0.32	0.34	6.0	6.0	0.067	0.95
B1	0.33	0.33	0.33	6.0	3.0	0.067	0.93
C1	0.40	0.34	0.35	5.1	2.0	0.069	0.93
C2	0.40	0.34	0.35	5.1	3.0	0.069	0.93
C3	0.40	0.34	0.37	5.1	3.0	0.075	0.93
C4	0.40	0.34	0.35	5.5	2.0	0.068	0.92
D1	0.50	0.34	0.40	5.0	5.0	0.069	0.90
D2	0.50	0.33	0.36	5.2	5.2	0.067	0.90
D3	0.50	0.35	0.40	5.5	5.5	0.067	0.92
E1	0.60	0.32	0.36	6.0	3.0	0.065	0.93
E2	0.60	0.31	0.34	6.0	6.0	0.069	0.92

Table 5.1: Parameters for models that yield a good fit to the GRIP ice core and acceptable agreement with GISP2, Dye 3 and Camp Century. Note: Model C3 uses an isotopic lapse rate of β_δ=$-$4.9 $‰\,\mathrm{km}^{-1}$ (instead of $-6.2\,‰\,\mathrm{km}^{-1}$).

A selection of models, all of which satisfy the above criteria, is given in Table 5.1. Each of these models represents a family of end-member possibilities resulting from a more extensive search and demonstrates that many different combinations of climatic and ice dynamic parameters yield good agreement with the GRIP records. Models are ordered and named according to the value of α_{cE} (letter) and E_{I} (number). For example A1 denotes a model with low α_{cE} ($0.25\,‰\,\mathrm{K}^{-1}$) and stiff interglacial ice (E_{I}=2). The best fits to presently-observed elevations at GRIP and GISP2 are achieved with an enhancement factor E_{G}=5.5–6 for glacial ice and any reasonable value for interglacial ice, thus a low sensitivity to E_{I}. Precipitation parameters D_{acc} and F_{acc} are constrained within a tight range. For the glacial period, α_{cG} leads to a maximum temperature uncertainty of $2.5\,^{\circ}\mathrm{C}$; for the Holocene, variations in α_{cH} are equivalent to $0.6\,^{\circ}\mathrm{C}$; uncertainty associated with the Eemian α_{cE} is larger and is discussed in subsequent sections.

Table 5.2 isolates some of the most representative models for assessing the state of the Greenland ice sheet during the Eemian. For these models, the match to present volume is satisfactory and overestimation of volume is mainly attributed to model-based limitations at representing the detailed topography near the margins, especially the ablation zone, which is concentrated in a narrow band at the ice margins (Ritz et al., 1997). For the last interglacial, the predicted minimum ice volume

Model	Present		Eemian			
	Vol.	Ext.	Vol.	Ext.	ΔT_c^{127}	ΔT_c^{128}
	$10^6\,\mathrm{km}^3$	$10^6\,\mathrm{km}^2$	$10^6\,\mathrm{km}^3$	$10^6\,\mathrm{km}^2$	°C	°C
A1	3.06	1.63	1.06	0.59	7.3	12.6
A3	3.00	1.65	1.09	0.62	6.1	12.4
B1	3.03	1.65	1.50	0.81	7.3	12.2
C1	3.07	1.65	1.97	1.04	7.4	11.3
C4	3.10	1.68	2.01	1.08	7.2	10.9
D3	3.11	1.75	2.55	1.40	5.5	8.5

Table 5.2: Significant models for Eemian study and their corresponding present and past minimal volume and extent and Eemian temperature change. For reference: present ice sheet volume is $2.92\times10^6\,\mathrm{km}^3$, areal extent is $1.65\times10^6\,\mathrm{km}^2$. Past minimal extent occurs at $127\,\mathrm{kyr}$ BP, with associated climate change relative to the present ΔT_c^{127}. Maximal Eemian temperature change is ΔT_c^{128} found at $128.4\,\mathrm{kyr\,BP}$ in the modelled GRIP-Vostok time scale.

and extent strongly depend on α_{cE} for that period, and less strongly on the flow enhancement factor E_{I}. Because the δ^{18}O record has both a temperature and an elevation component (Eq. 4.2.2), the δ^{18}O-based estimate of Greenland temperature variation depends on both the isotopic sensitivity α_{c} and the flow enhancement factor of ice (stiff ice yields a high dome, increasing ΔS_{G} in Eq. 4.2.2. A comparison of A1 and A3 in Table 5.2 illustrates that models with the same isotopic sensitivity and an increased flow enhancement factor can lead to a lower estimate of Eemian climate change (ΔT_c^{127}).

5.2.3 Sensitivity of parameters

Climatic and dynamic parameters have a strong influence on the predictions for the present ice sheet geometry, borehole temperature and isotopic profiles. These effects can combine nonlinearly, cancel or amplify one another, complicating the search for acceptable models. By separately perturbing each of the variable parameters, I summarize their effect on the modelled properties as follows: (1) The isotopic sensitivity α_{c} strongly influences the simulated GRIP borehole temperature profile. Modifying either one of α_{cH}, α_{cG} or α_{cE} significantly alters the entire profile. The effect of α_{c} is amplified because the resulting change in temperature also affects accumulation rate and ice creep rate. (2) Correcting the precipitation by adjusting F_{acc} and $P(x, y, 0)$ in Eq. 2.16 directly influences the depth of the glacial transition in modelled ice core records, and to a lesser degree the ice column height. Changing the precipitation sensitivity D_{acc}, which controls the accumulation contrast between glacial and interglacial periods, modifies the thickness of annual layers in the glacial (i.e., deep) portion of the modelled ice core records. (3) The flow enhancement factor E has a direct effect on surface elevation because it controls the steepness of ice divides — low values raise surface elevation at GRIP. Isolating the effect of varying E_{I} (flow enhancement of present and interglacial ice) is non-trivial because its effect is convolved with other processes. Additionally, because most of the interglacial ice is located in the upper part of the ice sheet, where stresses are low, ice flow is not sensitive to E_{I}. Opposite considerations apply to E_{G}, which is a sensitive parameter and thus well constrained. (4) The isotopic lapse rate β_δ determines the magnitude of the correction for the varying elevation of Summit (Eq. 4.2.2). If I assume an isotopic lapse rate equivalent to the

isotopic surface slope (i.e., taking β_δ=−4.9 ‰ km^{-1} instead of β_δ=−6.2 ‰ km^{-1}), then minor adjustments to α_{cH} (increased by 0.02) and D_{acc} (increased from 0.069 to 0.075) are required to match the GRIP ice core and borehole temperature and the Eemian conditions remain essentially unaffected.

5.3 Modelling the GRIP records

We now focus on the GRIP ice core because, through Eqs. 4.2.2, 4.2.2 and 2.16, its isotopic record yields the climate forcing that drives my model. Although it seems a trivial matter to simulate the GRIP ice core with a model driven by the GRIP record, this is not the case. There are many steps at which this process could fail.

5.3.1 Age–depth profile

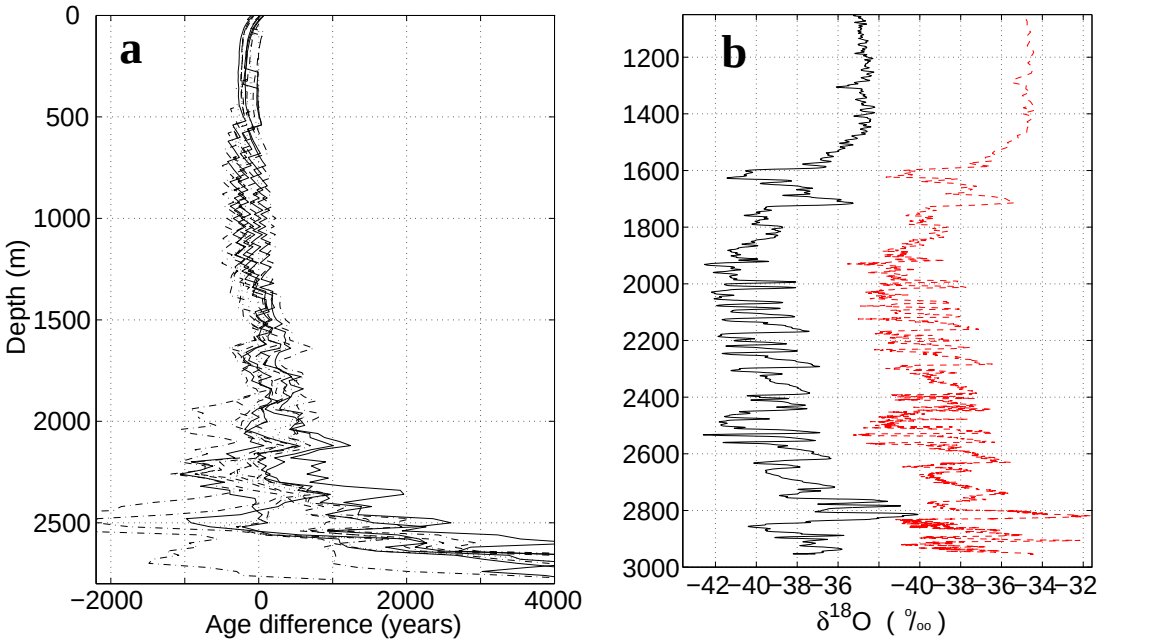

Figure 5.1: (a) Scatter plot of the difference in age between modelled GRIP ice cores and the GRIP-SS09 time scale. (b) Lower portion of the modelled ice core and record showing fi t with depth: GRIP record on the left side, predicted stratigraphy with model

The predicted age–depth misfit for the best models at GRIP relative to the SS09 chronology is presented in Fig. 5.1a. Though the SS09 chronology shows discrepancies with other dated records, for instance a 2–3-kyr-young bias between $20 - 40\,\mathrm{kyr}$ ago (Johnsen et al., 2001), I keep this chronology for consistency of my method and comparison to other studies. This approach is justified by the similar use of a simple accumulation model here and for dating the core (Johnsen et al., 1995): accumulation depends exponentially on ice-core $\delta^{18}\mathrm{O}$. In Fig. 5.1a, comparison with my predictions shows that for the upper $2000\,\mathrm{m}$ of the core, where ice is less than $25\,\mathrm{kyr}$ old, the age discrepancy with SS09 never exceeds 300 years. Age error remains within $1\,\mathrm{kyr}$ for the next $500\,\mathrm{m}$

where age reaches 61 kyr BP. Age–depth error increases below 2500 m before entering the Eemian portion of the record where the discussion on age is senseless given the mixing of layers in that ice (Chappellaz et al., 1997). Fig. 5.1b gives a visual comparison of the predicted δ^{18}O layering with a portion of the GRIP record (left), showing excellent agreement at most depths. The lowest part of the simulated record presents a very thin Eemian section relative to what is believed to be Eemian ice in the record. The small thickness of the predicted Eemian section is a constant feature in my simulations for most temperature and accumulation histories considered here. I predict that the oldest ice at this site dates from 300 to 350 kyr BP but no comparison is possible and this age is contentious because the high disturbance in GRIP basal ice resulting from basal mechanical processes cannot be resolved by my model.

5.3.2 Borehole temperature

Bearing in mind the low vertical resolution of the thermodynamic computational grid ($\sim$150 m at GRIP) and the absence of representation of firn in the ISM, I compare the simulated borehole temperatures at GRIP to the record of Dahl-Jensen et al. (1998) to eliminate my worst model candidates. Spatial resolution and the lack of ice-divide specific type of flow regime in the model prevent me from directly using my results to infer past temperatures at the site, so I accept a tolerance that is over one order of magnitude larger than the accuracy of borehole temperature measurements (5–10 mK). In contrast, one-dimensional heat-flow models (Cuffey and Clow, 1997; Dahl-Jensen et al., 1998) are better suited for that task when forced with an accurate ice chronology because they can use high resolution and a systematic Monte-Carlo parameter search. Borehole temperature is strongly controlled by heat advection, thus by the vertical ice velocity in the Summit region (Cuffey and Clow, 1997). Assessing the influence of three-dimensional ice flow with the ISM, I find that borehole temperature is highly sensitive to changes in the isotopic sensitivity $\alpha_{\rm c}$ and the dynamical parameter E, which is known to affect surface elevation and intensity of ice flow. In the following sections I show that the relative location of the ice divide and the GRIP ice origin is also highly sensitive to those parameters. This can explain the exceptional sensitivity of the predicted borehole temperature and the difficulty to obtain a good fit with the data.

Fig. 5.2 shows observed and predicted present borehole temperature profiles at GRIP. Temperature misfit lies within ± 0.25°C at most depths except for the lower 700 m of the simulated borehole. Most models that are identified in table 5.1 resolve the amplitude of temperature change $\Delta T_{\rm bor}$ (between 600 and 1500 m) within 0.05°C (not distinguishable on the graph: A1, B1, C1, C2, D1, D2, E1 and E2). Relative failure to match the temperature profile can be attributed to uncertainty in the reference present surface temperature at the site, which linearly translates down the borehole. This applies to most retained models with $\alpha_{\rm cE} \geq 0.5\,‰\,{\rm K}^{-1}$ (D1, D2, E1 and E2) that are systematically 0.25°C colder than the measured borehole. Model A3 overestimates $\Delta T_{\rm bor}$ by 0.20°C; the coldest and warmest temperatures for the upper borehole are symetrically too cold and too warm by 0.10°C; $E_{\rm I}$ or $\alpha_{\rm cG}$ could be slightly diminished. Other models underestimate $\Delta T_{\rm bor}$ by $\sim$0.40°C: C3 because of its reduced isotopic lapse rate $\beta_\delta = -4.9\,‰\,{\rm km}^{-1}$ (instead of $\beta_\delta = -6.2\,‰\,{\rm km}^{-1}$) and D3 because of its combination of high flow parameter E, which accelerates heat transport, and high isotopic sensitivities $\alpha_{\rm C}$'s, which diminish $\Delta T_{\rm c}$, compared with D1 with lower E and $\alpha_{\rm cG}$.

Temperature in the lower part of the GRIP borehole is generally too cold in my simulations. The measured basal temperature at GRIP is -8.6°C (Dahl-Jensen et al., 1998) whereas predicted basal temperature at the site is -11 to -9.5°C for present. Plotted but not conspicuous in Fig. 5.2, profiles with the coldest bias correspond to the coldest Eemian predictions ($\alpha_{\rm cE} = 0.5 - 0.6\,‰\,{\rm K}^{-1}$).

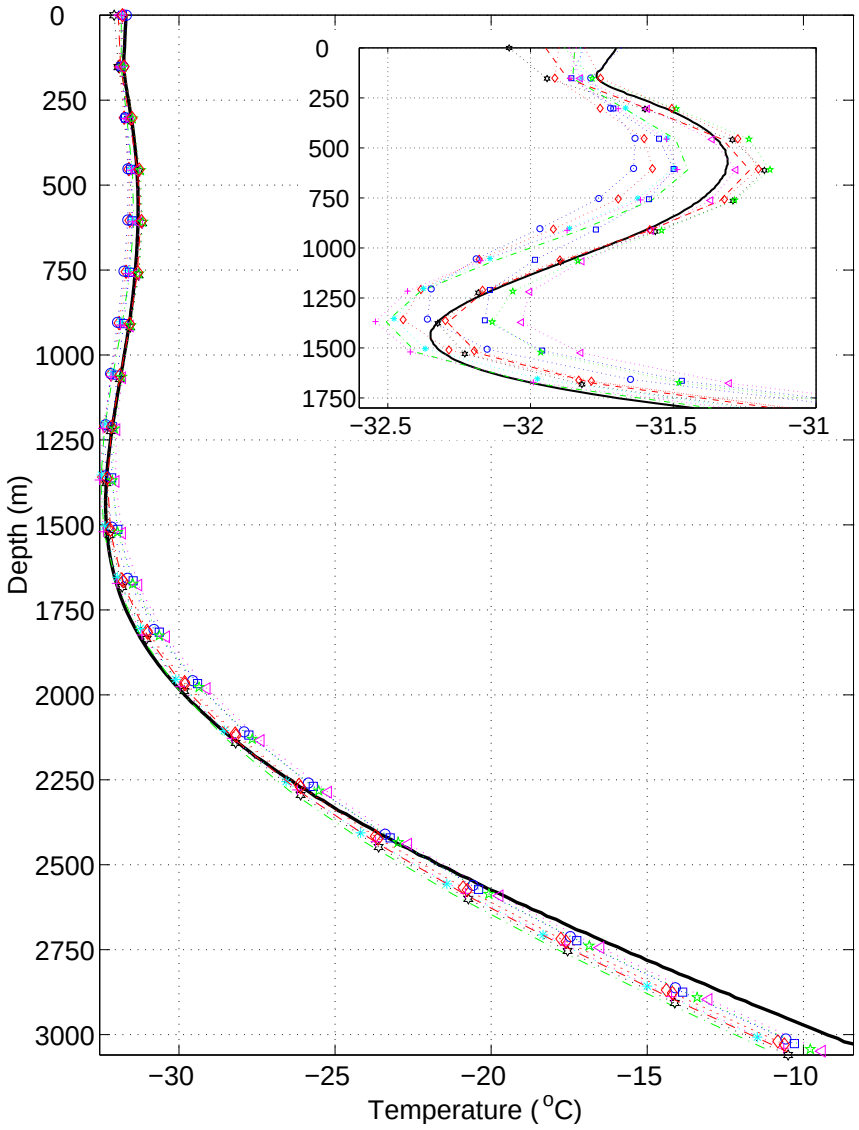

Figure 5.2: Scatter plot of predicted borehole temperature at GRIP: data in black thick line, output from different models in thin lines.

Excessive cold temperatures can also be attributed to the low-resolution grid used to solve the thermodynamics equations. Tarasov and Peltier (2003) find that improved vertical resolution increases modelled basal temperature. Simplicity of the ice-flow model can also have an effect because strain concentrates in the lowest part of the core, where the model fails to represent the faulting and folding processes that are clearly responsible for the highly disturbed basal ice (Alley et al., 1995; Chappellaz et al., 1997; Johnsen et al., 1997). Strain heating due to these unaccounted processes may contribute to a slight warming of the ice. I find that heating from shear strain is non-negligible in the ISM, with an average rate of $\sim$1.5°C per 100 kyr 100 m above the bed over the last glacial cysle, which I model but may not catch fully, depending on the amount of time that the deep ice may have spent under vertical shear. Underestimation of the geothermal heat flux is possible because one-dimensional estimates of 51.3 mW m^{-2} (Dahl-Jensen et al., 1998) are also missing physical

processes and rely on simple assumptions for the past elevation and ice origin. Using the EISMINT (uniform) prescription of 53.0 mW m^{-2}, we recall that a $+1$ mW m^{-2} change is shown to increase basal temperature by 0.4°C (Tarasov and Peltier, 2003). Finally, the model predicts that basal temperatures are in the range -3.8 to -2.5°C at 100 kyr BP, which is close to the melting temperature and indicates that ice at that period was extremely ductile, thus more prone to intense deformation, and that partial melting might have affected GRIP ice.

5.3.3 Paleotemperature

I use the tracer model to obtain the provenance structure ($\lambda_{\rm d}$,$\theta_{\rm d}$,$t_{\rm d}$) of ice cores. The depositional archive holds a record of the spatial and temporal variation of surface properties such as ice surface elevation, temperature, mass balance, δ^{18}O and impurity concentrations. Used together, it is possible to predict attributes of the core that could not be directly measured, for example, the ice surface temperature and elevation at the time and place of deposition, which can be distant from the present ice core sites and can vary over time. The age–depth relationship from the tracer model can be used to represent the variation with depth of these and other ice core properties in the form of a time series. The history of simulated surface temperature for the GRIP ice core is presented in Fig. 5.3.

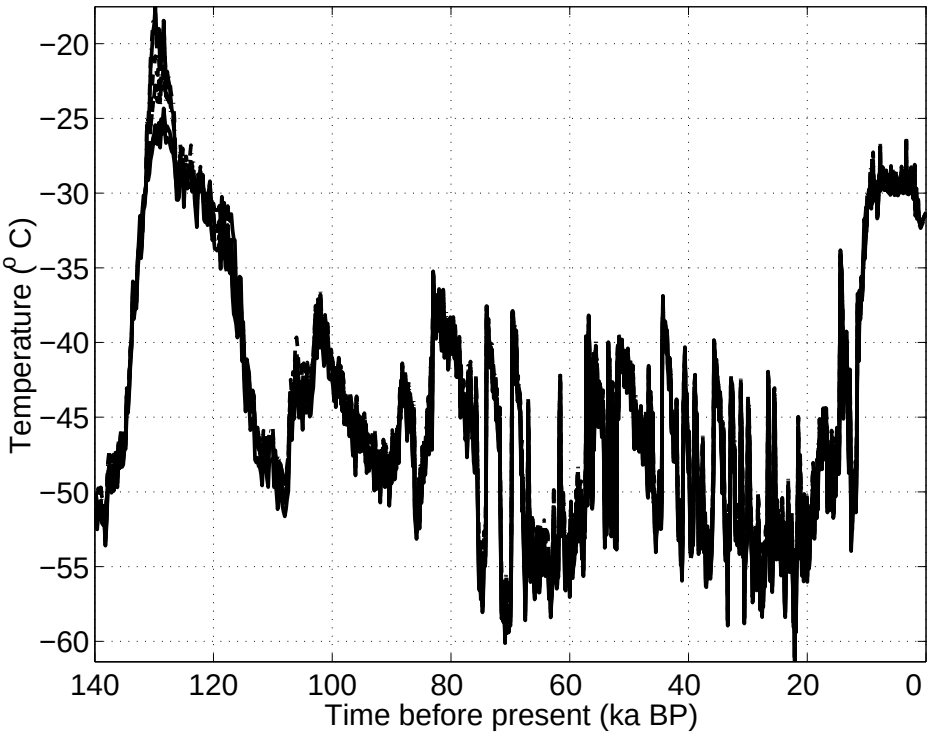

Figure 5.3: Depositional surface temperature for ice from the simulated GRIP ice core. Predictions with acceptable models are overlaid to illustrate the plausible range of temperature compatible with the ISM for the past 140 kyr.

In nature, as in the ice sheet model, surface temperature varies in response to changes in both

climate and ice surface elevation. The simulated surface temperature is 15°C to 25°C colder than present during most of the last glacial period, with a dispersion between the models of ±2°C at GRIP for the LGM, in agreement with the range of uncertainty on past glacial temperatures found by Dahl-Jensen et al. (1998). Given the assumption of a Vostok-like Eemian isotopic signal to palliate for the disturbed GRIP record, simulations with α_{cE}=0.25 ‰ K^{-1} imply that surface temperature at the beginning of the Eemian could have remained 12°C warmer than present for 3 kyr with a maximum of 14°C warmer than present, before cooling to temperatures 1–3°C warmer than present. The possibility of such high temperatures is not corroborated by available climate proxies and here merely represents an end-member to my study, although a persistent 10 kyr-long warm period starting with a climate optimum is also recorded at Dome Fuji (Watanabe et al., 2003), EPICA–Dome C (EPICA community members, 2004) and in deep North Atlantic marine sediments (Adkins et al., 1997). Between $131 - 126\,\mathrm{kyr}$ BP, simulations with α_{cE}=0.33, 0.40 and $0.50 - 0.60$ ‰ K^{-1} are ∼10, 8 and 6°C warmer than present, respectively. Further implications on the Eemian are discussed in a later section.

5.3.4 Paleo-elevation

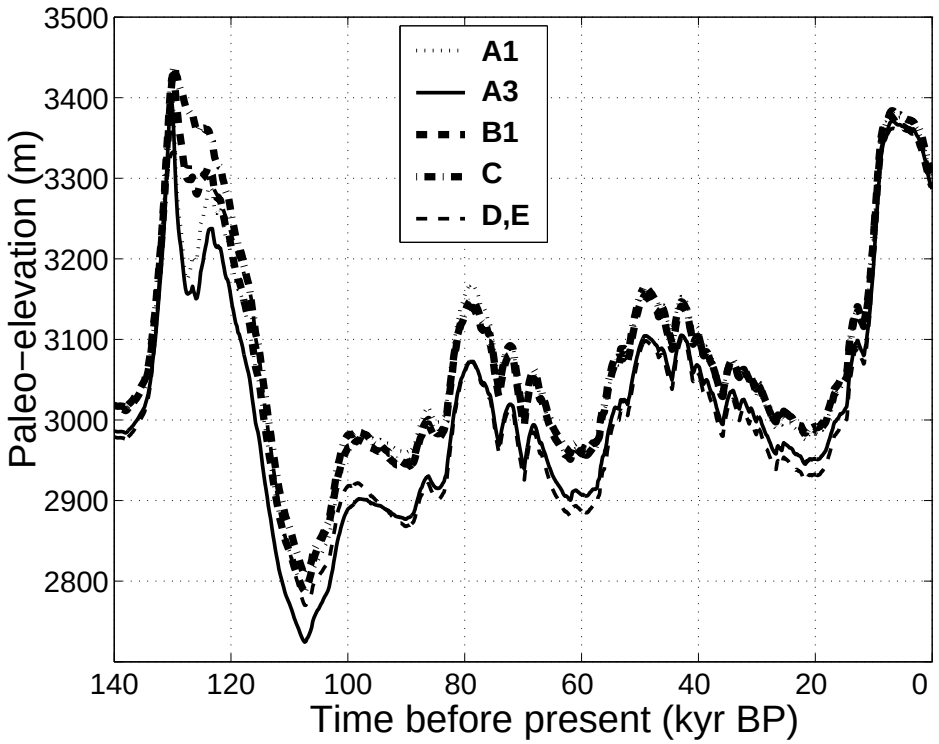

Figure 5.4: Depositional elevation of GRIP ice for the most representative models. C, D and E represent models C1–C4, D1–D3, E1 and E2.

The history of depositional elevation of the GRIP ice is presented in Fig. 5.4. As shown in the next section, depositional origin of the GRIP ice always remains near the contemporaneous summit of the ice sheet; thus, the paleo-elevation history of GRIP ice can be considered to generally represent the behaviour of Central Greenland. This observation relates to a particular concern for the

climate forcing (Eq. 4.2.2), for which I assume that the elevation change ΔS between the deposition of ice from GRIP and its present elevation is equal to the difference between the instantaneous maximum modelled elevation and present elevation at Summit. Examining the modelling results, I confirm that the elevation error and the corresponding error in the climate forcing are less than 5 m and $+0.1°C$, respectively, during the Eemian, and never exceed 15 m and $+0.3°C$ for glacial periods.

Depositional elevation of GRIP ice fluctuates near $3000\,\mathrm{m}$ for most of the last glacial period, in particular during the LGM. This is $300\,\mathrm{m}$ lower than the present. Uncertainty resulting from plausible choices of dynamic and climatic parameters is ± 40 m during glacial periods and $\pm 100\,\mathrm{m}$ during the Eemian. High frequency variations in the modelled surface elevation result from fluctuations in temperature associated with Dansgaard-Oeschger oscillations, a direct consequence of the way I derive precipitation from temperature (or $\delta^{18}O$, Eqs. 4.2.2, 4.2.2 and 2.16). Rapid thickening of the ice sheet at the end of the glacial period and a moderate decrease during the last $2\,\mathrm{kyr}$ are consistent with air content measurements in gas bubbles trapped in ice (Raynaud et al., 1997). Likewise, all simulations indicate a rapid rise of Central Greenland at the beginning of the Eemian, 350–400 m in $3\,\mathrm{kyr}$, because high accumulation rates result from temperatures warmer than present. I note, however, that this relationship is speculative, and is not supported by Holocene accumulation rate reconstructions at the Summit site (Cuffey and Clow, 1997). The same phenomenon affects termination of the past glacial periods because there is a positive feedback loop between temperature, accumulation rate and Summit elevation through Eqs. 4.2.2, 4.2.2 and 2.16) that leads to high temperatures and rise of Central Greenland until other processes with longer characteristic timescales start having an effect (e.g., ice flow, isostasy). Therefore all models predict maximum elevation after a glacial termination at the same dates, $130\,\mathrm{kyr}$ and $8\,\mathrm{kyr}$ ago. At the onset of the last glaciation, $110\,\mathrm{kyr}$ ago according to my climate forcing, surface elevation rapidly drops down to $2800\,\mathrm{m}$ as a quick response to change in accumulation rate when surface temperature plummets.

Not clearly visible in Fig. 5.4, predictions for the Eemian Summit elevation rank according to α_{cE}, which controls surface temperature, and E_{I} for the intensity of ice flow. Models with $\alpha_{\mathrm{cE}} \leq 0.40 ‰\ \mathrm{K}^{-1}$ or stiff interglacial ice (low E_{I}) reach above 3400 m at $130\,\mathrm{kyr}$ BP, 30–60 m higher than my maximum predictions for the Holocene. Simulations with lower α_{cE} and higher E_{I} only rise to 3330–3370 m because of lower accumulation rate and faster ice flow. The later evolution of Central Greenland is significantly more sensitive to α_{cE}. Simulations with α_{cE}=0.25 $‰\ \mathrm{K}^{-1}$ are remarkable because the Early Eemian peak only lasts $0.5\,\mathrm{kyr}$ and quickly lowers in less than $2\,\mathrm{kyr}$ by 260 m (E_{I}=2) to 300 m (E_{I}=6). Given that the predicted surface temperature is 12–14°C warmer than present for these models, the global elevation of the ice sheet is rapidly drawn down because intense melting affects the margins that massively retreat. For instance, the ice margin directly east of Summit recedes by ∼400 km from its modern position, ∼950 km east of Summit, and remains at that position for $\sim 2\,\mathrm{kyr}$. Furthermore, melting affects the summit in the summer time even though surface mass balance remains over its modern value (0.23 m a^{-1}) between 130–$128\,\mathrm{kyr}$ ago: the model predicts an accumulation rate of 0.50–0.55 m a^{-1} and melt rates that increased from 0.10 to 0.30 m a^{-1}. Consequently, ice quickly warms up even in Central Greenland because of the new deposition of warmer ice, the diffusion of sustained warm surface temperatures to the deeper ice and the release of latent heat when summer meltwater refreezes (not represented in this study), all contributing to accelerate the ice flow. Hence minimal ice volume and extent are achieved near $127\,\mathrm{kyr\,BP}$. After stabilization of surface elevation from 128–$126\,\mathrm{kyr\,BP}$, a later elevation increase occurs when the ice flow regime is established and surface melting stops. All the previously

described variations are attenuated if α_{cE}=0.33‰ K^{-1} (model B1): a smaller 100-m elevation loss, Summit melt up to 0.15 m a^{-1} and no subsequent elevation gain. The other simulations, all colder without any melting at Summit, show a steady but smaller elevation decrease during the Eemian as margins partially retreat. In all predictions, I also find that elevation lowering in Central Greenland is faster when the contrast between the flow enhancement of glacial and interglacial ice is larger.

The elevation history shows larger variations between present and LGM than simpler models assumed for assessing ice-divide migration (Anandakrishnan et al., 1994), dating ice cores (Johnsen et al., 1995) and inferring past temperatures (Cuffey and Clow, 1997; Dahl-Jensen et al., 1998). Results from three-dimensional modelling could be used to refine their estimates. Having predicted the history of both surface temperature and elevation, I can separate the climate influence and the elevation influence. Performing this separation, I estimate that the LGM cooling is 23 ± 1.3°C and the Eemian temperature optimum 6°C to 12°C warmer than present in the context of the assumed Vostok-based isotopic reconstruction.

5.3.5 Ice origin and ice-divide migration

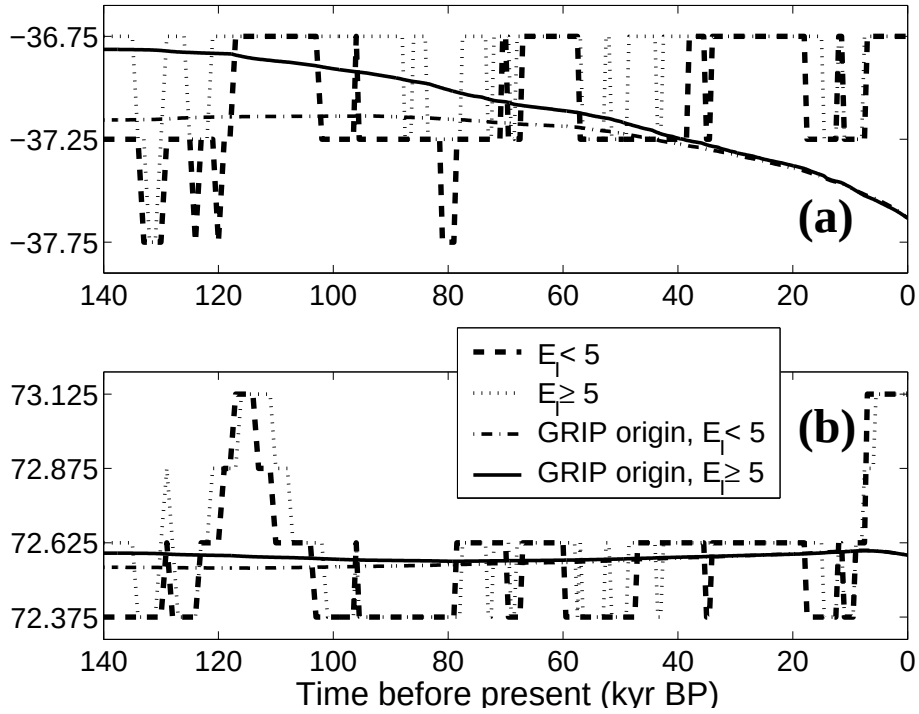

Figure 5.5: Summit (i.e., ice-divide) position for two different flow enhancement parameters of glacial ice (E_{I}) on the computational grid (0.5° longitude, 0.25° latitude). GRIP ice origin for two different E_{I}. (a) Longitude. (b) Latitude.

Previous studies with a similar version of a three-dimensional model (Marshall and Cuffey, 2000) or with a flow-line model (Anandakrishnan et al., 1994) suggest that the location of the Greenland summit migrated over time, which prevented the development of bumps in isochronal layers at the present ice divide (Raymond, 1983). I complement their work by using ice core constraints and testing the influence of differing values for the flow enhancement factor and isotopic sensitivity on

summit mobility and GRIP ice origin. Dashed and dotted plots in Fig. 5.5 illustrate that the modelled summit (point on the computational grid) of the ice sheet never remained at the same exact location for more than $20\,\mathrm{kyr}$ during the past $140\,\mathrm{kyr}$ and that it stood 55 to 85 km south during glacial periods before shifting abruptly back to its present location $10\,\mathrm{kyr}$ ago. I also find westward excursions of 16–33 km with the duration and amplitude depending on the flow enhancement factor of interglacial ice (Fig. 5.5a), but no evidence for a stable 40-km eastward location expected from advance of the ice margin during glacial periods (Anandakrishnan et al., 1994). Noting that my study uses a longitude-latitude grid (equivalent to 16×28 km near GRIP) whereas Marshall and Cuffey (2000) used a 20×20 km cartesian grid and a uniform flow enhancement factor, my results show a smaller amplitude than their 150-km north–east displacement of the ice divide, but a similar bimodal glacial–interglacial location pattern. Not shown here, I find that large values of α_{cE} tend to stabilize the longitudinal position of the Eemian summit and that its latitudinal position is at all times comparatively insensitive to changes in E and α_{c}.

Fig. 5.5 also shows that the origin of GRIP ice is mostly local and in close proximity with the predicted ice divide during the past glacial period, whereas the present summit is simulated 65 km northeast from the GRIP site, which is the current location of the ice divide. The model does not indicate any north–south motion of GRIP ice; thus, the weak westward flank-flow towards GRIP remains qualitatively valid as most of the flow South of the divide is oriented away from the north–south ridge that ends at the main divide. I find that depending on E_{I}, ice from GRIP older than $100\,\mathrm{kyr}$ was deposited 16–27 km east from the present location of the site.

5.3.6 Constraints from GRIP

Predictions of the GRIP fine layering and borehole temperature profile and comparison to the records here impose strong constraints on the acceptable range of dynamic and climatic model parameters. The ability to track the age of ice with high accuracy constitutes a major advance in using numerical ice dynamics models to test and validate internally consistent climate histories for Greenland. Large uncertainties nevertheless remain on the plausible state of the ice sheet during the Eemian when using only constraints from the GRIP records. Assuming that model overestimation of ice volume at present (Table 5.2) applies to the past and that the present ice sheet would raise sea level by 7 m if it totally melted (Huybrechts, 2002), maximum Eemian sea level rise is calculated by taking the percentage loss between the predicted volume at 127 BP and at present. Thus, I predict a sea level contribution ranging from 1.5 to 4.6 m, lower values than those favoured by Cuffey and Marshall (2000). We must not lose sight of the fact that, although the model uses the GRIP record to construct the climate forcing and a depositional archive, it is capable of predicting the isotopic stratigraphy of the entire ice sheet. Thus, data from deep ice cores at GISP2, Dye 3 and Camp Century can further limit the range of acceptable climate and ice sheet reconstructions.

5.4 Constraints from other Greenland cores

5.4.1 GISP2

The age–depth misfit of simulated ice cores at GISP2 for my best models compared with Grootes and Stuiver (1997) is presented in Fig. 5.6. The simulated ice cores were obtained after iteratively tuning present reference surface precipitation near the site so that the predicted fine $\delta^{18}\mathrm{O}$ layering (i.e., the $\delta^{18}\mathrm{O}$–depth profile) matches the GISP2 record within $10\,\mathrm{m}$ for the upper $2700\,\mathrm{m}$ of the

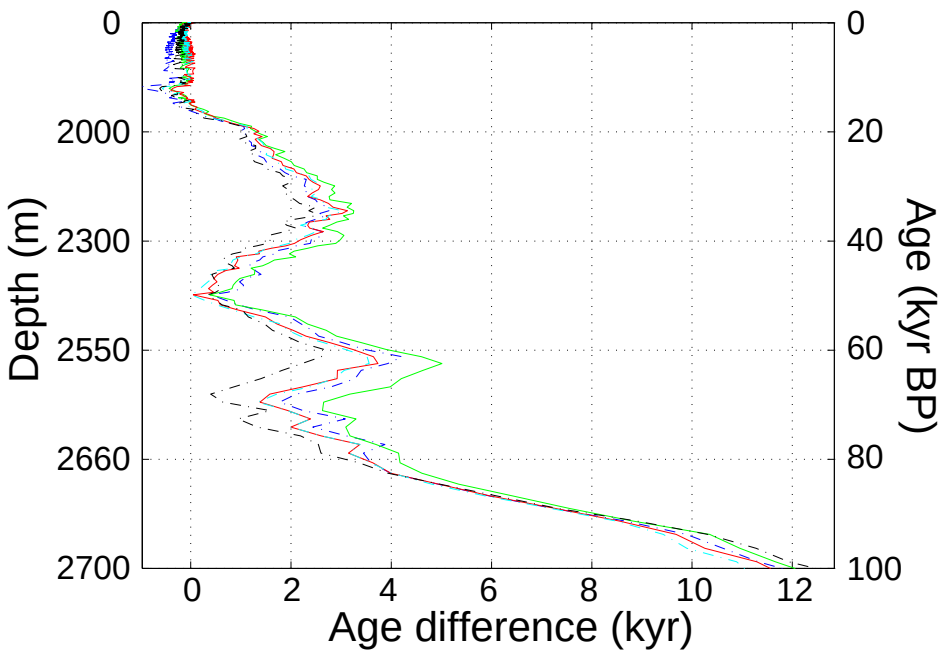

Figure 5.6: Scatter plot of age difference between predicted GISP2 ice core obtained with acceptable models (from Table 5.2) and the reference GISP2 time scale. Age difference is represented as a function of depth (left axis) and as a function of age (right axis). Models are considered to be acceptable if the predicted δ^{18}O vs. depth profi les visually matches the GISP2 ice core record. Lines are not defi ned because the individual error of each model is not discussed in the text.

core (last $45\,\mathrm{kyr}$ BP). The accurate prediction is also illustrated in the previous chapter. The ability to closely match the δ^{18}O variations with depth in the GISP2 record shows the potential of the three-dimensional approach to predict the GISP2 ice core with a GRIP-based timescale and resolve the significant age discrepancies between their chronologies (Grootes et al., 1993). In principle, the GRIP timescale should apply to the GISP2 ice core record and discrepancies in timing could be explained by the accumulation and ice flow simulated with a three-dimensional ice sheet model if the complexity of surface accumulation and ice dynamics was adequately modelled. I do not make this claim here because I acknowledge that the accumulation model is too simple, as evidenced by the improved GRIP timescale SS09sea (Johnsen et al., 2001) obtained after seawater-δ^{18}O-correction of the accumulation model. I also recognize that the GISP2 timescale is better than GRIP-SS09 for the past $38\,\mathrm{kyr}$ because of the high accuracy of the annual-layer counting technique used for dating GISP2 (Alley et al., 1997; Meese et al., 1997). I do not exclude the possibility that my ice sheet model, driven by a GISP2-based climate forcing and with an appropriate set of parameters, could simultaneously fit the GRIP and GISP2 δ^{18}O–depth profiles. As yet, I have not succeeded in demonstrating this point, certainly because of the simplicity of the accumulation model, which is well suited for tracking millennial trends in accumulation rate, but not for accounting for smaller centennial-scale variations in temperature (Cuffey and Clow, 1997).

I also find that modelling the basal part of GISP2 does not add any useful constraint on Eemian conditions because of the limited dynamical processes resolved by the ISM. The lack of sensitivity of the predicted Summit ice cores to Eemian climate is also due to their relative remoteness to the ice margins. In these regions, local climate determines the extent of the ice sheet and leaves an

isotopic imprint. Thus, I can further limit the range of uncertainty in Greenland history by referring to ice cores from Dye 3 and Camp Century, sites that could have been near the ice sheet margin during the Eemian.

5.4.2 Dye 3

Our sensitivity tests confirm that the Dye 3 and Camp Century ice cores are very sensitive to prescribed climatological and dynamical parameters. The cores are also affected by significant ice flow, which complicates the task of determining the local surface precipitation that best fits the age–depth profile of the ice cores, in particular the depth of last deglaciation. This uncertainty does not affect my continuing discussion of the Eemian.

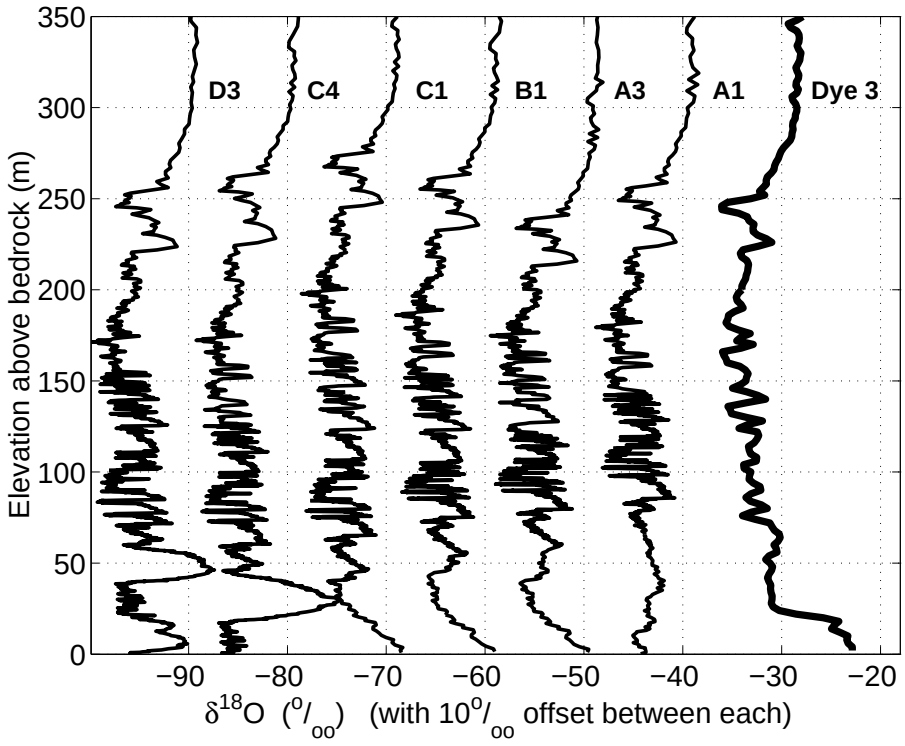

Figure 5.7: Modelled vertical profi les of δ^{18}O and ice core record at Dye 3.

Fig. 5.7 presents the lowest section of the predicted Dye 3 record compared with the actual record. Fig. 5.8 shows the corresponding depositional elevation of ice for each of these simulations. The modelled age of basal ice at the site (Fig. 5.7) provides information on ice coverage during the last interglacial period. I find that basal temperature for Dye 3 (not shown) is $\sim$3 °C warmer than the observed -13.2°C (Dahl-Jensen et al., 1998), but still cold enough to prevent any recent basal melting. Surface elevation is 150 m too low at the exact location of the core, whereas bedrock elevation matches the data (after iterative adjustment of initial topography). Our prediction of overly warm deep ice in this region is consistent with the error in my reconstructed ice thickness; warmer ice is more deformable, drawing down the local ice surface. I believe that small discrepancies on basal temperature and surface elevation do not significantly alter simulations of the Eemian at Dye 3,

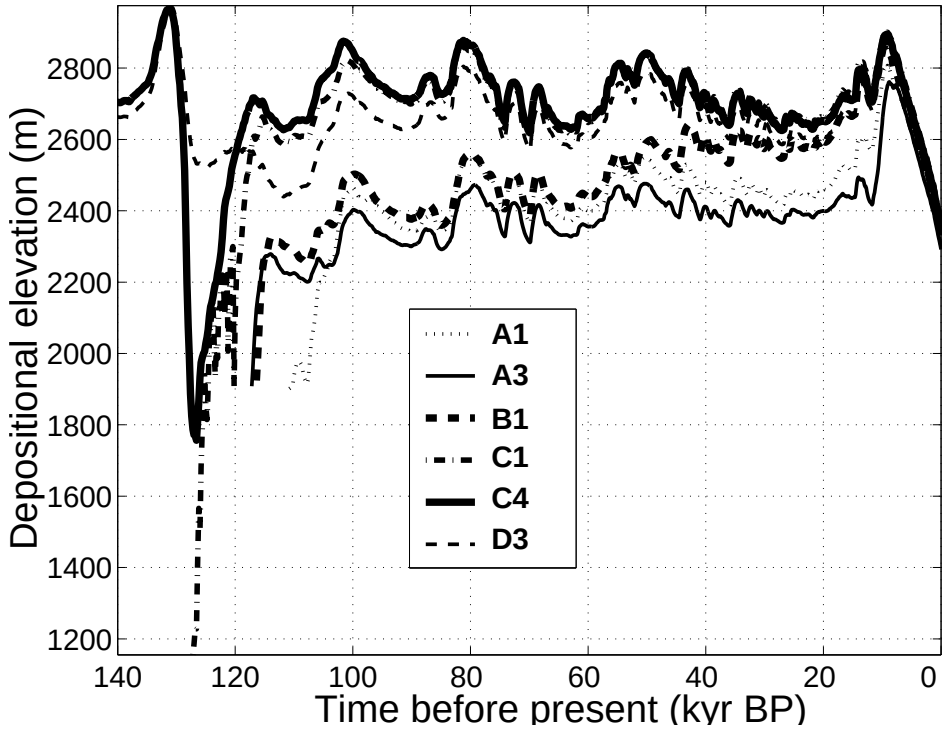

Figure 5.8: Depositional elevation for Dye 3 ice for the most representative models.

although the mismatches call for reducing the local geothermal heat flux below that specified for the uniform EISMINT parameterization (Payne et al., 2000).

From right to left in Fig. 5.7, the first curve (thick line) is the observed Dye 3 ice core record. The remaining curves correspond to results from simulations with increasing values of α_{cE} and that give good fits to the GRIP and GISP2 records. For all the models there is good agreement between the Dye 3 record and the simulated $\delta^{18}\mathrm{O}$ variation for the glacial–interglacial transition. This strongly suggests that the isotopic sensitivity for Summit can also be applied for Dye 3, a conclusion consistent with results from an atmospheric isotopic model (Jouzel et al., 1991).

Model A1 illustrates a warm Eemian climate (α_{cE}=0.25 $^{\circ}/_{\circ\circ}\,\mathrm{K}^{-1}$) with stiff interglacial ice (E_{I}=2). Expressed as a percentage of the modelled present ice volume, the ice sheet loses 65% of its volume and 65% of its extent at $127\,\mathrm{kyr\,BP}$ (Table 5.2). However, the graph for A1 indicates that the bottom portion of the record is missing and consequently basal ice is too young ($110\,\mathrm{kyr\,BP}$). On this basis, I reject model A1. Models A3, B1 and C1 generate plausible records (Fig. 5.7) despite very different parameters. Basal ice ages range from 118.2 to $117.2\,\mathrm{kyr\,BP}$; the corresponding ice sheets lose 36 to 64$\%$ of their present volume at $127\,\mathrm{kyr\,BP}$ (Table 5.2), equivalent to 2.5 to 4.5 m of sea level rise. The corresponding climate reaches a maximum of 11.3 to 12.4°C warmer than present during the early Eemian. Close examination also shows that A3 and B1 have very similar surface temperature and elevation during the Eemian, although the dynamic and climatic parameters and the ice extent are significantly different. Profile C4 relative to C1 illustrates the sensitivity of the ice margins to the assignment of flow law parameters. Despite very similar model parameters and global geometry (Table 5.2), a small change in flow enhancement parameter

E_{G} (from 5.1 to 5.5) determines whether ice reaches the Dye 3 site. Thus, I reject C4. Lastly, basal ice is clearly too old for models with $\alpha_{\mathrm{cE}} \geq 0.50\,{}^{\circ}/_{\circ\circ}\,\mathrm{K}^{-1}$ that predict a climate that is at most 8.5°C warmer than present and a 15% volume decrease (e.g., D3).

Not shown here, I also find that models A1 to C2 have a northern origin for their oldest ice whereas models C3 to E2 have a southern origin resulting from a southern dome. The ISM predicts that this dome is detached from the main ice sheet after the warmest stage of the Eemian for the rejected models C2–C4. Thus, flank drilling sites such as Dye 3 introduce useful new constraints on the range of plausible models.

5.4.3 Camp Century

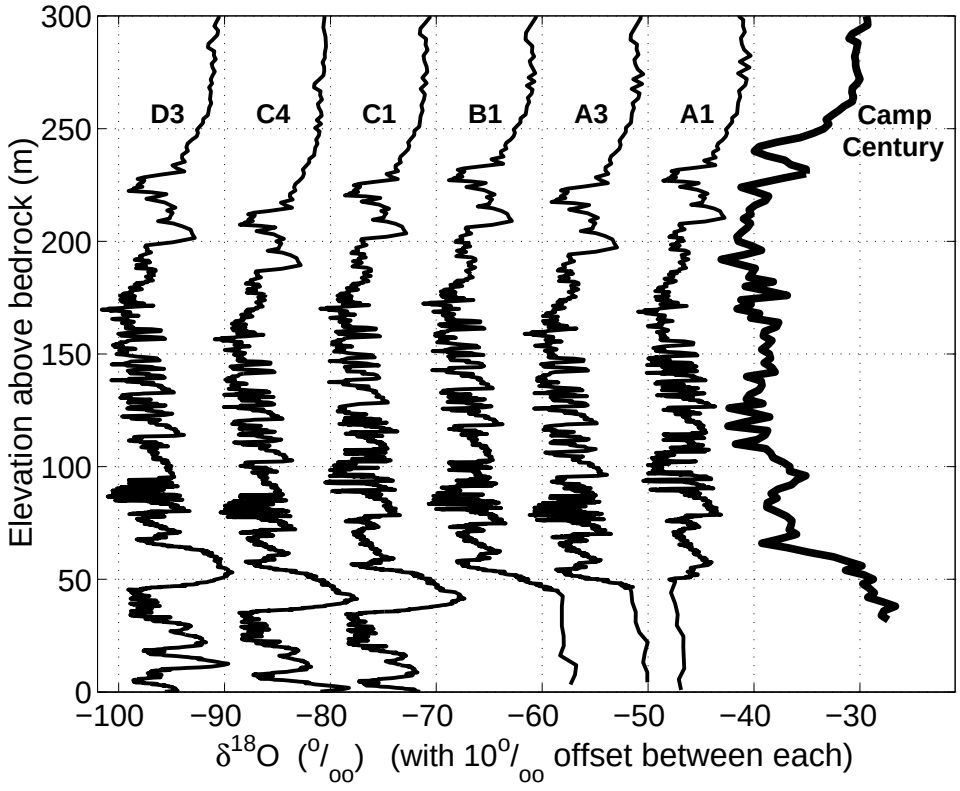

Figure 5.9: Values of $\delta^{18}\mathrm{O}$ for modelled ice cores and record for Camp Century.

The bottom 300 m of the observed and modelled records for Camp Century are shown in Fig. 5.9 and the associated modelled depositional elevation history in Fig. 5.10. As for Dye 3, the depth error in the glacial–interglacial transition does not affect the interpretation of the Eemian. From right to left, the first profile is the ice core record and the remaining curves are for the models given in Table 5.2. Data for the lowest 30 m of the core are not posted on the WDC-A website so I omit this portion of the core. The missing section is known to be rich in silt and has not been dated; the isotopic signal (Johnsen et al., 1989), if not corrupted, would indicate the presence of Eemian ice (high $\delta^{18}\mathrm{O}$) and large variability near the bed. For all the models, the predicted amplitude of the isotopic signal along the entire simulated cores is 60–70% less than the observed signal.

This implies that either the local surface temperature change should be larger between glacial and interglacial periods (a regional temperature effect) or that the isotopic sensitivity should be larger for this region of Greenland (a regional isotopic effect, e.g., a different moisture source), in agreement with GCM studies of isotopic processes (Jouzel et al., 1991; Hoffmann et al., 2000).

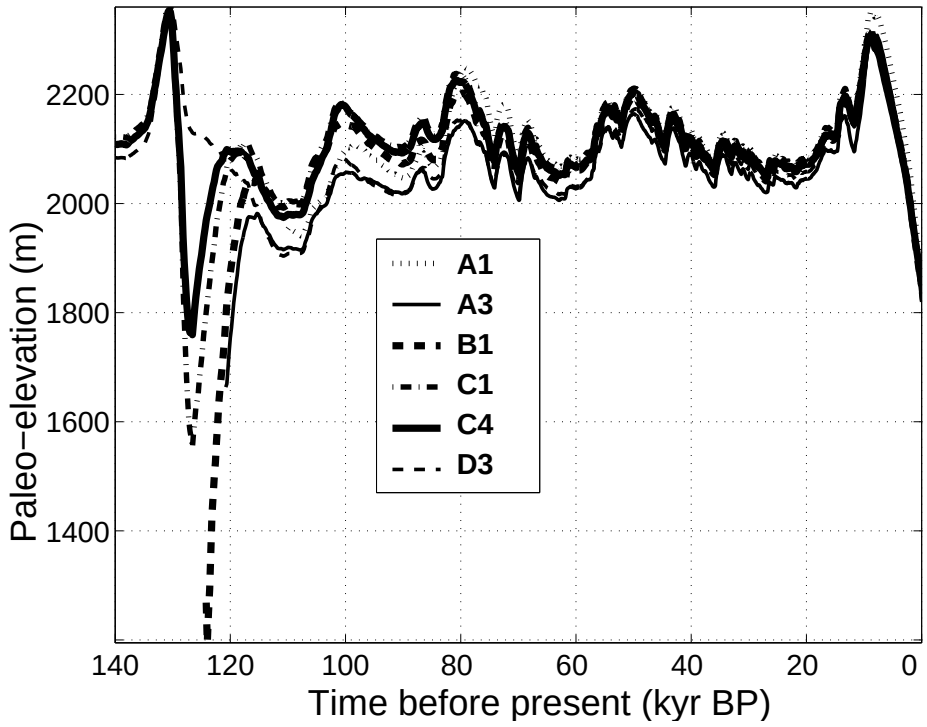

Figure 5.10: Depositional elevation of Camp Century ice for the most representative models.

Models A1, A3 and B1 show similar predictions until 50 m above the bedrock, at which depth disruptions appear. Detailed analysis reveals that age is quasi-uniform below 50 m ($110\,\mathrm{kyr\,BP}$ for A1, $121\,\mathrm{kyr\,BP}$ for A3 and $125\,\mathrm{kyr\,BP}$ for B1) and that ice has similar $\delta^{18}\mathrm{O}$ values but different origin (50 km eastwards for A3 and B1, 70 km for A1 and A2) and minimum depositional elevations (1950, 1650 and 1200 m). I suspect that these features are associated with an age inversion in the ice column, a possibility that was not considered when I developed the balance-based interpolation scheme, though this shortcoming does not affect the predicted spatial provenance of ice. The unusual situation might arise when the ice sheet advances over a recently glaciated cell and older is mixed with recent ice. I believe that the modelled age of the deepest ice corresponds to the first direct deposition of new ice over mixed ice, which approximates the time of post-Eemian reglaciation. This interpretation is consistent with that of Koerner and Fisher (2002): their analysis suggests that Dye 3 and Camp Century were ice-free during the early Eemian when the ice sheet retreated. Then summer cooling at a later stage of the last interglacial period allowed snowfields to persevere and superimposed ice to form before the newly growing ice sheet overwhelmed those sites. By this thinking, basal ice in A1 and A2 (not shown) (α_{cE}=0.25 $^{\circ}/_{\circ\circ}\,\mathrm{K}^{-1}$) may be too young for the expected late-Eemian glacial inception at these sites, casting doubt on these models. I believe them less likely, although I cannot preclude these cases. A3 and B1 give somewhat better agreement with

the timing of the Eemian termination and with the basal temperature at Camp Century (–10.5 to $-10°$C compared with the measured $-12°$C). If only models A3 and B1 are accepted, the sea level equivalent of the Eemian deglaciation of Greenland ranges from 3.5 to 4.5 m.

Models C1, C4 and D3 also match the Camp Century ice core record above $50\,\mathrm{m}$. Below, their Eemian section is too thin and basal age is $230\,\mathrm{kyr}$ old or older, so I am tempted to eliminate all these models and favour an extensive Eemian retreat of the ice sheet. However, given the previously mentioned problems in interpreting the bottom 50 m of the Camp Century ice core, caution should be exercised when drawing conclusions upon that record. Climate near the ice margins determines the extent of the ice sheet, but ice-marginal climate is not resolved by my GRIP-based climate forcing. Furthermore, the ice dynamics model is least accurate near the margins, as a result of limited model resolution, uncertainties in parameterization of basal sliding, and the lack of longitudinal stress coupling in the approximation to ice sheet dynamics.

The case of C1 , the only model with α_{cE}=0.40$^{\circ}/_{\circ\circ}$ K^{-1} retained from analysis at Dye 3, merits special consideration. The Camp Century record contains silty superimposed ice deposited at low elevation, according to its δ^{18}O signature (Koerner and Fisher, 2002). Detailed analysis shows that the simulated basal ice for C1 has always been deposited above an elevation of 1600 m and at least 1000 m above the bedrock, too high to carry any superimposed-ice characteristics. The predicted ice originates at least 30 km upstream from the location of the drilling site, thus relatively far from the ice margin at all times, even during the smallest ice sheet configuration (Fig. 5.12), which leaves no place for deposition of superimposed ice. Therefore, even if the physical flow model lacks folding processes, which are known to potentially affect the ice stratigraphy high above the bedrock (e.g., GRIP/GISP2, Alley et al., 1995), there is no ice of the kind found at Camp Century to be picked up by an advancing ice sheet. Hence the model C1 cannot under any circumstance be reconciled with the actual ice core record; thus, I choose to dismiss C1.

5.4.4 NorthGRIP

The location of the NorthGRIP site was intended to resolve outstanding questions of the Eemian conditions in Greenland. Difficulties encountered while drilling the core imply the presence of warm basal ice and bottom melting (Dahl-Jensen et al., 2003). In my modelling, the assumed geothermal heat flux, which follows the EISMINT prescription, is much too low and the predicted present bed temperature is $-14°$C. Thus my simulations of the deep part of the NorthGRIP record are certain to be wrong. Furthermore, the NorthGRIP site occupies an area that is presently drained by the vigorous NE Greenland ice stream (Fahnestock et al., 2001), which is not represented in the model. Having tested many realistic accumulation histories and failed to predict the depth of last glacial termination in the NorthGRIP record with my model, I deduce that the basal melting at this site and the enhanced vertical advection under the influence of the NE Greenland ice stream (due to increased horizontal divergence) exert significant controls on the age–depth scale at the NorthGRIP site. Thus I choose not to present any simulated ice cores in this paper. However, I consistently find that NorthGRIP remains glaciated at all times and believe that the simulated paleo-elevations may be less affected by the sources of error; thus, I suggest a plausible elevation history in Fig. 5.11.

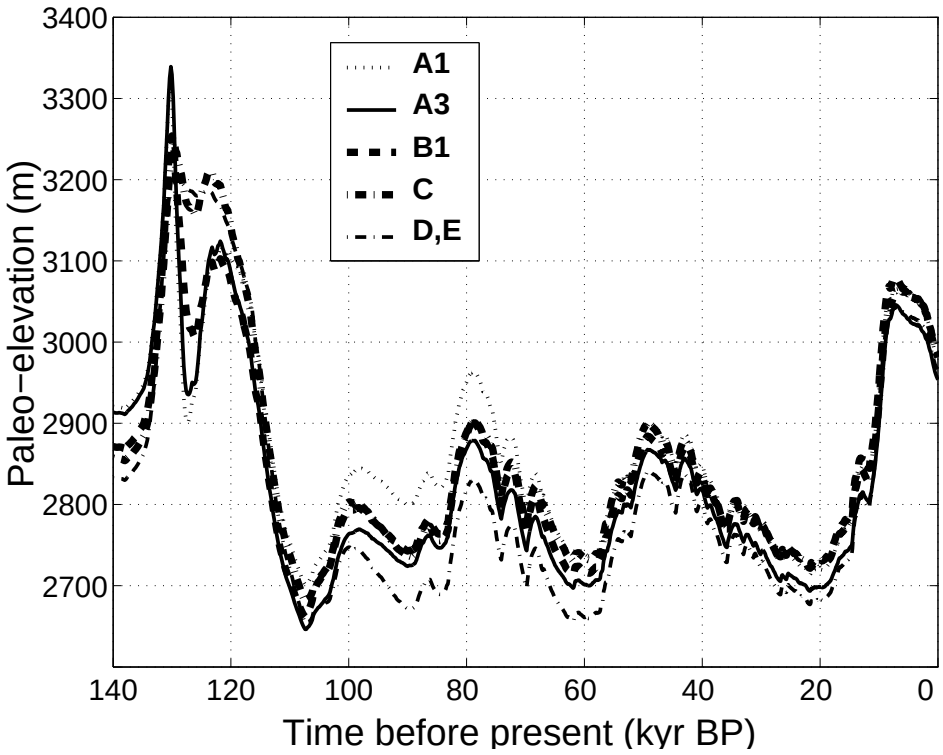

Figure 5.11: Depositional elevation of NorthGRIP ice for the most representative models. C, D and E represent models C1–C4, D1–D3, E1 and E2.

5.5 Minimal configuration during the Eemian

Joint examination of the ice cores from GRIP, Dye 3 and Camp Century imposes strong constraints on the plausible model reconstructions of the Eemian ice sheet. The minimal configuration for the most likely models A3, B1 and C1 is shown in Fig. 5.12 and discussed hereafter. Recalling the simplicity of climate in the ISM, the assumption of spatially uniform climatic change derived from the GRIP and Vostok isotopic records and an unsophisticated treatment of melting processes that could affect my interpretation of phenomena near ice margins, I acknowledge that my results are not definitive. Using the Vostok record could also be misleading, though the recent record from NGRIP (NGRIP Members, 2004) seems to support the Vostok-type history back to 123 kyr BP. The duration and change in temperature of the last interglacial period could significantly deviate from my assumption. However, the similar study by Cuffey and Marshall (2000), more complete in terms of tested Eemian climate although not exhaustive, and taken here as the reference, suggests that amplitude of initial warming is the main control on maximum contribution of the Greenland Ice Sheet to sealevel rise. They find that the duration of the warming period and the accumulation sensitivity D_{acc} do not significantly alter the estimated contribution because of the rapid reaction of the ice sheet to margin position and accumulation rate. Rapid reaction indeed. In my simulation, temperature starts exceeding modern values at 132 kyr BP and gradually increases until 130 kyr BP. The minimal configuration is approached as early as 128 kyr BP.

Changes at the margins are expected between my studies because I attribute different flow strength E to glacial and interglacial instead of a standard value of 5. This is illustrated by models

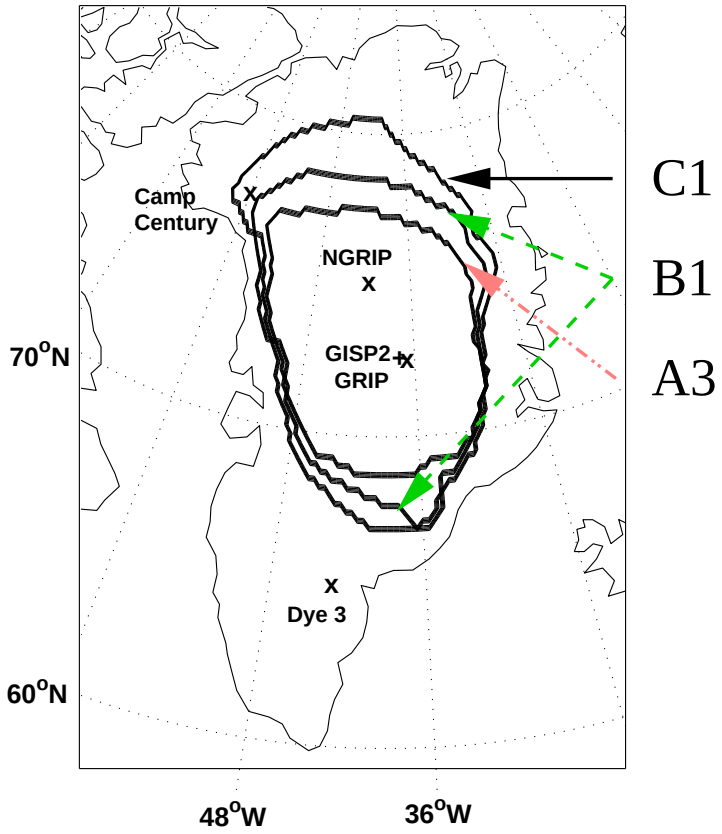

Figure 5.12: Ice sheet minimal extent (127 kyr BP) for the three most likely scenarios A3 and B1. Model C1 is also shown for comparison.

C1, C2 and C4, which use the same climatic parameters (α_c) and predict similar Eemian minimal ice volume (Table 5.2), but differences in E_I and E_G disqualify C2 and C4 at the site of Dye 3, as shown in a previous section, because these simulations keep a detached Southern dome throughout the Eemian, as opposed to C1 (Fig. 5.12). A Southern dome also appears in most predictions in Cuffey and Marshall (2000), for instance with α_{cE}=0.40 $^\circ/_{oo}$ K^{-1} in their Fig. 3b, even though they assume warmer pre-Eemian conditions with α_{cG}=0.40 $^\circ/_{oo}$ K^{-1} (here 0.34 $^\circ/_{oo}$ K^{-1}). Fig. 5.12 and Table 5.2 show that use of specific flow enhancement factor for interglacial ice (E_I=2) in C1 has a significant impact on the predicted minimal ice sheet configuration and eliminates the residual Southern dome. For α_{cE}=0.40 $^\circ/_{oo}$ K^{-1} my study estimates a maximum contribution of 2.5 m (C1, Table 5.2) instead of their 4.5 m; for α_c=0.25 $^\circ/_{oo}$ K^{-1} I predict 4.5 m instead of 5.5 m. There are several differences between my study and those of Marshall and Cuffey that can explain that effect. Here, with lower values of E_I, freshly deposited ice is stiffer, the predicted ice sheet is steeper and higher than their simulations. This has two conter-acting effects. On the one hand, ablation is reduced because there is less ice at low elevation. On the other hand, a higher elevation means a slightly warmer temperature for the climate forcing because the isotopic content at GRIP is fixed. Another possible explanation for the different degree of retreat of the ice sheet is their use of a special subgrid ablation scheme at the ice margins, estimating positive degree days (hence, energy available for ablation) based on a bilinear interpolation of the surface topography in neighbouring

grid cells. This results in significantly higher marginal ablation. I do not adopt this scheme here, choosing instead to use the standard EISMINT mass balance methodology. Finally, differences can also arise because the precipitation schemes differ. I include a modification to local precipitation rates in response to the evolution of local surface slopes (γ in Eq. 2.16), to parameterize the effects of changing orographic forcing (Ritz et al., 1997). Marshall and Cuffey (2000) did not include this feedback.

Differences in parameterization between the two studies are likely to be amplified because changes in the predicted Summit elevation influence the interpretation of the climatic temperature through Eq. 4.2.2. For a given value of $\delta^{18}\mathrm{O}$, interpreted climate is warmer if elevation is higher, leading to large accumulation over the ice sheet and intense melting at the margins. From previous sections we know that most simulations (A1–C4) predict similar GRIP depositional elevation at 130 kyr BP (∼3400 m) but differing evolution depending on α_{cE} and E. For instance, A2 and A3 (α_{cE}=0.25 $^{\circ}/_{\circ\circ}$ K^{-1}) have similar elevation history between 130 and 127 kyr ago whereas for E1 and E2 (α_{cE}=0.60 $^{\circ}/_{\circ\circ}$ K^{-1}), E1 is 120 m higher than E2 throughout the Eemian; thus, climate is ∼1°C warmer. This also affects the predicted climate trend: maximum temperature with 14°C above modern conditions occur 130 kyr BP for A1–A3 before elevation drops, whereas for C1 temperature continues to increase after 130 kyr BP by 1.5°C and reaches a 12°C excess 128 kyr ago. Unfortunately, the GRIP and GISP2 records cannot favour any scenario because the mixed up $\delta^{18}\mathrm{O}$ signal cannot be used and the highest gas content of ice does not indicate any significant deviation of Summit altitude with present (Chappellaz et al., 1997).

Large uncertainties remain in my reconstructions because of model limitations. Our analysis of the Dye 3 and Camp Century favours a deglaciation of these sites (Koerner and Fisher, 2002) but smaller retreat than suggested by Cuffey and Marshall (2000). I find the case of Camp Century delicate to decide upon because the site is located close to the maximum predicted Eemian retreat of the ice sheet for most predictions, even though the Northward ice extent significantly varies (Fig. 5.12); this must be remembered when chosing to eliminate model C1, which corresponds to α_{cE}=0.40 $^{\circ}/_{\circ\circ}$ K^{-1} and a 2.7-m sealevel rise. The remaining models find a maximum loss of 50–64% in volume and 51–62% in areal extent at 127 kyr BP relative to present; thus, 3.5 to 4.5 m of sea level. Regionalization of the geothermal flux distribution could also affect the predicted margins, as shown in Bamber et al. (2000), where use of a spatially uniform geothermal flux is proven to underestimate velocities near the Northern margins and overestimate velocities near the Southern margins at present. That result may apply for the Eemian ice sheet during retreat and advance of the margins near the Dye 3 and Camp Century sites.

Predicted maximum temperatures are much warmer than present and could shock the reader, especially when considering the lack of direct evidence for such warming. I interpret the dramatic Eemian warming as a regional climate signal that reflects the large positive feedbacks associated with ice sheet retreat at this time. With extensive areas of low-albedo bedrock exposed by the diminished ice sheet, Eemian warming would be highly amplified in Greenland. Further amplification would result from the reduction of iceberg production and the expected decline in sea ice cover in the Greenland region at this time. In addition to its low albedo, open water acts as a source of latent and sensible heat flux. Detailed regional climate studies are needed to assess whether a 10–12°C warming is plausible in Greenland at this time, but a warming of this magnitude may well be consistent with a much more modest degree of hemispheric or circum-Arctic warming in the Eemian.

5.6 Conclusion

I have developed a new model for accurately tracking the age and origin of ice in a numerical ice dynamics model. This capability allows one to simulate the time-evolving three-dimensional stratigraphic structure of the Greenland Ice Sheet and to incorporate age-dependence in the flow rheology. This also opens the possibility to track the layers of ice impurities using the tracing method. Simultaneous modelling of ice core records at the major Greenland sites allows direct comparison of data and model-predicted isotopic stratigraphy, imposing strong new constraints on ice sheet models. Good models, which yield a close fit to the present ice geometry and to the temperature and isotopic profiles at ice core sites, are identified by exploring the influence of key model parameters that govern the climate forcing and the ice dynamics. The simulated ice core records are substantially more sensitive to parameter assignments than is the simulated ice sheet geometry, demonstrating that tracer modelling offers a significant improvement for studying the ice sheet history.

Among hundreds of models that matched the present ice geometry, I found fewer than twenty that yielded acceptable agreement with the GRIP ice core and borehole temperature records. When these results are compared with data from Dye 3 and Camp Century, only a handful of candidates remain viable. Dye 3 is particularly useful for constraining the Eemian extent of the Greenland Ice Sheet. Model candidates share the following common features: a flow enhancement factor of 5–6 for glacial ice, 2–6 for interglacial ice, and an isotopic sensitivity of $\sim 0.35 ‰\,\mathrm{K}^{-1}$ for the Holocene and $\sim 0.33 ‰\,\mathrm{K}^{-1}$ for glacial period, which corresponds to an LGM cooling of 23 ± 1.3°C, in agreement with borehole temperature studies (Cuffey and Clow, 1997; Dahl-Jensen et al., 1998). For the Eemian, the isotopic sensitivity of the preferred models ranges from 0.25 to 0.33 $‰\,\mathrm{K}^{-1}$, though a more conservative 0.25–0.40 $‰\,\mathrm{K}^{-1}$ is not fully excluded. The value of any of the above dynamic and climatic parameters cannot be randomly picked within the suggested range: acceptable values for α_c, E and D_acc are mutually dependent. This result illustrates the power of this method relative to previous studies (Cuffey and Marshall, 2000; Ritz et al., 1997): applying standard evaluation criteria to assess model performance (e.g., match to contemporary geometry), acceptable agreement could have been obtained by setting E_I=E_G.

In the context of a simple climate forcing derived from GRIP and Vostok and an unsophisticated treatment of ice margins, the maximum contribution of the Greenland Ice Sheet to sea level rise near 127 kyr BP is estimated. I infer a conservative bound of 2.5 to 4.5 m with a preference for 3.5 to 4.5 m, nuanced by the particular sensitivity of the Camp Century site. These predictions are lower than Cuffey and Marshall (2000). The minimum Eemian ice extent that corresponds to my results is illustrated by Fig. 5.12. Surface temperatures that are consistent with the isotope–elevation history in the Summit region, as well as ice retreat from Dye 3 and Camp Century, are extremely warm in my reconstruction. The 10–12°C warming that I propose should be interpreted as a regional signal, relevant only to Greenland. These high temperatures are the result of a strong regional amplification of the more modest, larger-scale Eemian warmth that is reported in other proxy data (Adkins et al., 1997). The regional character of the climate over Greenland is illustrated by the isotopic record at Camp Century, which I find to require a significantly larger isotopic sensitivity than the GRIP and Dye 3 sites to be reconciled with my Summit-derived temperature predictions.

I suggest that the depositional history of ice predicted by this method could be used to improve the dating of ice cores, where annual layers cannot be counted, and also to help estimate past temperature from the inversion of borehole and isotopic measurements. Simulations predict large shifts in the GRIP depositional elevation history, small variations in the depositional origin and predict

that the ice-sheet main divide occupied different locations during glacial and interglacial periods. The three-dimensional model has the potential to unify most of the GRIP and GISP2 time scales, although the deep and complex Eemian record cannot be addressed by the limited physics resolved in the model.

Future effort is warranted in several directions. (1) A better representation of the spatially-varying geothermal heat flux is essential to match the evidence of basal melt (e.g., Fahnestock et al., 2001) and ice velocites near the margins. For paleoclimatic studies, the age of the oldest ice is of special interest and this is strongly influenced by the basal melt rate. This improvement must precede a detailed examination of the NorthGRIP record. (2) Substantial improvements to the treatment of ice-marginal climate and dynamical processes are needed. (3) A critical examination of how the shallow-ice approximation and the choice of flow law influence the simulated stratigraphy could also be performed.

CHAPTER 6

Global stratigraphy of the Antarctic Ice Sheet

Having successfully predicted the fine stratigraphy of the Greenland Ice Sheet and demonstrated that the tracer tracking method can also apply for Antarctica, I use the method to predict the ice layering of the Antarctic Ice Sheet, which is roughly ten times as large as the Greenland Ice Sheet. For that purpose I rely on the ice sheet model developed by Ritz et al. (2001) to study the evolution of the Antarctic Ice Sheet over several glacial cycles. The description of the model and experiment applies for every chapter involving Antarctica and is presented here once and for all.

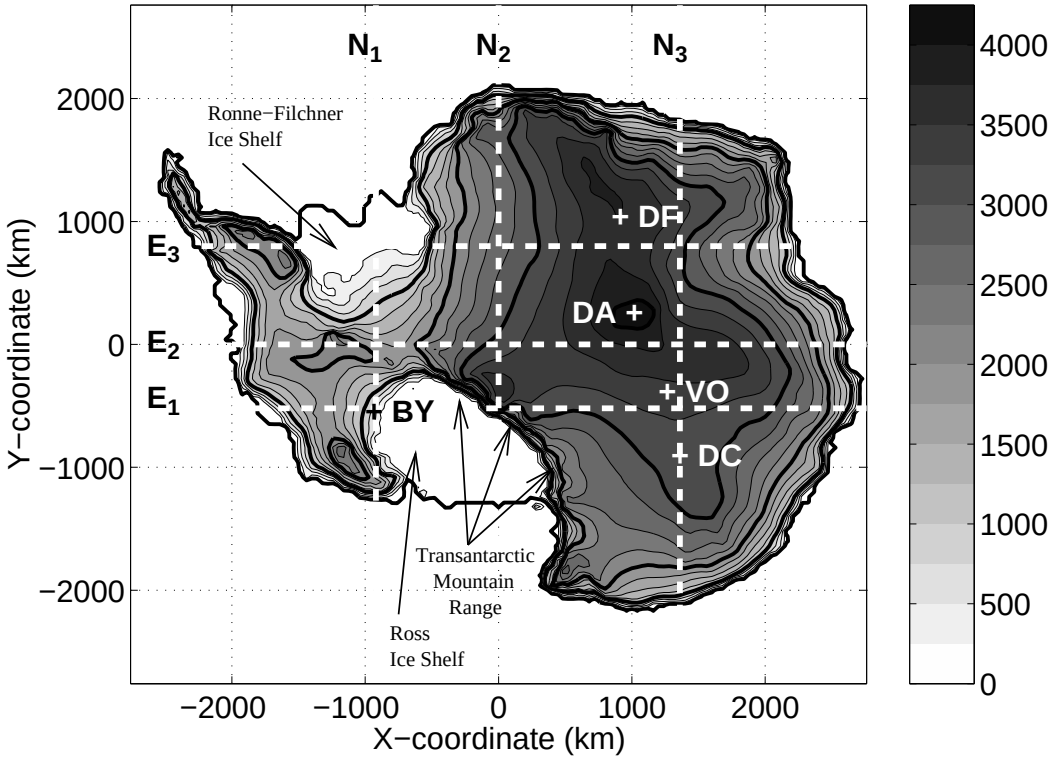

Figure 6.1: Simulated present surface elevation of the Antarctic Ice Sheet and location of domes and drilling sites: DC=Dome C, VO=Vostok, DF=Dome Fuji, BY=Byrd and DA=Dome A Ridge B is the ridge that flows from Dome A toward the ocean almost parallel with X. The ice margin is closer to Byrd than in reality because unresolved physical processes in the ISM misplace the margin. Contours every 250 m up to 4000 m, thicker contour every 1000 m. White dashed lines indicate cross-section lines.

6.1 Description of the model

6.1.1 Ice dynamics

The thermomechanical three-dimensional Ice Sheet Model (ISM) is based on the numerical integration of the continuity equation to obtain the temporal and spatial evolution of the ice thickness and the time-evolving three-dimensional ice flow field (Huybrechts, 1990, 2002). The model incorporates all the types of ice flow regimes found in Antarctica: moderately slow inland flow where vertical shearing dominates (using Glen's flow law, n=3, Glen (1955)), fast flow in ice-stream regions, and Newtonian flow for ice shelves (Rommelaere and MacAyeal, 1997). The isostatic response of the Earth to change in surface load (ice and seawater) is treated by an elastic lithosphere-relaxed asthenosphere model (Le Meur and Huybrechts, 1996) that is coupled with the ice dynamics model.

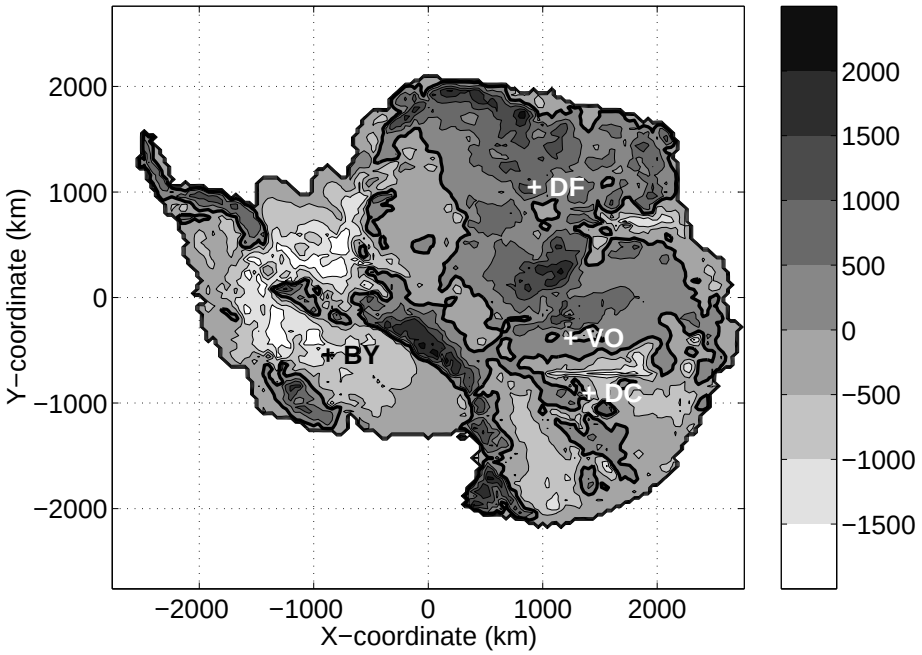

Figure 6.2: Simulated present bedrock elevation of Antarctica with 500-m contour lines, thicker line for 0 m (present sea level).

In the present configuration of the model, the numerics are solved on a cartesian square grid of 40 km resolution (141×141 to cover Antarctica) with 21 vertical levels using a time-marching finite difference method. The grid is oriented so that the X-axis is parallel to the 90°E meridian and the Y-axis parallel to the 0°E meridian. The mass-conservation equation is solved at the time step that yields stability for the largest velocity found in the grounded ice sheet ($\sim$1 yr). Longer time steps (typically 20 yr) are used for the other equations: heat equation, equation for ice shelf and dragging ice shelf flow, bedrock reaction, surface mass balance and tracer transport. A Weertman-type sliding law controls basal motion with an adjustable parameter $k_{\rm sl}$=0.2–0.5$\times 10^{-8}\,{\rm m\,yr^{-1}\,Pa^{-2}}$. The geothermal heat flux $q_{\rm geo}$ is assumed to be temporally constant and spatially uniform throughout Antarctica (even for the tectonically active West Antarctica) with a value of 55 mW m^{-2} validated by ice sheet studies and borehole temperature measurements in East Antarctica (Ritz et al., 2001). Distributions of present-day ice thickness, surface and bedrock elevations (Fig. 6.2) are adapted

to the computational grid from the 5-km Bedmap topographical compilation (Lythe et al., 2000) to define the present reference.

6.1.2 Climate forcing

The climate forcing uses the principles described in Section 1.5.3. I choose to adopt the temperature ($T_{\rm s}(t)$) and accumulation history EDC2 reconstructed by F. Parrenin (EPICA community members, 2004) from the EPICA-Dome C δD ice-core record because it is the longest climatic timeseries and it originates from a dome, where the ice flow is simple and predictible, thus yielding a more reliable interpretation of the climatic record than flow-affected sites like Vostok. As the simulation proceeds, the temperature forcing is applied in two steps. The large-scale temperature change $\Delta T_{\rm c}$ is deduced from the reconstruction of past surface temperature at Dome C (DC) after correction of the change in elevation at the site ($\Delta S(DC,t)$):

$$\Delta T_{\rm c}(t) = \Delta T(DC,t) - \beta_{\rm T} \Delta S(DC,t) \tag{6.1}$$

That correction assumes that all the ice in the DC record has a local origin, an hypothesis that can be validated *a posteriori* with the tracer transport model. Then annual surface temperature is redistributed over the ice sheet according to Eq. 1.15. As a sensitivity study I also test the effect of reducing the surface temperature change of EDC2 by 15%. This defines two different temperature forcings $\Delta T_{\rm c}$ with 10°C (model T1, reduction) and 11.5°C (model T2, like EDC2) amplitude between the present and Last Glacial Maximum (LGM), 20 kyr ago, when Northern ice sheets reached their maximum size and the Antarctic Ice Sheet was significantly larger (Fig. 6.3) than its modern configuration.

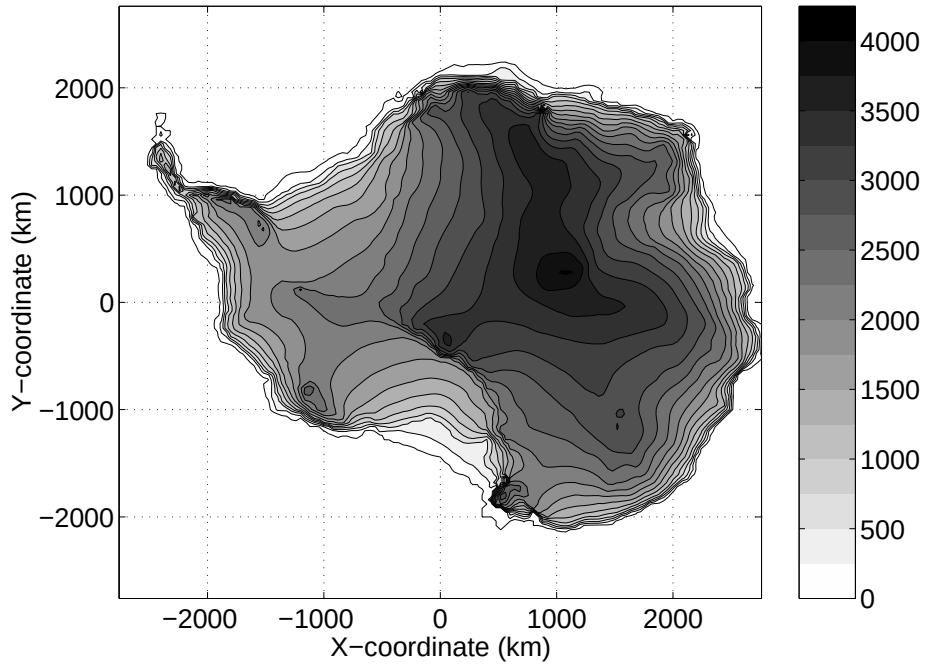

Figure 6.3: Modelled surface elevation of the Antarctic Ice Sheet at 20 kyr BP with 250-m contour lines (no ice above 4000 m).

The temperature forcing determines precipitation rate according to Eq. 1.16. The accumulation sensitivity $D_{\rm acc}$ for models T1 and T2 is obtained from the temperature and accumulation history of EDC2 by reversing Eq. 1.16. The value of $D_{\rm acc}$ generally varies between 0.070 to 0.085 K^{-1} and is here confined to that range away from DC. Sensitivity tests on $D_{\rm acc}$ are also done with a fixed predefined value for the entire ice sheet or just for special regions of interest. I denote T1A and T2A the climate forcings derived from T1 and T2, respectively, with a time-invariant regional (20×20 mask) value of $D_{\rm acc}$=0.070 K^{-1} in the vicinity of Dome Fuji. These forcings yield better agreement with modern surface elevation at the site; justification is provided in Appendix D.1.2. Similarly I denote T1D and T2D the climate forcing with a time-invariant and uniform value of $D_{\rm acc}$=0.070 K^{-1}. The present distribution of temperature and precipitation is shown in Appendix A. The temperature climate forcing is also used to prescribe basal melting under the ice shelves because a model of ice-shelf–ocean interaction would have to depend on the global ocean circulation and be too complicated to implement for this kind of study. I keep the default method of Ritz et al. (2001) who assume a linear relationship between basal melting and $\Delta T_{\rm c}$ with modern values for $\Delta T_{\rm c}$=0 and no melting for $\Delta T_{\rm c}$=-10°C (LGM). The definition of the different climatic parameters is summarized in Table 6.1.

Climate Forcing	Chronology	$\Delta T_{\rm c}$	$D_{\rm acc}$	$D_{\rm acc}(DF)$
T1	EDC2	10°C	DC	DC
T2	EDC2	11.5°C	DC	DC
T1A	EDC2	10°C	DC	0.070 K^{-1}
T2A	EDC2	11.5°C	DC	0.070 K^{-1}
T1D	EDC2	10°C	0.070 K^{-1}	0.070 K^{-1}
T1D	EDC2	11.5°C	0.070 K^{-1}	0.070 K^{-1}

Table 6.1: Definition of climatic parameters for Antarctic simulations.

The third climate forcing is the evolution of sea level, which controls grounding line migration. Following Ritz et al. (2001), I assume that sea level is independent of the volume of the Antarctic Ice Sheet (no coupling) because past sea level changes are mostly governed by the volume of continental ice in the Northern Hemisphere. I use the δ^{18}O record of Bassinot et al. (1994) with a calibration such that sea level at LGM is 120 m below present. As noted by Ritz et al. (2001), the choice of this record rather than the SPECMAP compilation (Imbrie et al., 1990) has little effect on the evoluton of central Antarctica.

6.2 Experimental design

6.2.1 Adjustments near ice core sites

I find that the reference bedrock elevation, present surface temperature and accumulation rate in the vicinity of the drilling sites must be corrected from their standard value to allow direct comparison of the properties of simulated ice cores with the actual records. The ISM initial bedrock elevation is locally modified so that the predicted bedrock at the end of a simulation (finishing at the present epoch) matches observations at the sites so that predicted ice cores start at the right depth. The correction is non-trivial. The simulated present bedrock depends on the Earth's mantle response

to the regional loading history caused by changes in ice thickness during glacial cycles. I adjust basal topography from Ridge B to Vostok by referring to the interpretation of airborne radar data from Siegert and Kwok (2000) that is also used in Parrenin et al. (in press). Depth is adjusted near Dome Fuji according to Watanabe et al. (2003). Present observations show a dome at the site of DC whereas the ISM does not reproduce this feature. This discrepancy can be attributed to the coarse spatial resolution of the model, to uncertainty of the bedrock map and to the physical assumptions inherent in large-scale ice sheet modelling: longitudinal stresses, which are negligible almost everywhere but exercise a control on ice domes, must be ignored for the sake of computability. Thus the modelled ice sheet can show fewer or different topographical features than the real ice mass. A broad ridge sloping gently down from the region of Ridge B towards DC, visible on Fig. 6.1, drives ice flow in that direction. Surface slope is weak near DC so it flows almost like a dome, though flank flow from the ridge is non-negligible. I apply a new correction by including a recently discovered deep trough (800 m below the reference Bedmap) that is oriented toward the ocean and runs perpendicularly to the Vostok–DC ridge (Forieri et al., 2003). This adjustment effectively reduces the incoming flow at DC by increasing drainage towards the ocean, significantly improving the modelled flow regime at DC and facilitating simulation of its ice core record.

Based on field observations, present annual surface temperature is set to $-54°$C for DC and $-58°$C for Dome Fuji (DF) on a spatially uniform 5×5-grid-point mask around the sites. The relationship between δD and T_s is rather complex in the vicinity of Vostok. For instance, δD at Dome B is higher ($-430‰$ δD) at present than at Vostok ($-441‰$ δD) even though present surface temperature is $2°$C colder and surface elevation is 160 m higher (Masson et al., 2000). In order to ease the reconstruction of δD in my predicted Vostok ice cores, I assume that δD reflects a similar surface temperature all the way from Vostok to Ridge B and correct surface temperature accordingly. Practically, I apply a correction on a 10×5 grid mask above that region with a 75% reduction of the thermal lapse rate and a reference temperature of $-55°$C at Vostok.

Field measurements also show that the standard present distribution of accumulation rate is overestimated at DC, Vostok and Dome Fuji. I choose to impose the same regional masks as for temperature because I find that globally reducing precipitation unacceptably lowers the general elevation of the entire ice sheet. DC directly receives the accumulation rate inferred in the chronology EDC2 at all times for the entire mask, $\sim$3 cm yr^{-1} for the present. For Vostok, I use the presently observed value at the site of $\sim$2 cm yr^{-1} (Petit et al., 1999) and apply a 1.6-fold increase towards Ridge B (Ritz, 1992). For Dome Fuji, tuning starts with estimates of $\sim$3 cm yr^{-1} from Parrenin (2002). As discussed in the next chapter and in Appendix D.1, the impact of these corrections on the depth–age profile of the simulated ice cores is significant; thus, present mass balance is a sensitive model parameter.

6.2.2 Model spin-up

All simulations start at a distant time t_init in the past and run to the present. The low accumulation rate in central Antarctica implies that ice has a long residence time, as evidenced by the three deep ice cores showing basal ice that is older than 300 kyr. The model confirms that prediction for most of central Antarctica and finds sites with basal ice reaching over one million years old. I ensure that any long-lasting memory effect from the initial state of the ice is erased by running the simulation for several glacial cycles, from t_init=688 kyr to present. Simulations with 4 glacial cycles provide similar results but fail to produce a long-enough timeseries for the stratigraphy of the Dome C record. A second safeguard is guaranteed by initializing the model at t_init with the

result of a previous simulation that yields a close match to present observations (volume, extent, topography, age–depth profile at ice core sites), assuming than the climate at t_{init} resembles the present. Initialization of the distribution of provenance variables is obtained by pre-aging ice by the final result from the previous run and assuming ice to be of local origin.

6.2.3 Validation process

The coupled ice sheet–tracer model predicts the three-dimensional time-evolving structure of the Antarctic Ice Sheet and its fine layering as the response to a temporal climate forcing ΔT_{c}. The final result of a run is the reconstruction of an ice sheet for which its geometric features and "synthetic" ice cores can be compared to present records and observations. I define a successful simulation as one that generates (1) a present Antarctic ice sheet in close agreement with the geometric features of the present observations (surface elevation, volume and extent within 5%) and (2) ice layering at drilling sites that accurately matches the ice core records of DC (EPICA community members, 2004), Vostok (Petit et al., 1999) and DF (Watanabe et al., 2003), especially the depths of the last major climatic transitions within 5%. Given that adequate treatment of firn dynamics and densification requires too much spatial and temporal resolution (e.g., Goujon et al., 2003) for an ISM, precipitation is assumed to be instantly transformed into ice. Thus the reference elevation is lowered by $30 - 35\,\mathrm{m}$ to account for the compaction of the upper $\sim$100 m of firn covering the central Antarctic Plateau. The resulting targets are 3200 m at DC, 3450 m at Vostok and 3775 m at DF.

In the following simulations I decide to test the source of model uncertainty associated with the climatic parameters ΔT_{c}, D_{acc} and $A(t{=}0)$, and the dynamical parameters k_{sl}, q_{geo} defined in Sections 6.2.1 and 6.1.2. Sensitivity tests are performed to obtain a semi-optimal value by a trial-and-error approach, acknowledging that a systematic inverse method is currently beyond reach because of the computational intensity of such complex ISMs. Convergence toward these hand-picked values is facilitated by diagnosing the effect of these parameters on ice sheet geometry and on simulated ice cores, a task described in the next chapter and in Appendix D.1.

6.3 Depositional provenance stratigraphy

As for the Greenland Ice Sheet we can look at the present distribution of provenance labels across Antarctica to demonstrate the capabilities of tracer transport modelling. This is achieved by simulating the present three-dimensional stratigraphic structure of the ice sheet and comparing model predictions with the observed ice core stratigraphy at deep drilling sites. The locations of these sites and of the profile lines used to present and discuss tracer-provenance cross sections are shown in Fig. 6.1. Six lines are chosen so that they cut near interesting features such as ice core sites, the South Pole, ice divides and ice shelves. Lines E_1, E_2 and E_3 are parallel to the X axis and slice through the West and the East Antarctic Ice Sheet; lines N_1, N_2 and N_3 are parallel to the Y axis.

I will refer to X and Y in the following sections to characterize the direction and origin of ice flow and tolerate loose terminology such as "east–west" and "north–south" or "Easting" and "Northing", respectively, though strictly wrong, because the top of topographic maps usually points to the North. I choose to remain in the cartesian system rather than converting positional variables to longitude and latitude because, as illustrated in Fig. 6.1, most surface topographic features and resulting ice flow directions show better alignment with X and Y than with geographical orientation points.

6.3.1 "East–west" profiles

Line E_1 crosses through both ice sheets, passing by the Byrd site, the Ross Ice Shelf, through the Transantarctic mountain range or barrier, towards Vostok and across the East Antarctic Plateau, along $Y = -520$ km. The provenance labels show a fairly regular structure in Fig. 6.4 and a clear

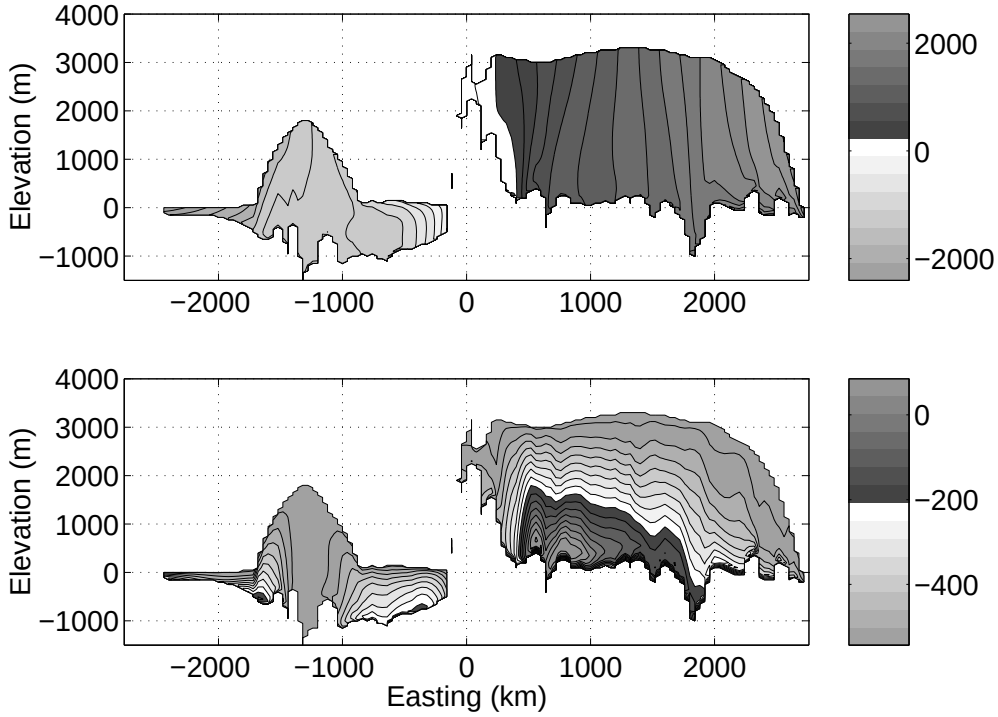

Figure 6.4: Cross section of provenance variables, along line E_1 (parallel to the X axis, through Byrd). The upper panels shows the X provenance (x_{d}), the lower panel the Y provenance (y_{d}). Easting corresponds to distance along the X axis.

separation between the East and the West, as no ice seems to cross the mountain barrier. The upper panel shows that there is little divergence of ice flow in the X direction, as iso-X lines are almost parallel over most of the section. Signs of lateral flow appear expectedly near the flank of the ice sheet as a result of the steep surface slope.

The lower panel displaying Y depositional origin completes the description of the flow by confirming that most of the ice originates in the central part of the ice sheet. The pattern is very regular for the East, showing a steady flow down from Dome A, the summit of the ice sheet. Ice originating from Dome A appears in the deepest layers of the cross section, 600 km from its depositional site. A hiatus in the upper layers around 1400 km corresponds to the particular flow of the Vostok-to-Dome C ridge divide. Ice flow is distinctively eastward (X direction) on the east side of that ridge, therefore most of the ice has a local y_{d} origin. A deep trough at 1900 km introduces significant distortions in ice layers. Transport along Y is also reduced near the Transantarctic barrier because the transverse orientation of the mountain range deflects and resists ice flow.

For the upper panel showing West Antarctica, ice deposited on the lee side of the mountain range penetrates the basal layers of most of the ice sheet as seaward ice flows downslope. In the lower panel, most of the ice under the divide is local, signifying the potential for a reliable ice core

site there. More distant depositional origin is found on the seaward side as ice flows down from the west central ice divide. On the Ross Ice Shelf side, which drains a large part of the West Antarctic Ice Sheet, ice originates up to 300 km upstream, less than I would have expected. This can be explained by the fact that modern surface accumulation rate and basal melt rate near $\sim$0.50 m yr^{-1}, effectively renewing a 500-m thick layer of ice in 1 kyr at the current rate and significantly reducing the storage of old and distant ice in the Ross Ice Shelf.

I note for this graph and the following ones that the model predicts an ice shelf around the ice sheet at present time, here for the regions delimited by $X \leq -1800$ km and $X \geq 2350$ km. This floating ice is irrelevant for this study. It is an artifact because calving is not included in the model: either melting (basal and surface) is strong enough to remove it, or the ice shelf extends as far as the limit of the time-invariant mask used for its boundary condition (Ritz et al., 2001).

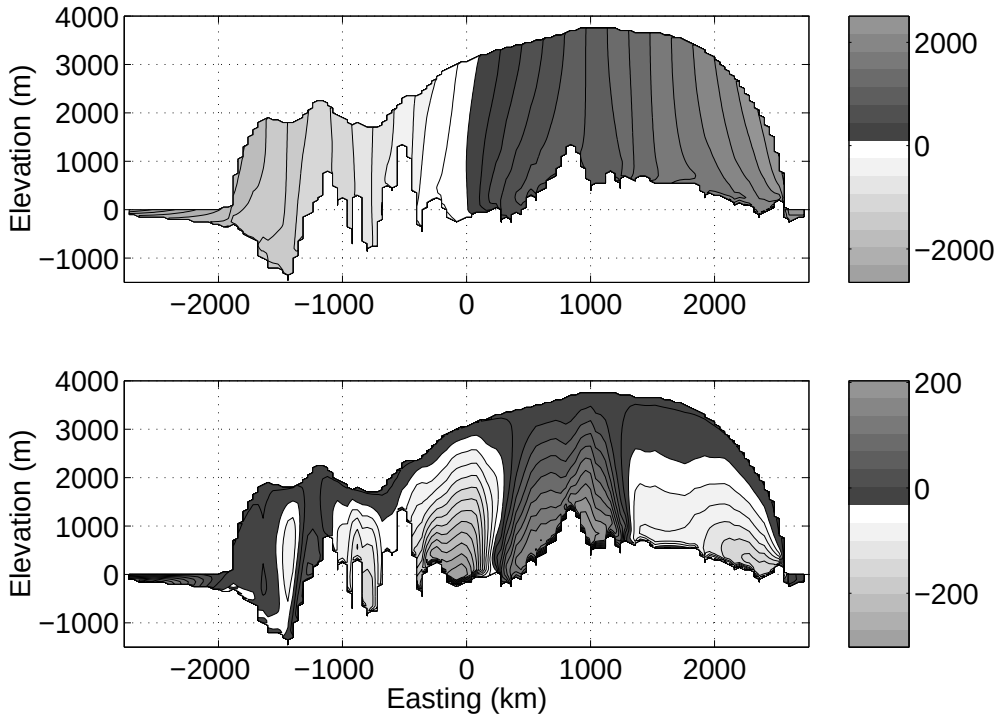

Figure 6.5: Cross section of provenance variables, along line E_2 (parallel to the X axis, through South Pole). The upper panels shows the X provenance ($x_{\rm d}$), the lower panel the Y provenance ($y_{\rm d}$). Easting corresponds to distance along the X axis.

The second cross section E_2, shown in Fig. 6.5, follows meridian 90°E (Y=0) and cuts through the West central ice divide, the Ross–Ronne saddle and continuously into the east side between Dome A and Vostok. Combination of the two panels again indicates that most of the ice flow is aligned with the Y-oriented surface topographic features, with a slight divergence in the X flow along the main west ridge, which coincides with a high subglacial mountain, and flank flow near the east side. Noticeably on the upper panel, despite the physical connection between the two ice sheets and the steep slope descending from the east side, there is no apparent sign of mixing between the two, no cross provenance. The lower panel also shows interesting flow patterns. Recalling the location of Dome A and the four ridges that drain it (Fig. 6.1), flow along and away from these

ridges is clearly manifest in the east part of cross section E_2, as central ice originates from Dome A, 200 km upstream, whereas ice on either side flows in the opposite direction because of the relative position of side ridges and E_2. This implies strong shearing along the Y component of the ice flow and large provenance gradient near X=300 km and X=1300 km, illustrating the advantage of using a semi-Lagrangian method to preserve such sharpness, rather than an Eulerian one.

The western part of the profile cuts through the Weddell side of the ridge divide; therefore all the ice shows an upstream origin near the ridge. Deeper layers seem to originate from even further. Comparison of surface topography at present (Fig. 6.1) and at $20\,\mathrm{kyr\,BP}$ (Fig. 6.3) shows that the glacial western divide was located slightly south of its modern position.

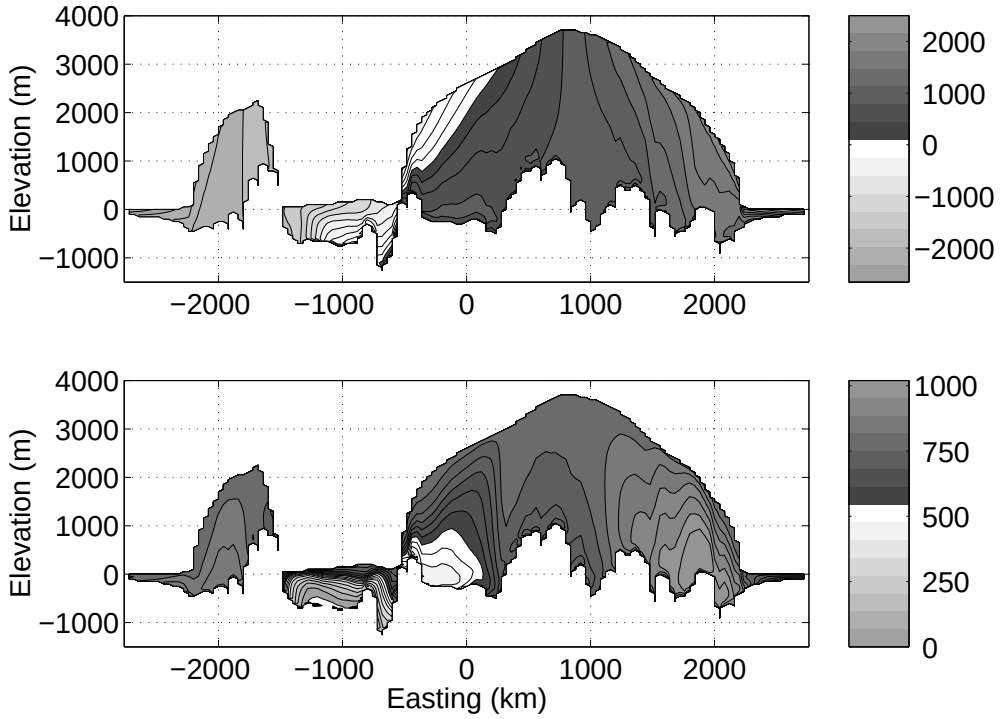

Figure 6.6: Cross section of provenance variables, along line E_3 (parallel to the X axis, near Vostok and Dome C). The upper panels shows the X provenance (x_d), the lower panel the Y provenance (y_d). Easting corresponds to distance along the X axis.

The third pseudo-east–west cross section E_3 shown in Fig. 6.6 cuts through the Antarctic Peninsula, the Ronne-Filchner Ice Shelf and the east Antarctic plateau between Dome Fuji and Dome A along Y=800 km. On the east side, the distribution of provenance labels is simpler than the previous lines because the pronounced east–west slopes on either side of the main divide drive ice flow. This effect is perfectly illustrated on the upper panel of Fig. 6.6 for the X component. In the lower panel, the highest contour centred at the divide corresponds to locally-deposited ice and embraces most of the ice in the central region. Ice directly below and westward has a southern origin from Dome A and the ridge between Dome A and the Transantarctic mountain range (Fig. 6.1), because most of the ice south of E_3 flows northward (along Y), as previously observed. The ice-shelf part of the profile gathers a wide range of depositional origins. The deepest ice comes from as far as the central west ridge, 800 km upstream (lower panel). Berckner Island, visible at X=–800 km and the loca-

tion of a new drilling site, appears to sample ice with a high provenance variability and should carry a strong flow signature, a potential complication for its interpretation. To the west, the Peninsula shows a slow and regular flow pattern with low X divergence oriented towards its northern tip and the Weddell Sea.

6.3.2 "North–south" profiles

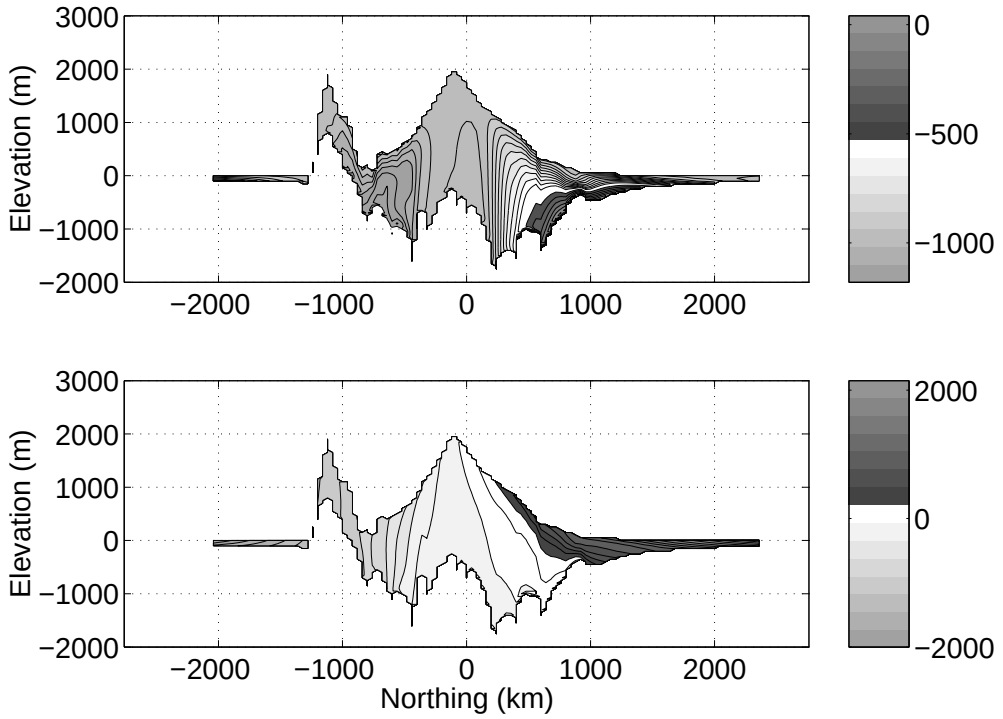

Figure 6.7: Cross section of provenance variables, along line N_1 (parallel to the Y axis, through Byrd). The upper panels shows the X provenance (x_{d}), the lower panel the Y provenance (y_{d}). Northing corresponds to distance along the Y axis.

Line N_1 traverses the West Antarctic Ice Sheet at X=–920 km through the Byrd drilling site, first hitting a mountain range, then nearing the western side of the Ross Ice Shelf enroute to Byrd (Y=–520 km), up to the ridge divide and down along the Ronne-Filchner Ice Shelf. In the lower panel of Fig. 6.7, the distribution of y_{d} illustrates the downward flow on either side from the central ridge. The upper panel accordingly shows limited cross flow in the central area and intense flank flow from the steep northern part of the Antarctic Ice Sheet pouring into the Ronne-Filchner Ice Shelf (origin of the deepest ice 900 km away).

Line N_2 (X=0) cuts through the Ross Ice Shelf, the Transantarctic barrier, the South Pole and the East Antarctic Ice Sheet. The lower panel of Fig. 6.8 shows weak north–south flow despite the steep slope immediately next to the mountain range. As illustrated in the upper panel, the ice flow regime for that part of the ice sheet is dominated by the slope on the side of the ridge between Dome A and Dome Fuji, which drains ice deposited up to 800 km away. Ice has a more local origin closer to the Transantarctic Mountains, as previously seen in line E_2. For the ice shelf, ice is pre-

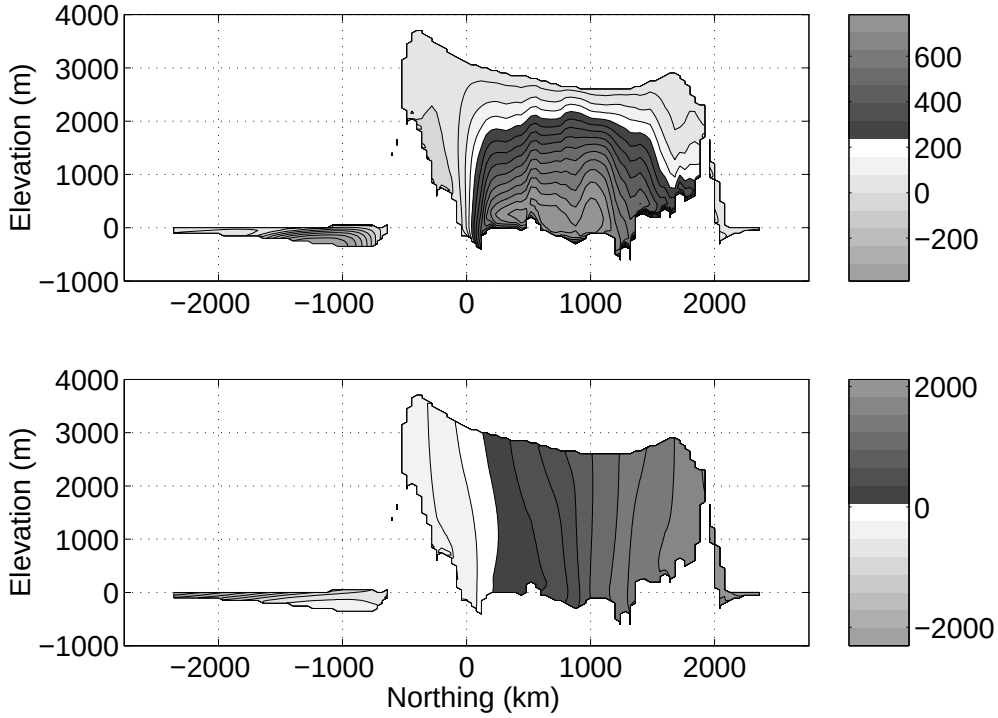

Figure 6.8: Cross section of provenance variables, along line N_2 (parallel to the Y axis, through South Pole). The upper panels shows the X provenance ($x_{\rm d}$), the lower panel the Y provenance ($y_{\rm d}$). Northing corresponds to distance along the Y axis.

dominantly coming from the central part of the West Antarctic Ice Sheet because the current spatial resolution of the ice sheet model (40-km grid) forbids any ice flow through the Transantarctic range, in contradiction with satellite interferometric measurements of ice velocity (Testut, 2000).

Line N_3 cuts through the East Antarctic Ice Sheet at X=1400 km close to the Vostok–Dome C ridge and downslope from Dome A and Dome Fuji. Fig. 6.9 shows that most of the ice flow for $Y \leq$–800 km is oriented in the X direction with a slow rate; thus, ice at Dome C (Y=–880 km) is mostly local. As the distorted contours of $y_{\rm d}$ in the lower panel suggest and a parallel section through Vostok confirms (not shown), deep ice at Vostok has a distant origin. This is caused by a pronounced flow in the Y direction between Vostok and Dome A because of the steep surface slope and the orientation of the central ridges (Fig. 6.1). Further north, though there is some Y divergence away from the domes, most of the ice flows from the Dome A–Dome Fuji ridge (deepest ice deposited $\sim$500 km upstream) and drains toward the Indian Ocean.

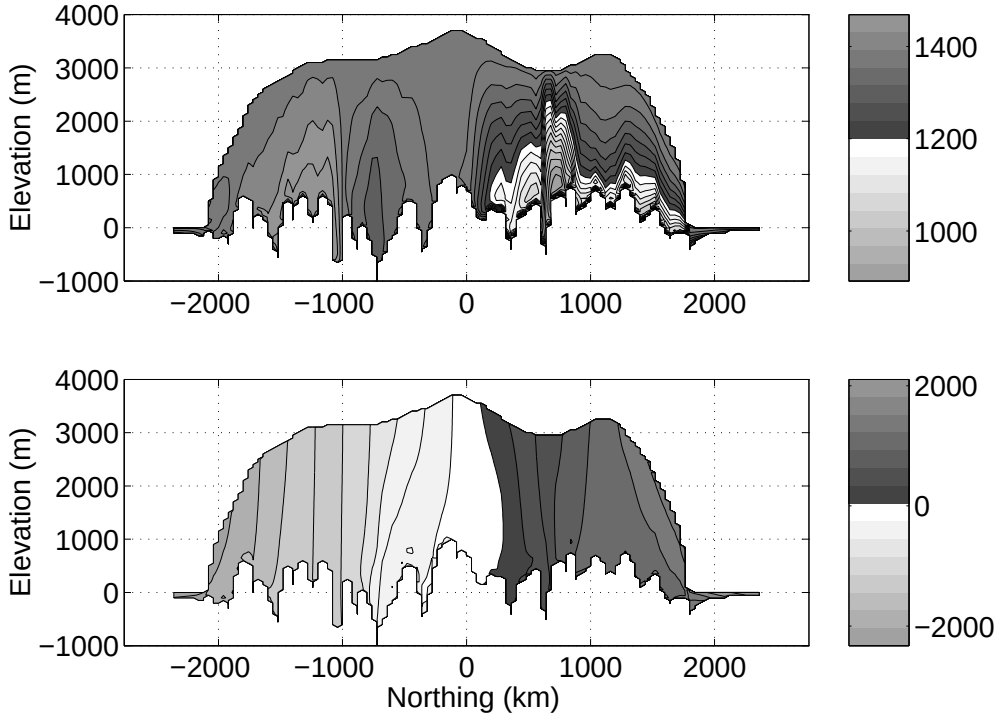

Figure 6.9: Cross section of provenance variables, along line N_3 (parallel to the Y axis, between Dome Fuji and Vostok). The upper panels shows the X provenance ($x_{\rm d}$), the lower panel the Y provenance ($y_{\rm d}$). Northing corresponds to distance along the Y axis. Vostok is locate at Y=–360 km, Dome C at Y=–880 km.

6.4 Deposition age

6.4.1 Age stratigraphy

Isochrones along the "east–west" transects show a regular vertical distribution of depositional age (Fig. 6.10). Bumps in these isochrones follow the underlying bedrock topography and become largely attenuated towards the surface. Most of West Antarctic ice is younger than 10 kyr, thus deposited during the recent warm Holocene period. In East Antarctica, the mid-ice-thickness isochrone corresponds to –75 kyr BP for the central part of the ice sheet, –50 to –20 kyr BP closer to the margins where strong accumulation rate and fast flow refreshes the upper ice layers more quickly, especially for the line E_1 where surface slope is the steepest.

Similar patterns are observed along the "north–south" transects shown on Fig. 6.11, where I also note that the ice in the shelves is no older than 10 kyr. Line N_1 through the West Antarctic Ice Sheet indicates an older average age than the other sections with a mid-thickness age of –20 kyr. This is explained by Fig 6.7 where we saw that most of the ice in the N_1 transect has a local origin, a sign of slow flow that preserves the old ice in place because of a lower surface slope than the other sections.

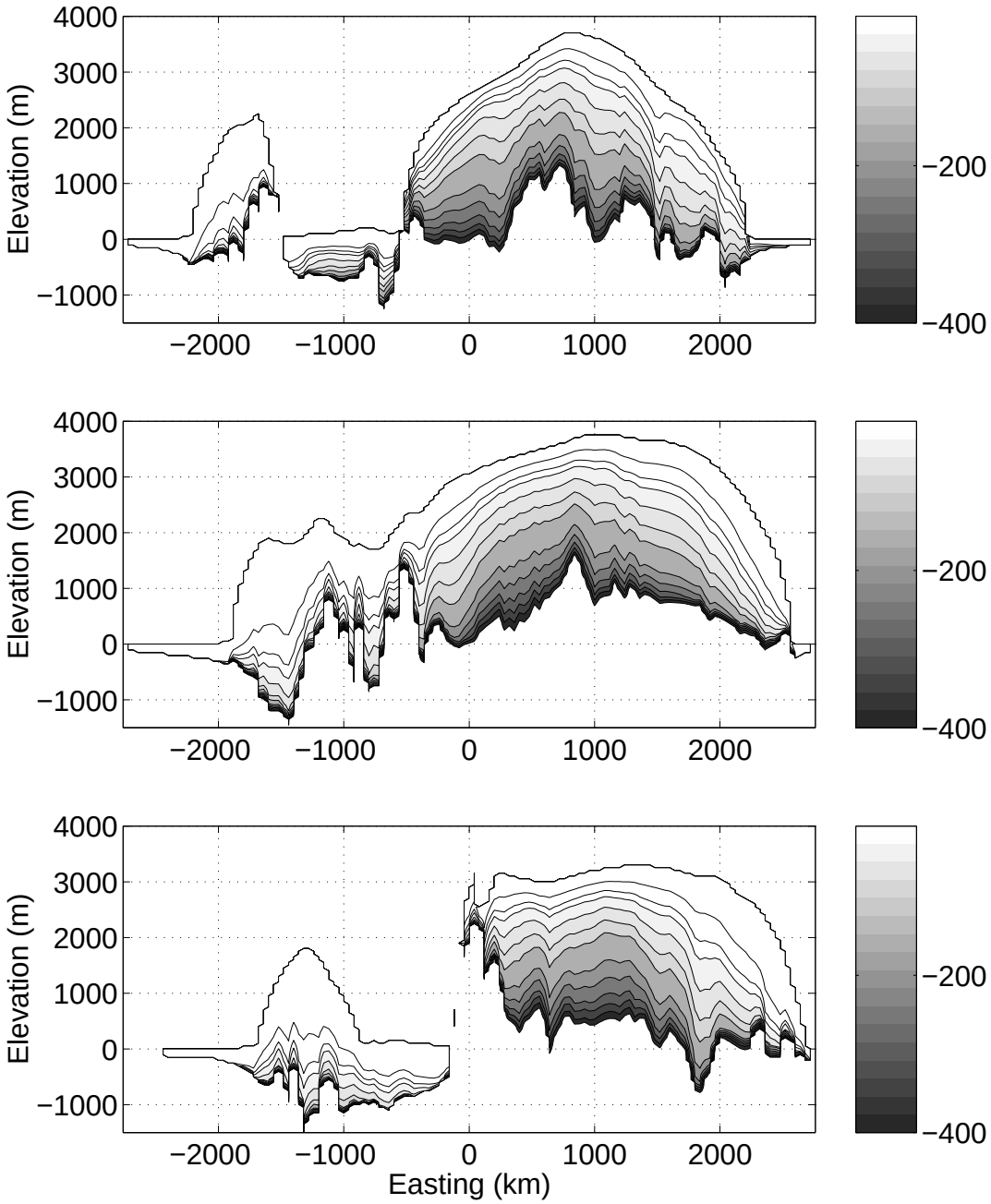

Figure 6.10: Cross section of depositional age (kyr BP, contours and colorbar) in the direction parallel to X: lower panel=E_1 (through Byrd), middle=E_2 (through South Pole), upper=E_3. Contour lines for 0, −10, −20, −30, −50, −75 kyr and every 50 kyr from −100 to −400 kyr BP.

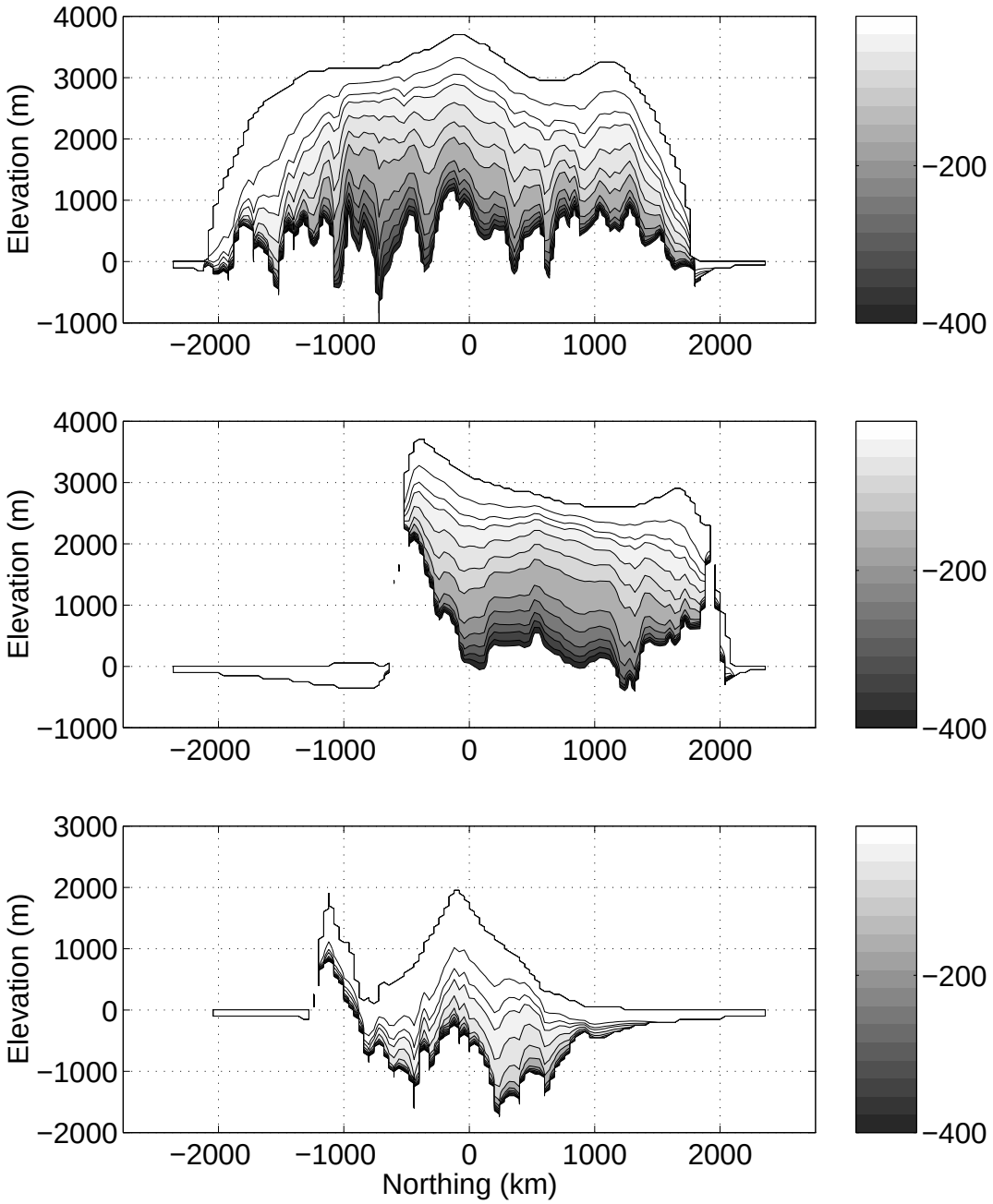

Figure 6.11: Cross section of depositional age (kyr BP) parallel to Y: lower panel=N_1 (through Byrd), middle=N_2 (through South Pole), upper=N_3 (through Dome C). Contour lines for 0, −10, −20, −30, −50, −75 kyr and every 50 kyr from −100 to −400 kyr BP.

6.4.2 Age of deep ice

The tracer transport model has the ability to predict where to encounter the oldest ice, a valuable diagnosis for exploring new ice core drilling sites. Fig. 6.12 presents the depositional date distri-

bution of deep ice located above the bedrock at 5% of the ice thickness. The oldest ice appears to concentrate in a crescent from Dome Fuji to Vostok through Dome A, and in the vicinity of Dome C. There are also small pockets of old ice in West Antarctica. That distribution can be explained by three factors. First, the crescent-shaped distribution of old ice corresponds to the ridge in the highest part of the East Antarctic plateau, a region where ice is the thickest, where surface accumulation is extremely low (less than 3 cm per yr at present) and ice flow is slow because of the negligible surface slope. All the conditions are gathered to ensure long preservation of local ice, up to 800–900 kyr as suggested by the recent Dome C ice core record (EPICA community members, 2004). Secondly, the age pattern shows a strong correlation with the bedrock topography map in Fig. 6.2, and thus with ice thickness. Large ice thickness and slow ice flow imply that ice gets trapped in bedrock depressions and remains there for long periods of time, the only removal factor being basal melting. A third favourable condition is my reduction of surface accumulation near the three deep ice core sites to correct the excessive rate predicted by the large-scale ice-velocity based distribution of Huybrechts et al. (2000). One may argue that I could have globally reduced surface accumulation rate in central Antarctica, but I found that such drastic measure slows down ice flow, contradicting observations reported by Huybrechts et al. (2000), and excessively lowers the whole Antarctic plateau. For instance, a 20% reduction provokes a 70–100 m lowering of elevation, whereas accumulation had to be reduced by $\sim$30% at ice core sites to match their ice stratigraphy and agree with present

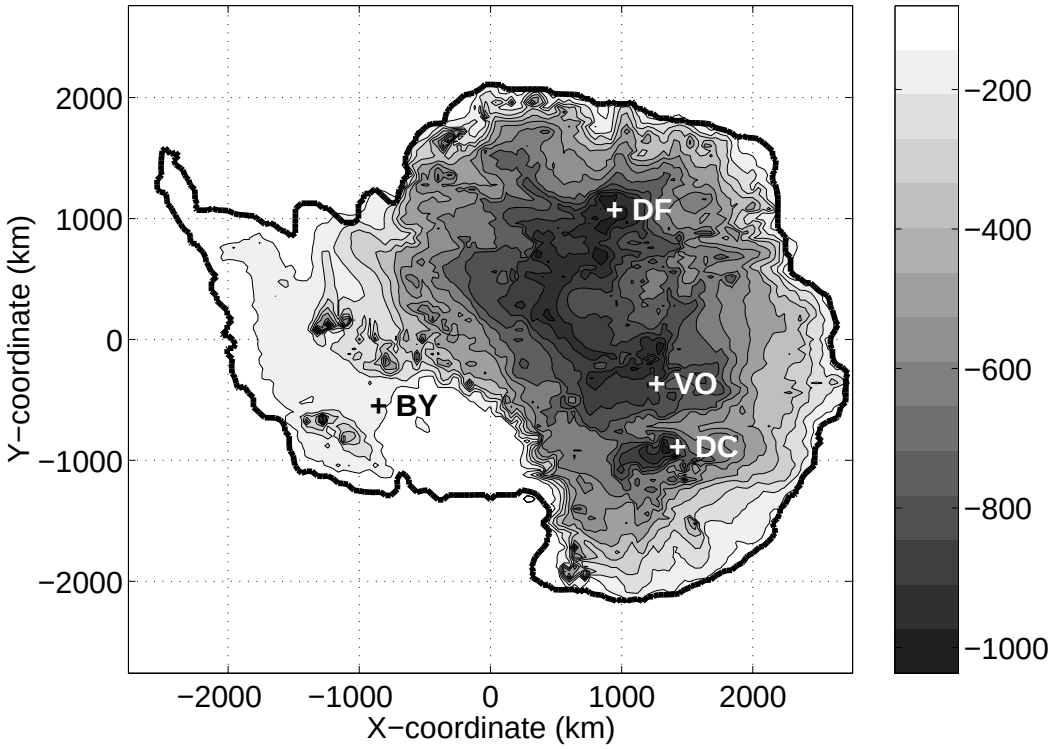

Figure 6.12: Depositional age distribution (kyr BP) at 5% of the ice thickness above bedrock.

observations. I believe that my local hand tuning is legitimate given the high spatial variability at short-distance scale of precipitation (because of redistribution by the wind) and the paucity of measurements at the surface of the ice sheet to validate any distribution of accumulation.

6.4.3 Average age of the ice sheet

Using the method described in Chapter 3 to derive the time-evolving global properties of an ice sheet, I calculate the average birth date of the ice sheets as a function of time for each ice mass and for the sum of both. The average birth date history is presented in Fig. 6.13 for the past 140 kyr to extend beyond the past interglacial period. The age of the entire Antarctic Ice Sheet is regulated by the influence of the overwhelming East Antarctic Ice Sheet, which explains the parallelism of the two lowest series of birth-date curves. The average birth date increases almost linearly with time because of the great stability of the East Antarctic Ice Sheet during the glacial–interglacial cycles. The much more dynamic West Antarctic Ice Sheet gets rejuvenated at the end of each of the past two glacial periods as it gets destabilized and loses much volume (Fig. 6.3) following the post-glacial rise in sea level and gets new ice because of increased precipitation rate in a warm climate. The present average age of the Antarctic Ice Sheet is –110 to –106 kyr; I find –127 to –124 kyr for the East Antarctic Ice Sheet and –45 to –43 kyr for the West Antarctic Ice Sheet.

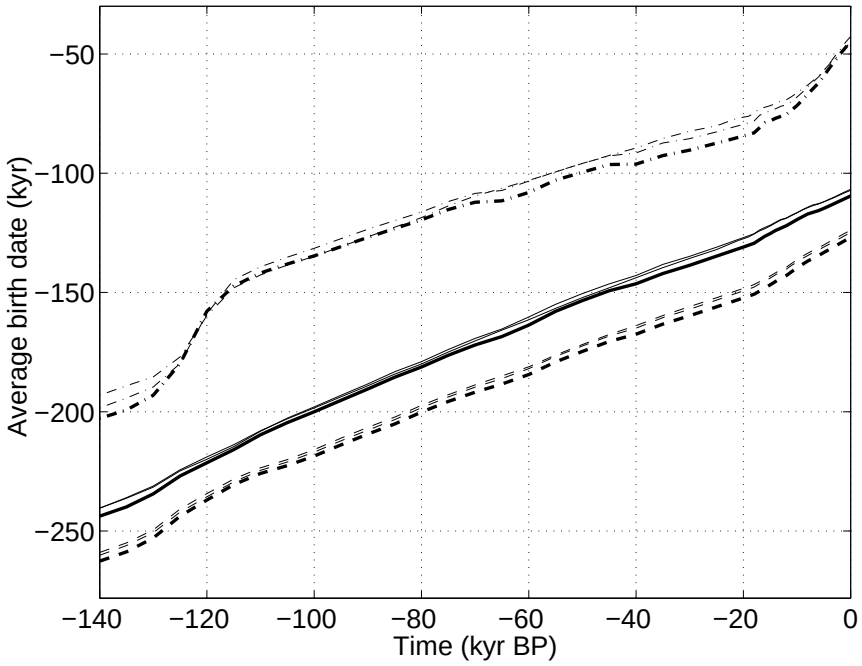

Figure 6.13: Average birth age of the Antarctic Ice Sheet (solid line), the East Antarctic Ice Sheet (dashed line) and the West Antarctic Ice Sheet (dash-dotted line) during the past 140 kyr for different experiments, the thickest line corresponding to the reference model T2, the others to T1 (youngest) and T2D.

6.5 Isotopic stratigraphy at ice core sites

The previous sections have illustrated the capability of the combined tracer transport and ice dynamics models to predict the time-evolving three-dimensional stratigraphy of the Antarctic Ice Sheet. I now make use of the proclaimed accuracy of the method to test the validity of the assumptions on the climatic and dynamic history of the Antarctic Ice Sheet by comparing the simulated fine layering at ice core sites and the actual ice core records retrieved at Dome C, Vostok and Dome Fuji. I choose not to present the Byrd record because none of my simulations achieved an acceptable

match with present surface elevation at the site, making comparison there pointless. The isotopic content of ice is derived from the past surface temperature and elevation according to the protocol presented in Chapter 3, using the modern water isotope values recorded at the sites rather than the global distribution to obtain better local accuracy.

Fig. 6.14 presents the predicted and measured water isotope profiles, offset to facilitate comparison, for δD at Dome C (EPICA community members, 2004) and Vostok (Petit et al., 1999), δ^{18}O at Dome Fuji (Watanabe et al., 2003). The predicted ice cores show remarkable agreement with the actual records in terms of matching the surface and bedrock elevation, the depth of climatic events as expressed in the isotopic signal and the amplitude of these isotopic excursions. The results are briefly described here to illustrate the power of the tracer method. Complete discussion and implications follow in the next chapter.

6.5.1 Dome C

The fit for Dome C is almost perfect over most of the depth of the borehole; the bottom variability is missing because the simulation only ran for 688 kyr; I provide instead the average value through the lowest layers. Achieving such an exact match is not trivial. As previously discussed for Greenland, the process of matching the isotopic profile at the site where the climate forcing originates is not a circular one because of the complex interactions between climatic variables (surface temperature and accumulation rate) and ice dynamics–thermodynamics variables (velocity and temperature structure) and the uncertainties on parameterizations such as that for the effective viscosity of ice (via the enhancement factor in the ice flow law), the basal sliding behaviour and the basal geothermal heat flow. The ice cores presented here are obtained with the model "standard" parameters and local refinements presented in the previous sections using the reference climate forcing T2. Fine tuning details and improvements are kept for the next chapter.

6.5.2 Vostok

Simulation at Vostok is also satisfying, especially when acknowledging the complexity of the flow (discussed in the next chapter), which makes the task of attributing adequate present reference surface precipitation rate along the flow line and contrast between past and present accumulation rate particularly delicate. There are differences at certain depths in the relative location of special events, for instance from 500 to 1000 m, because of the spatial irregularity of surface mass balance, or in the δD amplitude, for instance near 1500 m and during the last interglacial period, but resolution of these differences would require a level of fine tuning that currently remains out of reach given the computational burden of long term climatic simulations.

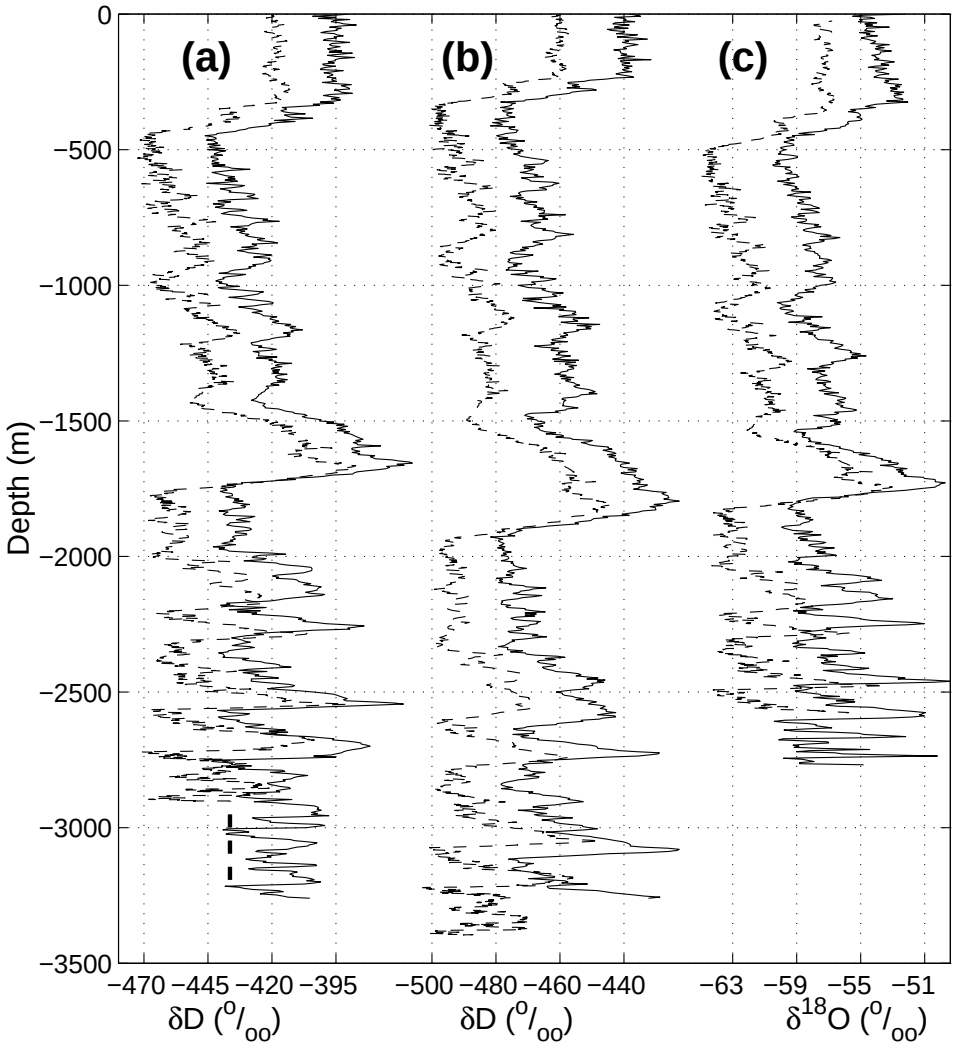

Figure 6.14: Simulated (dashed, left) and recorded (solid, right) ice core isotopic profiles in Antarctica, with offset for clarity of display. a. EPICA-Dome C with model T2. b. Vostok with T2 (longer modelled δ^{18}O-core than the actual record because the influence of Lake Vostok is not included in the ice sheet model.). c. Dome Fuji with T2A. Note that the actual record stops at 2503 m; the data presented underneath comes from Parrenin (*pers. comm.*).

6.5.3 Dome Fuji

The remote Dome Fuji record, 1500 km away from Vostok and 2000 km from the forcing site of Dome C, also displays acceptable agreement considering the simplicity of the climate forcing. The comparison is here possible because the record itself shows remarkable similarities with the two other deep ice core records, as noted by Watanabe et al. (2003), despite the large distance separating the sites, the isolating barrier made by the Dome A–Dome B "eastward" ridge (Fig. 6.1), and the probable exposure to different weather systems or moisture sources (different nearby oceans). Under these conditions the isotopic variability and the depth of most climatic events is reasonably matched, though peculiarities of the δ^{18}O signal, like the Holocene decreasing trend, fail to be

adequately captured.

6.6 Conclusion

This chapter shows that the time-evolving three-dimensional fine stratigraphy of the Antarctic Ice Sheet can be predicted with a combined ice sheet–tracer transport model. Using a rather simplistic climate parameterization, the model is capable of predicting the fine ice layering of the Dome C, Vostok and Dome Fuji ice core at most depths, a remarkable performance given the large distance separating those sites, the coarse spatial resolution of the ice dynamics grid and the treatment of the climate. This result confirms previous studies showing that similar climate change prevailed over most of the Antarctic Ice Sheet during the past three glacial cycles (e.g., Watanabe et al., 2003) and that models of ice sheet evolution can satisfactorily represent that variability (Ritz et al., 2001; Huybrechts, 2002).

Successful prediction at the ice core sites can be further used to examine the conditions under which ice was deposited, buried, deformed and transported to yield these records. In other words, the model has the potential to be directly used to interpret ice core records similar to simple flow dating models. This is the focus of the next chapter. The validated tracking method can be applied to any kind of non-diffusive property such as water isotope concentrations. This offers the possibility to assess the contribution of the Antarctic reservoir to the global hydrological cycle, the topic of Chapter 8.

CHAPTER 7

Simple vs. complex ice flow models for deep Antarctic records

7.1 Introduction

We saw in Chapter 6 that under favourable conditions the three-dimensional (3D) ice dynamics and tracer model can predict the fine layering of the ice core records from Vostok, Dome C and Dome Fuji. Accomplishing that task, though a necessary step to validate the global prediction of the Antarctic Ice Sheet stratigraphy, is also interesting because it relates our study to the task of interpreting these ice core records. With this parallel in mind, I shall particularly focus on the glaciologically based dating methods used as an alternative to annual-layer counting, a method which is practically useless for dating East Antarctic records because of the extremely low accumulation rate at these drilling sites. Glaciological methods involve the use of simple flow models with imposed surface elevation and velocity profile. Conveniently for the purpose of the following study, the Vostok, Dome Fuji and Dome C ice cores have been dated by the same model introduced by C. Ritz (1992) and recently developed and refined by F. Parrenin (2002). The following presentation will therefore emphasize their model, which I shall introduce in the next section.

Although results from the previous chapters suggest that 3D models could potentially be used to predict and interpret the fine stratigraphy of ice core records, there remain many valid reasons for using simpler flow models to perform that essential task. A quick comparison of the best features of each type of model shows for simple models that:

(i) they require shorter computational time, thus allowing increased spatial and temporal resolution, the use of Monte Carlo techniques and direct extraction of an optimum chronology;

(ii) Monte Carlo methods can help constrain poorly known parameters like basal melting and the amplitude of change between glacial–interglacial accumulation rate;

(iii) imposed geometry eases direct comparison of ice core stratigraphy from one simulation to the next whereas surface or bedrock elevation might change with 3D model.

In contrast, three-dimensional thermo-mechanical ice sheets models (ISMs)

(i) can compare several ice core sites with a single chronology at once;

(ii) calculate, instead of prescribe, variations in surface elevation as a result of the mass balance history and ice flow regime;

(iii) account for non-stationary effects like changes in the flow line;

(iv) include thermodynamical feedbacks on the ice flow so that the temperature history affects not only accumulation rate (Eq. 2.16) but also ice viscosity.

Using the 3D model, parameters and refinements introduced in the previous chapter, the following study aims to provide a detailed review of the climatic and ice-dynamic conditions revealed by the ice sheet model and compare these to those assumed or inferred by simple flow methods. Special attention will be given to the conditions of surface mass balance, ice depositional origin and elevation,

and to ice flow properties such as the vertical profiles of velocity and thinning so that the models can be thoroughly compared. Additional information on the sensitivity of the ice stratigraphy to model parameters and the study of other Antarctic ice cores are consigned to Appendix D.

7.2 Prediction of age–depth in an ice core

7.2.1 Ice flow dating model

The 2.5D glaciological model of Ritz (1992) was designed to date the Vostok ice core record by accounting for the significant transverse flow affecting the site without including all the complexity of a full blown 3D ice sheet model. The simpler design can be applied in inverse mode to interpret ice core records in a formalism described in Parrenin (2002). The ice flow model, like a 3D model, is based on the shallow ice approximation (Hutter, 1983); it assumes that the greatest surface slope upstream from Vostok can be used to locate the ice flow line and to compute the convergence and divergence of the flow along that line. The vertically integrated mass balance equation can then be written

$$\frac{\partial(\overline{U}_x H)}{\partial x} + \frac{H}{Y}\frac{\partial Y}{\partial x}\overline{U}_x = \dot{b} - \dot{f} - \frac{\partial H}{\partial t} \tag{7.1}$$

where x follows the flow line, Y is the distance between two parallel flow lines so that $1/Y\,\partial Y/\partial x$ is the inverse curvature radius of iso-elevation contours, e.g., positive in zones of diverging flow; $\overline{U}_x = 1/H \int_0^H u_x(z)dz$ is the average horizontal velocity, H the ice thickness, $\dot{b}$ the surface mass balance and $\dot{f}$ the basal melt rate. The model further assumes that the horizontal velocity profile obeys

$$u_x(x,z) = \Omega(\xi)\overline{U}_x = \Big(s + (1-s)\frac{m+2}{m+1}(1-\xi^{m+1})\Big)\overline{U}_x, \tag{7.2}$$

the vertical velocity profile at a dome follows

$$u_z(x,z) = \Big(\dot{b} - \frac{\partial H}{\partial t} - \dot{f}\Big)\,\xi\,\frac{m+2}{m+1}\left(\frac{\xi^{m+1}}{m+2} - 1\right) + \left(\dot{b} - \frac{\partial H}{\partial t} - \frac{\partial B}{\partial t}\right) \tag{7.3}$$

and supplementary terms are added for vertical velocity along a flowline (see Parrenin, 2002). The variable $\xi = (S-z)/H$ is the relative depth, s the basal sliding rate and m a shape parameter that depends on basal temperature gradient and the ice flow law exponent.

Because the layering of ice cores is directly controlled by surface precipitation (the climate is too cold for any surface melting), the dating model assumes a parameterized relationship between the measured isotopic ratios and past precipitation rate via surface temperature, which is only a byproduct of the method (no thermodynamical coupling of the flow law). An inverse method then recovers the optimum values of s, m and the precipitation parameters in a scheme that forces the timescale inferred from the ice core to match special dated events in the past within a pre-defined time window. Practically, ice particles are transported backward until they reach the surface at a time that indicates their age; the computational grid is 10-km across and uses 41 vertical levels whereas the ISM uses a 40-km horizontal resolution with 21 points in the vertical.

The method was simplified to a pure one-dimensional vertical flow to obtain the official timescale of the Dome Fuji (Watanabe et al., 2003) and Dome C (EDC2, EPICA community members, 2004) records. The chronology of the three major east Antarctic records is presented in Fig. 7.1. There

remain visible discrepancies for the timing of particular events, for instance the interglacial periods (120, 330 and 400 kyr BP) which stimulates further studies such as this one.

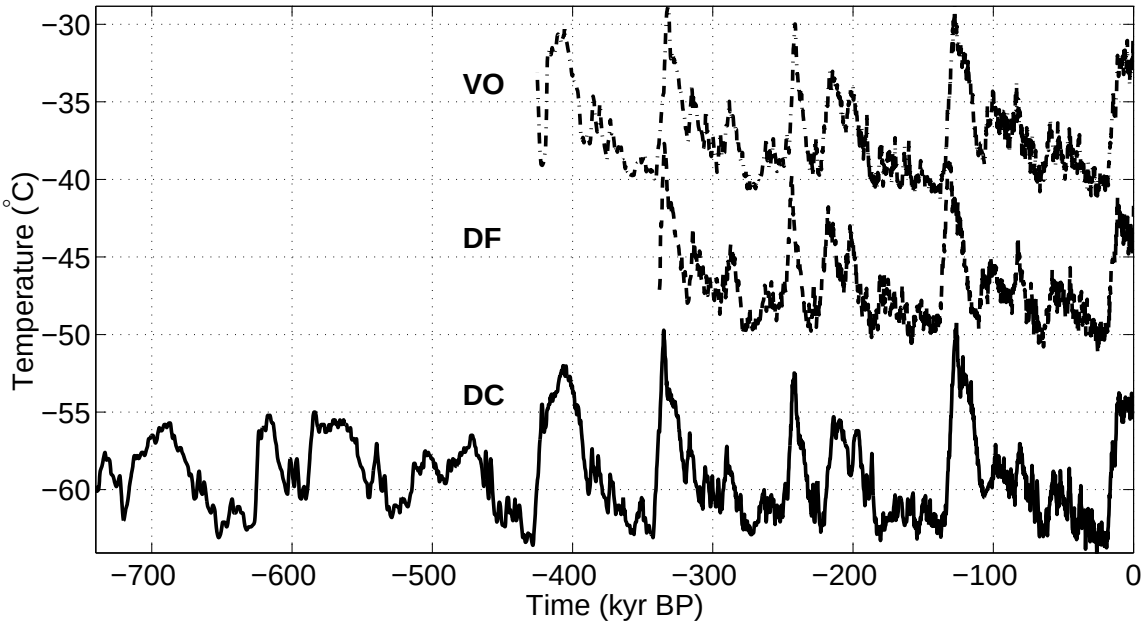

Figure 7.1: Time scales of Antarctic climate records from EPICA-Dome C (solid line, EPICA community members, 2004), Dome Fuji (dashed line + 15°C, Watanabe et al., 2003) and Vostok (dash-dotted + 25°C, Parrenin et al., in press) interpreted here in terms of temperature with an offset for clarity of display.

7.2.2 Age–depth for the ice sheet model

As seen in Fig. 6.14, the ice sheet and tracer transport model is capable of simultaneously and accurately matching the ice core layering for the three sites with a simple climate forcing (T1–T2 with special modulation T1A–T2A near Dome Fuji). The task is however non-trivial because of the particular parameterization of ISMs and because their non-linear sensitivity to climatic and dynamic variables introduces feedbacks that are ignored by simpler dating models. For an ISM, the main control on ice layering is the large-scale temperature change ΔT_{c} instead of precipitation because temperature determines both surface mass balance over the entire ice sheet (via the parameter D_{acc}, Eq. 2.16) and ice viscosity. This effect gets amplified as temperature modulations of the spatial distribution of precipitation and topography can induce variations of the ice flow pattern between glacial and interglacial periods, causing domes or flow lines to migrate. This motivated the refinements of regional surface temperature and precipitation rate and basal topography detailed in Section 6.2.1; the particular influence of each parameter is further discussed in Appendix D.1.

Detailed comparison of the stratigraphy of Dome C presented in Fig. 6.14 and predicted with the dating model and the ISM shows close agreement of their age–depth profiles: within 200 yr for the upper 500 m of the core (last 20 kyr), up to within 800 yr at 1700 m (last 130 kyr) and 5 kyr at 2600 m (last 350 kyr). The lowest section of the simulated cores is older than the age inferred for EDC2 and reaches 1040 kyr at the bedrock whereas EDC2 expects basal ice approaching $\sim$960 kyr. This shows that the overall age difference at any depth between the simple and complex models

is relatively low, an expected result given the use of similar climate forcings (details about the particular accumulation rate are exposed in the following section).

The predicted and observed depth–δD profiles at Vostok show remarkable agreement (Fig. 6.14), which implies that the age–depth relationship predicted by the ISM with the EDC2 timescale can be applied to date the Vostok record. This illustrates the potential to reconcile multiple ice core records on a single timescale. Comparison of the EDC2-forced age–depth profile to that directly inferred for Vostok (Parrenin et al., in press) shows a difference of less than 300 yr for the upper 300 m of the core (last 16 kyr) and less than 2 kyr for the upper 2300 m (last 180 kyr). Differences between the predicted and observed depth–δD profiles increase at greater depth, partly because of subtle errors in accumulation rate (especially for T1), but also because the effects of Lake Vostok on ice flow (no basal drag, flattening of the surface) and regelation are not included in the model. Thus the ISM predicts much older basal ice.

Close fit of the predicted and observed depth–δD profiles at Dome Fuji (Fig. 6.14), which involves special regional tuning of the accumulation sensitivity (climate forcing T1A and T2A with D_{acc}=$0.070\,\mathrm{K}^{-1}$), also suggest the possibility of using the EDC2 timescale for this remote ice core record (2000 km away from Dome C). There the age–depth misfit between the EDC2-based prediction and the published chronology of Dome Fuji lies within 500 yr for the upper 500 m (last 20 kyr) of the core. The difference with model T2A (the one displayed) remains within 1 kyr for the next 1100 m and within 5 kyr down to 2500 m below the surface ($\sim$360 $\mathrm{kyr\,BP}$), while for T1A the depth–δ^{18}O and depth–age misfits linearly increase with depth, e.g., age is underestimated by $2.5\,\mathrm{kyr}$ at 1000 m and up to 10 kyr at a depth of 2000 m ($\sim$160 kyr BP). Age and δ^{18}O below $2500\,\mathrm{m}$ are predictions from Parrenin (*pers. comm.*), the actual record stops at 2503 m (Watanabe et al., 2003). These results illustrate again the potential to unify the Antarctic timescales and resolve the peculiar time discrepancy between EDC2 and Dome Fuji for MIS 5.

7.3 Depositional conditions for the deep East Antarctic records

7.3.1 Surface mass balance

Combining the tracer transport and depositional archive, the history of surface mass balance for the simulated ice cores can be recovered. Mass balance is a critical variable because it determines the feeding regime of the ice sheet, thus the velocity at which ice has to be evacuated from its depositional site and ultimately the ice stratigraphy. The following presents the depositional mass balance for the Dome C, Vostok and Dome Fuji records while dynamical implications like thinnings for the ice sheet and dating models are discussed in a later section.

For Dome C, the EDC2 accumulation rate history (EPICA community members, 2004) was originally applied at and near the site. Recognizable δD layers appeared slightly too deep in ISM-predicted ice cores despite multiple trials tuning dynamical paramaters, regional distribution of precipitation and bedrock topography. The accumulation rate was finally reduced by 4% for the most recent 20 kyr and by 9% for older periods in order to match the age–depth profile presented in Fig. 6.14 and discussed in this and the previous chapter. The resulting surface mass balance history is illustrated for the past 150 kyr in Fig. 7.2 and compared to EDC2.

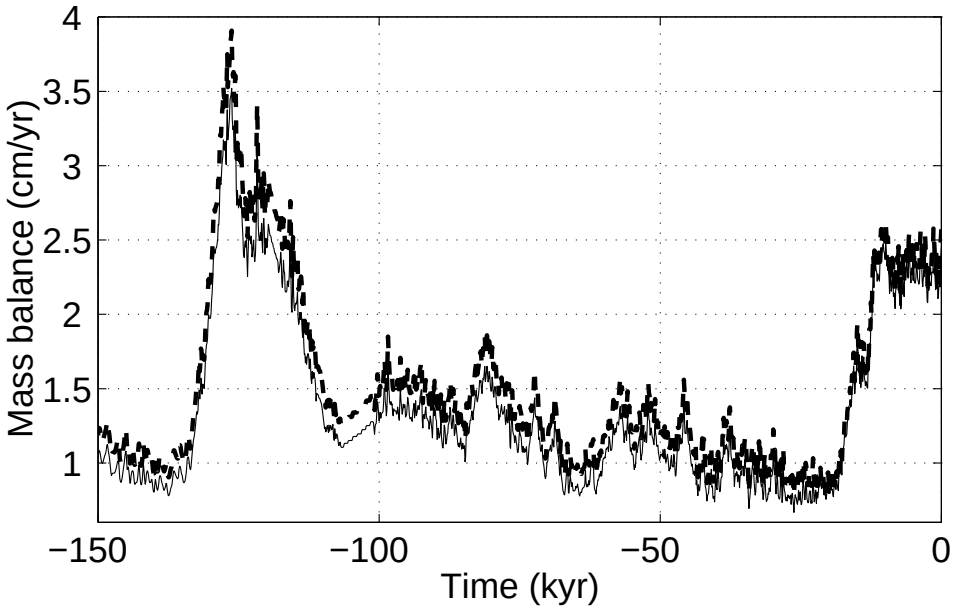

Figure 7.2: Accumulation rate at Dome C: inferred from core with 1D model (EDC2, thick dashed line), used by ISM to match the ice core (same for T1 and T2, thin solid).

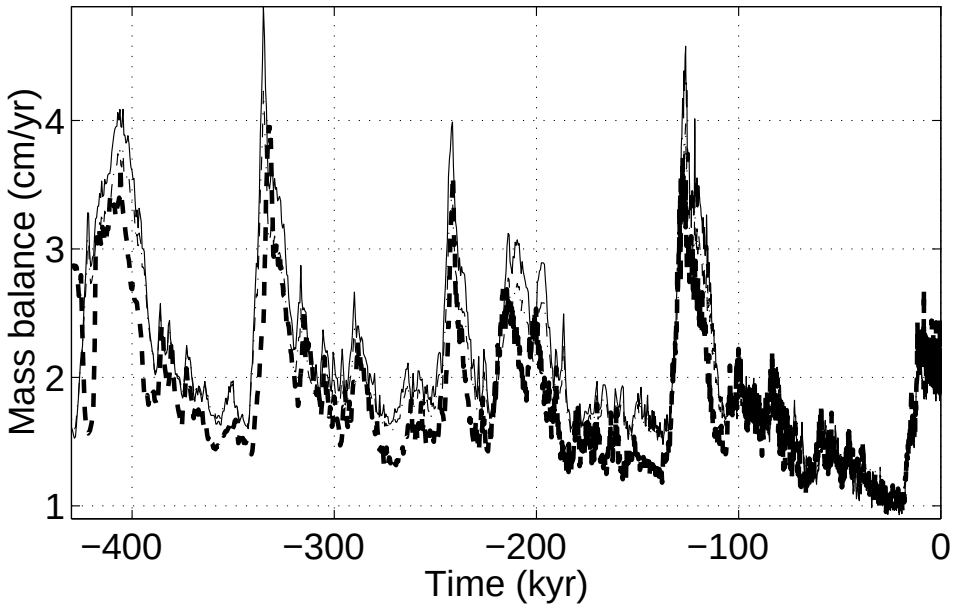

Figure 7.3: Accumulation rate at Vostok: inferred from core with 1D model (thick dashed line), used by ISM to match the ice core for T1 (thin dash-dot) and T2 (thin solid).

The well-known distant-ice-origin effect at Vostok (e.g., Ritz, 1992) complicates the task of assigning the optimal accumulation history to match the record. For the parameterization of the ISM, precipitation at the surface of the ice sheet is proportional to the present distribution and is also temperature-dependent (Eq. 2.16). At a site with such distant ice origin, the final ice layering

can be altered not only by precipitation rate along the flow line but also basal sliding and basal melting, in addition to other large-scale effects like the broader distribution of surface precipitation (e.g., global reduction). Fig. 7.3 shows that the paleo-mass balance of the ice sheet–tracer model is fairly similar to that inferred from the 2.5D model (Parrenin et al., in press) for the most recent $100\,\mathrm{kyr}$ and by up to 25% for older periods.

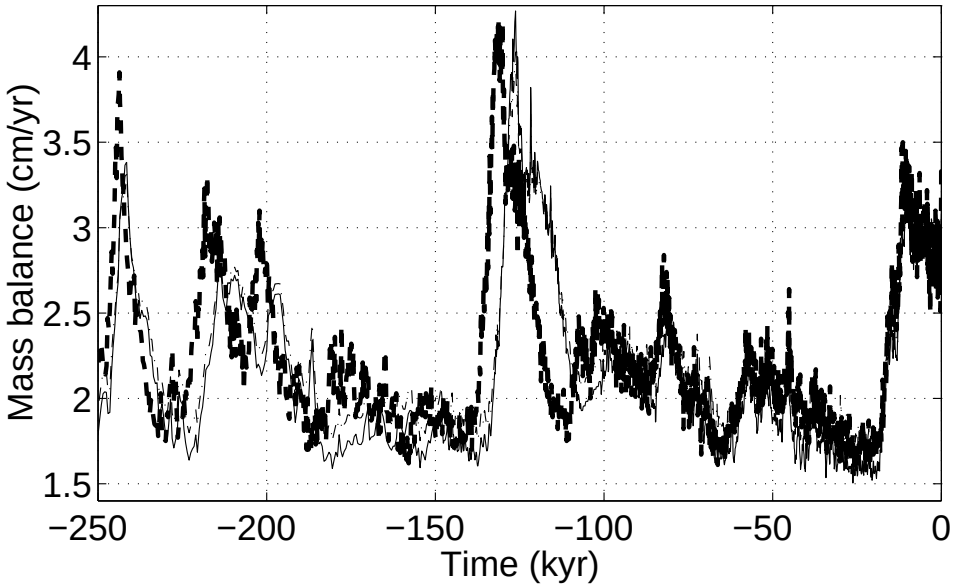

Figure 7.4: Accumulation rate at Dome Fuji: inferred from core with 1D model (thick dashed line), used by ISM to match the ice core for T1 (thin dash-dot) and T2 (thin solid).

At Dome Fuji, the ISM predicts lower accumulation rate than the 1D dating model at all times (Fig. 7.4). Several factors contribute to that effect. Firstly, the published chronology is older than EDC2 for the last interglacial period; thus, the ISM requires higher accumulation rate prior to that period to match the depth–δ^{18}O profile. Secondly, the accumulation sensitivity (D_{acc}) was modified to match the present surface elevation and depth of recorded climatic events without altering any large-scale uniform dynamic parameter (section 6.2.1). That choice might be wrong because other local physical processes like geothermal heating could yield the same desired effect. The current parameterization of the ISM cannot however handle spatially-varying bedrock properties yet (also discussed in Appendix D.1). Lastly, the δ^{18}O record of Dome Fuji shows a stronger cooling trend than EDC2 during the Holocene. Because δ^{18}O and precipitation co-vary in both dating and ice sheet models, accordingly their resulting mass balance histories differ (not conspicuous in Fig. 7.4).

7.3.2 Ice origin

Dating models assume a purely local source of ice at modern dome sites or a trajectory following the presently-observed topography. Three-dimensional time-evolving tracers can assess the long term stability of ice flow because the depositional origin of the predicted ice cores can be directly obtained from the tracer transport model. Fig. 7.5 shows the depositional origin for the simulated ice cores relative to their drilling site, along with labels displaying the approximate time of deposition. Tracers confirm that most of the ice at DC has a local origin: less than 80 km for the oldest ice, less

than 40 km for the last 200 kyr. As previously mentioned, the ice sheet model does not predict a dome at the modern site but a slow large-scale flow downstream from Dome A and through Vostok, though that flow can be countered or deflected during glacial periods, when a small dome grows near Dome C (e.g., at LGM, Fig. 6.3). In contrast, Dome Fuji remains very stable in the ice sheet model: its ice was deposited within 5 km for the past 700 kyr.

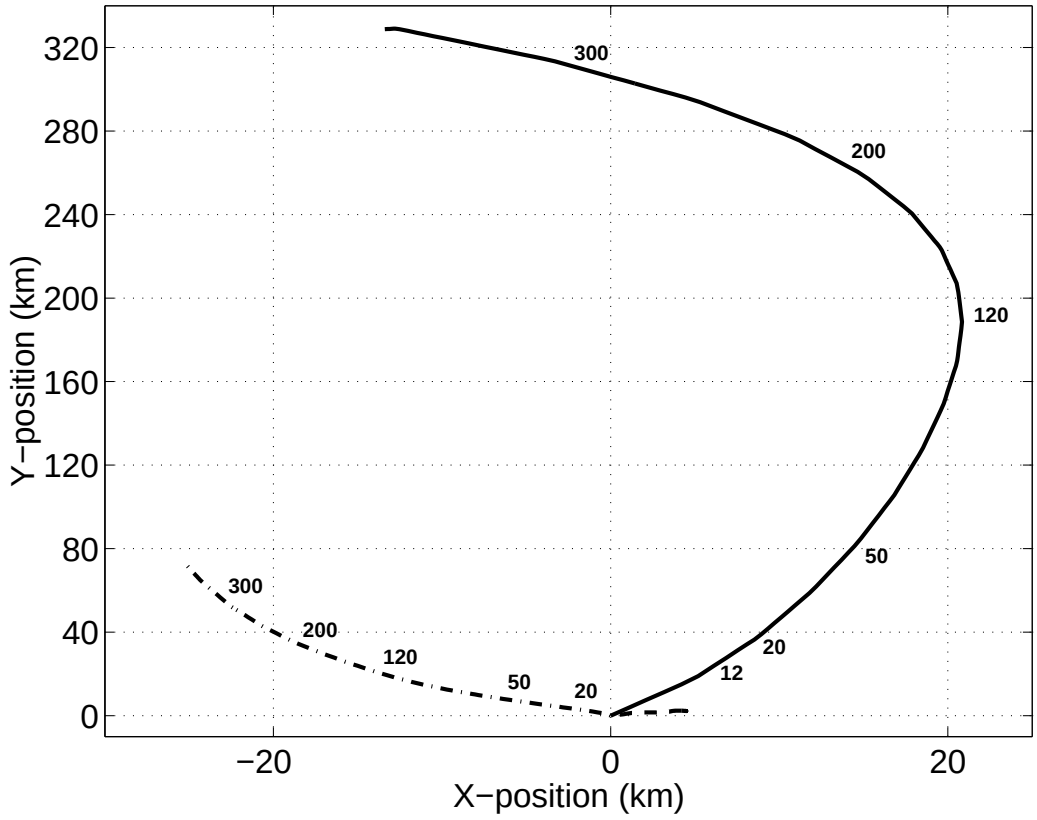

Figure 7.5: Distance from the depositional origin in the simulated ice cores at Dome C (dash-dot), Vostok (solid) and Dome Fuji (dash, the shortest). Attention, a different scale applies to each axis. Numbers along the lines indicate the depositional date of ice in kyr.

For Vostok, the distant origin of the oldest ice from Ridge B, 300 km upstream, is well predicted. Considering the time markers in Fig. 7.5, ice from the last interglacial period appears to be deposited $\sim$200 km upstream from Vostok, whereas the oldest ice originates only 100 km higher upstream, implying an acceleration of ice flow for the most recent period. The shape of bedrock topography, shown in Fig. 7.6 (thick bottom dash-dot line), provides a direct explanation for that effect. The rise of a 1500 m-high mountain above a deep valley 150–200 km upstream from Vostok sharply reduces ice thickness from 3700 m to 2000 m and slows down ice flow, as evidenced by the (not conspicuous in Fig. 7.6) steepening of surface slope downsteam from the mountain. Though spectacular in Fig. 7.6, this subglacial feature corresponds to a mere 4% bedrock slope when the difference in scale is taken into account (1500-m change in elevation over a 40 km horizontal distance); thus, the shallow

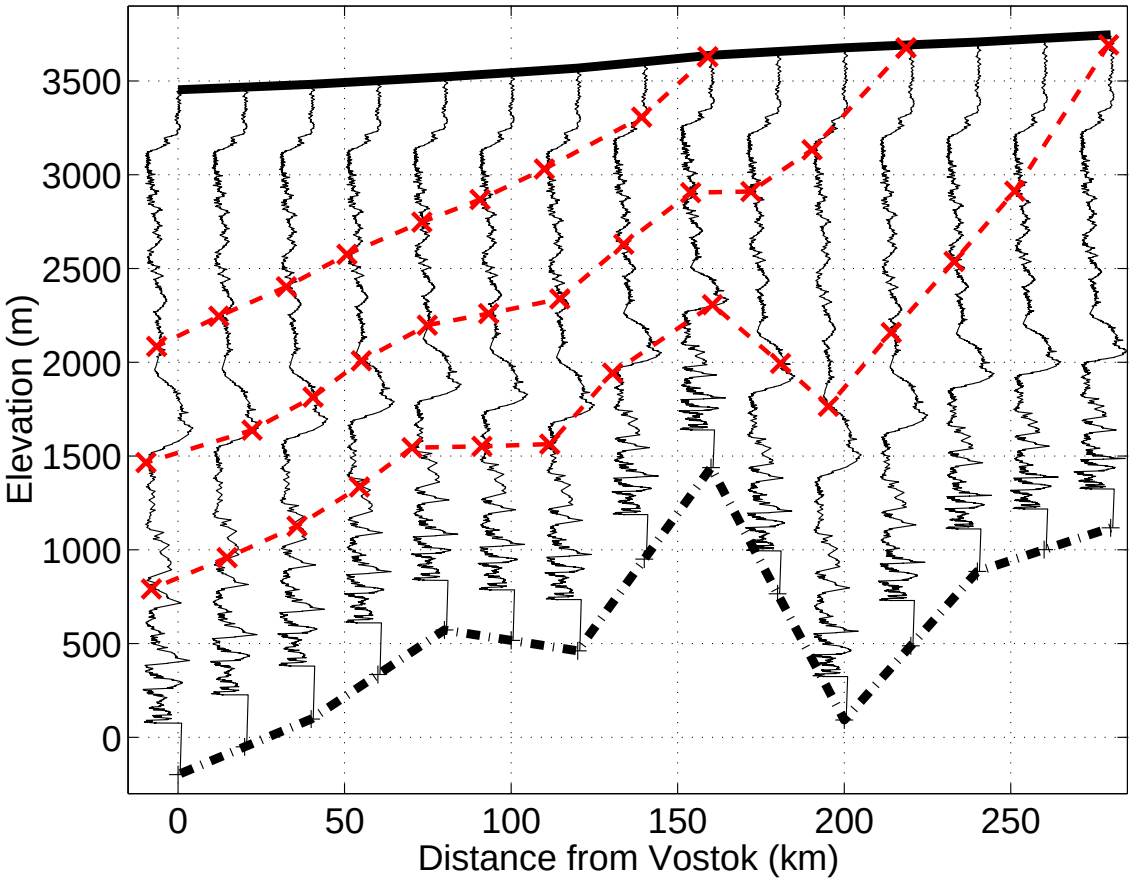

Figure 7.6: Flow line from Ridge B (right) to Vostok (left) with simulated ice cores every 20 km (40-km computational grid). Variations (of δD) along the simulated cores are synchronous and can be considered as isochrones. Dashed lines represent iso-origin contours for ice deposited 160, 200 and 280 km upstream from Vostok.

ice approximation used in both ice sheet and dating models remains valid. Comparison with radar profiles (Siegert and Kwok, 2000) also shows that the 40-km horizontal resolution catches the main features of bedrock spatial variability along the flow line, thus qualifying the ISM for a qualitative analysis of the subglacial topography effect on the Vostok record.

Fig. 7.6 shows a cross section of ice along the Ridge B–Vostok flow line at present, with fictional ice cores along the line to represent the ice layering and help identify isochrones. Present iso-origin curves of ice deposited 160, 200 and 280 km upstream are superimposed with dashed lines relating ice of similar geographical origin. This would be equivalent to the trajectory of ice in the Vostok core if ice flow had been in a steady state for the past 400 kyr (i.e., constant climate).

7.3.3 Paleo-elevation of depositional ice

Models used for dating ice core records generally rely on a pre-defined surface elevation history, assuming either no changes, or variations predicted by previous ice sheet modelling studies (e.g., Ritz et al., 2001). The depositional elevation of ice from the simulated ice cores is shown in Fig. 7.7. The modelled semi-local origin of ice at Dome C and Dome Fuji implies that the depositional

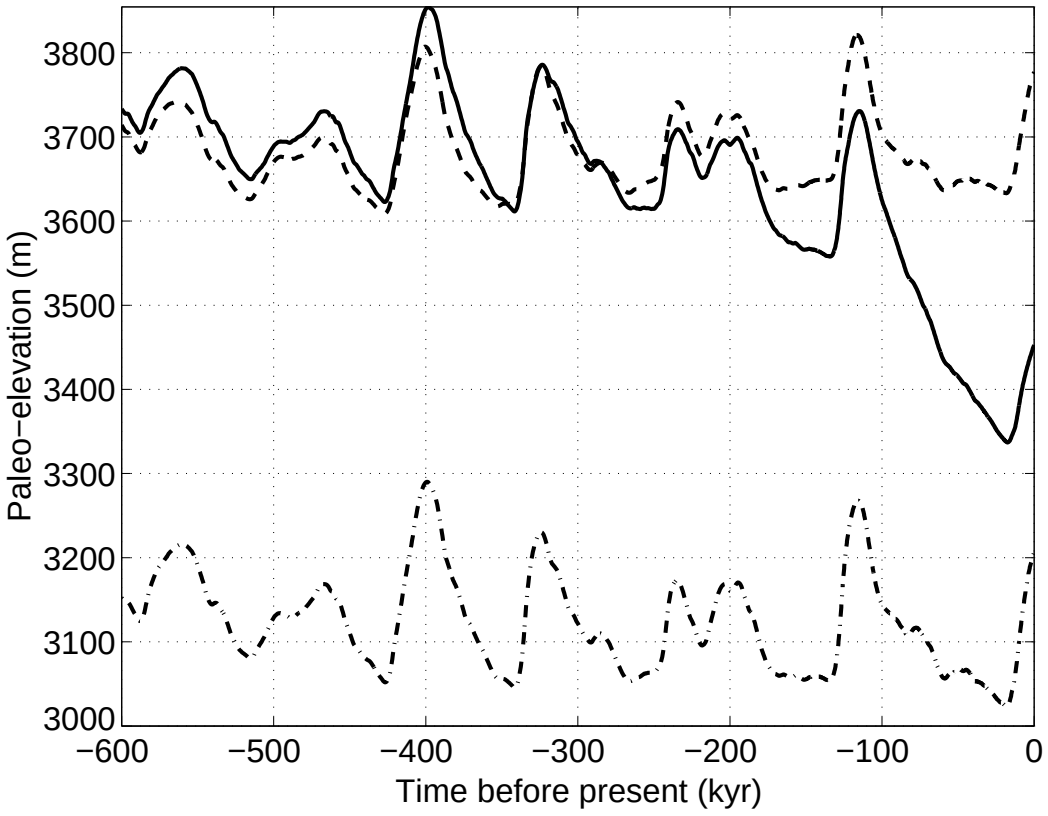

Figure 7.7: Depositional elevation for Dome C (dash-dot), Vostok (solid) and Dome Fuji (dash) predicted by the ISM using the T2 climate forcing .

conditions of ice are similar to the conditions at the sites. This observation is only valid for the most recent part of Vostok history. Depositional paleo-elevation is illustrated in Fig. 7.7 for the climate forcing T2, similar in effect to T1. The difference between present elevation and 20 kyr ago ranges from $\sim$100 m at Vostok and $\sim$120 m at Dome Fuji to $\sim$170 m at Dome C, which is a 60–80% larger amplitude than the elevation history of Ritz et al. (2001) that was prescribed to obtain, for instance, EDC2. The difference can be attributed to the accumulation forcing: Ritz used an accumulation sensitivity D_{acc}=0.070 K^{-1} that I tested and found incompatible with the age–depth profile at Dome C, whereas the EDC2 accumulation rate corresponds to a larger contrast between glacial–interglacial periods (D_{acc} $\sim$0.085–0.100 K^{-1} for T2 and T1) and implies larger variations of the surface elevation. Ideally, our results could be employed to iteratively improve dating of DC by incorporating the three-dimensional feedback of the ice sheet. Though such application is practically limited by the time-cost of running the ice sheet model over long periods of time, variations of depositional elevation could be prescribed to the dating model, either directly, or through a conceptual model that would represent the relationship between variations of elevation and precipitation rate at a given site evidenced by the ISM. Such an approach is justified by the observation that the elevation history is correlated with low frequency variations in the δD signal because changes in surface elevation follow variations in surface accumulation, which depend on temperature (Eq. 2.16), as does δD.

There is however a time lag, illustrated here for the last glacial termination and the twofold increase of precipitation in Fig. 7.8, because of the slow dynamical feedback of three dimensional ice flow.

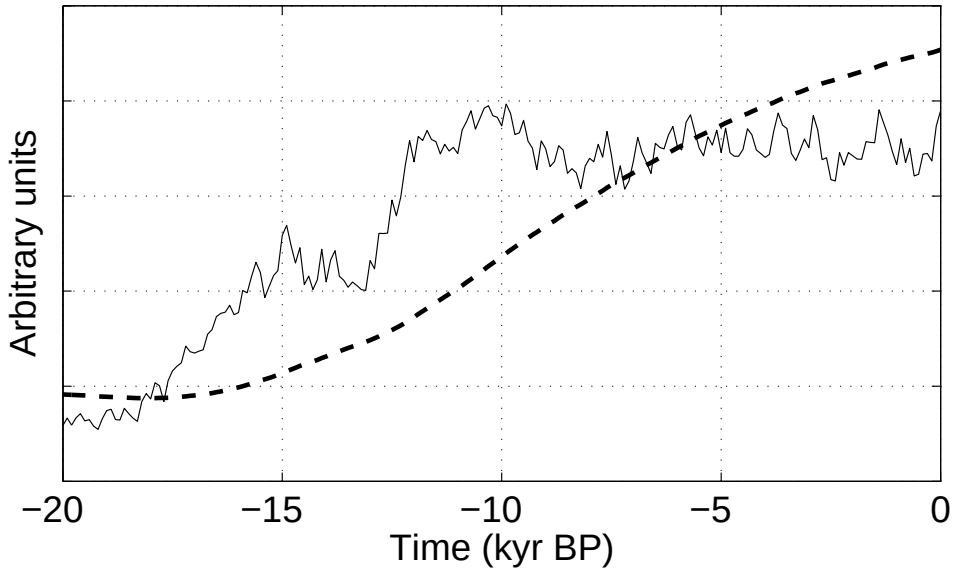

Figure 7.8: Surface mass balance (thin solid) and delayed change in surface elevation (thick dash) at Dome C simulated by the ISM using climate forcing T2.

In terms of amplitude, using the paleo-oceanographic terminology to identify past interglacial periods (Marine Isotope Stage=MIS), I find that past elevation at Dome C and Dome Fuji is higher than during MIS 5, 9 and 11, corresponding to higher δD than present, and accordingly lower during MIS 7, 13 and 15. Fig. 7.7 also shows large variations in the depositional elevation of Vostok ice caused by the distant origin of ice. A rapid 350-m drop from 120 kyr to 20 kyr ago is absent in the δ^{18}O signal, a contradiction with the usual spatial isotopic variation pattern. This is believed to be caused by a regional anomaly that effectively reduces the local isotopic lapse rate along the Vostok flow line (Petit et al., 1999). That large variation in elevation is however recorded in the gas content of air bubbles (Raynaud et al., in prep., of which I am a co-author). The combination of tracers with an ice dynamics model thus allows us to deconvolve the non-linear effects of (1) remote ice origin, (2) changes in depositional paleo-elevation along a surface that varies locally because of the surface slope and globally because of large-scale changes climatic conditions and (3) the non-trivial surface accumulation pattern (Parrenin, 2002), all of which complicating the task of accurately dating the Vostok ice core.

7.4 Internal ice flow properties at deep ice core sites

7.4.1 Thinning

The thinning $\tau(z)$ of an annual layer of ice at depth z below the surface can be defined as $\tau(z) = \omega(z)/\omega_\circ$ with $\omega_\circ$ the initial thickness of that ice when it was deposited (equivalent to surface accumulation) and $\omega(z)$ its thickness at depth z. In that manner, thinning is equal to 1 at the surface and generally decreases with depth as layers get compressed, especially at dome sites. Though confusing because one would intuitively think that thinning would increase with depth (with the definition

$1-\tau$), I adhere to the initial definition in order to directly compare my results with those of Parrenin (2002) and Parrenin et al. (in press).

Fig. 7.9 shows the thinning rates predicted by the ice sheet model (thick curves) and the one-dimensional flow dating model of Parrenin (nearest dash-dotted curves) for Dome C and Dome Fuji. The 1D model produces a smooth monotonic trend for both ice cores, except for a small bump for

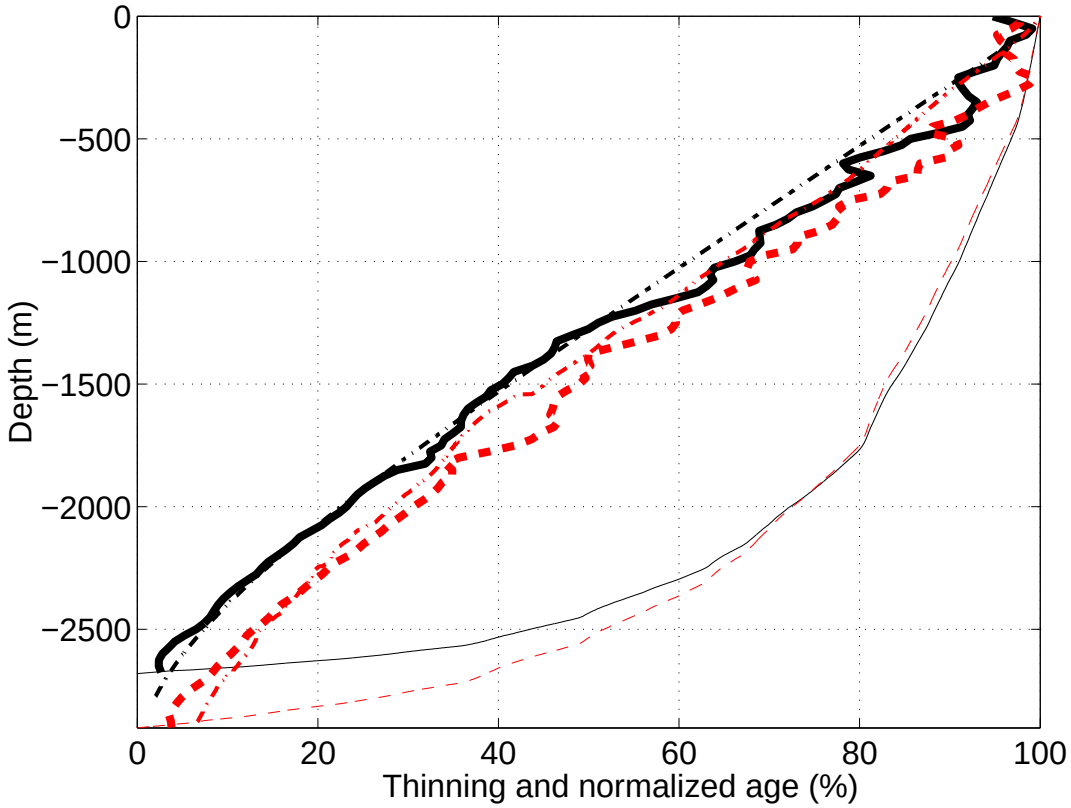

Figure 7.9: Thinning and normalized age (expressed in %) for the Dome C and Dome Fuji cores; Dome Fuji is the shallowest core. Prediction with the ISM at Dome Fuji are represented by the thick solid curve (climate T1A, T2A similar in effect); normalized age in thin solid; predicted thinning by 1D model used for Watanabe et al. (2003) in dash-dot. For Dome C, ISM prediction (climate T1 and T2 similar) for thinning is in thick dash and age in thin dash, 1D model used for EPICA community members (2004) in dash-dot.

DC near 1600-m depth, which corresponds to MIS 5, a bump that Parrenin (*pers. comm.*) attributes to a time discrepancy between the surface elevation forcing (from GT4, Petit et al., 1999) and the timescale derived from the inverse method; in contrast, constant surface elevation was prescribed to derive the timescale for Dome Fuji that yields a monotonic thinning. The three-dimensional model predicts a similar general decreasing trend with depth. Thinning is lower (layers are more compressed) with the 1D than with the 3D model, especially for Dome C, which explains the use of lower accumulation rate in the ISM to match the stratigraphy of both records. The ISM also produces oscillations at depths, which, comparing to those of climatic changes in Fig. 6.14, correspond to major warming events (glacial terminations), thus to large changes in precipitation rate (precipitation and temperature co-vary in the ISM, Eq. 2.16). Because surface mass balance controls (vertical) velocity (Eq. 2.12) and compressive strain is the derivative of vertical velocity with

respect to z, change in velocity could propagate into the thinning, thus imposing different thinnings for ice deposited before or after a major climatic transition. This effect could possibly be amplified by the relative delay between the ice flow regime and mass balance induced by the lagged rise of surface elevation that follows any sustained increase of mass balance (Eq. 7.3 and Fig. 7.8). Spurious oscillations could also be introduced as an artifact of the low resolution (21-point-vertical) of the ice sheet–tracer model, coming either from the tracer transport method or the reconstruction of continuous ice cores. The next section on vertical velocity profiles provides additional clues to understanding thinning.

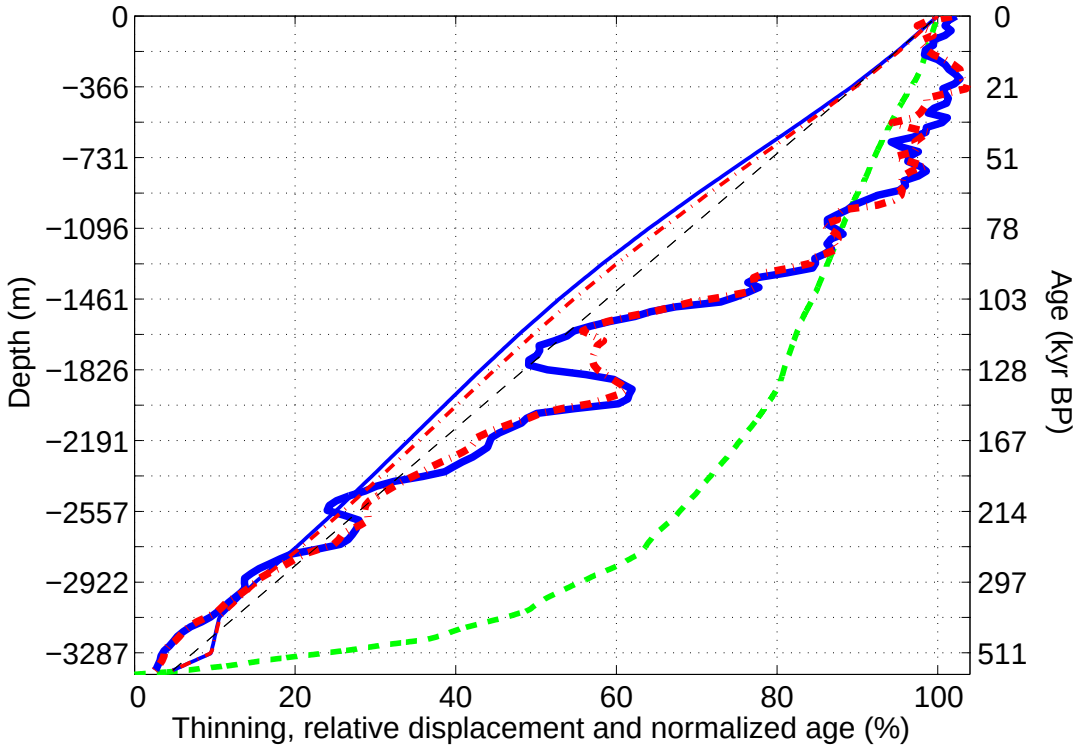

Figure 7.10: Vostok ice core: simulated thinning (thickest lines), relative displacement defined as the depositional distance from Vostok normalized by the distance between Vostok and Ridge B (thin concave lines) and normalized age defined as the depositional age divided by the oldest age in the predicted core (mid-thick gray dash). Properties are represented as a function of the depth (left axis) and predicted depositional age (kyr BP, right axis). Dash-dot line for T1, solid line for T2.

Fig. 7.10 shows the thinning predicted by the ISM at Vostok as a function of depth for models T1 and T2 (thick lines). Also represented are the normalized age–depth profile (dashed line, time on the right axis) and the normalized depositional distance as a function of depth along the core (thin curves). The latter graph relates to the study of ice origin in Section 7.3.2 and shows concave shape, whereas Parrenin et al. (in press, Fig. 4) find a linear-to-convex shape for most of their sensitivity studies, except for the one that neglects the flow divergence contribution to ice velocity. That implies differences in ice velocity between the 3D and the 2.5D studies. Comparing the ISM thinning with that of Fig. 9 in Parrenin et al. (in press), the ISM shows a similar non-monotonic trend with a distinctive "bump" at a depth of 1700–2000 m, which, according to Fig. 7.5, corresponds to ice

deposited during the last interglacial period near the high subglacial mountain. Given that ISMs use the shallow-ice approximation for the ice flow law, only normal stress (gravity) and vertical shear stresses (change in surface slope) are accounted for; thus, the usually monotonic thinning trend can be altered if ice has crossed through ice columns where different compression rates apply. This happens for Vostok ice because of the irregular underlying topography (Fig. 7.6). Short ice columns 160 and 80 km upstream have a lower thinning than neighbouring tall ice columns directly downstream, therefore ice that originates 160 km upstream is comparatively as much as or less thinned than ice from 120 km as shown on Fig. 7.10 for ice at 1700–2000 m depth. A similar case occurs for the upper 800 m of the core. The thinning is additionally complicated by the decreasing present-day accumulation rate from Ridge B to Vostok and its temporal modulation during glacial and interglacial periods. All these non-linear processes contribute to a complex thinning function along the Vostok ice core that complicates the tasks of accurately dating the record, of estimating past accumulation rate and interpreting radar images.

7.4.2 Velocity profiles at domes

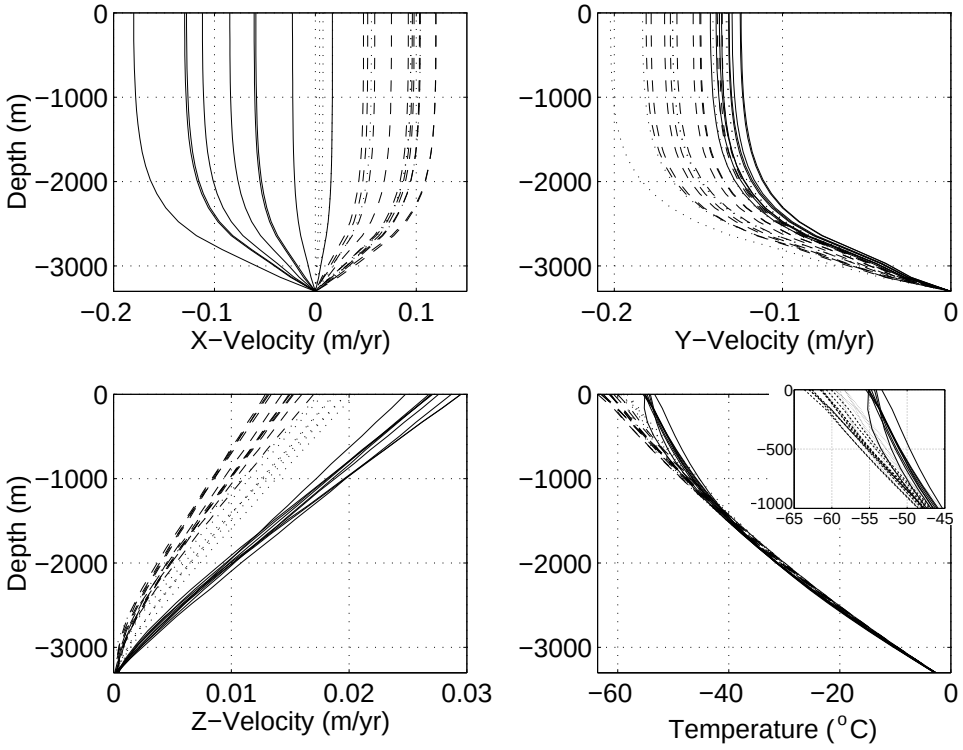

Figure 7.11: Velocity and temperature profiles at Dome C during interglacial periods (solid), glacial periods (dash) and transitions (dot). Vertical velocity is defined relative to the surface of the ice sheet.

Fig. 7.11 shows the velocity and temperature profiles predicted by the ice sheet model at Dome C. The graphs illustrate that the ice flow regime significantly varies between glacial and interglacial

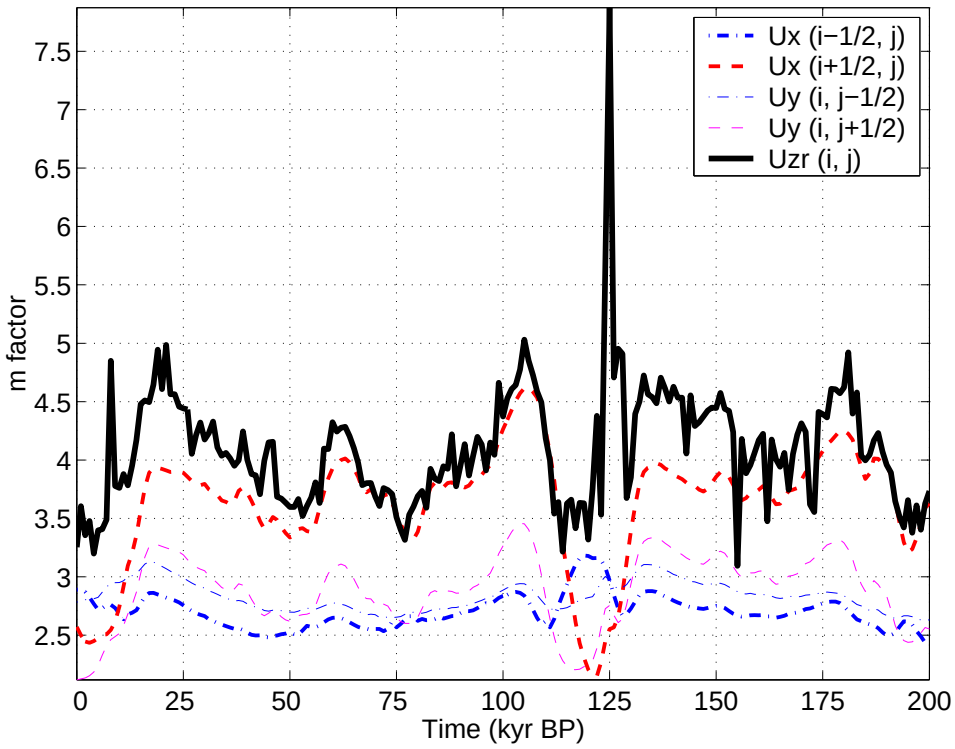

Figure 7.12: Optimum m coefficient as defined in Eq. 7.2 for the vertical profiles of horizontal velocity Ux (dash and dash-dot thick lines) and Uy (dash and dahs-dot thin lines) and with Eq. 7.3 for the vertical velocity profile Uz (thick solid line) predicted by the ice sheet model at Dome C. Note that horizontal velocities are computed at half-grid points because the ice dynamics grid is alternated.

climate. High surface precipitation during warm periods increases vertical velocity (relative to the ice surface) as expected. Note that vertical velocity here is shown relative to the ice surface; absolute vertical velocity can be obtained by correcting for changes in surface elevation ($\sim 1.5 \mathrm{cm\,yr^{-1}}$ during the Holocene) and changes in bedrock elevation (∼–0.4 cm $\mathrm{yr^{-1}}$ during the Holocene). Horizontal velocity is non-negligible over long timescales contradicting the hypotheses used for dating the core, though this effect can be an artifact from the coarse physics and spatial resolution of the ISM. Interestingly, the ice flow in the X direction is oriented inland (negative value) during a warm climate (upper left panel), and toward the ocean (positive) and slower during the longer glacial periods, effectively limiting transport along the X-direction as previously seen for the ice origin in Fig. 7.5. Velocity in the Y-direction is larger during cold periods despite lower surface accumulation. These flow regimes can be explained by changes in surface topography between the present (Fig. 6.1) and the LGM (Fig. 6.3), when the Vostok–Dome C ridge steepened and slightly shifted to the east. Basal horizontal velocity vanishes at the site as basal temperature has always remained close to freezing conditions (∼–2.8°C), allowing minimal melting (between 1.5–5.2$\times 10^{-4}\,\mathrm{m\,yr^{-1}}$, with $3.2 \times 10^{-4}\,\mathrm{myr^{-1}}$ at present) and negligible basal sliding. Therefore basal ice remains at Dome C for long periods of time and the ISM predicts ice up to 1 Myr old.

To compare the predicted vertical velocity profiles with those assumed by Parrenin's dating model, I used a simple optimization procedure to find the best m value as defined in Eq. 7.2 to characterize the shape of the velocity profile (using $fminbnd$ in MATLAB within the range 0–50

with a L_2 norm and no regularization). Results are presented in Fig. 7.12 for the vertical profiles of horizontal and vertical velocity. Vertical profiles of horizontal velocity are presented at half-grid points around Dome C (i, j) because the ice dynamics grid is alternated. Firstly, I find that the value of m is different for each velocity at any given time. This is due to the fact that the velocity is computed at a different location and thus different bedrock elevation and ice thickness; therefore the temperature gradient of basal ice that influences m is also different. Secondly, every m curve exhibits a similar variability in time that is generally negatively correlated with surface temperature and mass balance. High frequency variability, especially for the vertical velocity, results from advective terms that I have neglected for the calculation of m. The glacial–interglacial variability of m is also apparent in the changes of curvature for the lower part of the vertical velocity profiles in Fig. 7.11, lower left panel. In contrast, the simple flow model of Parrenin assumes that m is constant in time and finds with the inverse method that it ranges from 2 to 3, which is similar or lower than the values predicted by the ISM. The difference of shape (m) between vertical velocity profiles imply that the ISM generally produces less thinning in the upper part of Dome C and explains why it requires lower accumulation rate to match the stratigraphy of the Dome C ice core.

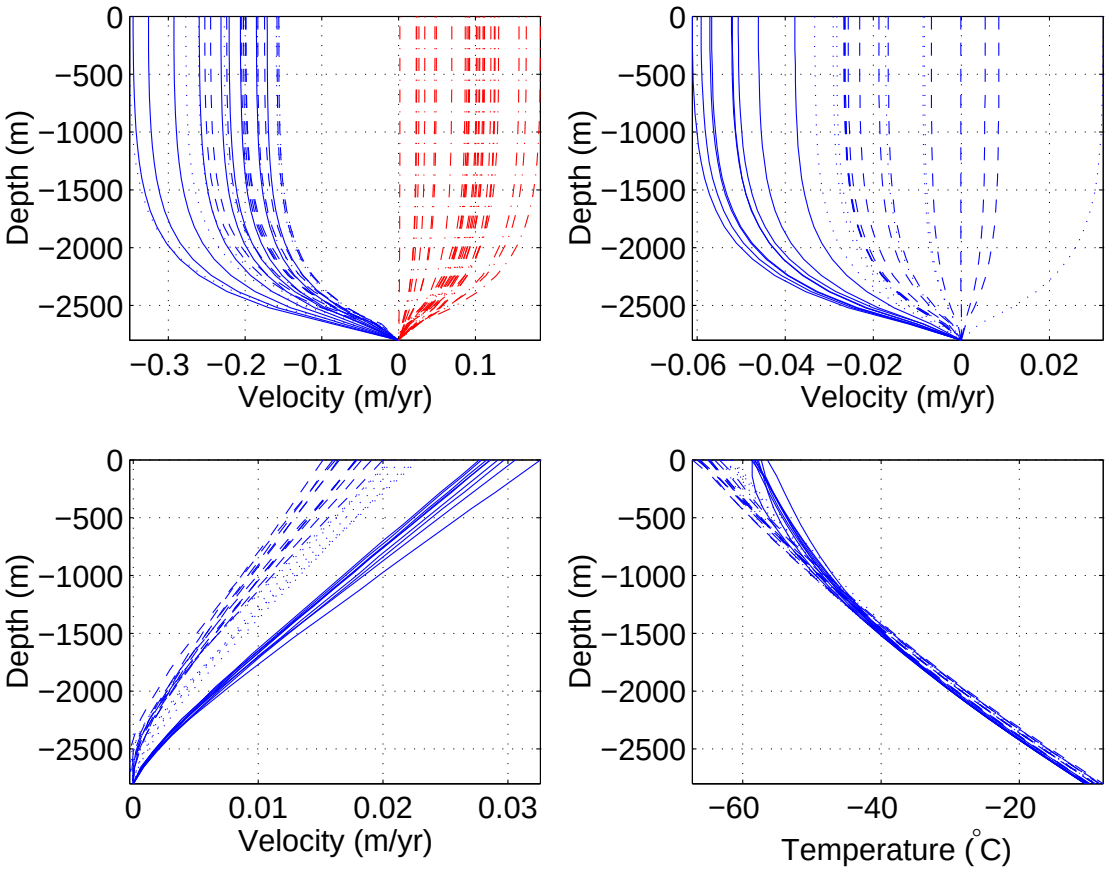

Figure 7.13: Velocity and temperature profiles at Dome Fuji during interglacial periods (solid), glacial periods (dash) and transitions (dot). In the upper left panel, dash-dotted lines correspond to the first neighbour in the X direction; opposite X-flow direction explains the dome stability illustrated in Fig. 7.5.

Velocities at Dome Fuji, presented in Fig. 7.13, are enhanced during warm periods because

of the high accumulation rate. Recalling the provenance of ice shown in Fig. 7.5, low horizontal velocities were expected at the site. The upper left panel in Fig. 7.13 shows surprisingly large negative velocities in the X direction at the Dome Fuji grid point; velocities at the next grid point in the X direction are plotted in dash-dotted lines and show an opposite flow direction. The upper right panel shows that the flow along Y is extremely limited. Thus the ISM does simulate a dome at the drilling site and the negative X velocities plotted in Fig. 7.13 correspond to the large-scale drainage toward the Weddell Sea that originates along the Dome Fuji–Dome A flow divide. Basal sliding and melting are completely negligible because basal temperature always remains below –8°C, well below the melting point. The m coefficient corresponding to the vertical velocity profile, shown in Fig. 7.14, reveals the same kind of spatial and temporal variability as that of Dome C and ranges from 3.5 to 6, also showing a negative correlation with surface temperature and mass balance. The predicted values are again larger than those inferred with 1D models (2 to 3).

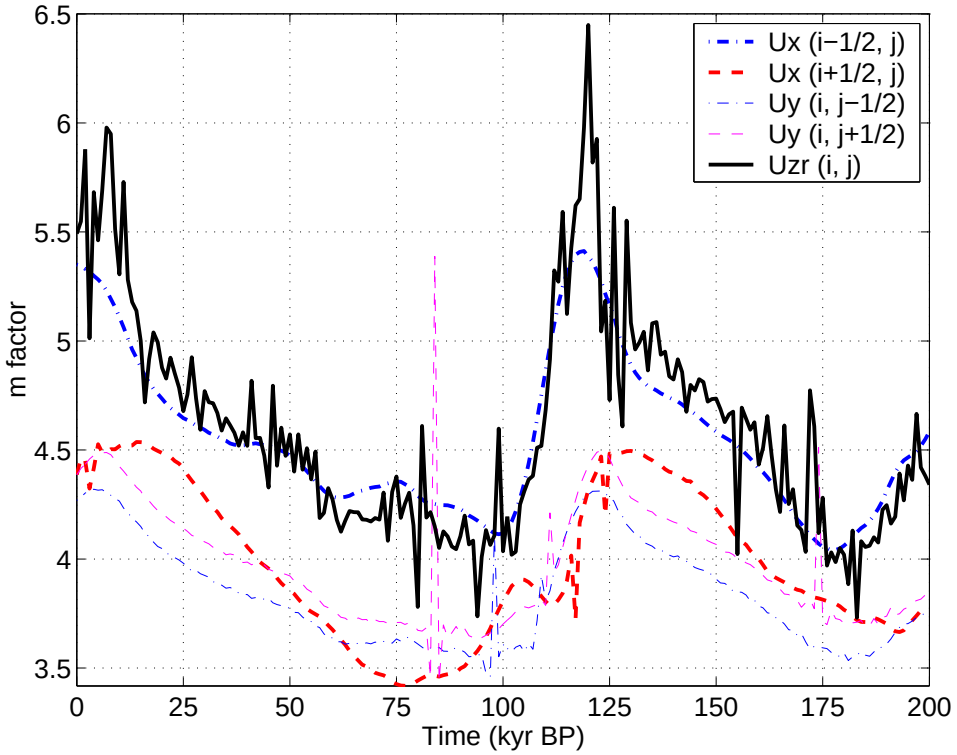

Figure 7.14: Optimum m coefficient as defined in Eq. 7.2 for the vertical profiles of horizontal velocity Ux (dash and dash-dot thick lines) and Uy (dash and dahs-dot thin lines) and with Eq. 7.3 for the vertical velocity profile Uz (thick solid line) predicted by the ice sheet model at Dome F. Note that horizontal velocities are computed at half-grid points because the ice dynamics grid is alternated.

7.4.3 Velocity profiles at Vostok

Fig. 7.15 displays in a rather complex manner the velocity and borehole temperature profiles representative of glacial (dash) and interglacial (solid) conditions along the Ridge B to Vostok flow line (large dots for computational grid points, Vostok leftmost). The corresponding elevation and ice thickness at those grid points was previously shown in Fig. 7.6 (every second virtual ice core),

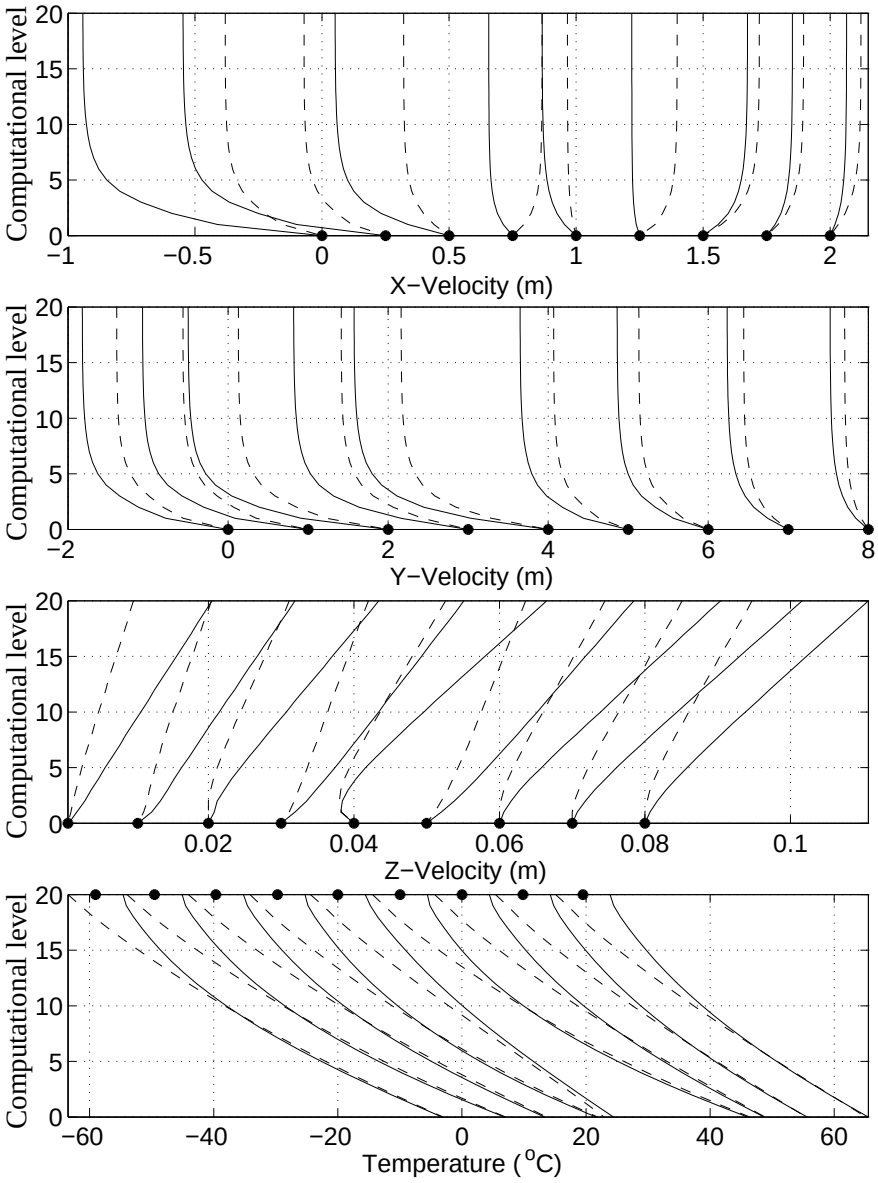

Figure 7.15: Velocity and borehole temperature along the Vostok flowline. Large dots on horizontal axes correspond to computational grid points along the flowline, with Vostok located at the leftmost dot; spacing between the dots is chosen so that plotted properties can be attached to their location and juxtaposed (because basal velocity is zero in all three directions). Borehole temperatures are plotted with a 10°C offset, locating dots are placed between their corresponding glacial and interglacial surface temperature. Solid lines illustrate interglacial conditions whereas dashed lines correspond to glacial periods, when precipitation was 50% lower than its modern value. Vertical axes indicate computational levels starting from the base.

so that the 5^{th} point (middle) represents the high subglacial mountain. Vertical axes correspond to computational levels for ease of display; these can be converted in terms of elevation above bedrock with Fig. 7.6. As expected, velocities are larger during warm periods because of higher precipitation rate, especially in the Y (along the flowline) and Z (vertical) directions. The X-velocity, which represents transverse flow with respect to the main flow direction and is shown in the uppermost panel,

does not follow such predictible behaviour. The X flow switches orientation between climate states for the three computational nodes located near the subglacial mountain. As seen for Dome C, the change is due to a migration of the Dome A–Dome C ridge between glacial and interglacial periods. This phenomenon, plausible because the East Antarctic Ice Sheet advanced over its surrounding continental shelf during glacial periods, implies that the modern observed surface topography along the Vostok flowline cannot be applied to predict the past divergence of ice flow, as is assumed by glaciological dating models for Vostok (Ritz, 1992; Petit et al., 1999; Parrenin et al., 2001, in press).

Additional differences and potential complications for the 2.5D model of Ritz and Parrenin also arise for the vertical velocity (third panel from the top). The ISM predicts its vertical profile has different curvature along the flowline, concave next to convex shape. This is found to be incompatible with a simple shape characterized by any m coefficient. Trials to find an optimum m, not shown here, provide climate-dependent values varying from 2.5 to 10 at the 3^{rd}, 7^{th}, 8^{th} and 9^{th} nodes, from 0.3 to 3 at the 5^{th} node and no optimum value for the 1^{st} (Vostok), 2^{nd}, 4^{th} and 6^{th} nodes. Borehole temperatures, presented in the lowest panel, show that basal temperature conditions, which are determined by ice thickness and thus negatively correlated with bedrock elevation (Fig. 7.6), significantly vary along the flowline, hence affecting deformation and basal melting rates. We note that Lake Vostok is not represented in the ice sheet model; thus, there are missing dynamical processes (no basal friction from the lake) and thermodynamical processes (basal melting and freezing on either side of the lake) that alter the ability of the ice sheet–tracer model to thoroughly represent the conditions for the Vostok ice core record.

7.4.4 Simple vs. 3D calculation of velocity

Overall, velocity regimes and the shape of velocity profiles show a dependence on the climate state because of the corresponding changes in surface temperature, mass balance and sea level and the resulting spatial re-organization of the ice sheet topography. In particular, migration of ridges and flowlines are large scale processes that are best addressed with three-dimensional ice sheet models. This is especially true for studying the Vostok ice core. These models however suffer limitations at dome sites because their founding principle, the shallow-ice approximation, fails where ice flow is controlled by longitudinal stress instead of simple shear. Previous studies agree that deformation is larger in the upper part of the ice column at dome sites than down the flowline, which makes domes particularly attractive for drilling because deep layers remain better preserved by experiencing less thinning (e.g., Raymond, 1983; Dahl-Jensen, 1989; Parrenin, 2002). The m coefficient in Eq. 7.3 controls the deformation rate balance between the upper and the lower part of the ice column. Therefore, large values of m at domes found with the ice sheet model correspond to a concentration of ice deformation in the deep layers, a result that is in clear contradiction with the glaciological models used for dating the deep East Antarctic ice cores and with previous theoretical studies. Ice sheet models with nested physics including deviatoric stress gradients (e.g., Albrecht, 2000) in crucial areas like domes and ice margins would certainly improve the calculation of velocity at domes and the reliability of tracer transport predictions for such sites.

7.5 Discussion and conclusion

In this chapter a three-dimensional ice sheet–tracer model was used to test and validate the assumptions used for interpreting ice core records. Such a study is particularly useful for the East Antarctic

records from Dome C, Vostok and Dome Fuji because the low accumulation rate at these sites implies that annual layers are too thin for the application of visual layer counting techniques and thus requires the use of glaciological models. I find that ISMs based on the shallow-ice approximation can provide valuable information as long as one remains aware of their physical limitations. The ISM is an efficient tool for assessing large-scale phenomena like the reorganization of flow patterns and the changes in surface elevation that occur during glacial–interglacial cycles because of the changes in temperature, surface mass balance and sea level. In that respect, the relative stability of Domes C and Fuji is reassuring. For Vostok, though the model finds an ice origin similar to the location of the flowline assumed for dating the ice core record, the model also predicts that the general flow and surface topography of that region varied during glacial periods. That effect could potentially modify the timing of the last interglacial period inferred with the simple flow model, an important period for climate studies for which the exact timing, duration and temperature remain to be resolved (e.g., Parrenin et al., in press; NGRIP Members, 2004). The 3D model can also facilitate the interpretation of ice cores by providing a surface elevation history that is coherent with the surface mass balance inferred from the ice core record, an iterative task that could be formalized into a conceptual surface mass balance–elevation model. This study shows that variations of elevation are non-negligible at all sites and also provide the convoluted depositional elevation of Vostok ice, which includes a source effect. This information can be applied to interpret finer climatic footprints entrapped for instance in the gas content of air bubbles.

Caution should be exercised when considering properties that relate too closely to the limitations of this type of ISM, namely when the shallow-ice approximation breaks down. This implies that velocity profiles given by the ISM at domes might lead to underestimation of the thinning in the upper part of the ice column and thus require a lower accumulation rate for the most recent period (last 20 kyr) to match the present ice stratigraphy. The ISM still raises the possibility of climate-dependent shape for the velocity profiles; further sensitivity studies and alternative treatments of the ice flow at domes are warranted.

As shown in Fig. 7.6, tracer techniques also open the possibility of interpreting isochronal layers in radar images and adding new constraints on past precipitation rates and patterns at the surface of the Antarctic Ice Sheet. Because tracers can be applied to predict the stratigraphy of any ice core, we have great hope that forecoming improvements in the Antarctic ice sheet model will soon allow us to help interpret the Holocene record of shallow ice cores (e.g., Masson et al., 2000, and Appendix D.2) drilled near sensitive regions of Antarctica, especially the coasts and the West Antarctic Ice Sheet, by separating the climatic signal and the effects of changes in elevation. The potential of our method multiplies with the prospect of new ice cores to study, for instance the ongoing drilling projects in Dronning Maud Land (Kohnen Station) and at Berkner Island.

CHAPTER 8

Global budget of water isotopes inferred from polar ice sheets

8.1 Introduction

The oxygen isotope composition (δ^{18}O) of carbonate shells in marine sediments has been widely used for reconstructing past regional and global temperatures on a wide range of time scales, from centuries to millions of years (e.g., Zachos et al., 2001). Interpretation of these sedimentary records is complicated by the fact that δ^{18}O reflects the combined influence of ocean temperature and global sea-water $^{18}O/^{16}O$ composition ($\delta^{18}O_{sw}$) (Shackleton, 1974; Labeyrie et al., 1987). Distinguishing the effects of temperature and $\delta^{18}O_{sw}$ remains a long-standing problem in oceanography (Adkins et al., 2002; Duplessy et al., 2002), largely because of uncertainties concerning the amount of ^{18}O-depleted water stored in continental ice masses. The composition of these ice reservoirs remains, however, poorly established, even for the modern Greenland and Antarctic Ice Sheets, from which few deep ice cores have been retrieved. The consequences are especially serious for evaluating ocean temperature at the Last Glacial Maximum (Dansgaard and Taubert, 1969; Waelbroeck et al., 2002), 20 kyr ago, when the equivalent of 120 m of sea level and an unknown quantity of water isotopes were stored in the Laurentide and Fennoscandian Ice Sheets. Previous attempts to gauge the isotopic content of polar reservoirs have assumed that their bulk composition is proportional to that of single ice cores, from Camp Century for Greenland (Dansgaard and Taubert, 1969) and Vostok for Antarctica (Duplessy et al., 2002).

The scaling premise that underlies these estimates ignores the facts that isotopic deposition rates and patterns vary spatially and temporally and that isotopic signatures in snowfall are redistributed by ice flow. These complexities are best addressed using numerical three-dimensional ice sheet models that include physical models of isotopic deposition and tracer transport to predict the fine-scale layering of ice sheets. The following study completes the main goal of my thesis study by providing an estimate of the past and present isotopic composition of polar ice sheets and the resulting changes in sea level and seawater composition during the past glacial cycle.

8.2 Conditions for an accurate diagnosis

8.2.1 Ice sheet reconstruction

In the previous chapters, I introduced ice sheet models for Greenland and Antarctica and identified plausible climatic reconstructions that produced simulated ice sheets having geometric features (volume, areal extent, surface elevation) and ice layering that were in close agreement with present-day observations and major ice core records. From these I can select suitable candidates to calculate the corresponding bulk isotopic composition. We saw that the climate forcing for the ISMs pre-

scribed the surface temperature, accumulation and ablation rates as functions of time and space using standard parameterizations (Ritz et al., 2001; Cuffey and Marshall, 2000; Huybrechts, 2002). Past surface temperature and mass balance were obtained by scaling the present distributions of temperature and precipitation according to a history of temperature change (ΔT_c) inferred from an ice core record representative of each ice sheet, the recent 740-kyr long EPICA-Dome C (DC) record (EPICA community members, 2004) for Antarctica and GRIP (GRIP Members, 1993) spliced with Vostok (Petit et al., 1999) for Greenland, the latter corresponding to the methodology used for the most recent studies on Greenland evolution (Cuffey and Marshall, 2000; Marshall and Cuffey, 2000; Clarke and Marshall, 2002; Tarasov and Peltier, 2003). Because differences between the chronologies of Vostok and Dome C remain to be resolved by the ice core community and, for practical reasons mentioned above and linked to the fact that my studies of Greenland and Antarctica were conducted independently, the climate forcings were not synchronized; thus, I shall refrain from any direct comparison of the ice sheet volumes or composition at any given time.

The merit of the ice sheet and climate reconstructions was evidenced by comparing the fine layering of deep ice cores from Greenland and Antarctica with model predictions for the same sites. In Antarctica, excellent agreement was obtained for Dome C, Vostok and Dome Fuji (Watanabe et al., 2003) (see Fig. 6.14). The remarkable fit in terms of isotopic variations and age–depth profiles confirmed previous studies showing that very similar climate changes prevailed over much of Antarctica (Watanabe et al., 2003) and that models of ice sheet evolution relying on a simple climate forcing can satisfactorily represent the climate variability (Ritz et al., 2001; Huybrechts, 2002). The reconstructed ice cores were compatible with a present–LGM amplitude of 10 to 12°C, which I here take as lower and upper bounds on our assumed climate forcing in subsequent calculations. These successes for the East Antarctic Ice Sheet (EAIS), which accounts for ∼85% of the present Antarctic ice volume and 75% at LGM, confirmed that, under favourable circumstances, the fine layering of ice sheets can be accurately predicted. Comparison with cores from the smaller West Antarctic Ice Sheet (WAIS) was not attempted because, in general, the ISM does not adequately resolve the topography at the Byrd and Siple Coast core sites, a problem beyond the capabilities of present models. I believe that this does not significantly affect the estimate of the bulk composition of the ice sheet because (1) the climate over the EAIS is confirmed by the observed similarities in the isotopic records of Byrd with EDC and Dome Fuji (Watanabe et al., 2003), (2) the accuracy of the ice evolution and tracking schemes has been demonstrated (Ritz et al., 2001; Huybrechts, 2002, for the ISM and Chapter 3 for the tracers), and (3) relative to EAIS, WAIS makes a small contribution to the bulk composition of the entire ice sheet. I shall however carefully distinguish the contribution of each Antarctic Ice Sheet in the following.

Similar success was achieved for Greenland, where the GRIP, GISP2, Dye 3 and Camp Century records were closely reproduced (Fig. 4.8), despite discrepancies for the lowest part of GRIP and GISP2 originating from basal flow disruption processes (Alley et al., 1995) not represented in the ISM. As for Antarctica, I found that the climate derived from a single record encapsulated most of the Greenland variability and that the prediction of ice layering was accurate. Given the uncertainty in climatic and ice-dynamic parameters, constrained by the simulated cores, I select suitable models that correspond to an LGM cooling of 22–24°C in Greenland (Dahl-Jensen et al., 1998) and a maximum of 2–4 m sea level rise during the last interglacial period.

8.2.2 Deposition rate of water isotopes

The principles of the isotopic thermometer and depositional model are presented in Sections 2.3.6, 3.4.2 and 3.4.3 and quickly summarized here. Because of the prohibitive computational-time requirements of AGCMs that include isotopic fractionation processes, such models cannot be used to predict the δ^{18}O and δD content of precipitation and incorporate the feedbacks of ice sheets on topography and water storage during a full glacial cycle. Therefore, I choose to merely rely on their ability to predict the relationship between surface temperature and δ^{18}O at present (the spatial slope) and at the Last Glacial Maximum (the temporal slope α_{c}=dδ^{18}O/dT) to estimate past isotopic depositional rates. In this manner, past surface δ^{18}O is derived from its present spatial distribution (Giovinetto and Zwally, 1997; Zwally and Giovinetto, 1997) after correction for changes in surface temperature (modulated by α_{c}) and surface elevation (Cuffey, 2000, and Eq. 3.25). For Antarctica, AGCMs suggest that the modern relationship remained mostly valid in the past (Krinner and Genthon, 1997; Delaygue et al., 2000); thus, I assume a constant and spatially uniform value of α_{c} and test the effect of this calibration on the bulk composition of the ice sheet. For Greenland, borehole thermometer measurements at GRIP (Dahl-Jensen et al., 1998) and GISP2 (Cuffey and Clow, 1997) and atmospheric models (Krinner and Genthon, 1997; Jouzel et al., 1997, 2000) show that changes in the seasonality and origin of precipitation during glacial periods modify the relationship between surface temperature and δ^{18}O. Thus α_{c} varies spatially and temporally. To test the uncertainty associated with both phenomena, past surface δ^{18}O is obtained from the present distribution by using either a uniform α_{c} derived from GRIP/GISP2 (Cuffey and Clow, 1997) or regional values of α_{c} predicted by the Goddard Institute for Space Studies AGCM (GISS-AGCM), which includes isotopic fractionation processes (Jouzel et al., 1991, 2000).

8.2.3 Stability of the Antarctic Ice Sheets

Antarctica is covered by two ice sheets with different dynamic behaviour: the large and stable East Antarctic Ice Sheet (EAIS) and the comparatively small and potentially unstable West Antarctic Ice Sheet (WAIS). Though we have not been concerned so far with their degree of stability because we were mostly interested in their stratigraphy and the conditions at ice core sites, stability becomes an important factor when considering the contribution of the Antarctic Ice Sheets to ocean volume and composition. The different ice flow regime between the two ice masses is mostly due to their differing bedrock topography, shown in Fig. 6.2 for the present.

The eastern part is mostly perched above modern sea level and reaches near the edge of the continental shelf, leaving little room to expand. The direct consequence is little variation in ice volume and surface elevation for the EAIS between glacial and interglacial periods, as predicted by most ice sheet modelling studies (e.g., Ritz et al., 2001; Huybrechts, 2002) including this one, and inferred from the geomorphologic data (e.g., Bentley, 1999) and the variations in isotopic ice core records (Petit et al., 1999; Watanabe et al., 2003; EPICA community members, 2004).

In contrast, the bedrock of the WAIS is almost entirely below modern sea level and surrounded by a shallow continental shelf underneath and beyond its ice shelves. Sea level rise can trigger enhanced calving and lift any ice below a critical thickness, reducing basal drag and accelerating ice flow and retreat; sea level drop dries the continental shelf, allowing the ice sheet to expand. Ample evidence suggests that both phenomena have happened in the past. During glacial periods, sea level dropped by up to 120–135 m (e.g., Yokoyama et al., 2000; Clark and Mix, 2002), after the buildup of the voluminous Northern Hemisphere continental ice sheets (volume twice as large

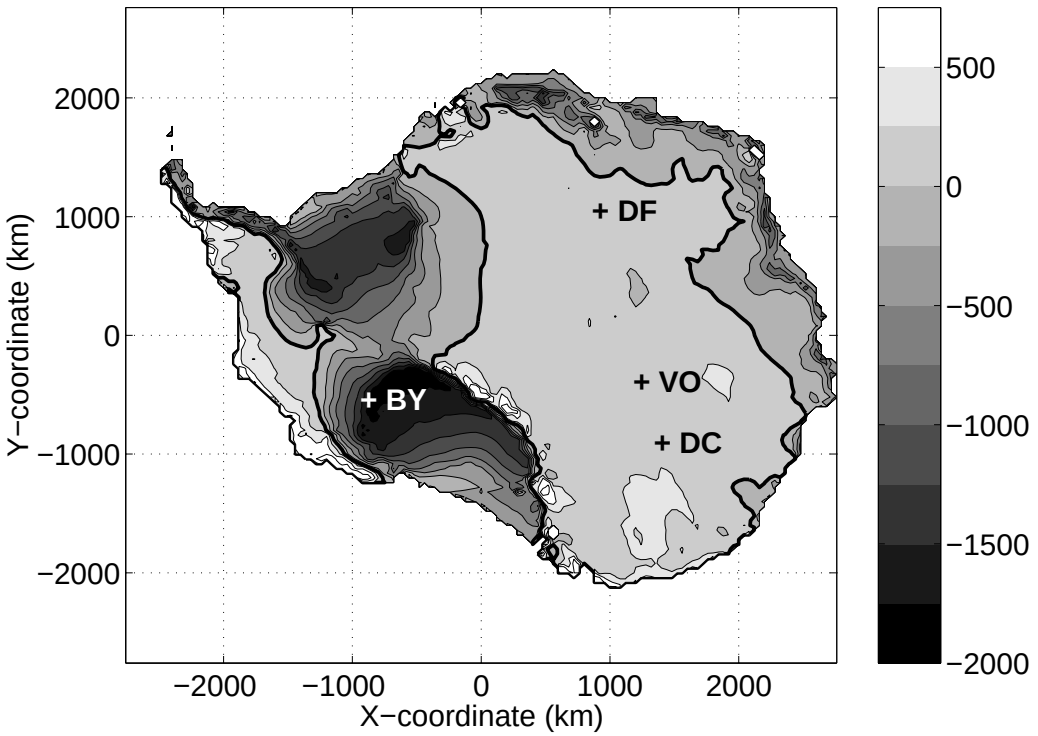

Figure 8.1: Difference in Antarctic surface elevation between present and LGM (20 kyr BP). Contour every 250 m; thick contour at 0 m to separate zones of gain and loss of ice. Colour scale in m.

as modern Antarctica), allowing the WAIS to override its continental shelf and build a large land-based ice reservoir. This is confirmed by the geomorphologic and modelling studies cited above and illustrated by the predicted difference in surface elevation between the present and the LGM shown in Fig. 8.1 and earlier in Figs. 6.1 and 6.3. Reduction of the WAIS from its modern configuration is speculated for MIS 5 (120 kyr BP), when sea level was 6 m higher than present (e.g., Mercer, 1978; Rostami et al., 2000), and almost certainly during MIS 11 (400 kyr BP), when sea level rose by 13–20 m (Drowler et al., 2002). The shape and quality of the bedrock introduces additional sources of instability for the WAIS by sustaining a faster ice-flow regime than the EAIS. A steep surface slope above the high subglacial mountain range located below the main western central ice divide (Fig. 6.2) favours fast flow. Higher basal heat flux than in the East, evidenced at Ross Island, is believed to stimulate melting and warming of basal ice. As a result, thick lubricated and deformable sediments in bedrock depressions reduce basal friction and provide favourable conditions for the development of ice streams (see review in Oppenheimer, 1998). The WAIS therefore sits at a lower elevation than the EAIS, implying warmer surface and internal temperature, further enhancing ice flow.

8.2.4 Presentation mode

The differences in dynamical history between the two Antarctic Ice Sheets are such that I choose to distinguish their respective contribution to the ocean volume and composition. The boundary line between the East and the West is here assumed to depend on bedrock topography and follows

the Transantarctic mountain range for the Pacific side and its continuation along $X = -500$ km for the Atlantic side (Fig. 6.2). Study of the volume and composition of the East Antarctic, West Antarctic and Greenland Ice Sheets in the next sections focuses on the past 160 kyr and adopts the same graphic presentation style: six panels plot the ice sheet volume and equivalent change in sea-level, the ice-sheet-averaged $\delta^{18}\mathrm{O}$ and $\delta\mathrm{D}$ compositions and the corresponding changes in seawater composition ($\delta^{18}\mathrm{O}_{\mathrm{sw}}$, $\delta\mathrm{D}_{\mathrm{sw}}$). Left panels show the global characteristics of the ice sheets, right panels present the effect on the ocean.

8.3 Volume and composition of the East Antarctic Ice Sheet

8.3.1 Ice volume and sea level

Variations in the areal extent of the East Antarctic Ice Sheet are controlled by sea level and by the limit of the continental shelf, ∼200 km away from the modern ice margin, because it is nearly impossible to ground ice in the abyss (Oppenheimer, 1998). Therefore the EAIS shows little variation in surface area during glacial cycles. Ice core records throughout the ice sheet suggest that surface mass balance diminished by $\sim 50\%$ during glacial periods, effectively starving the ice sheet in its high central plateau and consequently lowering surface elevation by 60–120 m near its deep ice core sites (e.g., Fig. 7.7). This phenomenon causes most of the changes in ice volume and explains the ~ 1 Mkm^3 decrease observed in Fig. 8.2a during glacial periods. This corresponds to 2.5–3 m of sea level rise during an epoch when the WAIS and the Laurentide and Fennoscandian Ice Sheets were drawing sea level down by 120–135 m. For the last interglacial period (MIS 5), warm temperature caused enhanced precipitation while ablation remained limited because most of the ice sheet stood at high elevation; thus, ice volume increased.

The three curves in Fig. 8.2a correspond to a sensitivity test including the reference climate forcing T2 (ΔT_{c}=12°C, solid curve), T1 (ΔT_{c}=10°C, dashed curve) and experiment T2D (dash-dot curve) which climate forcing uses T2 for temperature and a time-invariant and spatially-uniform $D_{\mathrm{acc}} = 0.070°\mathrm{C}^{-1}$ (same D_{acc} as in Ritz et al., 2001), whereas D_{acc} is inferred from EDC2 in the standard T1 and T2 models. Though the variations in ice volume are similar for all three experiments, the latter predicts a larger modern ice sheet.

8.3.2 Isotopic composition of the EAIS

Analysis of ice core records (Petit et al., 1999; Masson et al., 2000) and AGCM simulations (Krinner and Genthon, 1997; Delaygue et al., 2000) in East Antarctica indicate that $\mathrm{d}\delta\mathrm{D}/\mathrm{d}T_{\mathrm{s}}$=6–6.5‰ °C^{-1}, which is equivalent to $\alpha_{\mathrm{c}}=\mathrm{d}\delta^{18}\mathrm{O}/\mathrm{d}T_{\mathrm{s}}$=0.75–0.8‰ °C^{-1} using the meteoric water line (Eq. 2.3). To test the sensitivity of that calibration, I calculate the bulk isotopic composition of the EAIS with a constant and spatially uniform value of α_{c}=0.8‰ °C^{-1} taken as the reference (thick lines in Figs. 8.2c–f) and a lower value of α_{c}=0.6‰ °C^{-1} (thin lines). Fig. 8.2c shows that the bulk $\delta^{18}\mathrm{O}$ composition of EAIS remained quasi-constant through the last glacial cycle with variations of less than 0.3‰. Several phenomena contribute to that effect. Firstly, the volume of the ice sheet deviates by at most 6% from its modern value. Secondly, the low accumulation rate that characterizes the climate of EAIS implies that variations in the composition of precipitation are buffered by the bulk of the ice sheet, which contains over 300 kyr of ice at any given time. Thirdly, the ice contribution of 60–80-kyr-long glacial periods is compensated by the ∼20-kyr-long interglacial periods that have

double the accumulation rate and increase the overall ice volume. Variations in the bulk isotopic composition of EAIS are thus dampened.

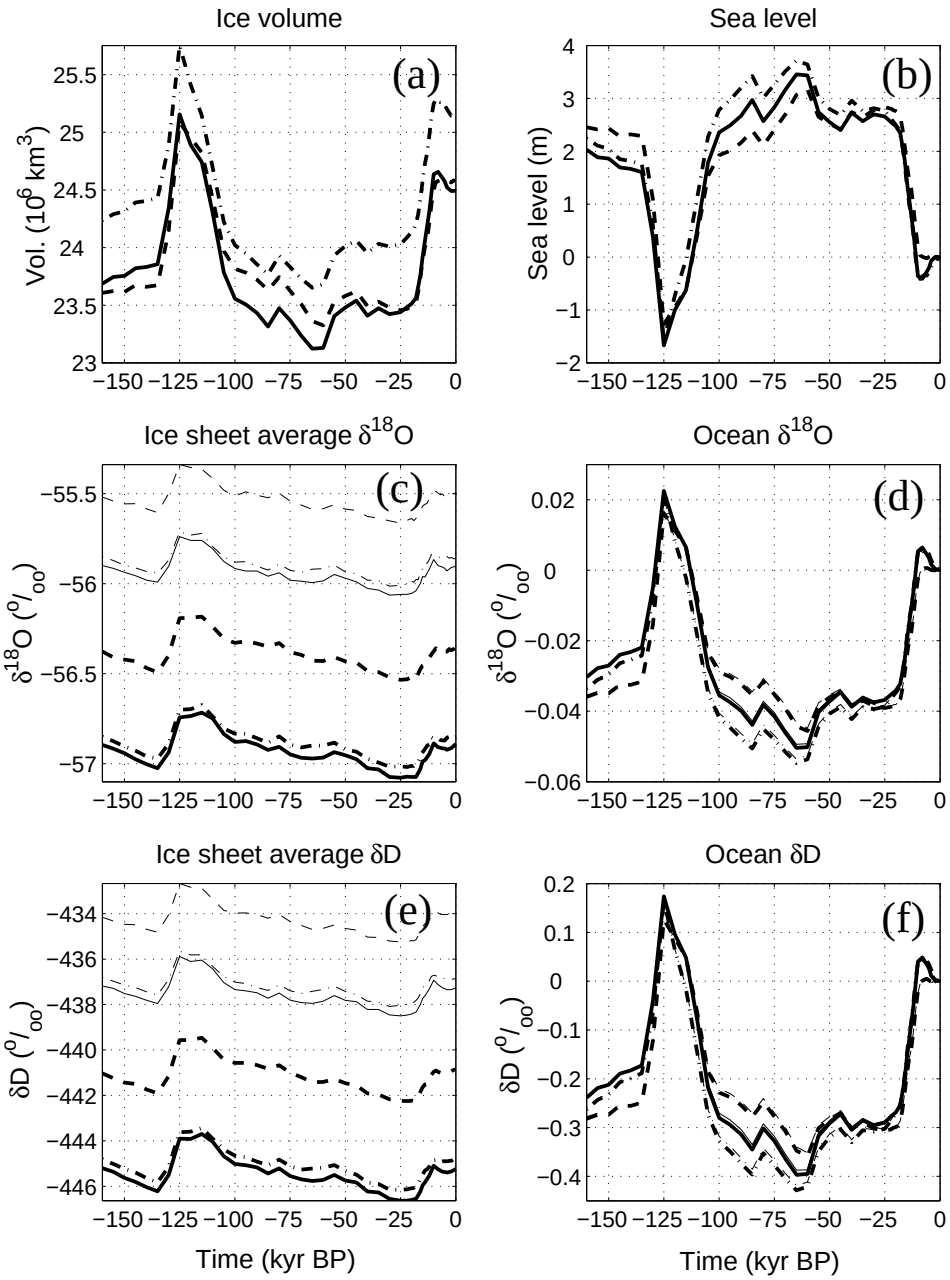

Figure 8.2: Volume and water isotope composition of the EAIS for models T1 (dash), T2 (solid) and T2D (dash-dot). The thickness of the curves distinguishes two different calibrations of the isotopic thermometer: thick curves correspond to $\alpha_c = 0.8‰\,^\circ\mathrm{C}^{-1}$ and thin curves to $\alpha_c = 0.6‰\,^\circ\mathrm{C}^{-1}$. Note that there is no offset in (c) and (e).

Considering individually each climatic and isotopic sensitivity experiment, the reference (thick solid curve) composition nears an average of $-57‰$ δ^{18}O (Fig. 8.2c) and $-446‰$ δD (Fig. 8.2e).

Different values of D_{acc} provide a similar estimate (thick dash-dotted line). Experiments with a smaller glacial–interglacial amplitude of temperature (T1, dashed line) translates into a slightly isotopically heavier ice sheet, nearing $-56.5‰$ δ^{18}O and $-441‰$ δD. Tests with a lower isotopic sensitivity, which corresponds to a lower climatic amplitude, give estimates that are $\sim 1‰$ heavier for δ^{18}O than the reference α_{c}, $\sim 8‰$ heavier for δD.

8.3.3 Effect of the EAIS on ocean composition

Fig. 8.2d and f show the change in the average δ^{18}O and δD composition of seawater ($\delta^{18}\mathrm{O}_{\mathrm{sw}}$, $\delta\mathrm{D}_{\mathrm{sw}}$) induced by the changes in volume and composition of the EAIS. Description of the calculation procedure is given in Section 3.5.4. By definition $\delta^{18}\mathrm{O}_{\mathrm{sw}}$ and $\delta\mathrm{D}_{\mathrm{sw}}$ of modern seawater is equal to 0. Because of the quasi-constant composition of EAIS, variations in seawater composition are determined by the changes in ice volume; thus, there is little deviation amongst the sensitivity tests. I find that the EAIS caused $\delta^{18}\mathrm{O}_{\mathrm{sw}}$ to decrease by $0.04‰$ during most of the past glacial period and increased by up to $0.02‰$ right after the peak of MIS 5.

8.4 Volume and composition of the West Antarctic Ice Sheet

8.4.1 Ice volume and sea level

Fig. 8.3a shows the volume of the West Antarctic Ice Sheet predicted by the ISM for the past $160\,\mathrm{kyr}$. The simulated modern volume of the WAIS is 4.7–5.0 Mkm^3 whereas observations give $3.8\,\mathrm{Mkm}^3$ (Oppenheimer, 1998). The difference can be attributed to the uncertainty on the exact border of the WAIS and to the fact that the predicted ice sheet is still rapidly losing excess mass from its extensive glacial configuration, possibly owing to a lack of fast flow physics in the model, which diminishes drainage into the Weddell, Ross and Amundsen Seas (Pine Island Bay). The rhythm and relative timing of the sea-level climate forcing could also delay the response of the WAIS (Appendix A.3). The ISM predicts that the volume of the WAIS steadily increased in phase with the sea-level forcing during the glacial period as the ice sheet was overriding its continental shelf. A maximum of 8.7–10 Mkm^3 was reached during the last glacial termination, 12–14 kyr ago, at a time when sea level was still low, because northern hemisphere ice sheets had only started to recede, and precipitation on the ice sheet was rapidly increasing as temperature was rising.

Because most of the bedrock of the WAIS is located below sea level, replacement of water and floating ice by grounded ice over the continental shelf has no effect on sea level even though the volume of the ice sheet is increased; thus, tedious book-keeping of the grounding of ice has to be performed for the WAIS. Fig. 8.3b shows that the ice sheet removed up to the equivalent of 8–10 m of sea level during the past glacial period and might have helped raise sea level by 1.5–2 m during MIS 5 without enduring a complete retreat. The simulation with a lower climate amplitude (T1) has the least influence on sea level.

8.4.2 Isotopic composition of the WAIS

The bulk δ^{18}O and δD composition of the WAIS are shown in Figs. 8.3c and 8.3e with the same conventions to represent the sensitivity study. As for the EAIS, the calculation was performed using two different calibrations of the isotopic thermometer. Though the ice core record from Byrd shows a similar amplitude of δ^{18}O and δD change as for deep East Antarctic cores (Epstein et al., 1970),

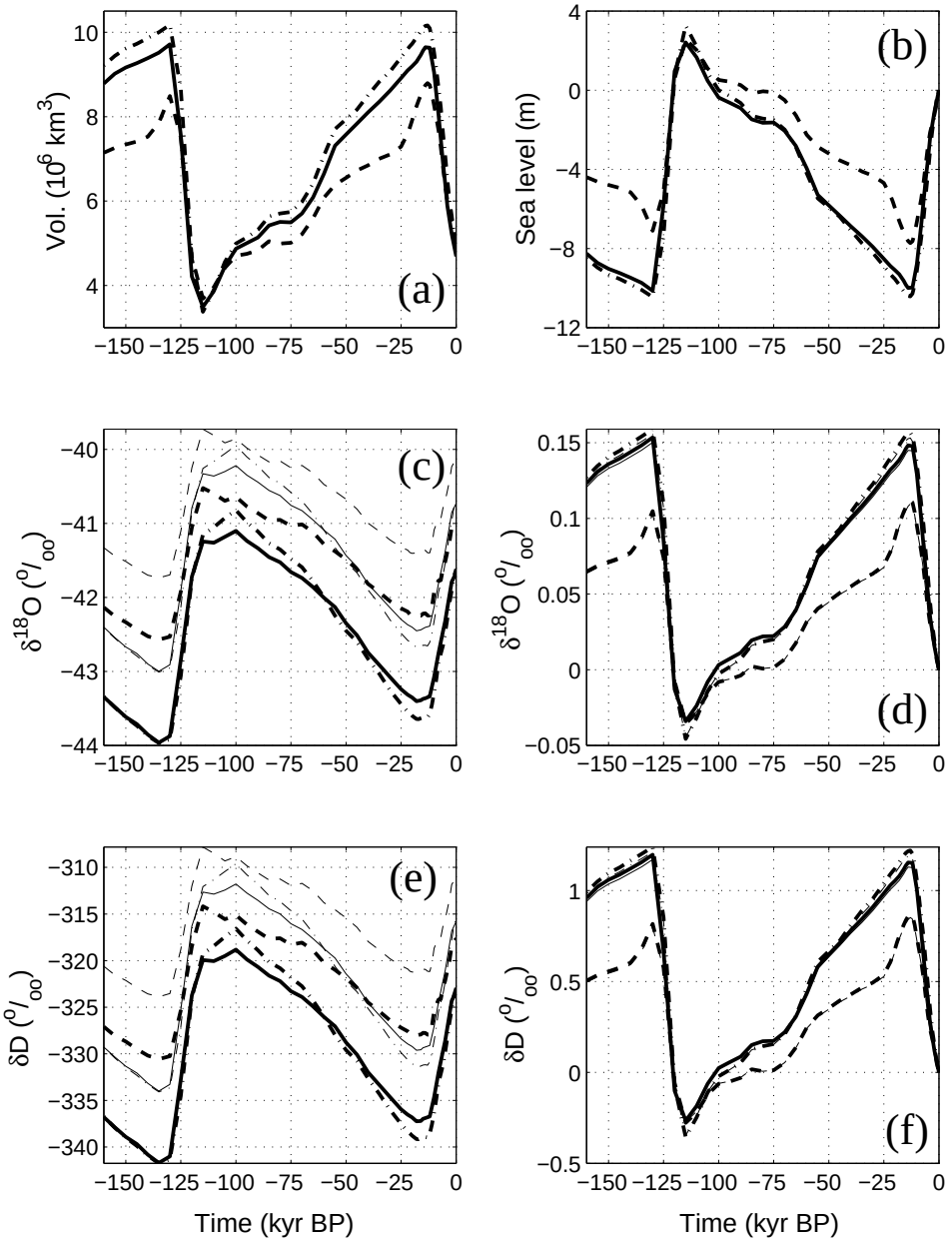

Figure 8.3: Volume and water isotope composition of the WAIS for models T1 (dash), T2 (solid) and T2D (dash-dot). The thickness of the curves distinguishes two different calibrations of the isotopic thermometer: thick curves correspond to $\alpha_c = 0.8‰\,^\circ\mathrm{C}^{-1}$ and thin curves to $\alpha_c = 0.6‰\,^\circ\mathrm{C}^{-1}$.

other Antarctic sites with oceanic-type climate, which characterizes climate over the WAIS, indicate that the isotopic sensitivity α_c can be lower in other parts of Antarctica. For instance at Law Dome, a coastal site along the Vostok–South Pole radial path, $\alpha_c(\delta\mathrm{D}) = 3.5‰\delta\mathrm{D}\,^\circ\mathrm{C}^{-1}$ (Morgan et al., 1997). At Taylor Dome, near the Pacific coast and the separation line between the EAIS and WAIS, $\alpha_c(\delta\mathrm{D}) = 4‰\,\delta\mathrm{D}\,^\circ\mathrm{C}^{-1}$ (Steig et al., 1998). These values suggest that $\alpha_c(\delta^{18}\mathrm{O})$ could be as low as $0.4 - 0.5‰\,^\circ\mathrm{C}^{-1}$ in a coastal environment. Therefore, I attribute equal value to the estimate of bulk isotopic composition calculated with $\alpha_c(\delta^{18}\mathrm{O}) = 0.6$ and $\alpha_c(\delta^{18}\mathrm{O}) = 0.8‰\,^\circ\mathrm{C}^{-1}$, the thin

lines and thick lines, respectively.

Averaging the different climate forcings and isotopic sensitivity, the modern average bulk $\delta^{18}\mathrm{O}$ composition of the WAIS is $-41.1 \pm 0.7‰$ (Fig. 8.3c). During the past glacial period, the average $\delta^{18}\mathrm{O}$ composition of the WAIS lightened as the ice sheet grew and incorporated $^{18}\mathrm{O}$-depleted snow deposited in a cold climate. Depletion became further enhanced because the average surface elevation of the ice sheet increased with ice volume. In this manner, the WAIS received precipitation with a lighter (more negative) $\delta^{18}\mathrm{O}$ composition than the bulk composition of the ice sheet as the glacial epoch progressed, and reached a minimum value 22 kyr ago that was 1.5–$2.0‰$ lighter than the present. That minimum remained quasi-stable between 11–22 kyr BP despite the continuous increase of ice volume and surface elevation during that period because after 18 kyr ago, the beginning of post-glacial warming in Antarctica, high-altitude depletion of $\delta^{18}\mathrm{O}$ became progressively compensated by warming temperature, yielding a higher depositional $\delta^{18}\mathrm{O}$ composition closer to the average value of the ice sheet at that time. Precipitation rate also increased, adding new snow with heavier (less negative) $\delta^{18}\mathrm{O}$. Sea level started to rise 15 kyr ago (Fig. A.5) but the WAIS continued to grow for another 2–3 kyr because of the enhanced precipitation and kept a stable isotopic composition. Then the WAIS quickly lost its large bulges located in the Weddell and Ross basins and composed of old ice with low $\delta^{18}\mathrm{O}$ composition while simultaneously accumulating new snow with heavier $\delta^{18}\mathrm{O}$ in the central region. As a result, the bulk composition of the ice sheet rapidly increased toward its modern value.

A similar $\sim$20-kyr-long quasi-plateau was found between the end of MIS 5 and the beginning of the next glaciation, from 115 to 95 kyr BP. The period began just before the ice sheet reached its minimal volume, receding to a high standing configuration and losing old glacial ice with low $\delta^{18}\mathrm{O}$ composition, leading to a bulk $\delta^{18}\mathrm{O}$ composition $\sim 0.5‰$ heavier than the modern one because of a smaller size and a warmer climate. Climate cooled off in the ensuing years, the WAIS started to spread again and lower its elevation because its warm internal ice temperature (from MIS 5) decreased ice viscosity. Therefore the new ice was deposited at a similar composition as the average ice sheet because of the compensating effect of colder climate and lower elevation. That trend lasted until 95 kyr as the WAIS regained a configuration similar to the modern one, growing at relatively low elevation in a cold stable climate; thus, the bulk composition of the ice remained quasi-stable. The same analysis applies to the bulk $\delta\mathrm{D}$ composition (Fig. 8.3e) of the WAIS via the water meteoric line with a present–LGM amplitude of 12–$16‰$.

8.4.3 Effect of the WAIS on sea water composition

Given the relatively light composition (strong $^{18}\mathrm{O}$-depletion) of the West Antarctic Ice Sheet and its large volume change between the present and the end of the last glacial period, the storage and release of water isotopes in the WAIS has a significant impact on the composition of the ocean. Calculations in Fig. 8.3d show that the ice sheet caused a 0.03–$0.05‰$ decrease of $\delta^{18}\mathrm{O}_{\mathrm{sw}}$ when it lost mass during MIS 5, before increasing $\delta^{18}\mathrm{O}_{\mathrm{sw}}$ up to 0.12–$0.16‰$ at the end of the last glaciation, enriching the $^{18}\mathrm{O}/^{16}\mathrm{O}$ ratio of the ocean by sequestering $^{18}\mathrm{O}$-depleted ice in the growing ice reservoir. The result is relatively insensitive to the calibration of α_{c} because the dominant factor is the change of volume. The equivalent change in $\delta\mathrm{D}_{\mathrm{sw}}$ is $-0.3‰$ at the end of MIS 5 and 0.8–$1.2‰$ at 15 kyr BP (Fig. 8.3f).

8.5 Volume and composition of the Greenland Ice Sheet

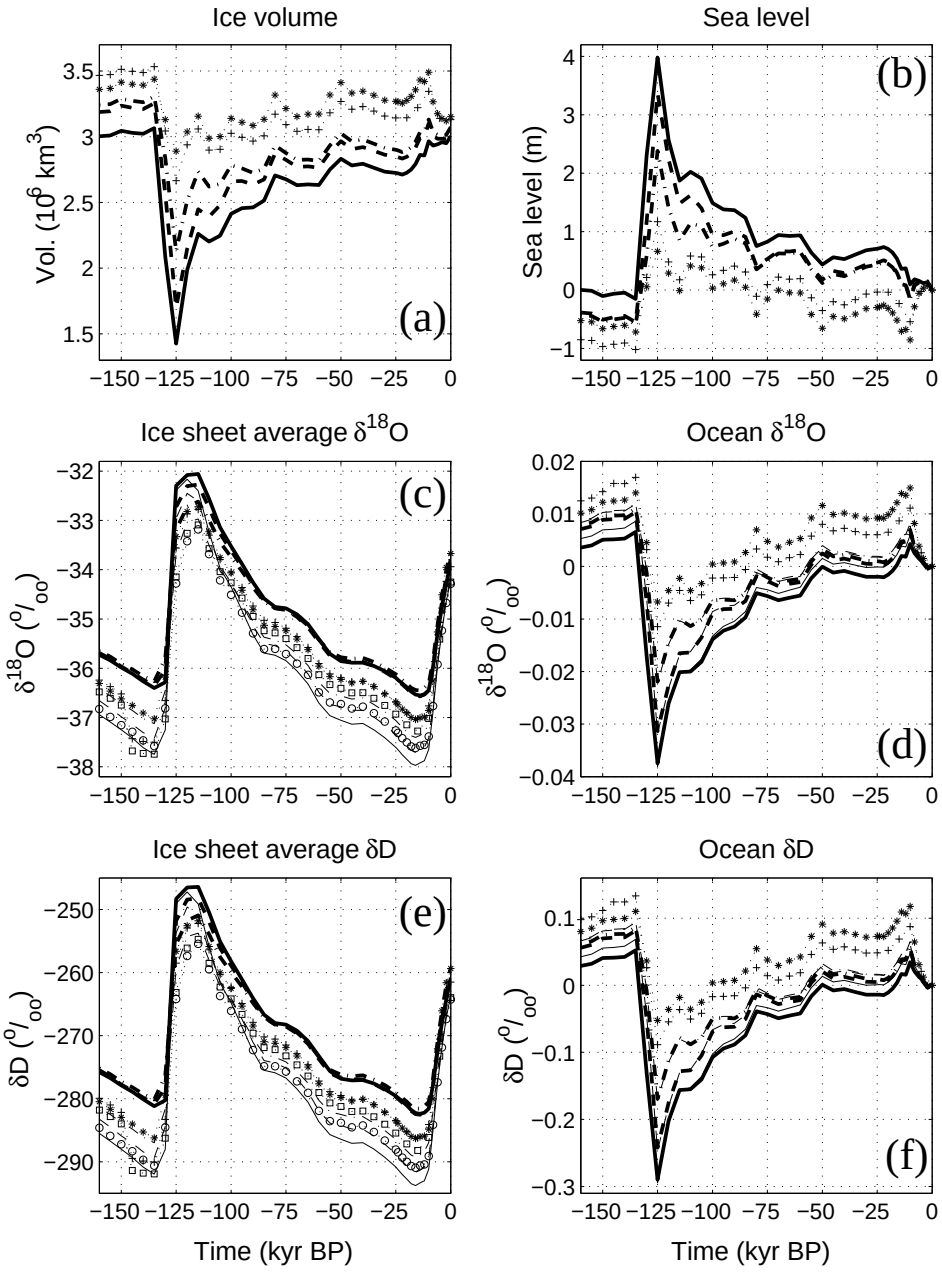

Figure 8.4: Volume and isotopic composition of the GIS for the best models from Chapter 5 (Table 5.1): model A3 (solid), B1 (dash), C1 (dash-dot). Different calibrations are used: time-varying α_c from each climate forcing (thick lines), spatially-varying α_c (thin lines) predicted by an AGCM. Models D1 ($+$ symbols) and E1 ($\times$ symbols) that predict larger volume and extent of the GIS than A3–C1 are added: $+$ and $\times$ for the time-varying α_c, squares and circles for the spatially-varying α_c, respectively.

8.5.1 Ice volume and sea level

Models A3, B1 and C1 were considered as the most compatible with the present Greenland ice cores and ice-sheet geometric features (Chapter 5). As shown in table 5.1, each model has different climatic and dynamic parameters, especially the viscosity of interglacial ice and the isotopic sensitivity of MIS 5. The effect on the volume of the Greenland Ice Sheet (GIS) is presented in Fig. 8.4a. Predictions for models A3–C1 appear to depend inversely on the flow enhancement factor, C1 showing the largest volume through the past 160 kyr with $E_{\rm I} = 2.0$ and $E_{\rm G} = 5.1$ (Section 4.2.1). Thus, the stiffest ice results in the largest volume. Considering the glacial period, it seems surprising at first that the volume of the GIS was equal or smaller than its modern value for these models.

Several factors can limit the past size of the ice sheet. Firstly, the surface mass balance was 3–4 times lower during the glacial period, lowering surface elevation in the central part of the ice sheet by 300–400 m at LGM (Fig. 5.4), thus a $\sim$10% reduction of ice thickness. Secondly, the modern ice sheet only covers $\sim$1.6 Mkm^2 of the $\sim$2 Mkm^2 emerged area of Greenland; thus, there is ample space for the GIS to expand. That open space was even larger during the glacial period when the decrease of sea level dried parts of the narrow continental shelf. The ice sheet was then expected to spread beyond its modern margins because 20°C-colder surface temperature should have limited or eliminated summer melting at low elevation. Close analysis of the results for models A3–C1 indicates that the reconstructed ice sheet remained within 5% of its modern surface area throughout the last glaciation. As previously discussed in Chapter 5, the coarse and simplified parameterization of surface climate adopted in this study might underestimate the accumulation of new ice at the poorly resolved ice margins, where the distribution of elevation plays an important role on the surface mass balance (Marshall and Clarke, 1999).

In contrast to models A3–C1, non-selected models like D1–3 and E1–2 predict that the ice sheet reached the modern sea shores, covering $\sim$2 Mkm^2 during most of the glacial period. Models A3 and E2, B1 and E1, use the same type of parameterization and the same value of dynamical factors and glacial isotopic sensitivity. My results therefore suggest that the predicted GIS cannot grow much beyond its modern boundaries if $\alpha_{\rm cE} \leq 0.4‰\,^\circ{\rm C}^{-1}$ (E for Eemian or MIS 5), that is if it lost a substantial amount of ice during MIS 5. The volume and isotopic composition predicted by models D1 ($+$ symbols) and E1 ($\times$ symbols) are therefore added to Fig. 8.4 to illustrate the particular sensitivity of the ice sheet model to the Eemian isotopic factor.

8.5.2 Isotopic composition of the GIS

Two different methods are tested to calculate the bulk δ^{18}O composition of the GIS. The reference method (thick lines in Fig. 8.4) consists in applying the spatially uniform but time-varying $\alpha_{\rm c}$ that was used to define the climate forcing of each model. Thus the calibration is different between each of the presented models and corresponds to the values in Table 5.1. I denote this calibration $Cal1$. A second method $Cal2$ uses the spatially varying $\alpha_{\rm c}$ obtained with the GISS 8°$\times$10° (latitude, longitude) AGCM that includes isotopic processes (Jouzel et al., 2000), illustrated in Fig. 8.5. Given that the latitudinal resolution of the GISS-AGCM grid is especially coarse at the latitude of Greenland, a pseudo-linear interpolation was performed to increase that resolution to 4°, imposing lower values south of GRIP to reflect results from borehole studies (e.g., $\alpha_{\rm c}$=0.33$‰\,^\circ{\rm C}^{-1}$, Cuffey and Clow, 1997). In this manner, the domain is divided in 4°$\times$10° boxes where a uniform $\alpha_{\rm c}$ value is applied. Values for the 72–76°N latitudinal band (0.50, 0.48, 0.41) are clearly in contradiction with borehole

studies. I refrain however from freely modifying these for the sake of the sensitivity study so that the effect on the predicted bulk δ^{18}O composition can be measured, even though I recognize that some of the GISS-AGCM predictions are likely to be erroneous because Jouzel et al. (2000) assumed that central Greenland reached 3600 m at the LGM (ICE-4G, Peltier, 1995), whereas all subsequent studies including this one find a lowering to 3000 m. An opposite bias is known to contaminate the topography of the Laurentide Ice Sheet, implying changes in the atmospheric circulation and thus in isotopic depositional patterns, adding to the uncertainty of the temporal slopes predicted by the GISS-AGCM, especially in its $8^\circ\times10^\circ$ configuration. For the same reasons I do not attempt to perform a smooth interpolation of the GISS-AGCM values at the surface of the ice sheet. I note here that the flexibility of the tracer transport and depositional archive is particularly well-suited to measure the sensitivity of the bulk isotopic composition of the ice sheet relative to the uncertainty in isotopic depositional rate and pattern.

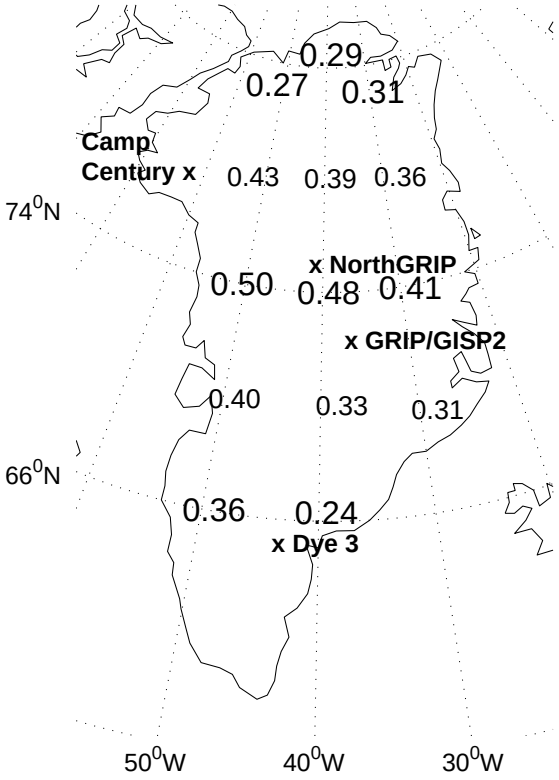

Figure 8.5: Values of the temporal slope α_c predicted with the GISS-AGCM on a $8^\circ\times10^\circ$ grid (Jouzel et al., 2000) are indicated in large characters, interpolated values are in smaller font. Ice core drilling sites are located near $\times$ marks.

Fig. 8.4c shows the average δ^{18}O composition of the Greenland Ice Sheet over the past 160 kyr; Fig. 8.4e the δD content. As expected, the GIS became lighter in ^{18}O (and D) as the past glaciation progressed because the ice sheet received and stored ice with low δ^{18}O value, e.g., $-41^\circ/_{\circ\circ}$ at GRIP as opposed to $-35^\circ/_{\circ\circ}$ for modern conditions. The Eemian composition is heavier than the modern value because all my simulations predict warmer climatic conditions and a smaller ice sheet, increasing the relative contribution of ice that carries a warm δ^{18}O. The present bulk composition is $-34\pm0.2^\circ/_{\circ\circ}$ for δ^{18}O and $-262\pm2^\circ/_{\circ\circ}$ for δD. For the LGM, δ^{18}O lies between $-36.5^\circ/_{\circ\circ}$

and $-38.0‰$, thus a 2.5–4$‰$ variation between the present and the LGM, less than the 5–6$‰$ suggested by earlier studies (e.g., Dansgaard and Taubert, 1969; Duplessy et al., 2002). The Eemian prediction ranges from$-32.0‰$ to $-33.2‰$. Differences of bulk composition at any given time between each prediction result from the different dynamic and isotopic sensitivities (climate forcing and isotopic deposition).

The water isotopic compositions for models A3–C1 are lighter with calibration $Cal1$ (thick lines) than with $Cal2$ because the latter generally uses larger α_c's, increasing the isotopic contrast during glacial periods. For instance, a $18°$C cooling diminishes δ^{18}O by $6‰$ from its modern value with α_c ∼0.33 used in $Cal1$; with α_c=0.40, an average value for $Cal2$, δ^{18}O decreased by $7‰$. Consequently, the difference in bulk composition between the two calibrations differs the least at present and during the Eemian and the most at the end of a glacial period. This particularly applies to model A3 because it predicted the most ice loss during the Eemian, allowing the ice sheet to incorporate a larger proportion of ^{18}O-depleted ice during the subsequent glacial period. Models B1 and C1 accordingly rank as a function of their minimal Eemian ice volume for $Cal2$ because the same α_c's are used (thin lines), whereas A3–C1 overlap with $Cal1$ despite different glacial ice volume because of the compensating effect of their different time-varying α_c's (thick lines): e.g., the small glacial volume of A3 contains highly depleted ice because of the low α_{cG} (glacial value) and α_{cE} (Eemian).

The bulk isotopic composition for experiments $D1$ and $E1$ had an intermediate value throughout the past 160 kyr ($+$ and $\times$ overlap in Figs. 8.4c and e). The composition was lower with $Cal1$ than for A3–C1 during the glacial period and the Eemian because the ice sheet had a larger volume, incorporating more glacial ice; ice from the Eemian also had lower δ^{18}O because the predicted climate was colder. The difference between the compositions obtained with $Cal1$ and $Cal2$ is smaller than A3–C1, $0.2‰$ δ^{18}O for D1 and $0.5‰$ δ^{18}O for E1, because large α_{cE} compensates for low α_{cG} in $Cal1$ with respect to the values of $Cal2$, and also because the excess of ice relative to A3–C1 was deposited in the southern part of the ice sheet, where spatially-varying α_c's are similar to α_{cG} (Fig. 8.5). Not presented here, I tested the sensitivity of the calibration method, for instance lowering α_c in $Cal2$ for the central part of the GIS to reflect borehole temperature results, or using the relative change of α_c in $Cal1$ to perturb $Cal2$ and construct a time-and-space-varying calibration. I found that the calibrations $Cal1$ and $Cal2$ represent reasonable end-member methods to calculate the bulk isotopic composition of the Greenland Ice Sheet.

8.5.3 Effect of the GIS on sea water composition

The difference between calibration methods disappears when the contribution of the Greenland Ice Sheet to the ocean composition is calculated (Figs. 8.4d and f). Change in sea water composition is primarly influenced by ice volume. Therefore models A3–C1 have little effect during the glacial period, when the average δ^{18}O of the ocean increased by $\sim 1 \pm 0.3‰$ (e.g., Schrag et al., 1996; Waelbroeck et al., 2002). Greenland contributes at most 1% of that change for the simulations D1 and E1. The effect of the GIS is more significant during the Eemian, reducing $\delta^{18}O_{sw}$ by up to $-0.04‰$. The maximum corresponding changes in δD_{sw} from the GIS are $+0.1‰$ for the glacial period and $-0.3‰$ at the peak of the Eemian.

8.6 Discussion: ice sheets and sea water composition

8.6.1 Sea level vs. sea water composition

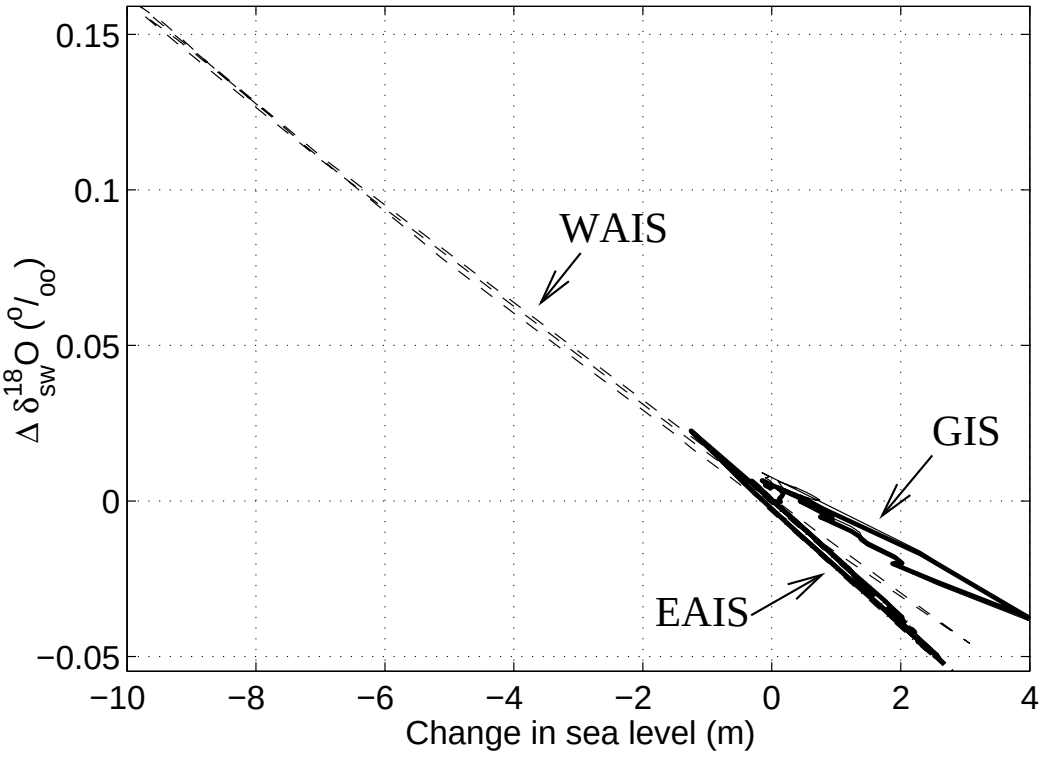

Figure 8.6: Influence of the glacial–interglacial volume changes of the ice sheets on sea level and sea water isotopic composition for the EAIS, WAIS and GIS.

Interpretation of δ^{18}O records, especially marine records, assumes a linear relationship between the ice volume and the isotopic composition $\delta^{18}\mathrm{O}_{\mathrm{sw}}$ of sea water. Rates of 0.085–0.011$^{\circ}/_{\circ\circ}$ per metre change in sea level have been estimated from corals and deep-sea sediments (e.g., Fairbanks, 1989; Schrag et al., 1996). Considering the relationship for each of the East Antarctic, West Antarctic and Greenland Ice Sheets in Fig. 8.6, there appears to be a high degree of correlation between our predicted $\delta^{18}\mathrm{O}_{\mathrm{sw}}$ and change in sea level. For the WAIS, which experienced the largest changes in volume, I find a rate of $\sim$0.015$^{\circ}/_{\circ\circ}\,\mathrm{m}^{-1}$ that includes the special relationship between ice volume and sea level of the WAIS. For the EAIS, a larger rate of $\sim$0.016$^{\circ}/_{\circ\circ}\,\mathrm{m}^{-1}$ illustrates that the average composition of the EAIS is lighter (δ^{18}O more negative). For the GIS, a lower rate of $\sim$0.010$^{\circ}/_{\circ\circ}\,\mathrm{m}^{-1}$ reflects the heavier bulk composition of the warmest polar ice sheet. I find that, for each of the ice sheets, these same rates apply for all the calibrations and climatic experiments that were tested in this study.

8.6.2 Last Glacial Maximum

With a contribution to $\delta^{18}\mathrm{O}_{\mathrm{sw}}$ of $-0.04^{\circ}/_{\circ\circ}$ for the EAIS, $+0.11$ to $+0.15^{\circ}/_{\circ\circ}$ for the WAIS and less than $+0.01^{\circ}/_{\circ\circ}$ for the GIS, polar ice sheets account for at most 10% of the measured change in sea

water composition at the peak of the last glaciation (e.g., Labeyrie et al., 1987; Adkins et al., 2002). This polar contribution of $0.10‰$ also corresponds to the admitted error in the interpretation of sea-sediment records (Labeyrie et al., 1987) and is lower than the current level of uncertainty on the value of $\delta^{18}O_{sw}$ at LGM of $\pm 0.3‰$. The joint change in ice volume due to the polar ice masses drew down sea level by 5–10 m at LGM, which is insignificant relative to the total change of 120–135 m.

Amongst the polar ice sheets, the Greenland Ice Sheet most resembles the former Laurentide and Fennoscandian Ice Sheets (LIS and FIS) because Antarctica experiences a much colder climate. Greenland is located between 60–85°N whereas the Northern Hemisphere glaciated region extended as far south as 45°N, reaching into a warmer climate than southern Greenland. A significant part of the former ice sheets was initially formed at low elevation (e.g., Marshall, 1996). Therefore the LIS and FIS certainly received on average higher $\delta^{18}O$ (less depleted) than Greenland during the first half of the glacial period; thus, the bulk isotopic composition of the GIS is an absolute lower bound for their composition. In the latest phase of the glaciation, the LIS and FIS grew high domes with climatic conditions possibly similar to central Antarctica, but also expanded southward to warmer conditions, while keeping some ice from the first phase of the glaciation with relatively warm $\delta^{18}O$. Their average isotopic composition at LGM must consequently have remained larger or equal to the GIS, which was also becoming increasingly ^{18}O-depleted.

8.6.3 In an ice-free world

Another question of interest is the composition of sea water if all the ice sheets melted or before they formed. I find that complete melting of the ice sheets would decrease $\delta^{18}O_{sw}$ by $0.91 \pm 0.02‰$, $0.13 \pm 0.01‰$ and $0.07‰$ for the EAIS, WAIS and GIS, respectively, yielding a total effect of $1.11 \pm 0.03‰$. This estimate is consistent with the $\sim 1‰$ step increase that is recorded in deep-sea sediments when, 34 Myr ago, a full-scale Antarctic Ice Sheet developed and persisted (Zachos et al., 2001). Using the meteoric water relationship, all the above results can be extended to yield estimates of δD. The calculated joint contribution of $-1.11 \pm 0.03‰$ $\delta^{18}O$ and $-8.88 \pm 0.24‰$ δD of modern polar ice sheets closes the global water-isotope budget of the Earth and can be used to obtain the ocean composition of an ice-free world.

8.6.4 Interglacials

Great attention has been directed to the Eemian (MIS 5) and MIS 11 (Fig. 8.7) because their warm climatic conditions provide valuable insight into the sensitivity of the current climate. The Eemian was believed to be ~ 2°C warmer than modern conditions in central Antarctica (Fig. 8.7 and EPICA community members, 2004) and ~ 5°C warmer in Greenland (NGRIP Members, 2004). The Vostok record (GT4, Petit et al., 1999) used for predicting the climate in Greenland before 100 kyr BP and the EPICA-Dome C record (EDC2, EPICA community members, 2004) for Antarctica show differences in the timing and duration of MIS 5. The peak of temperature in the GRIP–Vostok forcing occurred near 128–129 kyr BP while it appeared 2–3 kyr later for Dome C. Therefore we cannot strictly compute the joint contribution from Greenland and Antarctica at any given time during that period, though the EAIS and WAIS can be compared and we can still discuss their own effect on $\delta^{18}O_{sw}$ in the context of a 5–6-m sea level rise.

For the EDC2 timescale, results show that the EAIS might have grown for a short period during MIS 5 because of the increased precipitation rate, removing up to 1.5 m of sea level equivalent and

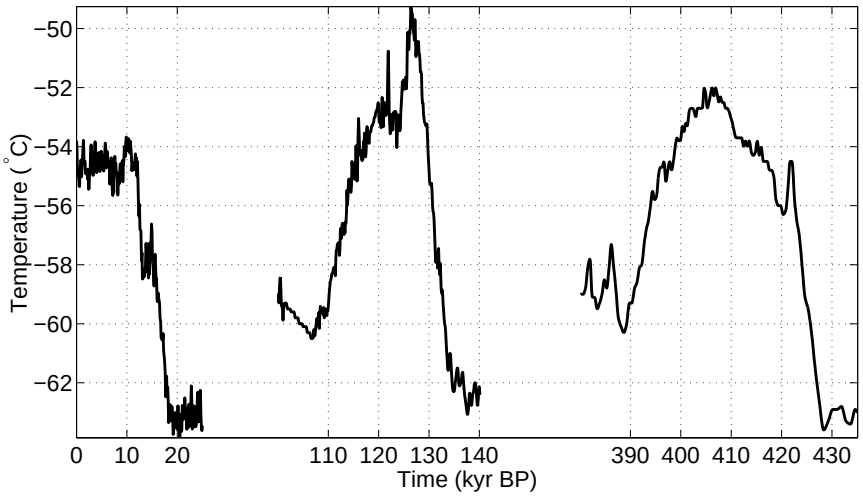

Figure 8.7: Marine Isotope Stages 1, 5 and 11 in the Dome C record (EDC2 chronology).

increasing $\delta^{18}\mathrm{O_{sw}}$ by $0.02‰$ at 125 kyr BP, 1 m at 120 kyr BP and 0 m at $\sim$112 kyr BP and later losing mass as the next glaciation started. In contrast, the WAIS considerably diminished between 130 and 115 kyr BP, receding from a configuration in which it was removing 8–10 m of sea level to one in which it added 2.5–3 m relative to its present size. The minimum volume at 115 kyr BP occurred 11 kyr after the peak of MIS 5 and at the beginning of the cooling phase into the next glaciation. The 2.5–3-m rise corresponds to -0.03 to $-0.04‰$ of $\delta^{18}\mathrm{O_{sw}}$. We can speculate that $5\,\mathrm{m}$ of melting from the WAIS would decrease $\delta^{18}\mathrm{O_{sw}}$ to $\sim -0.08‰$, half as much a change as the $\sim -0.15‰$ inferred from a compilation of marine sediment records by Labeyrie et al. (1987), which means that their study might have underestimated seawater temperature for that time.

The dynamical history of the Greenland Ice Sheet significantly differs from that of Antarctica. The GIS reached its minimum volume and extent near 127 kyr BP immediately following the peak of MIS 5, then growth resumed even though temperature in our climate forcing remained warm and similar to modern values, whereas the WAIS continued to shrink during that warm period, irrespective of the difference between the GT4 and EDC2 chronologies. Therefore the two ice sheets could not have reached their minimal configuration at the same time even if the MIS 5 warm period had been synchonized. The earlier melting in Greenland provided up to $4\,\mathrm{m}$ of sea level rise, $4.5\,\mathrm{m}$ during a brief period near 127 kyr BP (not apparent in Fig. 8.4 because of the time step of the provenance archive), and a negligible 0.03–0.04‰ decrease of $\delta^{18}\mathrm{O_{sw}}$ at 125 kyr BP (GT4 time). The results from Chapter 5 on Greenland ice core rule out further melting of the GIS: $0.04‰$ is therefore the maximum possible reduction in $\delta^{18}\mathrm{O_{sw}}$ from the GIS in the middle of MIS 5.

MIS 11 is also a period of interest because its astronomical characteristics most resemble the Holocene (e.g. Berger and Loutre, 2002). A rise of 13–20 m of the global sea level has been suggested (e.g., Drowler et al., 2002), yielding the prospect of a complete disappearance of the WAIS and GIS, and possibly parts of the EAIS. My calculations show that the direct decrease in $\delta^{18}\mathrm{O_{sw}}$ from the equivalent of 13 m of ice volume from the entire GIS and WAIS is $0.20‰$ and that additional melting in East Antarctica to reach 20 m would diminish $\delta^{18}\mathrm{O_{sw}}$ by $0.31‰$. These estimates could be used to study the temperature of the ocean during MIS 11.

8.7 Conclusion

The foregoing estimates of polar ice composition are the first to use a framework that is consistent with most ice core records and the state-of-the-art in ice sheet modelling. Different calibration methods were applied to reflect the current uncertainty concerning the past $\delta^{18}\mathrm{O}$ pattern. Further studies with finer parameterization of $\delta^{18}\mathrm{O}$ obtained from climate–ice sheet models should certainly improve these estimates but should still fall within the suggested range of values. The LGM composition of Greenland ice (–37‰) establishes an absolute lower bound on the past composition of the Laurentide and Fennoscandian Ice Sheets, a composition that remains the biggest challenge for inferring the temperature of the glacial ocean. Detailed studies of Northern Hemisphere ice sheets are in progress.

CHAPTER 9

Conclusion

The following paragraphs review key issues raised in this thesis and present some concluding thoughts without repeating the results of the research chapters, which contain their own discussions and conclusions.

9.1 Tracers

This manuscript has presented a new method for accurately and efficiently tracking ice particles from the point of deposition on an ice sheet. The method, based on the original work by Clarke and Marshall (2002), constitutes a significant improvement in tracer transport models for ice sheet studies because it specifically addresses the special age–depth relationship observed in ice (e.g., Dahl-Jensen, 1989). This is achieved by the introduction of a cumulative balance function that accounts for the variable thickness of annual layers of ice along vertical profiles. The simplest form of this age-interpolation technique is shown to apply satisfactorily for modelling the stratigraphy and evolution of the Greenland and Antarctic Ice Sheets. Indeed, evidence from ice core records retrieved from both polar ice masses suggests that large-scale and quasi-uniform changes in temperature and temperature-dependent changes in surface mass balance have affected Greenland (Johnsen et al., 2001) and Antarctica (Watanabe et al., 2003) over the past hundreds of kyr. Therefore I could use a spatially-uniform climate forcing (ΔT_{c}) and balance function (Ω) primarily constructed, for Greenland, with the GRIP ice core record (Johnsen et al., 1997), and for Antarctica with the EPICA-Dome C ice core record (EPICA community members, 2004). I note that more complex forms of the interpolation technique can readily be used for modelling large ice masses for which distinct regional climatic regimes apply because, in essence, the tracer provenance method contains the source information that allows the use of a region-specific cumulative balance function for ice of a given age. I believe that this geographic adaptability would be especially useful, for instance, for large-scale modelling of former Northern Hemisphere ice sheets, where oceanic, topographic and continental effects result in spatially-variable changes in surface temperature and mass balance.

The tracer provenance model is used in conjunction with a depositional model, an archive that contains so-called construction variables (surface temperature, elevation and mass balance) from which the past distributions of water isotopic depositional rate can be derived. This framework is particularly interesting because the sensitivity of the relationship between construction variables and water isotopes could be tested without having to redo a simulation of Greenland or Antarctic past evolution. Therefore estimations of the bulk isotopic composition of the polar ice sheets can either reflect the relative simplicity assumed for the climate forcing, using a spatially uniform climatic sensitivity, or incorporate some regional effects suggested by Atmospheric General Circulation Models that include isotopic processes.

9.2 Glaciological results

In the different studies presented in Chapters 4 to 7, I have considered some glaciological questions that tracers can help elucidate, with the over-arching goal of designing a well-constrained reconstruction of the Greenland and Antarctic Ice Sheets for Chapter 8. For this purpose tracers have directly been combined with the state-of-the-art ice sheet models from UBC and LGGE, performing only minor modifications to study Greenland (age-dependent ice rheology, climate-dependent isotopic sensitivity, local change of bedrock topography) and Antarctica (local change of bedrock topography, temperature and precipitation, climate forcing taken from Dome C), especially for the detailed analysis of ice layering at ice core sites. Matching the stratigraphy of the deep ice cores from GRIP, GISP2, Dye 3 and Camp Century for Greenland, Dome C, Vostok and Dome Fuji for Antarctica has added a valuable constraint on ice sheet models.

With this framework I have predicted the three-dimensional depositional stratigraphy of the Greenland (Chapter 4) and Antarctic Ice sheets (Chapter 6). This has illustrated the main patterns of ice flow, the regions where old ice can be expected and the average age of the ice sheets. Detailed analysis of the predicted depositional properties at ice core sites have provided useful information regarding the dynamic and climatic state of both ice sheets during critical epochs.

In Chapter 5 on Greenland, the depositional conditions of GRIP ice have been studied by forcing the ice sheet model with a GRIP-based climate to reproduce with acceptable accuracy the fine layering of the GRIP ice core. This constraint has provided a test on the climatic and dynamic parameters of the model and demonstrated their sensitive effect on the ice origin of GRIP, the depositional elevation and the migration of the Summit of the ice sheet during the past glacial cycles. By predicting the bottom stratigraphy at Camp Century and Dye 3, records which had previously been dismissed for revealing useful information on the last interglacial period, I improved the reconstruction of the minimal extent and volume of the Greenland Ice Sheet for that period. I find a maximum contribution of 3.5 to 4.5 m to sea level rise near 127 kyr BP. Results just published for the NorthGRIP ice core record (NGRIP Members, 2004), not available when Chapter 6 was written and the corresponding paper was submitted (Lhomme et al., in press), do not appear to contradict my conclusions. In fact, this new record cannot readily be included as a constraint because the current configuration of the model does not include the strong geothermal heat flux anomaly and the intense nearby drainage by the northestern ice stream, which both significantly affect NorthGRIP.

In Chapter 7 on Antarctica I have discussed the hypotheses used for dating the deep ice core records from Vostok, Dome C and Dome Fuji and the potential to improve their interpretation through the combined ice sheet–tracer model. I demonstrate that the three-dimensional thermomechanical ice model reveals valuable information on past depositional conditions, ice origin and re-organization of ice flow and surface topography resulting from glacial–interglacial variations. Although these features should be incorporated in future attempts at interpreting ice core records, I acknowledge that missing physical processes such as longitudinal stresses, which are especially active at domes, limit the applicability of my method. Future work warrants efforts towards addressing this issue.

Finally in Chapter 8 I have proposed the first glaciologically based and ice-core-constrained estimates of the bulk isotopic composition of the Greenland and Antarctic Ice Sheets. This study addresses an essential question that had so far been treated by assuming that a single ice core record could represent the average layering of an entire ice sheet (Dansgaard and Taubert, 1969; Duplessy et al., 2002). Because large uncertainty remains in the past distribution of water isotopic depositional rates over polar ice sheets, several calibrations of the isotope–temperature relationship have been

tested. For Greenland, for which I tested uniform and AGCM-derived spatially-varying isotopic sensitivities (Jouzel et al., 2000), I find that the combined effect of dynamic, climatic and isotopic parameters cause a standard deviation on the predicted bulk composition of the Greenland Ice Sheet of $0.2\,{}^{\circ}\!/_{\!\circ\circ}$ for the present and $0.8\,{}^{\circ}\!/_{\!\circ\circ}$ for the Last Glacial Maximum. There is ample room for future work to improve these estimates.

9.3 Suggestions for future work

Modifications to the standard setup of the UBC and LGGE Ice Sheet Models have been kept to a minimum to emphasize the net benefit of including tracers. Further improvements are suggested throughout this manuscript but would necessitate significant testing and calibration before being applicable. Years of research have taught me that the smallest alterations of the ice sheet and tracer models represent a large time investment. Even though the duration of a simulation has diminished by a factor of 20 since the beginning of my thesis, it still takes 20–50 hours to run a simulation and several more hours to analyse its output.

Among the much needed improvements, I believe that the first and most straightforward one is the implementation of a spatially varying distribution of the geothermal heat flux for Greenland and Antarctica, instead of the assumed uniform value in the two models. This has already been tried for Greenland (Tarasov and Peltier, 2003) and would provide more reliable predictions of basal conditions principally at NorthGRIP, but also at Dye 3 and Camp Century. Though there are fewer data to constrain such a representation for Antarctica, the discussion on model parameters in Chapter 7 and Appendix D.1 suggests that the lack of spatial variability limits comparison of the Dome C and Dome Fuji records.

Discussed in Chapter 7 and also relevant for Chapter 5, the absence of longitudinal stresses in the shallow-ice approximation used for ice sheet studies particularly undermines the predicted stratigraphy at domes. Because these missing stresses would mostly affect the upper part of the ice column (Raymond, 1983; Dahl-Jensen, 1989; Parrenin, 2002), my reconstruction of Holocene surface mass balance at GRIP, Dome C and Dome Fuji is certainly underestimated. Comparision at Dome C of the precipitation inferred from the record and that used in my model suggests a difference of $\sim$4%. More work is warranted.

The simple dynamic and climatic treatment of ice margins is an additional source of uncertainty in my predictions, especially for the reconstruction of the Greenland Ice Sheet during the Eemian. In general, margins also play a crucial role because their shape influences ice flow far inland (e.g., Cuffey and Clow, 1997) and because ablation is mostly confined to that region (e.g., Ritz et al., 1997). The shape of margins depends on the vertical distribution of surface mass balance, a subgrid process in most ice sheet models that refined treatment can improve (Marshall and Clarke, 1999). The simple calculation of ablation with the Positive Degree Day method (Reeh, 1991) might however introduce large errors because its calibration based on modern melt rate fails if the frequency of precipitation events changed in the past (feedback on surface albedo, Lhomme, 1999). Ice dynamics are also poorly treated at the margins because outlet glaciers, which drain most of the ice sheets, are ignored by the grid resolution, and because the shallow-ice approximation fails in this region where the width of glaciers is considerably reduced relative to their thickness. Adequate treatment of the margins would therefore require much work and dramatically increase computational time. Ice dynamics models could furthermore be improved by including the effect of ice streams and basal hydrology, processes that exert an especially strong control on the West Antarctic Ice Sheet (Payne,

1999).

The basic treatment of climate at the margins relates to the broader lack of regional representation of the climate in ice sheet models. Although records suggest similar large-scale changes at the surface of ice sheets, small-scale patterns have certainly had an effect. Their signature is visible, for instance, at Camp Century, where the isotopic sensitivity appears to differ from that at GRIP (Chapter 5). Future work with AGCMs is warranted. Preference would be given to models like ECHAM and the one from the GISS (Jouzel et al., 2000) because these could simultaneously provide temperature, precipitation and water isotopic deposition on ice sheets. For the immediate future, these models remain however too computationally intensive to run with an ice sheet model. I have tried to use snapshots of the climate at critical periods obtained by the ECHAM model (Hoffmann, *pers. comm.*) for predicting the stratigraphy and isotopic composition of the Greenland Ice Sheet (Lhomme et al., 2002), but I believe that my estimates could be improved with an updated distribution of ice sheet topography and sea surface temperature in ECHAM.

One large question remains to be addressed: the volume and bulk isotopic composition of Northern Hemisphere ice sheets during the Last Glacial Maximum, a result that the paleo-oceanographic community requires to estimate temperature in the glacial ocean. My thesis constitutes a significant step towards the resolution of that question. Detailed studies with a model of Northern Hemisphere ice sheets derived from Ritz et al. (2001) and coupled with the CLIMBER climate model in relation with the study of Roche et al. (2004) are in progress.

REFERENCES

Abe-Ouchi, A., H. Blatter, and A. Ohmura, 1994: How does the Greenland Ice Sheet geometry remember the ice age. *Glob. Plan. Change*, **9**, 133–142.

Adkins, J. F., E. A. Boyle, L. Keigwin, and E. Cortijo, 1997: Variability of the North Atlantic thermohaline circulation during the last interglacial period. *Nature*, **390**, 154–156.

Adkins, J. F., K. McIntyre, and D. P. Schrag, 2002: The salinity, temperature and δ^{18}O of the glacial deep ocean. *Science*, **298**, 1769–1773.

Albrecht, O., 2000: Dynamics of glaciers and ice sheets. A numerical model study, Ph.D. thesis, ETH, Zürich, Switzerland.

Alley, R. B., D. A. Meese, C. A. Shuman, A. J. Gow, K. Taylor, M. Ram, E. D. Waddington, and P. A. Mayewski, 1993: Abrupt increase in Greenland snow accumulation at the end of the Younger Dryas event. *Nature*, **362**, 527–529.

Alley, R. B., A. J. Gow, S. J. Johnsen, J. Kipfstuhl, D. A. Meese, and T. Thorsteinsson, 1995: Comparison of deep ice cores. *Nature*, **373**, 393–394.

Alley, R. B., et al., 1997: Visual-stratigraphic dating of the GISP2 ice core: Basis, reproducibility, and application. *J. Geophys. Res.*, **102**, 26,367–26,381.

Anandakrishnan, S., R. B. Alley, and E. D. Waddington, 1994: Sensitivity of the ice-divide position in Greenland to climate change. *Geophys. Res. Lett.*, **21**, 441–444.

Baertschi, P., 1976: Absolute ^{18}O content of standard mean ocean water. *Earth Plan. Sci. Lett.*, **31**, 341–344.

Bamber, J. L., R. J. Hardy, P. Huybrechts, and I. Joughin, 2000: A comparison of balance velocities, measured velocities and thermomechanically modelled velocities for the Greenland Ice Sheet. *Ann. Glaciol.*, **30**, 211–216.

Barkov, N. I., and F. G. Gordienko, 1976: Isotope studies of ice cores from vostok antarctica down to the depth of 950 m. *Rep. Acad. Sci. USSR (in Russian)*, **230**, 656–659.

Barnola, J.-M., D. Raynaud, Y. S. Korotkevitch, and C. Lorius, 1987: Vostok ice core record provides 160,000-year record of atmospheric CO_2. *Nature*, **329**, 408–414.

Bassinot, F., L. Labeyrie, E. Vincent, X. Quidelleur, N. J. Shackelton, and Y. Lancelot, 1994: The astronomical theory of climate and the age of the Brunhes-Matuyama magnetic reversal. *Earth Plan. Sci. Lett.*, **126**, 91–108.

Bender, M., T. Sowers, M.-L. Dickson, J. Orchardo, P. Grootes, P. A. Mayewski, and D. A. Meese, 1994: Climate correlations between Greenland and Antarctica during the past 100,000 years. *Nature*, **372**, 663–666.

Bentley, M., 1999: Volume of Antarctic ice at the Last Glacial Maximum, and its impact on global sea level change. *Quat. Sci. Rev.*, **18**, 1569–1595.

Berger, A., 1978: Long-term variations of daily insolation and Quaternary climate change. *J. Atmos. Sci.*, **35**, 2362–2367.

Berger, A., and M. F. Loutre, 2002: An exceptionally long interglacial ahead? *Science*, **297**, 1287–1288.

Blunier, T., and E. Brook, 2001: Timing of millennial-scale climate change in Antarctica and Greenland during the last glacial period. *Science*, **291**, 109–112.

Bond, G., et al., 1992: Evidence for massive discharges of icebergs into the North Atlantic ocean during the last glacial period. *Nature*, **360**, 245–249.

Chappellaz, J., E. Brook, T. Blunier, and B. Malaize, 1997: CH_4 and $\delta^{18}O$ of O_2 records from Greenland and Antarctic ice: a clue for stratigraphic disturbance in the bottom part of the GRIP and GISP2 ice cores. *J. Geophys. Res.*, **102**, 26,547–26,557.

Clark, I., and P. Fritz, 1997: *Environmental Isotopes in Hydrogeology*. Boca Raton ed., Lewis.

Clark, P. U., and A. C. Mix, 2002: Ice sheets and sea level of the Last Glacial Maximum. *Quat. Sci. Rev.*, **21**, 1–7.

Clarke, G., and S. J. Marshall, 2002: Isotopic balance of the Greenland Ice Sheet: Modelled concentrations of water isotopes from 30,000 BP to present. *Quat. Sci. Rev.*, **21**, 419–430.

Clarke, G. K. C., N. Lhomme, and S. J. Marshall, in press: Tracer transport in the Greenland Ice Sheet: three-dimensional isotopic stratigraphy. *Quat. Sci. Rev.*.

Craig, H., 1961: Isotopic variations in meteoric waters. *Science*, **133**, 1702–1703.

Crutzen, P. J., 2002: Geology of mankind. *Nature*, **415**, 23.

Cuffey, K. M., 2000: Methodology for use of isotopic climate forcings in ice sheet models. *Geophys. Res. Lett.*, **27**, 3065–3068.

Cuffey, K. M., and G. D. Clow, 1997: Temperature, accumulation, and Ice Sheet elevation in central Greenland through the last deglacial transition. *J. Geophys. Res.*, **102**, 26,383–26,396.

Cuffey, K. M., and S. J. Marshall, 2000: Sea level rise from Greenland Ice Sheet retreat in the last interglacial period. *Nature*, **404**, 591–594.

Cuffey, K. M., and E. J. Steig, 1998: Isotopic diffusion in polar firn: implication for interpretation of seasonal climate parameters in ice-core records, with emphasis on central Greenland. *J. Glaciol.*, **44, No. 147**, 273–284.

Cuffey, K. M., G. D. Clow, R. B. Alley, M. Stuiver, E. D. Waddington, and R. W. Saltus, 1995: Large Arctic temperature change at the Wisconsin-Holocene glacial transition. *Science*, **270**, 455–458.

Dahl-Jensen, D., 1989: Two dimensional thermomechanical modelling of flow and depth age profiles at crête, central Greenland. *Ann. Glaciol.*, **12**, 31–36.

Dahl-Jensen, D., K. Mosegaard, N. Gundestrup, G. D. Clow, S. J. Johnsen, A. W. Hansen, and N. Balling, 1998: Past temperatures directly from the Greenland Ice Sheet. *Science*, **282**, 268–271.

Dahl-Jensen, D., N. Gundestrup, P. Gogineni, and H. Miller, 2003: Basal melt at NorthGRIP modeled from borehole, ice-core and radio-echo sounder observations. *Ann. Glaciol.*, **37**, 207–212.

Dansgaard, W., 1964: Stable isotopes in precipitation. *Tellus*, **16**, 436–468.

Dansgaard, W., and S. J. Johnsen, 1969: A flow model and a time scale for the ice core from Camp Century, Greenland. *J. Glaciol.*, **8**, 215–223.

Dansgaard, W., and H. Taubert, 1969: Glacier oxygen-18 content and Pleistocene ocean temperature. *Science*, **166**, 499–502.

Dansgaard, W., S. J. Johnsen, J. Moller, and C. J. Langway, 1969: One thousand centuries of climatic record from Camp Century on the Greenland Ice Sheet. *Science*, **166**, 377–381.

Dansgaard, W., H. B. Clausen, N. Gundestrup, and N. Reeh, 1982: A new Greenland deep ice core. *Science*, **218**, 1273–1277.

Dansgaard, W., et al., 1993: Evidence for general instability of past climate from a 250 kyr ice-core record. *Nature*, **264**, 218–220.

Delaygue, G., J. Jouzel, V. Masson, R. D. Koster, and E. Bard, 2000: Validity of the isotopic thermometer in central Antarctica: limited impact of glacial precipitation seasonality and moisture origin. *Geophys. Res. Lett.*, **27**, 2677–2680.

Dewit, J. C., C. M. VanderStraaten, and W. G. Mook, 1980: Determination of the absolute hydrogen isotope ratio of V-SMOW and SLAP. *Geostandards Newsletter*, **4**, 33–36.

Dole, M., 1935: The relative atomic weight of oxygen in water and air. *J. Am. Chem. Soc.*, **57**, 2731.

Drowler, A. W., R. Z. Poore, and L. H. Burckle, 2002: *Earth's climate and orbital eccentricity. The Marine Isotope Stage 11 question*. Geophysical Monograph, American Geophysical Union.

Duplessy, J.-C., L. Labeyrie, and C. Waelbroeck, 2002: Constraints on the oxygen isotopic enrichment between the Last Glacial Maximum and the Holocene: Paleoceanographic implications. *Quat. Sci. Rev.*, **21**, 315–330.

Durand, G., 2004: Microstructure, recristallisation et déformation des glaces polaires de la carotte EPICA, Dome Concordia, Antarctique, Ph.D. thesis, Université Joseph Fourier.

Emiliani, C., 1955: Pleistocene temperatures. *J. Geol.*, **63**, 538–578.

EPICA community members, 2004: Eight glacial cycles from an Antarctic ice core. *Nature*, **429**, 623–628.

Epstein, S., R. P. Sharp, and A. J. Gow, 1970: Antarctic ice sheet: stable isotope analyses of Byrd station cores and interhemispheric climatic implications. *Science*, **168**, 1570–1572.

Fahnestock, M., W. Abdalati, I. Joughin, J. Brozena, and P. Gogineni, 2001: High geothermal heat flow, basal melt, and the origin of rapid ice flow in central Greenland. *Science*, **294**, 2338–2342.

Fairbanks, R. G., 1989: A 17000-year glacio-eustatic sea level record: influence of glacial melting rates on the Younger Dryas event and deep-ocean circulation. *Nature*, **342**, 637–642.

Faure, G., 1986: *Principles of Isotope Geology*. 2nd ed., John Wiley and Sons.

Forieri, A., I. E. Tabacco, A. Della Vedova, A. Zirizzotti, C. Bianchi, P. De Michelis, and A. Passerini, 2003: A new bedrock map of Dome Concordia area. *Terra Ant. Rep.*, **8**, 169–174.

Fortuin, J. P. F., 1992: The surface mass balance and temperature of Antarctica, Ph.D. thesis, Utrecht Institute of Technology (Utrecht, Netherlands).

Genty, D., D. Blamart, R. Ouahdi, R. Gilmour, A. Baker, J. Jouzel, and S. Van-Exter, 2003: Precise dating of Dansgaard-Oeschger climate oscillations in western Europe from stalagmite data. *Nature*, **421**, 833–837.

Giovinetto, M. B., and H. J. Zwally, 1997: Areal distribution of the oxygen-isotope ratio in Antarctica: an assessment based on multivariate models. *Ann. Glaciol.*, **25**, 153–158.

Glen, J. W., 1955: The creep of polycrystalline ice. *Proceed. Roy. Soc.*, vol. A228, pp. 513–538.

Goujon, C., J.-M. Barnola, and C. Ritz, 2003: Modeling the densification of polar firn including heat diffusion : application to close-off characteristics and gas isotopic fractionation for Antarctica and Greenland sites. *J. Geophys. Res.*, **108**, 4792–4809.

Greve, R., 1997: Large-scale ice-sheet modeling as a means of dating deep ice cores in Greenland. *J. Glaciol.*, **43**, 307–310.

GRIP Members, 1993: Climate instability during the last interglacial period recorded in the GRIP ice core. *Nature*, **364**, 203–207.

Grootes, P. M., and M. Stuiver, 1997: Oxygen 18/16 variability in Greenland snow and ice with 10^3 to 10^5-year time resolution. *J. Geophys. Res.*, **102**, 26,455–26,470.

Grootes, P. M., M. Stuiver, J. W. C. White, S. J. Johnsen, and J. Jouzel, 1993: Comparison of oxygen isotope records from the GISP2 and GRIP Greenland ice cores. *Nature*, **366**, 552–554.

Hammer, C. U., H. B. Clausen, and H. Tauber, 1986: Ice-core dating of the Pleistocene/Holocene boundary applied by a calibration of the ^{14}C time scale. *Radiocarbon*, **28**, 284–291.

Hays, J. D., J. Imbrie, and N. J. Shackleton, 1976: Variations in Earth's orbit: pacemaker of ice ages. *Science*, **194**, 1121–1132.

Heinrich, H., 1988: Origin and consequence of cyclic ice-rafting in the northeast Atlantic Ocean during the past 130,000 yr. *Quat. Res.*, **29**, 141–152.

Hoffmann, G., J. Jouzel, and V. Masson, 2000: Stable water isotopes in atmospheric general circulation models. *Hydrol. Proces.*, **14**, 1385–1406.

Hutter, K., 1983: *Theoretical glaciology*. Dordrecht ed., D. Reidel.

Huybrechts, P., 1990: The Antarctic Ice Sheet during the last glacial-interglacial cycle: a three-dimensional experiment. *Ann. Glaciol.*, **14**, 115–119.

Huybrechts, P., 1993: Glaciological modelling of the late cenozoic East Antarctic Ice Sheet: Stability or dynamism? *Geog. Ann.*, **75A(4)**, 221–238.

Huybrechts, P., 2002: Sea-level changes at the LGM from ice-dynamic reconstructions of the Greenland and Antarctic Ice Sheets during the glacial cycles. *Quat. Sci. Rev.*, **21**, 203–231.

Huybrechts, P., A. Letréguilly, and N. Reeh, 1991: The Greenland Ice Sheet and greenhouse warming. *Glob. Plan. Change*, **3**, 399–412.

Huybrechts, P., D. Steinhage, F. Wilhelms, and J. Bamber, 2000: Balance velocities and measured properties of the Antarctic Ice Sheet from a new compilation of gridded data for modeling. *Ann. Glaciol.*, **30**, 52–60.

Imbrie, J., A. McIntyre, and A. C. Mix, 1990: Oceanic response to orbital forcing in the Late Quaternary: observational and experimental strategies. *Climate and Geosciences, a challenge for Science and Society in the 21st Century*, A. Berger, S. Schneider, and J.-C. Duplessy, Eds., D. Reidel.

IPCC, 2001: *Summary for Policymakers*. 3rd ed., Intergovernmental Panel on Climate Change.

Jean-Baptiste, P., J. Jouzel, M. Stievenard, and P. Ciais, 1998: Experimental determination of the firn diffusion rate of deuterated water vapor in ice and application to the stable isotope smoothing of ice cores. *Earth Plan. Sci. Lett.*, **158**, 81–90.

Jenssen, D., 1977: A three-dimensional polar ice-sheet model. *J. Glaciol.*, **18**, 373–389.

Johnsen, S. J., W. Dansgaard, and J. W. C. White, 1989: The origin of Arctic precipitation under present and glacial conditions. *Tellus*, **41B**, 452–468.

Johnsen, S. J., D. Dahl-Jensen, W. Dansgaard, and N. Gundestrup, 1995: Greenland paleotemperatures derived from GRIP borehole temperature and ice core isotope profiles. *Tellus*, **47B**, 624–629.

Johnsen, S. J., H. B. Clausen, K. M. Cuffey, G. Hoffmann, J. Schwander, and T. T. Creyts, 2000: Diffusion of stable isotopes in firn and ice: the isotope effect in firn diffusion. *Physics of ice core records*, T. Hondoh, Ed., Hokkaido Univ. Press.

Johnsen, S. J., D. Dahl-Jensen, N. Gunderstrup, J. P. Steffensen, H. K. Clausen, H. Miller, V. Masson-Delmotte, A. E. Sveinbjornsdottir, and J. W. C. White, 2001: Oxygen isotope and paleotemperature records from six Greenland ice core stations: Camp Century, Dye-3, GRIP, GISP2, Renland and NorthGRIP. *J. Quat. Sci.*, **16**, 299–307.

Johnsen, S. J., et al., 1997: The δ^{18}O records along the Greenland Ice Core Project deep ice core and the problem of possible Eemian climatic instability. *J. Geophys. Res.*, **102**, 26,397–26,410.

Joussaume, S., 1999: *Climat d'hier à demain*. Science au présent, CNRS / CEA.

Jouzel, J., R. D. Koster, and R. J. Suozzo, 1991: Simulations of the HDO and $\mathrm{h}_2^{18}\mathrm{o}$ atmospheric cycles using the NASA GISS general circulation model: Sensitivity experiments for present-day conditions. *J. Geophys. Res.*, **96**, 7495–7507.

Jouzel, J., G. Hoffmann, R. D. Koster, and V. Masson, 2000: Water isotopes in precipitation: data/model comparison for present-day and past climates. *Quat. Sci. Rev.*, **19**, 363–379.

Jouzel, J., F. Vimeux, N. Caillon, G. Delaygue, G. Hoffmann, V. Masson-Delmotte, and F. Parrenin, 2003: Magnitude of isotope/temperature scaling for interpretation of central Antarctic ice cores. *J. Geophys. Res.*, **108**, 4361–4370.

Jouzel, J., et al., 1997: Validity of the temperature reconstruction from water isotopes in ice cores. *J. Geophys. Res.*, **102**, 26,471–26,487.

Koerner, R. M., and D. A. Fisher, 2002: Ice-core evidence for widespread Arctic glacier retreat in the Last Interglacial and the early Holocene. *Ann. Glaciol.*, **35**, 19–24.

Krinner, G., and C. Genthon, 1997: GCM analysis of local influences in ice core δ signal. *Geophys. Res. Lett.*, **24**, 2825–2828.

Krinner, G., and C. Genthon, 1998: GCM simulations of the Last Glacial Maximum surface climate of Greenland and Antarctica. *Climate Dyn.*, **14**, 741–758.

Kroopnick, P., and H. Craig, 1972: Atmospheric oxygen: isotopic composition and solubility fractionation. *Science*, **175**, 54–55.

Labeyrie, L. D., J.-C. Duplessy, and P. L. Blanc, 1987: Variation in mode of formation and temperature of oceanic deep waters over the past 125,000 years. *Nature*, **327**, 477–482.

Le Meur, E., and P. Huybrechts, 1996: A comparison of different ways of dealing with isostasy: Examples from modelling the Antarctic ice sheet during the last glacial cycle. *Ann. Glaciol.*, **23**, 309–317.

Letreguilly, A., P. Huybrechts, and N. Reeh, 1991: Steady-state characteristics of the Greenland ice sheet under different climates. *J. Glaciol.*, **37**(125), 149–157.

Lhomme, N., 1999: Paramétrisation sous-maille des mécanismes sous-maille pour les modèles de couplage atmosphère-calotte de glace. D.E.A., Université Joseph Fourier.

Lhomme, N., G. K. C. Clarke, G. Hoffmann, C. Ritz, and S. J. Marshall, 2002: . Oxygen isotope composition of the Greenland Ice Sheet derived from an AGCM, EGS02-A-05723.

Lhomme, N., G. K. C. Clarke, and S. J. Marshall, in press: Tracer transport in the Greenland Ice Sheet: constraints on ice cores and glacial history. *Quat. Sci. Rev.*.

Lorius, C., and L. Merlivat, 1977: Distribution of mean surface stable isotope values in East Antarctica: observed changes with depth. *Isotopes and Impurities in Snow and Ice*, vol. 118, IAHS, pp. 127–137.

Lorius, C., L. Merlivat, J. Jouzel, and M. Pourchet, 1979: A 30000 yr isotope climatic record from Antarctic ice. *Nature*, **280**, 644–648.

Lorius, C., J. Jouzel, R. Ritz, L. Merlivat, N. I. Barkov, Y. S. Korotkevitch, and V. M. Kotlyakov, 1985: A 150,000-year climatic record from Antarctic ice. *Nature*, **316**, 591–596.

Lythe, M. B., D. G. Vaughan, and the BEDMAP Consortium, 2000: *BEDMAP - bed topography of the Antarctic. 1:10,000,000 scale map*. British Antarctic Survey.

Mahaffy, M. W., 1976: A three-dimensional numerical model of ice sheets: tests on the Barnes ice cap, Northwest Territories. *J. Geophys. Res.*, **81**, 1059–1066.

Malvern, L. E., 1969: *Introduction to the Mechanics of a Continuous Medium*. Prentice-Hall.

Marshall, S. J., 1996: Modelling Laurentide ice stream thermomechanics, Ph.D. thesis, University of British Columbia.

Marshall, S. J., and G. K. C. Clarke, 1997: A continuum mixture model of ice stream thermomechanics in the Laurentide Ice Sheet, 1. Theory. *J. Geophys. Res.*, **102**, 20,599–20,614.

Marshall, S. J., and G. K. C. Clarke, 1999: Ice sheet inception: Subgrid hypsometric parameterization of mass balance in an ice sheet model. *Climate Dyn.*, **15**, 533–550.

Marshall, S. J., and K. M. Cuffey, 2000: Peregrinations of the Greenland Ice Sheet divide through the last glacial cycle: implications for disturbance of central Greenland ice cores. *Earth Plan. Sci. Lett.*, **179**, 73–90.

Martinson, D. G., N. G. Pisisas, J. D. Hays, J. Imbrie, T. C. J. Moore, and N. J. Shackleton, 1987: Age dating and the orbital theory of the ice ages: development of a high-resolution 300000 year chronostratigraphy. *Quat. Res.*, **27**, 1–29.

Masson, V., et al., 2000: Holocene climate variability in Antarctica based on 11 ice-core isotopic records. *Quat. Res.*, **54**, 348–358.

Meese, D. A., A. J. Gow, R. B. Alley, G. A. Zielinski, P. M. Grootes, M. Ram, K. C. Taylor, P. A. Mayewski, and J. F. Bolzan, 1997: The Greenland Ice Sheet Project 2 depth-age scale: Method and results. *J. Geophys. Res.*, **102**, 26,411–26,423.

Mercer, J. H., 1978: West Antarctic Ice Sheet and CO Greenhouse Effect: A threat disaster. *Nature*, **271**, 321–325.

Milankovitch, M., 1930: Mathematische klimalehre und astronomische theorie der klimaschwankungen. *Handbuch der Klimalogie*, Borntrager.

Mook, W. G., and J. J. de Vries, 2001: *Environmental Isotopes in the Hydrological Cycle: Principles and Applications*. vol. 1.

Morgan, V. I., C. W. Wookey, J. Li, T. D. V. Ommen, W. Skinner, and M. F. Fitzpatrick, 1997: Site information and initial results from deep ice drilling on Law Dome. *J. Glaciol.*, **43**, 3–10.

NGRIP Members, 2004: High-resolution record of Northern Hemisphere climate extending into the last interglacial period. *Nature*, **431**, 147–151.

Nye, J. F., 1998: Diffusion of isotopes in the annual layers of ice sheets. *J. Glaciol.*, **44**, 467–468.

Ohmura, A., 1987: New temperature distribution maps for Greenland. *Zeitschrift für Gletscherkunde Glazialgeologie*, **23**, 1–45.

Ohmura, A., and N. Reeh, 1991: New precipitation and accumulation maps for Greenland. *J. Glaciol.*, **37**, 140–148.

Oppenheimer, M., 1998: Global warming and the stability of the West Antarctic Ice Sheet. *Nature*, **393**, 325–332.

Parrenin, F., 2002: Datation glaciologique des forages profonds en Antarctique et modélisation conceptuelle des paléoclimats: implications pour la théorie astronomique des paléoclimats, Ph.D. thesis, Université Joseph Fourier.

Parrenin, F., J. Jouzel, C. Waelbroeck, C. Ritz, and J.-M. Barnola, 2001: Dating the Vostok ice core by an inverse method. *J. Geophys. Res.*, **106**, 31,837–31,851.

Parrenin, F., F. Rémy, C. Ritz, M. J. Siegert, and J. Jouzel, in press: New modelling of the Vostok ice flow line and implication for the glaciological chronology of the Vostok ice core. *J. Geophys. Res.*.

Payne, A. J., 1999: A thermomechanical model of ice flow in West Antarctica. *Climate Dyn.*, **15**, 115–125.

Payne, T., et al., 2000: Results from the EISMINT model intercomparison : the effects of thermomechanical coupling. *J. Glaciol.*, **46**, 227–237.

Peltier, W. R., 1995: VLBI baseline variations from the ice-4G model of postglacial rebound. *Geophys. Res. Lett.*, **22(4)**, 465–468.

Petit, J.-R., et al., 1999: Climate and atmospheric history of the past 420000 years from the Vostok ice core, Antarctica. *Nature*, **399**, 429–436.

Rasch, P. J., and M. Lawrence, 1998: Recent development in transport methods at NCAR. *MPI Workshop on conservative transport schemes*, Max-Planck-Institute for Meteorology, Hamburg, Germany, pp. 265:65–75.

Raymond, C. F., 1983: Deformation in the vicinity of ice divides. *J. Glaciol.*, **29**, 357–373.

Raynaud, D., J. Chappellaz, C. Ritz, and P. Martinerie, 1997: Air content along the Greenland Ice Core Project core : A record of surface climatic parameters and elevation in central Greenland. *J. Geophys. Res.*, **102**, 26,607–26,613.

Reeh, N., 1991: Parameterization of melt rate and surface temperature on the Greenland Ice Sheet. *Polarforschung*, **59**, 113–128.

Reeh, N., H. H. Thomsen, and H. B. Clausen, 1987: The Greenland ice-sheet margin—A mine of ice for paleo-environmental studies. *Palaeogeography, Palaeoclimatology, Palaeoecology*, **58**, 229–234.

Riddaway, R. W., 2001: *Meteorological Training Course Lecture Series*.

Riishϕjgaard, L. P., S. E. Cohn, Y. Li, and R. Ménard, 1998: The use of spline interpolation in semi-Lagrangian transport models. *Mon. Wea. Rev.*, **126**, 2008–2016.

Ritz, C., 1989: Interpretation of the temperature profile measured at Vostok, East Antarctica. *Ann. Glaciol.*, **12**, 138–144.

Ritz, C., 1992: Un modèle thermo-mécanique d'évolution pour le basin glaciaire Antarctique Vostok-glacier Byrd: sensibilité des paramètres mal connus, Ph.D. thesis, Université Joseph Fourier.

Ritz, C., A. Fabre, and A. Letréguilly, 1997: Sensitivity of a Greenland Ice Sheet model to ice flow and ablation parameters: Consequences for evolution through the last climatic cycle. *Climate Dyn.*, **13**, 11–24.

Ritz, C., V. Rommelaere, and C. Dumas, 2001: Modeling the evolution of Antarctic Ice Sheet over the last 420,000 years: Implications for altitude changes in the Vostok region. *J. Geophys. Res.*, **106**, 31,943–31,964.

Robin, G. d. Q., 1977: *Ice cores and climatic change*. vol. 280 of *B*, Philosophical Transactions of the Royal Society of London.

Roche, D., D. Paillard, A. Ganopolski, and G. Hoffmann, 2004: Oceanic oxygen-18 at the present day and lgm: equilibrium simulations with a coupled climate model of intermediate complexity. *Earth Plan. Sci. Lett.*, **218**, 317–330.

Rommelaere, V., and D. R. MacAyeal, 1997: Large-scale rheology of the Ross ice shelf, Antarctica, computed by a control method. *Ann. Glaciol.*, **24**, 43–48.

Rostami, A., W. R. Peltier, and A. Mangini, 2000: Quaternary marine terraces, sea level changes and uplift history of Patagonia, Argentinian: Comparisons with predictions of the ice-4G (VM2) model of the global process of glacial isostatic adjustment. *Quat. Sci. Rev.*, **19**, 1495–1525.

Rozanski, K., L. Araguás-Araguás, and R. Gonfiantini, 1993: Isotopic patters in modern global precipitation. *Climate Change in Continental Isotopic Records*, P. K. Swart, K. C. Lohmann, J. McKenzie, and S. Savin, Eds., vol. 78 of *Geophysical Monograph*, AGU, pp. 1–36.

Rybak, O., and P. Huybrechts, 2004: A comparison of Eulerian and Lagrangian methods for dating in numerical ice sheet models. *Ann. Glaciol.*, **37**, 150–158.

Schrag, D. P., G. Hampt, and D. W. Murray, 1996: Pore fluid constraints on the temperature and oxygen isotopic composition of the glacial ocean. *Science*, **272**, 1930–1932.

Severinghaus, J. P., and E. J. Brook, 1999: Abrupt climate change at the end of the last glacial period inferred from trapped air in polar ice. *Science*, **286**, 930–933.

Shackleton, N. J., 1974: Attainment of isotopic equilibrium between ocean water and benthic foraminifera genus Uvigerina: isotopic changes in the ocean during the last glacial. *Les méthodes quantitatives d'étude du climat au cours du Pléistocène*, CNRS, Gif sur Yvette, pp. 203–209.

Shackleton, N. J., R. G. Fairbanks, T.-C. Chiu, and F. Parrenin, 2004: Absolute calibration of the Greenland time scale: implications for Antarctic time scales and for δ^{14}C. *Quat. Sci. Rev.*, **23**.

Siegert, M. J., and R. Kwok, 2000: Ice-sheet radar layering and the development of preferred crystal orientation fabrics between Lake Vostok and Ridge B, central East Antarctica. *Earth Plan. Sci. Lett.*, **179**, 227–235.

Staniforth, A., and J. Côté, 1991: Semi-Lagrangian integration schemes for atmospheric models - a review. *Mon. Wea. Rev.*, **119**, 2206–2223.

Steig, E. J., E. J. Brook, J. W. C. White, C. M. Sucher, M. L. Bender, S. J. Lehman, D. L. Morse, E. D. Waddington, and G. D. Clow, 1998: Synchronous climate changes in Antarctica and the North Atlantic. *Science*, **282**, 92–95.

Tarasov, L., and W. R. Peltier, 2003: Greenland glacial history, borehole constraints and Eemian extent. *J. Geophys. Res.*, **108**, 2124–2143.

Taylor, K. C., et al., 1993: Electrical conductivity measurements from the GISP2 and GRIP Greenland ice cores. *Nature*, **366**, 549–552.

Testut, L., 2000: Apport de la topographie à l'étude des calottes polaires, Ph.D. thesis, Université Toulouse III - Paul Sabatier.

Thorsteinsson, T., E. D. Waddington, K. C. Taylor, R. B. Alley, and D. D. Blankenship, 1999: Strain-rate enhancement at Dye 3, Greenland. *J. Glaciol.*, **45**, 338–345.

Vimeux, F., V. Masson, G. Delaygue, J. Jouzel, J.-R. Petit, and M. Stievenard, 2001: A 420,000 year deuterium excess record from east antarctica: information on past changes in the origin of precipitation at vostok. *J. Geophys. Res.*, **106**, 31,863–31,874.

Vreugdenhil, C. B., 1993: Numerical methods for advection-diffusion problems. *Notes on Numerical Fluid Mechanics*, C. B. Vreugdenhil and B. Koren, Eds., vol. 45, Vieweg.

Waddington, E. D., and G. K. C. Clarke, 1988: Stable isotope pattern predicted in surge-type glaciers. *Canadian J. Earth Sci.*, **25**, 657–668.

Waddington, E. D., E. J. Steig, and T. A. Neumann, 2002: Using characteristic times to assess whether stable isotopes in polar snow can be reversibly deposited. *Ann. Glaciol.*, **35**, 118–124.

Waelbroeck, C., L. Labeyrie, E. Michel, J.-C. Duplessy, J. F. McManus, K. Lambeck, E. Balbon, and M. Labracherie, 2002: Sea-level and deep water temperature changes derived from benthic foraminifera isotopic records. *Quat. Sci. Rev.*, **21**, 295–305.

Watanabe, O., J. Jouzel, S. Johnsen, F. Parrenin, H. Shoji, and N. Yoshida, 2003: Homogeneous climate variability across East Antarctica over the past three glacial cycles. *Nature*, **422**, 509–512.

Weertman, B. R., 1993: Interpretation of ice sheet stratigraphy: a radio-echo sounding study of the Dyer Plateau, Antarctica, Ph.D. thesis, Geophysics Program, University of Washington.

Werner, M., U. Mikolajewicz, M. Heimann, and G. Hoffmann, 2000: Borehole versus temperatures on Greenland: seasonality does matter. *Geophys. Res. Lett.*, **27**, 723–726.

Whillans, I. M., and P. M. Grootes, 1985: Isotopic diffusion in cold snow and firn. *J. Geophys. Res.*, **90**, 3910–3918.

Yokoyama, Y., K. Lambeck, P. De Deckker, P. Johnston, and L. K. Fifield, 2000: Timing of the Last Glacial Maximum from observed sea-level minima. *Nature*, **406**, 713–716.

Zachos, J., M. Pagani, L. Sloan, E. Thomas, and K. Billups, 2001: Trends, rhythms, and aberrations in global climate 65 Ma to present. *Science*, **292**, 686–693.

Zwally, H. J., and M. B. Giovinetto, 1997: Areal distribution of the oxygen-isotope ratio in Greenland. *Ann. Glaciol.*, **25**, 208–213.

APPENDIX A

Temperature, precipitation and sea level

A.1 Greenland

A.1.1 Temperature

Average annual temperature over Greenland are given by a regression by Huybrechts et al. (1991) from a compilation of measurements performed by Ohmura (1987). Present average annual temperature (T_{a0}) depends on surface elevation and latitude and includes two effects:

- temperature inversion: a larger temperature gradient in the winter time;
- a mixed layer of homogenous temperature in the foothills of Northern Greenland, modelled by a maximum mixing elevation S_{mel} located 300 m above sea levels at $80°$N and linearly decreasing Southward:

$$S_{\mathrm{mel}} = 300(\lambda - 65)/15, \tag{A.1}$$

  with λ the latitude. Temperature is uniform below that inversion elevation.

At elevation S, average annual surface temperature is given by:

- if $S \leq S_{\mathrm{mel}}$

$$T_{\mathrm{a0}}(S, \lambda) = 49.13 - 0.007992\, S_{\mathrm{mel}} - 0.7576\, \lambda, \tag{A.2}$$

- else

$$T_{\mathrm{a0}}(S, \lambda) = 49.13 - 0.007992\, S - 0.7576\, \lambda. \tag{A.3}$$

  Present average summer temperature (July, T_{j0}) is given by

$$T_{\mathrm{j0}}(S, \lambda) = 30.78 - 0.006277\, S - 0.3262\, \lambda. \tag{A.4}$$

  Notes on the parameterization:

- the continental effect that generally increases the difference between summer and winter temperature is not taken into account. This absence of representation is due to the lack of weather-stations in the central part of the ice sheet;
- the prevailing South-West cyclonic activity associated to air masses crossing the North Atlantic is not taken into account here.

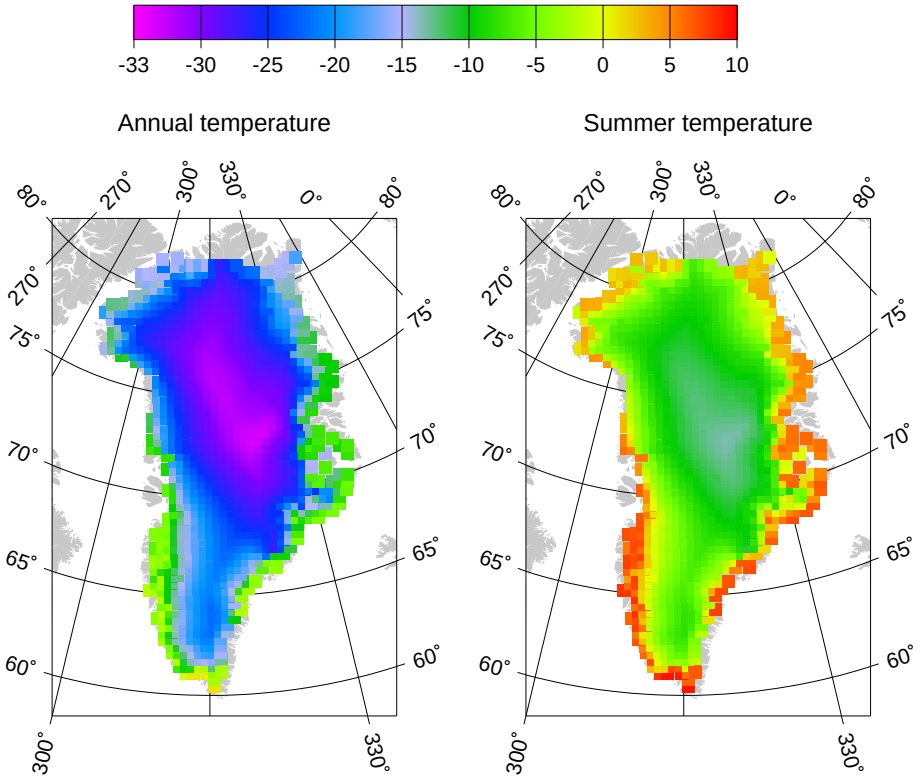

Figure A.1: Present surface annual and summer temperature in Greenland from Huybrechts et al. (1991). Colour version for this graph and the following one appear on the PDF version of my thesis that is posted on my web-page and the LGGE-thesis web-site.

A.1.2 Accumulation

The precipitation archive comes from Huybrechts et al. (1991). For ice sheet models using the Positive Degree Day method (Reeh, 1991) to calculate surface melting, daily temperature T_{day} during the year is assumed to follow a sinusoidal cycle with extremes in January and July. Temperature T during a day is assumed to be normally distributed around the daily temperature with a standard deviation σ_T usually equal to 5°C. The annual fraction of preciptation r_{snow} that falls as snow during a period τ (usually a year) is defined by:

$$r_{\text{snow}} = \int_0^{\tau} \int_{-\infty}^{T_{\text{snow}}} \frac{1}{\sigma_T \sqrt{2\pi}} e^{\frac{-(T-T_{\text{day}}(t))^2}{2\sigma^2}} dT dt \tag{A.5}$$

with T_{snow} the maximum temperature for which precipitation falls as snow, here set to 1°C (Marshall and Clarke, 1999). Using the error function erf, Lhomme (1999) showed that the previous equation is equivalent to

$$r_{\text{snow}} = \frac{1}{2} + \frac{1}{2} erf\left(\frac{T_{\text{snow}} - T_{\text{day}}(t)}{\sigma_T \sqrt{2}}\right). \tag{A.6}$$

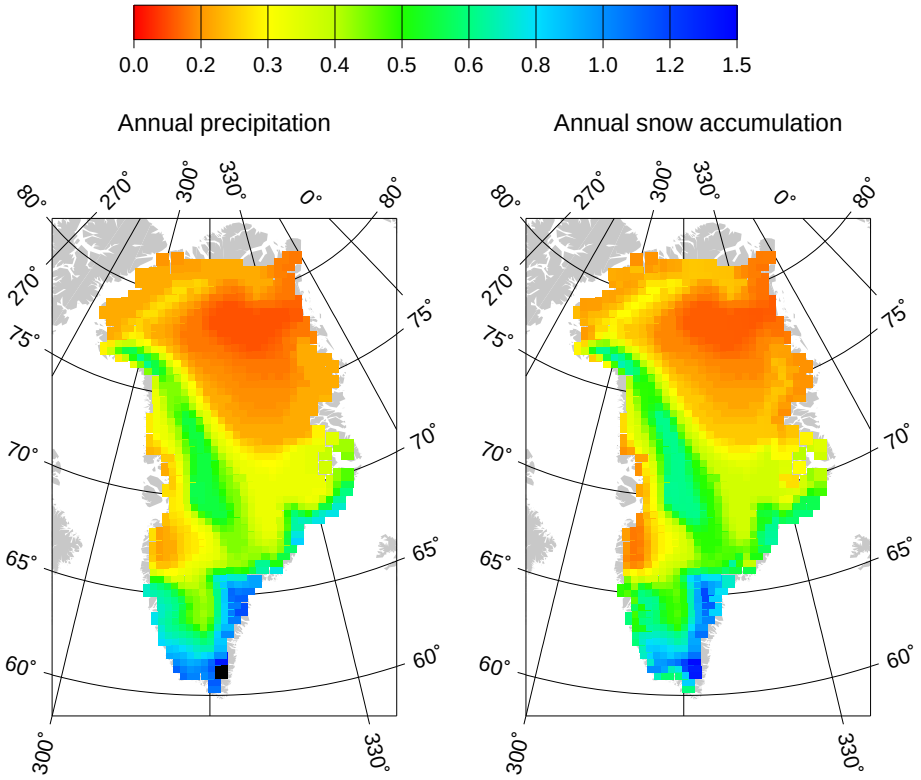

Figure A.2: Present surface preciptiation and snow accumulation in Greenland from Huybrechts et al. (1991).

Surface accumulation is defined as the product of precipitation times the fraction of precipitation that falls as snow. Present distributions of surface precipitation and accumulation are shown in Fig. A.2.

A.2 Antarctica

A.2.1 Temperature

The present distribution of temperature used in the LGGE model strictly follows Ritz et al. (2001) and is obtained with the parameterization of Fortuin (1992). From a multiple-regression analysis, three regions are distinguished according to their surface elevation S:

- ice shelves $S \leq 200$ m

$$T_{a0} = 49.642 - 0.943\lambda, \tag{A.7}$$

- escarpment $200 < S \leq 1500$ m

$$T_{a0} = 36.689 - 0.005102S - 0.725\lambda, \tag{A.8}$$

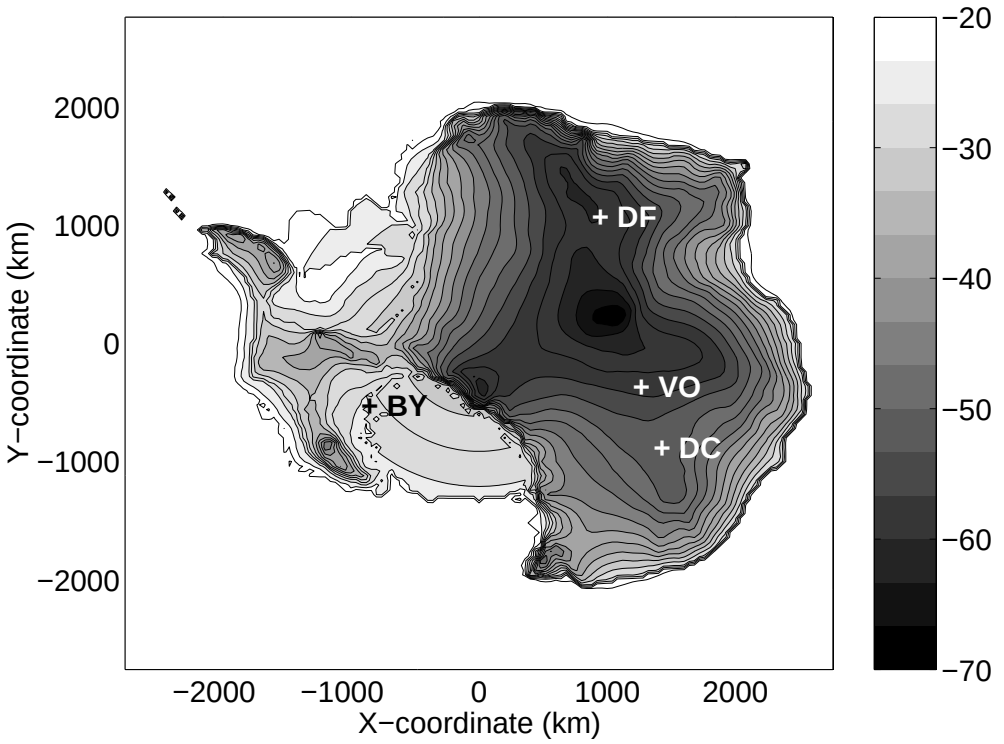

Figure A.3: Present surface temperature in Antarctica from Fortuin (1992) and drilling sites: DC=Dome C (-51.7°C), VO=Vostok (-55.8°C), DF=Dome Fuji (-60.1°C), BY=Byrd (-24.9°C).

- interior $S > 1500$ m

$$T_{\mathrm{a}0} = 7.405 - 0.014285S - 0.180\lambda \tag{A.9}$$

with $T_{\mathrm{a}0}$ the present annual temperature and λ the latitude. We shall note that this distribution, though in good agreement with global surface observation, is discontinuous at the boundary between the different regions, and that the pre-factor of S is not a lapse rate. A uniform lapse rate of 0.00914°C is taken to calculate the past elevation-induced changes of temperature.

Summer temperature $T_{\mathrm{j}}(t)$ at a given time t is derived from the annual temperature $T_{\mathrm{a}}(t)$ (obtained through Eq. 2.15) following Huybrechts (1993):

$$T_{\mathrm{j}}(t) = T_{\mathrm{a}}(t) - 17.65 + 0.00222S + 0.40802\lambda. \tag{A.10}$$

A.2.2 Accumulation

The present distribution of surface accumulation is shown in Fig. A.4 and taken from the compilation of Huybrechts et al. (2000). Local corrections apply near ice core sites.

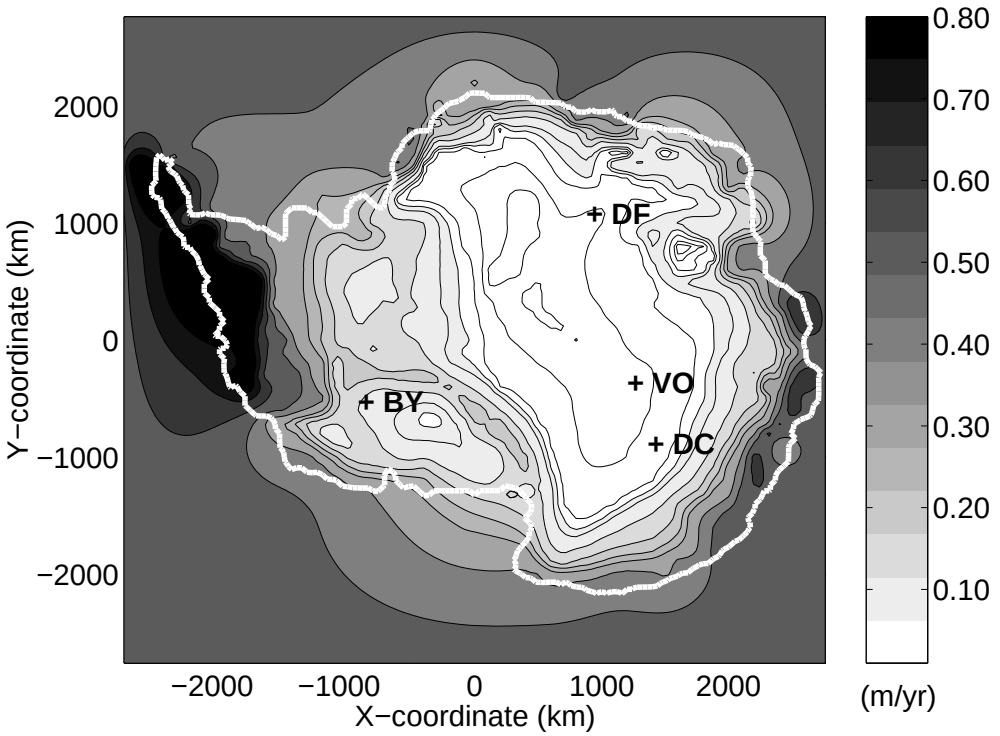

Figure A.4: Present surface accumulation in Antarctica from Huybrechts et al. (2000) and drilling sites: DC=Dome C (4.6 cm/a), VO=Vostok (3.3 cm/a), DF=Dome Fuji (3.8 cm/a), BY=Byrd (15.7 cm/a). Contours at 0.03, 0.04, 0.06, 0.08, 0.10, 0.15, 0.20, 0.25, 0.30, 0.40, 0.50, 0.60, 0.70 and 0.80 m yr^{-1}.

A.3 Sea level

Reconstructions of the past 160 kyr variations of temperature (inferred from the Dome C record) and sea level (Imbrie et al., 1990; Bassinot et al., 1994) are plotted in Fig. A.5. The Greenland model uses the SPECMAP sea level forcing represented by the dotted line whereas the LGGE model for Antarctica uses the sea level history reconstructed by Bassinot et al. (1994), not different in effect to SPECMAP for the elevation history in central Antarctica (Ritz et al., 2001). The standard configuration of the ice sheet models assumes different glacial–interglacial amplitude of sea-level change, an issue that remains to be resolved by the paleoclimatologists' community (e.g., Clark and Mix, 2002).

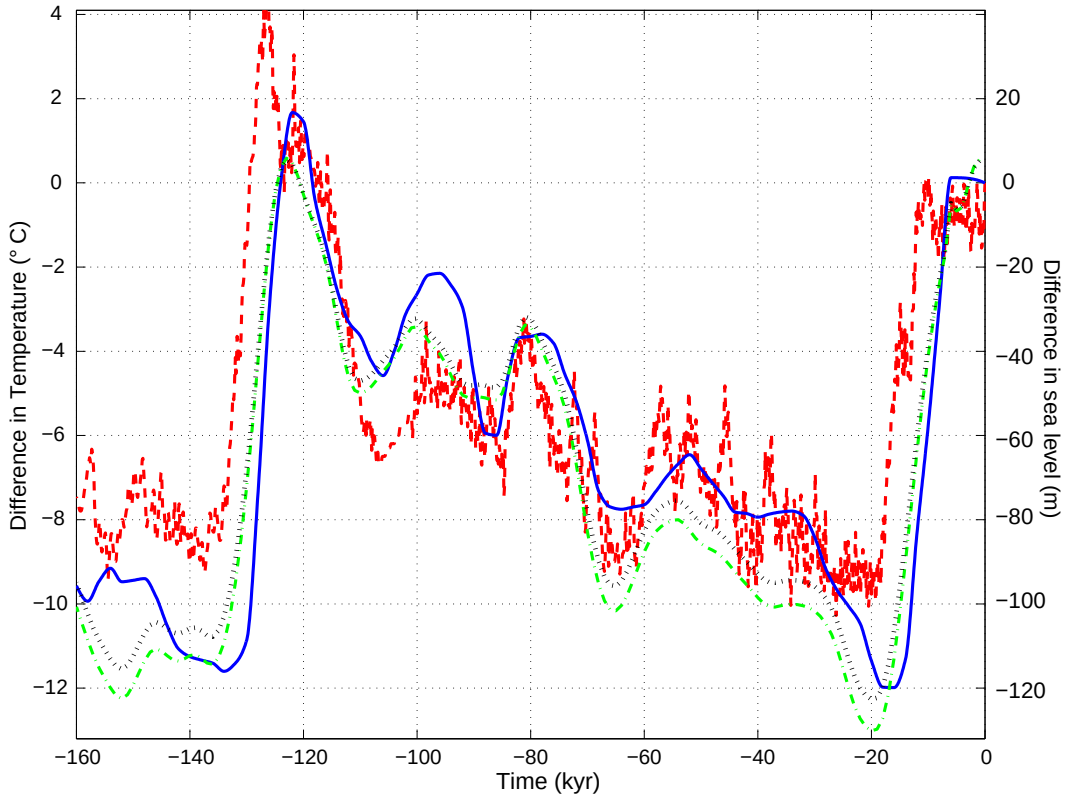

Figure A.5: Relative timing and amplitude of the temperature and sea level climate forcings. EDC2 temperature (dashed line), sea level from Bassinot et al. (1994) as in Ritz et al. (2001) (solid), SPECMAP (Imbrie et al., 1990) with two different calibrations (stacked δ^{18}O vs. sea level): SEALEVEL=-34.83(SPECMAP$+1.93$) used for simulations of Greenland and showed with the dash-dotted line and SEALEVEL=-32.83(SPECMAP$+1.93$) with the dotted line (shown here to match the amplitude of Bassinot et al. (1994) at 20 kyr BP). Sea level lags temperature by several kyr mostly because of the slow response of the large Northern Hemisphere ice sheets to climate change.

APPENDIX B

Implementation of the tracer tracking scheme

The following details the procedure to apply the tracer model to a geographically-oriented grid, which is the case for our simulations of Greenland.

B.1 Particle tracking in geographical and vertically-stretched coordinate systems

For continental-scale ice dynamics models the conventional coordinate system is one for which the vertical coordinate is spatially stretched and (x, y) coordinates are replaced by longitude and latitude coordinates (λ, θ). In general the stretched coordinate can be expressed as $\xi = \xi(\lambda, \theta, z, t)$.

For a particle P having spatial coordinates $[\Lambda(t), \Theta(t), Z(t)]$ moving through a spatially-fixed (λ, θ, z) coordinate system, Eqs. 3.2–3.3 become

$$\frac{\mathrm{d}\Lambda}{\mathrm{d}t} = \frac{1}{R\cos\,\Theta}\, v_\lambda(\Lambda, \Theta, Z, t) \tag{B.1}$$

$$\frac{\mathrm{d}\Theta}{\mathrm{d}t} = \frac{1}{R}\, v_\theta(\Lambda, \Theta, Z, t) \tag{B.2}$$

$$\frac{\mathrm{d}Z}{\mathrm{d}t} = v_z(\Lambda, \Theta, Z, t) \tag{B.3}$$

As mentioned, it is usual to replace z-dependent variables by ξ-dependent ones. Thus the coordinates of the moving particle P become $[\Lambda(t), \Theta(t), \Xi(t)]$ and the particle passes through a grid (x, y, ξ, t) with the velocity field of the continuum given by

$$\mathbf{v}(\lambda, \theta, \xi, t) = [v_\lambda(\lambda, \theta, \xi, t), v_\theta(\lambda, \theta, \xi, t), v_\xi(\lambda, \theta, \xi, t)] \tag{B.4}$$

As we shall see, replacing the evolution equation for $\mathrm{d}Z/\mathrm{d}t$ by one for $d\Xi/dt$ is not completely straightforward. In general $\xi = \xi(\lambda, \theta, z, t)$ so that

$$\frac{\mathrm{d}\Xi}{\mathrm{d}t} = \frac{\partial\xi}{\partial\lambda}\frac{d\Lambda}{dt} + \frac{\partial\xi}{\partial\theta}\frac{d\Theta}{dt} + \frac{\partial\xi}{\partial z}\frac{dZ}{dt} + \frac{\partial\xi}{\partial t} \tag{B.5}$$

which can be written

$$\frac{\mathrm{d}\Xi}{\mathrm{d}t} = \frac{\partial\xi}{\partial\lambda}\frac{d\Lambda}{dt} + \frac{\partial\xi}{\partial\theta}\frac{d\Theta}{dt} + v_\xi(\Lambda, \Theta, \Xi, t)\frac{\partial\xi}{\partial z} + \frac{\partial\xi}{\partial t} \tag{B.6}$$

where the ξ derivatives are evaluated at (Λ, Θ, Ξ). (Note that $d\Lambda/dt$ and $d\Theta/dt$ are given by Eqs. B.2 and B.3 so it is most efficient to evaluate $d\Xi/dt$ after these evaluations have been performed.)

B.2 Semi-Lagrangian method in vertically-stretched geographical coordinate system

At this point it is helpful to work with a specific example rather than the generalized case. Thus we take ξ=exp $\Big[A(h^{\rm I}-z)/H\Big]$, as assumed for the ice dynamics grid in Marshall (1996) and subsequent papers. Consider a point $(\lambda_i,\theta_j,\xi_k)$ in a quasi-Eulerian grid. (The grid is not fully-Eulerian because ξ_k varies with time as the ice geometry changes.) According to the Lagrangian evolution equations, a material point having position coordinates

$$\Lambda(t)=\lambda_i, \qquad \Theta(t)=\theta_j \quad \text{and} \quad \Xi(t)=\xi_k \tag{B.7}$$

at time t was located at position $[\Lambda(t-\Delta t),\Theta(t-\Delta t),\Xi(t-\Delta t)]$ at time $t-\Delta t$. From Eqs. B.2–B.3

$$\Lambda(t-\Delta t) = \Lambda(t)-\frac{\Delta t}{R\sin\theta}\,v_\lambda[\Lambda(t),\Theta(t),\Xi(t),t] \tag{B.8}$$

$$\Theta(t-\Delta t) = \Theta(t)-\frac{\Delta t}{R}\,v_\theta[\Lambda(t),\Theta(t),\Xi(t),t] \tag{B.9}$$

$$\Xi(t-\Delta t) = \Xi(t)-\Delta t\left\{\frac{\partial\xi}{\partial\lambda}\,\frac{d\Lambda}{dt}+\frac{\partial\xi}{\partial\theta}\,\frac{d\Theta}{dt}+v_\xi(\Lambda,\Theta,\Xi,t)\,\frac{\partial\xi}{\partial z}+\frac{\partial\xi}{\partial t}\right\} \tag{B.10}$$

with

$$\frac{\mathrm{d}\Lambda}{\mathrm{d}t} = \frac{1}{R\cos\,\Theta}\,v_\lambda(\Lambda,\Theta,\Xi,t) \tag{B.11}$$

$$\frac{\mathrm{d}\Theta}{\mathrm{d}t} = \frac{1}{R}\,v_\theta(\Lambda,\Theta,\Xi,t) \tag{B.12}$$

$$\frac{\partial\xi}{\partial\lambda} = +\frac{A\Xi}{H(\Lambda,\Theta)}\,\frac{\partial}{\partial\lambda}\,h^{\rm I}(\Lambda,\Theta)-\frac{\Xi\ln\Xi}{H(\Lambda,\Theta)}\,\frac{\partial}{\partial\lambda}\,H(\Lambda,\Theta) \tag{B.13}$$

$$\frac{\partial\xi}{\partial\theta} = +\frac{A\Xi}{H(\Lambda,\Theta)}\,\frac{\partial}{\partial\theta}\,h^{\rm I}(\Lambda,\Theta)-\frac{\Xi\ln\Xi}{H(\Lambda,\Theta)}\,\frac{\partial}{\partial\theta}\,H(\Lambda,\Theta) \tag{B.14}$$

$$\frac{\partial\xi}{\partial z} = -\frac{A\Xi}{H(\Lambda,\Theta)} \tag{B.15}$$

$$\frac{\partial\xi}{\partial t} = +\frac{A\Xi}{H(\Lambda,\Theta)}\,\frac{\partial}{\partial t}\,h^{\rm I}(\Lambda,\Theta)-\frac{\Xi\ln\Xi}{H(\Lambda,\Theta)}\,\frac{\partial}{\partial t}\,H(\Lambda,\Theta). \tag{B.16}$$

Finally, we return to the fact that the material point at $[\Lambda(t),\Theta(t),\Xi(t)]$ corresponds to a grid point $(\lambda_i,\theta_j,\xi_k)$. The scheme outlined in the equations above allows points in the Eulerian grid to be updated using a Lagrangian approach. Note, in particular, that the updating of values at $(\lambda_i,\theta_j,\xi_k)$ does not involve calculation of spatial gradients. Rather, one relies on the fact that tracer values ψ remain constant for a given material point. Thus

$$\psi[\Lambda(t),\Theta(t),\Xi(t),t]=\psi[\Lambda(t-\Delta t),\Theta(t-\Delta t),\Xi(t-\Delta t),t-\Delta t]. \tag{B.17}$$

B.3 Bilinear and trilinear interpolation

Consider a point with coordinates (λ,θ,ξ) lying within a cube-like grid cell having dimensions $\Delta\lambda$, $\Delta\theta$ and $\Delta\xi$ with vertices $(\lambda_i,\theta_j,\xi_k)$, $(\lambda_{i+1},\theta_j,\xi_k)$, $(\lambda_i,\theta_{j+1},\xi_k)$, $(\lambda_{i+1},\theta_{j+1},\xi_k)$, $(\lambda_i,\theta_j,\xi_{k+1})$,

$(\lambda_{i+1}, \theta_j, \xi_{k+1})$, $(\lambda_i, \theta_{j+1}, \xi_{k+1})$, $(\lambda_{i+1}, \theta_{j+1}, \xi_{k+1})$ and consider some traced property Ψ which is defined at these vertices. For notational simplicity we write $\Psi_{i,j,k}$ to denote $\Psi(\lambda_i, \theta_j, \xi_k)$ and introduce dimensionless distance variables

$$\lambda^* = (\lambda - \lambda_i)/\Delta\lambda \tag{B.18}$$

$$\theta^* = (\theta - \theta_j)/\Delta\theta \tag{B.19}$$

$$\xi^* = (\xi - \xi_k)/\Delta\xi. \tag{B.20}$$

Holding ξ fixed at ξ_k and employing bilinear interpolation to estimate Ψ gives

$$\begin{aligned}\Psi(\lambda, \theta, \xi_k) = {} & (1-\lambda^*)(1-\theta^*)\Psi_{i,j,k} + \lambda^*(1-\theta^*)\Psi_{i+1,j,k} \\ & +\theta^*(1-\lambda^*)\Psi_{i,j+1,k} + \lambda^*\theta^*\Psi_{i+1,j+1,k}.\end{aligned} \tag{B.21}$$

If ξ lies between ξ_k and ξ_{k+1} and trilinear interpolation is employed, the result is

$$\begin{aligned}\Psi(\lambda, \theta, \xi) = {} & (1-\xi^*)\Big\{(1-\lambda^*)(1-\theta^*)\Psi_{i,j,k} + \lambda^*(1-\theta^*)\Psi_{i+1,j,k} \\ & +\theta^*(1-\lambda^*)\Psi_{i,j+1,k} + \lambda^*\theta^*\Psi_{i+1,j+1,k}\Big\} \\ & +\xi^*\Big\{(1-\lambda^*)(1-\theta^*)\Psi_{i,j,k+1} + \lambda^*(1-\theta^*)\Psi_{i+1,j,k+1} \\ & +\theta^*(1-\lambda^*)\Psi_{i,j+1,k+1} + \lambda^*\theta^*\Psi_{i+1,j+1,k+1}\Big\}.\end{aligned} \tag{B.22}$$

Although we use trilinear interpolation to calculate $\lambda_{\rm d}$ and $\theta_{\rm d}$ we have found that this method can lead to large errors in $t_{\rm d}$. Therefore the balance-based approached is used for $t_{\rm d}$.

APPENDIX C

Accuracy of the balance-based method

C.1 Numerical considerations

C.1.1 Global cumulative-balance function

In the following presentation, I justify my method by considering the Greenland ice sheet and using the GRIP ice core record. The method is similarly applied to the Antarctic Ice Sheet with the EPICA-dome C record and justified in the following.

The time-evolving surface mass balance of the ice sheets is derived by using the GRIP isotopic record as an index to proportionally deduce the smoothly varying present distribution of precipitation over time (Eq. 2.16). As a result, changes in accumulation rate at distant sites are proportionally similar to the isotopic record unless large changes in surface elevation occur. The GRIP-based cumulative-balance function

$$\Omega(t) = \int_{t_{\mathrm{ref}}}^{t} \dot{b}(t')\mathrm{d}t' \tag{C.1}$$

is used in the vertical interpolation of age for the entire ice sheet. At any given location, the age and origin of ice varies along a vertical column; additionally, the layer thicknesses are affected by the surface mass balance at the place and time of deposition. Balance-based interpolation is used to account for these effects. As apparent in Eqs. 3.16–3.19, errors in the vertical interpolation at a location (λ, θ) can only occur when the depositional surface mass balance regime between the depositional origin of ice at $(\lambda, \theta, \xi_{k-1})$ and $(\lambda, \theta, \xi_{k+1})$ differs significantly from the accumulation history at GRIP between the times $(t_{\mathrm{d}})_{k-1}$ and $(t_{\mathrm{d}})_{k+1}$. These equations also show that the method applies if there is a proportionality relationship between the mass balance histories. This point can be demonstrated by replacing $\dot{b}(t)$ in Eq. 3.16 by $\kappa\dot{b}(t)$ and noting that ψ_k, $\widetilde{\psi}$ and Ω are scaled in the same way, e.g., $\kappa\psi_k$, etc. In central Greenland, changes in surface temperature are similar because sites have not experienced large elevation changes relative to GRIP and because the difference in origin between two vertical grid points is never large (slow ice flow), so there is a simple proportionality between the balance histories. The method also works satisfactorily in the ablation zone near the ice margin because, here too, the depositional source of ice is located in central Greenland. Thus the depositional source sites for two consecutive grid points are never far apart. The ice margins are where the interpolation error is expected to be the largest but the affected ice volume is small. For regions between central Greenland and the ablation zone, in the upper part of the vertical profiles, the potentially large difference of origin is compensated by the higher accumulation rates (increasing annual layers) and modest ice thickness ($\leq$2000 m), which reduce the age difference between computational levels and thus limit error. Deeper ice originates from central Greenland where interpolation is valid. Numerical tests presented in the following section further reinforce these arguments.

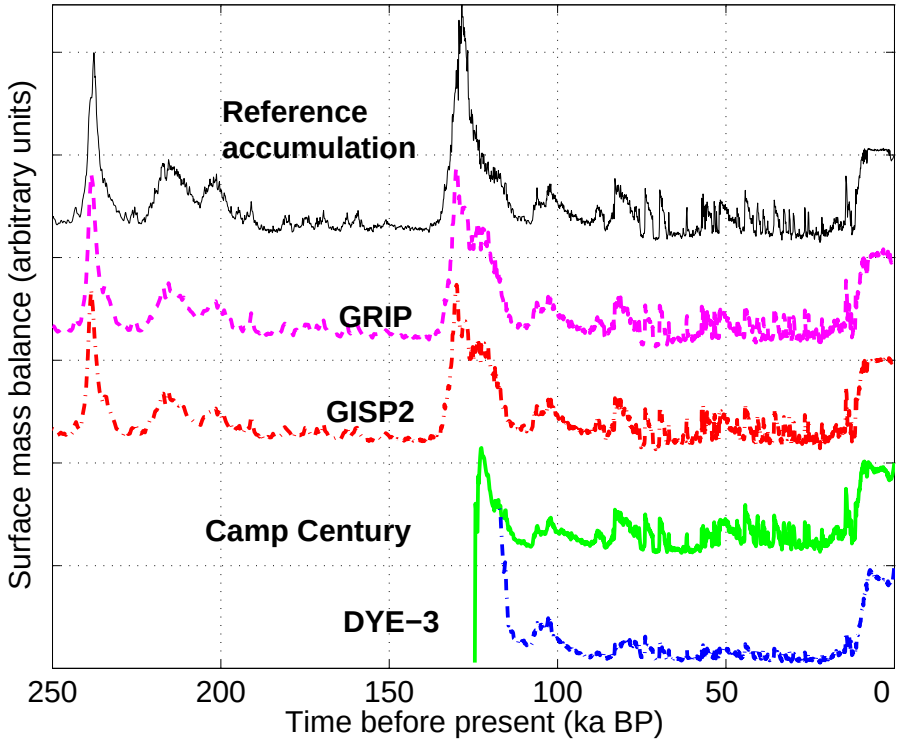

Figure C.1: Normalized accumulation rates for the modelled major ice cores. For all cores, the depositional sites show similar changes in accumulation rates to those at GRIP. This demonstrates that the GRIP-based balance interpolation function applies to the other cores as well.

To illustrate the global applicability of the balance function Ω constructed from the accumulation at GRIP, Fig. C.1 compares the normalized accumulation used for Ω with the modelled depositional mass balance for the GRIP, GISP2, Camp Century and Dye 3 records. All the modelled balance histories resemble the accumulation used for Ω, thus the same cumulative balance can be employed for these sites. Similar observation applies to the main Antarctic ice core sites, as shown in Fig. C.2. Additional tests (not presented here) demonstrate that the method is equally valid for the rest of both ice sheets.

Furthermore, the balance-based interpolation can easy accommodate use of region-specific accumulation histories because the source of ice is also tracked. Thus the method is suitable for modelling large ice sheets where different climatic regimes may apply. Such refinement is unnecessary for the Greenland and Antarctic Ice Sheet as most of their ice core records show the same pattern and rhythm of climate change, but that could apply for modelling the Laurentide and Fennoscandian Ice Sheets, where such regional contrast are expected due to their topography and the changes of moisture source occuring during glacial periods.

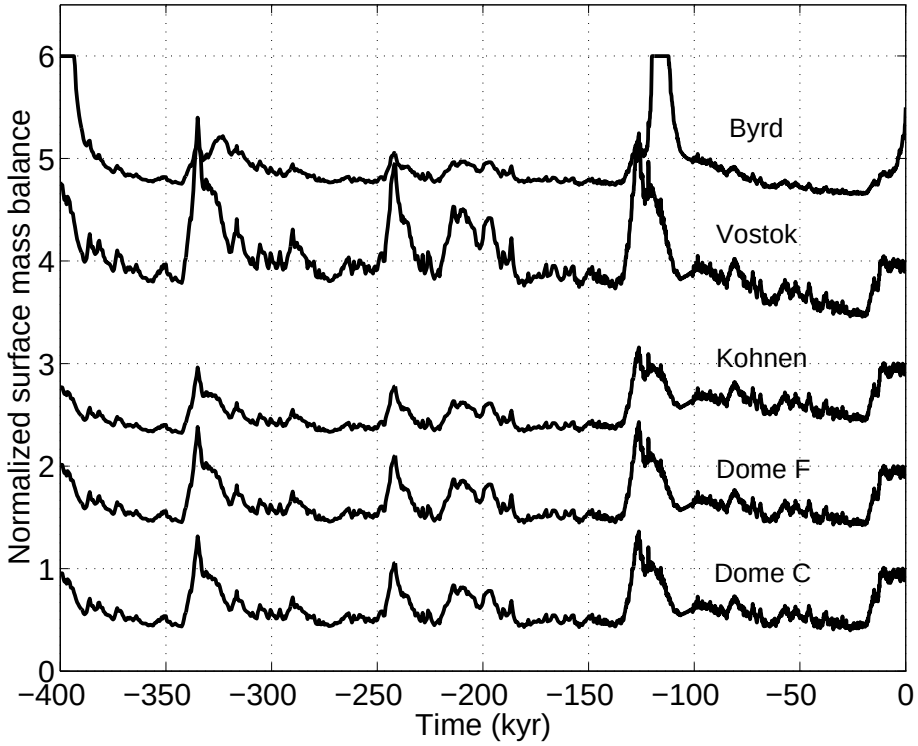

Figure C.2: Normalized accumulation rates for the modelled major ice core drilling sites: Dome C, Dome Fuji, Kohnen Station (Dronning Maudland), Vostok, Byrd. For all cores, the depositional sites show similar changes in accumulation rates to those at Dome C.

C.1.2 Numerical illustration of the accuracy of the balance-based scheme

We illustrate the accuracy of our interpolation scheme by considering the idealized one-dimensional cases of a linear and a parabolic vertical velocity profile. Age–depth profiles computed using the balance-based scheme are compared with those obtained using standard linear and cubic interpolation. As for the three-dimensional model, we use the GRIP accumulation history, but we use the exact (linear or parabolic) rather than model computed velocity to generate the reference age–depth profile. Fig. C.3a shows the depth–paleosurface balance obtained from the reference age–depth profile for the two velocity profiles. Fig. C.3b plots the age error as a function of depth, testing the two velocity profiles for all three different interpolation methods. The cumulative balance is clearly superior to the other methods. Fig. C.3c shows that the error associated with the cumulative balance is at least one order of magnitude better than the other methods for vertical resolution of 11–81 grid points and that cumulative balance has 4th-order accuracy for the linear velocity profile and 2nd-order for the parabolic velocity profile. Additional tests, not presented here, show that: (1) the method is also robust to large time steps (1 kyr is suitable for Central Greenland, in practice we reduce it because of the large melting rates and high velocities at the margins); (2) basal age is comparatively insensitive to how one-sided interpolation is effected in the bottom layer.

Similar tests were performed for mass balance histories that are more typical of the Antarctic Ice Sheetand presented in Fig. C.4. The two upper panels illustrate the case of site like Dome C with low accumulation rate and more than four glacial cycles represented in the ice column (Fig. C.4a). The balance-based method is strikingly superior than the other methods (Fig. C.4b, legend

in Fig. C.4f). The middle panels (c,d) show how a Dome C-based balance function can be used to interpolate age at a site where ice originates from a region with much larger accumulation rate than at the site. There again the cumulative method is more accurate. The lowest panels illustrate the opposite case of ice coming from an upstream region with lower accumulation rate than the site. Again the cumulative method performs better. These tests confirm that the use of a balance function derived from the climate forcing site provides superior accuracy than traditional interpolation method because (1) there are significant variations in ice annual layers due to changes in accumulation rate over time along the depth of an ice column, and (2) changes in accumulation rate affect the entire ice sheet in a similar fashion, thus the use of a balance based function to interpolate age between two computational grid levels remains valid because of the relative proximity of depositional origin of all the ice between these levels.

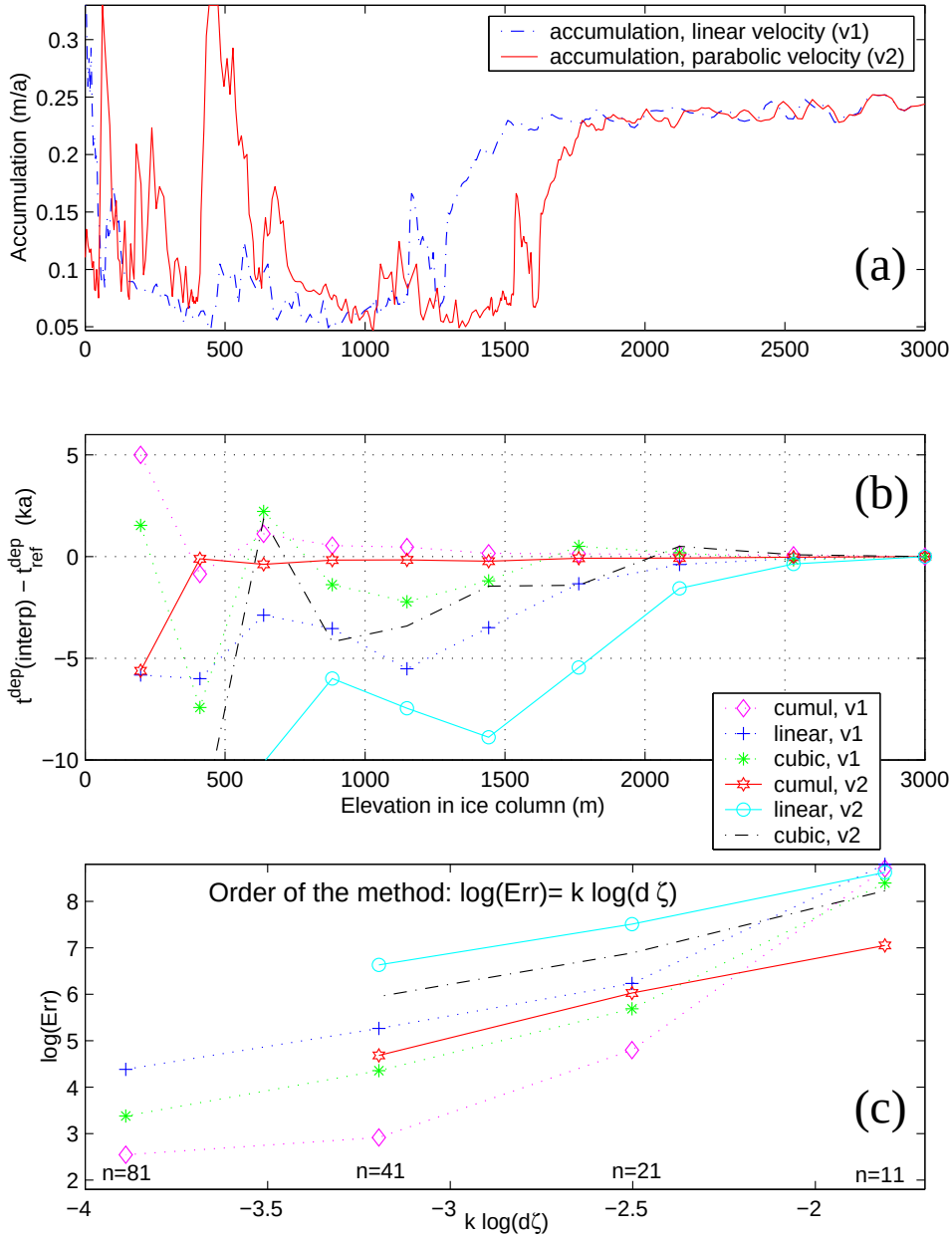

Figure C.3: Comparison of balanced-based interpolation with linear and cubic spline interpolation methods for a GRIP-like accumulation history. (a) Paleosurface mass balance as a function of the elevation above bedrock, obtained from the age–depth profile computed with the exact (linear (v1) or parabolic (v2)) velocity. (b) Age error as a function of elevation. The age difference between the modelled age for the three interpolation methods (balance-based, linear, cubic) and the reference is tested for the linear and parabolic velocity profiles. (c) Order of the interpolation method. Logarithm of the interpolation error plotted as a function of the logarithm of the grid spacing. The same legend applies for panels (b) and (c).

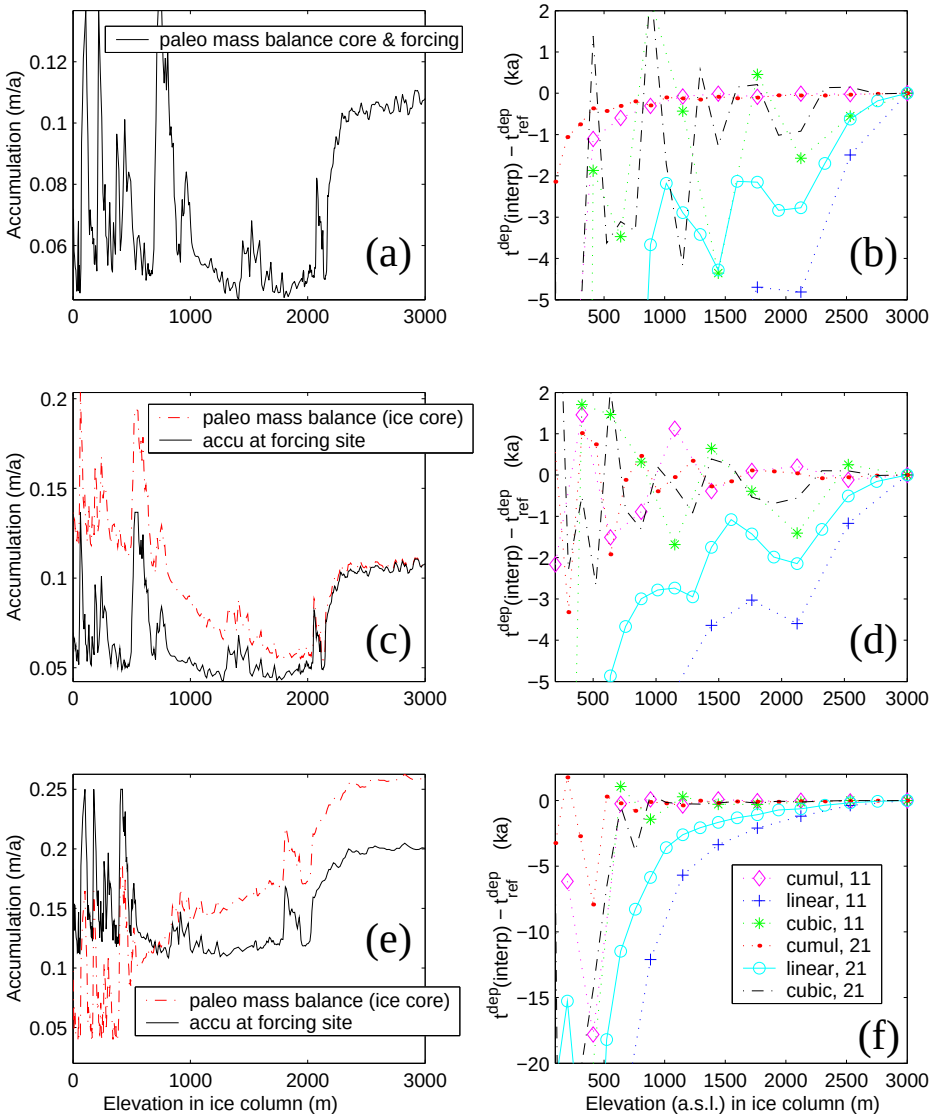

Figure C.4: Age–depth profile (e.g., for an ice core) computed with the balanced-based interpolation relative to linear and cubic spline interpolation methods for low-accumulation sites and sites with increasing or decreasing accumulation trend from upstream. (a, c, e) Paleosurface mass balance as a function of the elevation above bedrock, obtained from the age–depth profile computed with the exact parabolic velocity. (a) Similar balance for the balance function and the interpolated site. (c) Site with higher accumulation upsteam, typical of Vostok, interpolated with function without trend (DC). (e) Site with lower accumulation upstream, e.g. ice moving from desertic plateau to the margins. (b, d, f) Age error as a function of elevation for cases (a), (c) and (e) with 11 and 21-point vertical resolution. Same legend for (b) and (d) as (f).

C.2 Theoretical considerations

C.2.1 Average thinning

The thinning $\widetilde{\psi}$ between z^{D} and z_k is obtained by interpolation of ψ_{k-1} and ψ_k (Eq. 3.15) assuming a simple form for the vertical velocity profile

$$v_z(z,t) = \dot{b}(t)\left(\frac{z}{H}\right)^n - m(t) \tag{C.2}$$

with $n \geq 1$. With the further simplification that the surface mass balance $\dot{b}(t)=\dot{b}_0>0$ and the bottom melting rate $m(t)=m_0$, the vertical strain rate is given by

$$\dot{\epsilon}_{zz} = \dot{b}_0 \frac{\mathrm{d}}{\mathrm{d}z}\left[\left(\frac{z}{H}\right)^n\right]. \tag{C.3}$$

and compressive thinning is

$$\frac{1}{\psi(z)} = \frac{1}{\psi(h_s)} - \int_z^{h_s} \frac{\dot{\epsilon}_{zz}}{\dot{b}_0}\mathrm{d}z = \left(\frac{z}{H}\right)^n. \tag{C.4}$$

Thus the harmonic average of ψ better suits the physics of the problem than linear averaging so we perform a weighted interpolation of ψ using $f_\xi=(\xi^{\mathrm{D}} - \xi_k)/\Delta\xi$ to obtain

$$\frac{1}{\widetilde{\psi}} = \frac{1}{2}\left[(1-f_\xi)\frac{1}{\psi_{k-1}} + (1+f_\xi)\frac{1}{\psi_k}\right]. \tag{C.5}$$

C.2.2 Error estimation

When new numerical algorithms are introduced it is customary to establish their accuracy by operational testing and by a formal error analysis. For the balance-based interpolation scheme, the formal analysis proves to be algebraically tedious and only zealous readers should feel obliged to follow the detailed analysis presented below.

For the numerical implementation, we use ξ rather than z as the vertical coordinate and must therefore transform the equations introduced in Chapter 3 by replacing $\psi(z)$ with an analogous function $\phi(\xi)$ so that $\psi(z)\mathrm{d}z = \phi(\xi)\mathrm{d}\xi$ and Eq. 3.13 is equivalent to

$$b(t_{\mathrm{d}})\,\mathrm{d}t_{\mathrm{d}} = \phi(\xi)\mathrm{d}\xi \tag{C.6}$$

which by transforming Eq. C.5 gives

$$\frac{1}{\widetilde{\phi}} = \frac{1}{2}\left[(1-f_\xi)\frac{1}{\phi_{k-1}} + (1+f_\xi)\frac{1}{\phi_k}\right]. \tag{C.7}$$

Defining the integral function

$$\Phi(\xi) = \int_0^\xi \phi(\xi')\mathrm{d}\xi' \tag{C.8}$$

it follows that

$$\phi_k = \frac{1}{\xi_{k+1}-\xi_k}\int_k^{k+1}\phi(\xi)\mathrm{d}\xi = \frac{\Phi(\xi_{k+1})-\Phi(\xi_k)}{\Delta\xi} \tag{C.9}$$

with $\Delta\xi = \xi_{k+1} - \xi_k = 1/(N-1)$ (with N=21 in the present study), so that

$$\begin{aligned}\frac{1}{\widetilde{\phi}} &= \frac{1}{2}\left[\frac{(1-f_\xi)\Delta\xi}{\Phi(\xi_k)-\Phi(\xi_{k-1})} + \frac{(1+f_\xi)\Delta\xi}{\Phi(\xi_{k+1})-\Phi(\xi_k)}\right] \\ &= \frac{\Delta\xi}{2}\left[\frac{\Phi(\xi_{k+1})-\Phi(\xi_{k-1})+f_\xi(2\Phi(\xi_k)-\Phi(\xi_{k+1})-\Phi(\xi_k)}{[\Phi(\xi_{k+1})-\Phi(\xi_k)]\,[\Phi(\xi_k)-\Phi(\xi_{k-1})]}\right]. \end{aligned} \tag{C.10}$$

Taylor's series expansions of Φ near ξ_k give

$$\begin{aligned}\frac{\Phi(\xi_{k+1})-\Phi(\xi_{k-1})}{2\Delta\xi} &= \frac{d\Phi}{d\xi}(\xi_k) + O(\Delta\xi)^2 \\ \frac{\Phi(\xi_{k+1})-2\Phi(\xi_k)+\Phi(\xi_{k-1})}{\Delta\xi^2} &= \frac{d^2\Phi}{d\xi^2}(\xi_k) + O(\Delta\xi)^2. \end{aligned} \tag{C.11}$$

Substitution of Eqs. C.11 in C.10 and simplification yields

$$\begin{aligned}\frac{1}{\widetilde{\phi}} &= \frac{\Delta\xi}{2}\left\{\frac{2\Delta\xi\left(\dfrac{\mathrm{d}\Phi}{\mathrm{d}\xi}(\xi_k)+O(\Delta\xi)^2\right)-\Delta\xi^2 f_\xi\dfrac{\mathrm{d}^2\Phi}{\mathrm{d}\xi^2}(\xi_k)}{[\Phi(\xi_{k+1})-\Phi(\xi_k)]\,[\Phi(\xi_k)-\Phi(\xi_{k-1})]}\right\} \\ &= \frac{1}{F_1F_2}\frac{\mathrm{d}\Phi}{\mathrm{d}\xi}(\xi_k)\left\{1-\Delta\xi\frac{\dfrac{f_\xi}{2}\dfrac{\mathrm{d}^2\Phi}{\mathrm{d}\xi^2}(\xi_k)+O(\Delta\xi)^2}{\dfrac{\mathrm{d}\Phi}{\mathrm{d}\xi}(\xi_k)}\right\} \end{aligned} \tag{C.12}$$

with

$$\begin{aligned}F_1 &= \frac{\Phi(\xi_{k+1})-\Phi(\xi_k)}{\Delta\xi} = \frac{\mathrm{d}\Phi}{\mathrm{d}\xi}(\xi_k) + \frac{\Delta\xi}{2}\frac{\mathrm{d}^2\Phi}{\mathrm{d}\xi^2}(\xi_k) + O(\Delta\xi)^2 \\ F_2 &= \frac{\Phi(\xi_k)-\Phi(\xi_{k-1})}{\Delta\xi} = \frac{\mathrm{d}\Phi}{\mathrm{d}\xi}(\xi_k) - \frac{\Delta\xi}{2}\frac{\mathrm{d}^2\Phi}{\mathrm{d}\xi^2}(\xi_k) + O(\Delta\xi)^2. \end{aligned} \tag{C.13}$$

Inverting Eq. C.12 and applying the approximation $1/(1-x)$=$1+x+O(x)^2$ gives

$$\widetilde{\phi} = \frac{F_1F_2}{\dfrac{\mathrm{d}\Phi}{\mathrm{d}\xi}(\xi_k)}\left\{1+\Delta\xi\frac{\dfrac{f_\xi}{2}\dfrac{\mathrm{d}^2\Phi}{\mathrm{d}\xi^2}(\xi_k)+O(\Delta\xi)^2}{\dfrac{\mathrm{d}\Phi}{\mathrm{d}\xi}(\xi_k)}\right\}. \tag{C.14}$$

Isolating the product F_1F_2 and simplifying leads to

$$F_1F_2 = \frac{\mathrm{d}\Phi}{\mathrm{d}\xi}(\xi_k)\left[\frac{\mathrm{d}\Phi}{\mathrm{d}\xi}(\xi_k) + O(\Delta\xi)^2\right]. \tag{C.15}$$

Substituting into Eq. C.14 and simplifying, we get

$$\widetilde{\phi} = \frac{\mathrm{d}\Phi}{\mathrm{d}\xi}(\xi_k) + \frac{\Delta\xi}{2}f_\xi\frac{\mathrm{d}^2\Phi}{\mathrm{d}\xi^2}(\xi_k) + O(\Delta\xi)^2. \tag{C.16}$$

We define the mid-trajectory point ξ^{M}=$(\xi^{\mathrm{D}}+\xi_k)/2$ which leads to f_ξ=$(\xi^{\mathrm{D}}-\xi_k)/\Delta\xi$=$2(\xi^{\mathrm{M}}-\xi_k)/\Delta\xi$. Noting that ϕ=dΦ/dξ, Eq. C.16 becomes

$$\widetilde{\phi} = \phi(\xi_k) + (\xi^{\mathrm{M}}-\xi_k)\frac{\mathrm{d}\phi}{\mathrm{d}\xi}(\xi_k) + O(\Delta\xi)^2 \tag{C.17}$$

whereas Taylor's expansion of ϕ near ξ_k gives

$$\phi(\xi) = \phi(\xi_k) + (\xi - \xi_k)\frac{\mathrm{d}\phi}{\mathrm{d}\xi}(\xi_k) + O(\xi - \xi_k)^2 \tag{C.18}$$

with $O(\xi - \xi_k)^2 < O(\Delta\xi)^2$. Finally, recalling Eqs. 3.14, 3.18 and 3.19, the error in approximating $\Omega(t_\mathrm{d})$, equivalent to the error on t_d, is equal to

$$\begin{aligned}
\mathrm{Err}[\Omega](\Delta\xi) = \left|\Omega(t_\mathrm{d}) - \widetilde{\Omega}\right| &= \left|\int_{\xi_k}^{\xi^\mathrm{D}} \phi(\xi)\,\mathrm{d}\xi - \int_{\xi_k}^{\xi^\mathrm{D}} \widetilde{\phi}\,\mathrm{d}\xi\right| \\
&= \left|\int_{\xi_k}^{\xi^\mathrm{D}} \left[(\xi^\mathrm{M} - \xi)\frac{\mathrm{d}\phi}{\mathrm{d}\xi}(\xi_k) + O(\Delta\xi)^2\right]\mathrm{d}\xi\right| \\
&= |0 \times \frac{\mathrm{d}\phi}{\mathrm{d}\xi}(\xi_k) + (\xi^D - \xi_k)O(\Delta\xi)^2| \\
&= |\xi^D - \xi_k| O(\Delta\xi)^2
\end{aligned} \tag{C.19}$$

which demonstrates that the balance-based method is at least second-order in accuracy for any kind of accumulation history. In comparison, linear interpolation as in Clarke and Marshall (2002) gives, at best, an error

$$\begin{aligned}
|t_\mathrm{d} - \widetilde{t_\mathrm{d}}| &= \left|t_\mathrm{d}(\xi^\mathrm{D}) - t_\mathrm{d}(\xi_k) - (\xi^\mathrm{D} - \xi_k)\frac{t_\mathrm{d}(\xi_{k+1}) - t_\mathrm{d}(\xi_k)}{\Delta\xi}\right| \\
&= \left|(\xi^D - \xi_k)\left(\frac{\mathrm{d}t_\mathrm{d}}{\mathrm{d}\xi}(\xi_k) - \frac{t_\mathrm{d}(\xi_{k+1}) - t_\mathrm{d}(\xi_k)}{\Delta\xi}\right)\right| \\
&\geq |\xi^D - \xi_k|\, O(\Delta\xi)
\end{aligned} \tag{C.20}$$

that is first-order only if mass balance is constant. Otherwise, $(t_\mathrm{d}(\xi_{k+1}) - t_\mathrm{d}(\xi_k))/\Delta\xi$ is not even a first-order approximation of the rate of change of the depositional time. Cubic interpolation is similarly second-order only if annual layers have a constant thickness, which is not the case for Greenland history, whereas our method is always at least second-order because the variations of accumulation rate are an explicit part of the interpolation scheme.

APPENDIX D

Supplementary information for Antarctic ice cores

This appendix gathers results that pertain to the context of chapter 7, but might have distracted the reader away from the main issues of that chapter. The first section explores the influence of model parameters on the ice stratigraphy, the second section briefly presents the model predictions for shallow ice cores that were drilled in Antarctica and discussed in Masson et al. (2000).

D.1 Effect of dynamic and climatic parameters

D.1.1 Influence on ice stratigraphy

I now discuss and analyse the influence of the climatic and dynamic parameters of the ice sheet model on the geometry and layering of the Antarctic Ice Sheet. Surface elevation is essentially controlled by basal sliding and basal melting, and to a lesser extent by surface accumulation, with the remarkable exception of Dome Fuji. Given the thermomechanical nature of the model, temperature has an effect on flow (temperature-dependent ice viscosity) and on accumulation rate. Basal sliding ($k_{\rm sl}$ parameter) and the effective viscosity of ice influence flow rate by lowering the surface elevation and increasing the depth of annual layers as their value increases. We find an optimal value for $k_{\rm sl}$ of $\sim$0.25$\times10^{-8}$ m yr^{-1} Pa^{-2}. Geothermal heat flux ($q_{\rm geo}$) controls basal melting and the temperature of basal ice, where stress and deformation concentrate. Alternative values are tested but the standard $q_{\rm geo}$=55 mW m^{-2} is preferred because its value ensures enough basal melting to avoid infinitely old ice but limits basal warming so as to maintain a high standing Antarctic central plateau. These parameters also influence the depth of the oldest glacial cycles predicted by the tracer model. Accumulation rate has a major effect on the depth of annual layers. Its present value ($A(t=0)$) mostly controls the depth of the last glacial transition, whereas the precipitation sensitivity ($D_{\rm acc}$) affects the depth of glacial ice and the two last interglacial periods. Overall, these parameters behave non-linearly, their effects can cancel out each other, complicating the task of finding a unique set of optimum climatic and dynamical parameters. An inverse approach would help address the issue but is yet out-of-reach given the computational burden the method would impose. Therefore the present study illustrates an arbitrarily hand-picked choice of parameters that provides a reasonable fit.

D.1.2 Adjusting surface elevation with $D_{\rm acc}$ near Dome Fuji

Use of the standard parameterization failed to yield an acceptable match with present surface elevation at Dome Fuji. The simulations that best agreed with the Dome C and Vostok surface elevation and ice stratigraphy predicted an elevation of 3730–3740 m, 30–40 m lower than the target. There are various ways of increasing the dome elevation. Decreasing the geothermal heat flux ($q_{\rm geo}$) of 5–10% locally solves the discrepancy by reducing basal melting and lowering basal temperature where

stress concentrates. However, the method fails because ice sheet models for Antarctica assume a spatially uniform value of $q_{\rm geo}$, thus modifying $q_{\rm geo}$ disrupts DC and Vostok by raising their elevation, eliminating basal melting which over-ages basal ice by several 100 kyr without any possible compensating effect to dispose of that excessively old ice. Modification of the effective viscosity of ice or the basal sliding parameter also have global effects that degrade predictions at the other sites for this type of model.

As tuning of global parameters proves to undermine our purpose and similar changes in temperature are manifest at the three drilling sites (e.g., Watanabe et al., 2003), the most likely influential regional effect is a different accumulation regime in the Dome Fuji area. I find that the value of present precipitation at the site has a negligible effect on surface elevation but a significant impact on the depth of the last glacial termination in simulated ice cores. In contrast, lowering the precipitation sensitivity $D_{\rm acc}$ to 0.070 K^{-1} with both climate forcing $\Delta T_{\rm c}$=10°C and 11.5°C lifts the dome by $\sim$35 m; these are the climate forcings previously defined as T1A and T2A. Trials show that this modification must be applied to an extensive area around Dome Fuji to achieve that effect, but not to the entire ice sheet (T1D, T2D) because $D_{\rm acc}$ significantly alters surface elevation (elevation increase for low $D_{\rm acc}$) and depth of annual layers at the other sites. Regional values of $D_{\rm acc}$ are legitimate because different contrast between glacial and interglacial precipition rate can be expected for site having moisture sources in different ocean basins.

D.2 Shallow Antarctic ice cores

So far the main focus of my Antarctic studies has been oriented towards the deep ice cores from Dome C, Vostok and Dome Fuji because they contain the most climatic information and help constrain the predicted ice sheet stratigraphy. Inspired by Masson et al. (2000) who reviewed the Holocene record of 11 deep and shallow ice cores distributed across Antarctica, the following paragraphs document the depositional origin, elevation and temperature predicted by the ice sheet model for these records, combining provenance labels and the depositional archive to recover the conditions at their depositional source. The studied sites are located in the Atlantic quarter of East Antarctica (Dome Fuji, Kohnen Station, Plateau Remote), the central east Antarctic plateau (Dome C, Vostok, Dome B, Komsomolskaia), the nearby coast (Law Dome, D47), the vicinity of the Transantarctic Mountain Range (Taylor Dome near the coast, Dominion Range near the WAIS) and Byrd in the WAIS. References are in Masson et al. (2000).

D.2.1 Surface elevation and origin

Simulated present elevation for the previously selected sites are consigned in Table D.1. These show that the ice sheet model yields a reasonable representation of present surface topography at these sites, with the conspicuous exception of Byrd for which the elevation is greatly underestimated, especially for model T2 (largest glacial–interglacial amplitude). Fig. D.2 shows the difference between the depositional elevation predicted for the ice cores for the past 20 kyr and the simulated present elevation at their drilling site. The figure presents the results with model T2, similar in essence to T1, except for Byrd which lost 1800 m since 20 kyr BP with T2 and 1200 m with T1.

	DF (m)	KS (m)	PR (m)	DC (m)	VO (m)	DB (m)	KO (m)	LD (m)	D47 (m)	TD (m)	DR (m)	BY (m)
T1	3756	2862	3376	3202	3450	3727	3556	1405	1401	2370	2712	890
T2	3737	2876	3383	3206	3452	3737	3564	1418	1399	2396	2738	283
Obs.	3810	2882	3330	3230	3490	3650	3499	1370	1550	2365	2700	1530

Table D.1: Simulated present elevation with models T1 and T2 and observations at Dome Fuji (DF), Kohnen Station (KS), Plateau Remote (PR), EPICA-Dome C (DC), Vostok (VO), Dome B (DB), Komsomolskaia (KO), Law Dome (LD), D47, Taylor Dome (TD), Dominion Range (DR) and Byrd (BY).

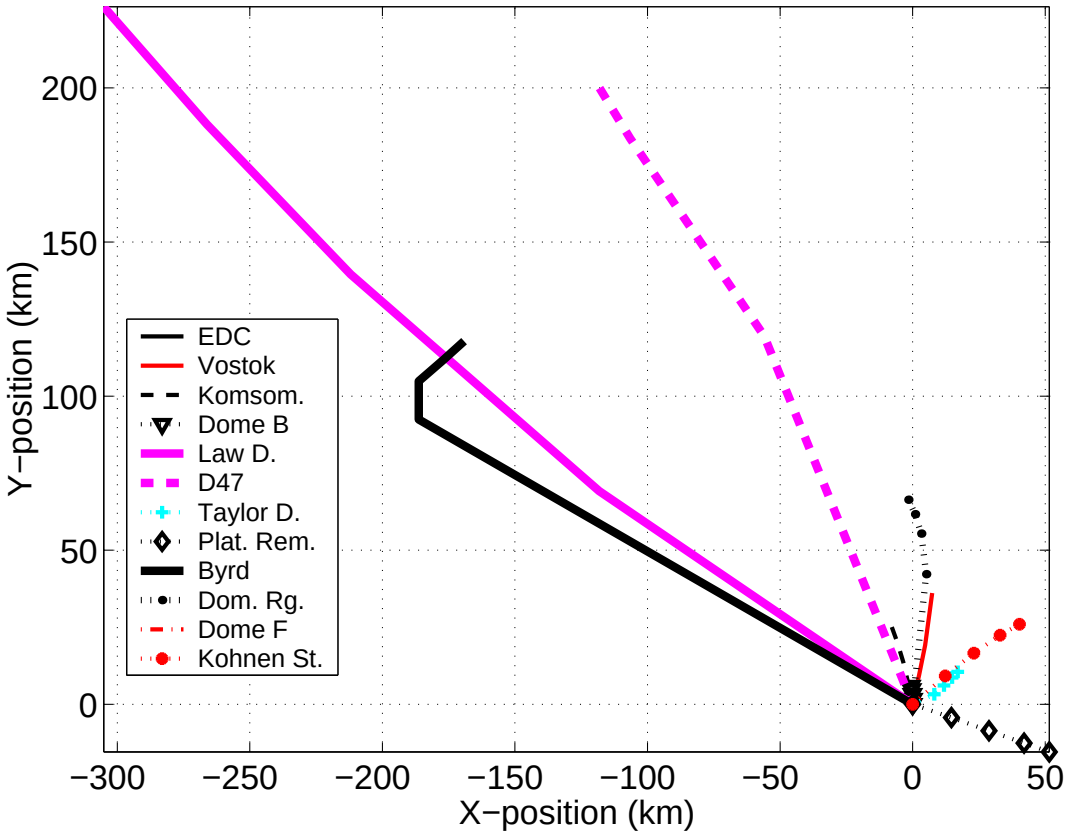

Figure D.1: Difference between the depositional origin predicted for selected ice core records and the present location of their drilling site. We show the result of model T2 for the past 20 kyr of the simulated cores.

Fig. D.1 illustrates the relative origin of ice in the predicted ice cores, with Law Dome, D47, Byrd and Dominion Range showing the furthest depositional origin. Thus the large changes in depositional elevation observed in Fig. D.2 are mostly caused by distant depositional origin.

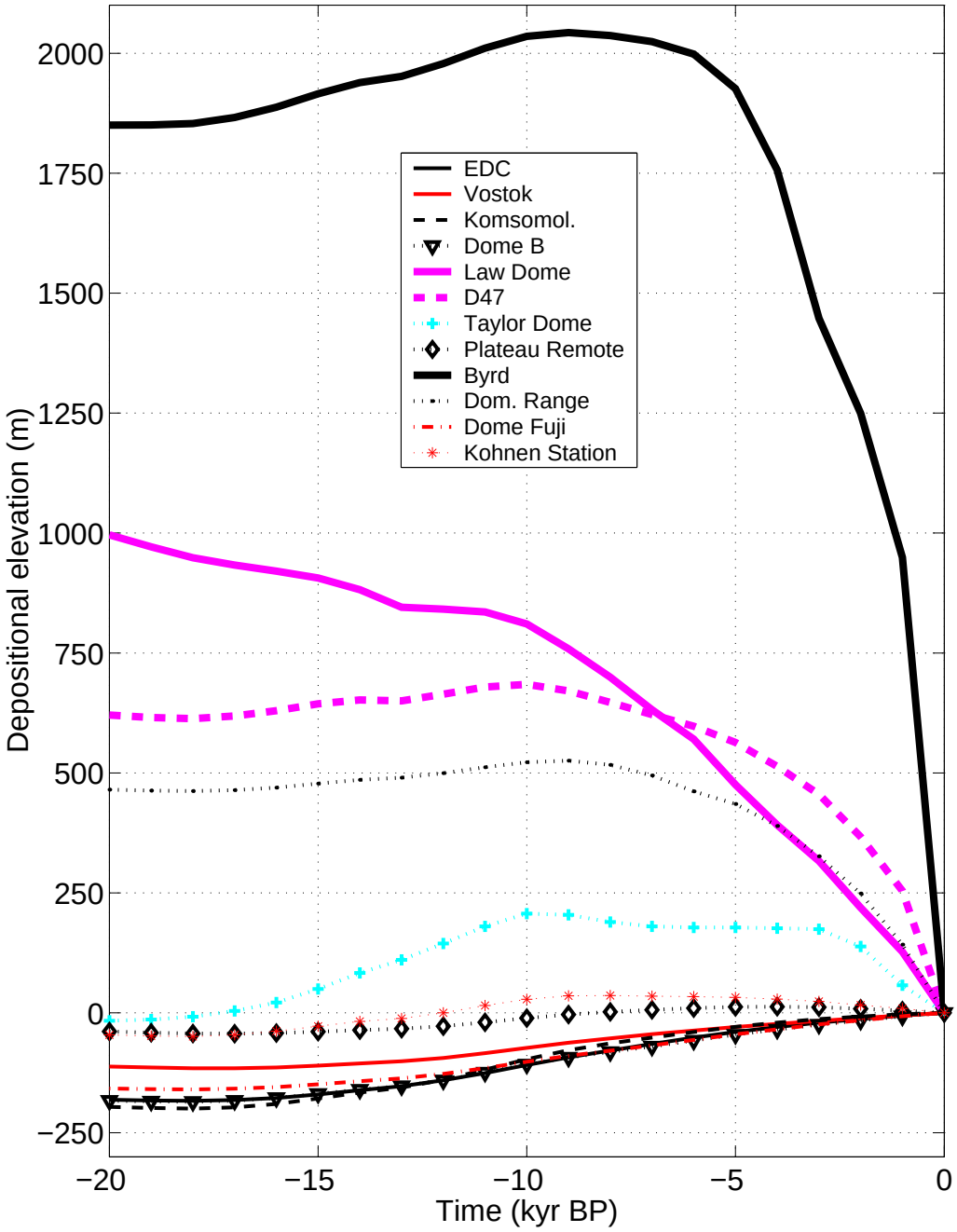

Figure D.2: Difference between the depositional elevation predicted for selected ice core records and the present elevation at their drilling site. We show the result of model T2 and focus on the past 20 kyr.

D.2.2 Paleotemperature

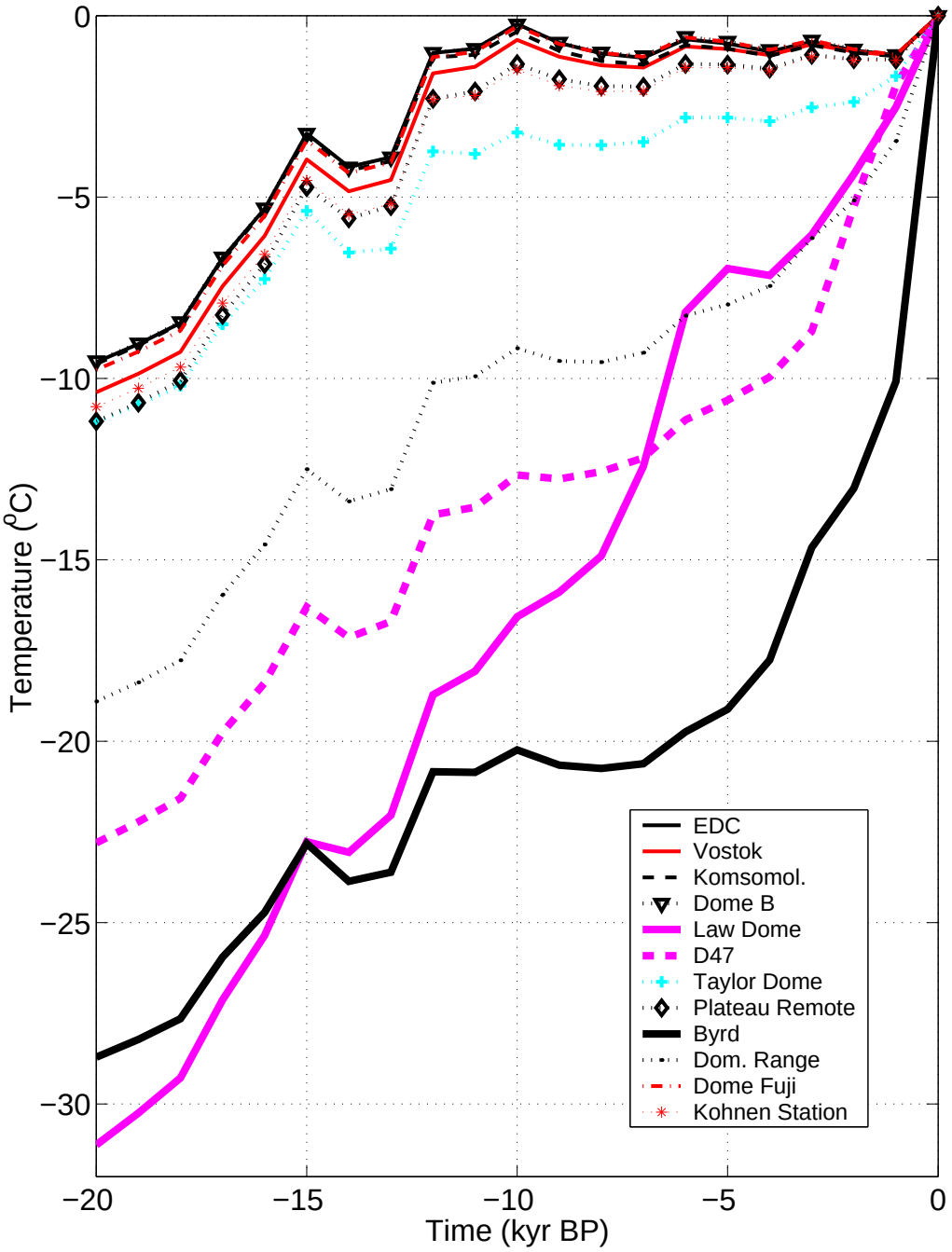

Figure D.3: Difference between the depositional temperature predicted along 12 ice core records and the present temperature at their drilling site, using model T2.

Fig. D.3 shows the difference between the depositional temperature predicted for the previously selected ice cores and the present temperature at their drilling site. Most sites show a relatively

stable temperature history in agreement with Vostok and Dome C. Plateau Remote and Kohnen Station show a small increase during the Holocene, Taylor Dome a slightly larger increase. The coastal records from Law Dome and D47 and the WAIS sites of Byrd and Dominion Range show a large increase in depositional temperature during that period because of the large predicted changes in elevation.

Ice cores with predicted stable temperature history agree with δD records in Masson et al. (2000). The recent increase in δ^{18}O at D47 is here explained by an origin effect from higher and colder depositional sites. Records for Law Dome and Taylor Dome show a decreasing δ^{18}O trend during the Holocene while the model predicts an increase. The largest differences appear for the West Antarctic records from Byrd and Dominion Range for which the model predict a distant origin and thus large changes in temperature and δD content. Current refinements of the ice sheet model, an increased spatial resolution and a better treatment of ice streams and ice shelves, should improve simulations of the WAIS in a near future.